About the Production of
Residual Nuclides by Neutron-Induced
Reactions
up to 180 MeV

Contents

Kurzzusammenfassung

Im Rahmen der Erforschung kosmochemisch relevanter Kernreaktionen in extraterrestrischer Materie hat unsere Arbeitsgruppe bereits um die 24.000 Reaktionsquerschnitte protoneninduzierter Reaktionen im Energiebereich bis 2.6 GeV bestimmt. Die hieraus resultierende Datenbank umfasst systematische Reaktionsquerschnittsmessungen von mehr als 550 Produkt/Target Kombinationen einschließlich der Messungen an C, N, O, Mg, Al, Si, Ca, Ti, V, Mn, Fe, Co, Ni, Cu, Rb, Sr, Y, Zr, Nb, Mo, Rh, Ag, In, Te, Ba, La und Pb.

Im Zuge der Erweiterung der bisherigen Forschung beschäftigt sich diese Arbeit nicht mit der Messung protoneninduzierter Reaktionsquerschnitte, sondern mit der Messung neutroneninduzierter Reaktionsquerschnitte. Hierfür stellt diese Arbeit einen neuen experimentellen Ansatz vor, der auf der Entfaltung der Anregungsfunktionen aus experimentellen Datensätzen beruht. In diesem Zusammenhang wurden insgesamt 21 Bestrahlungsexperimente mit quasi monoenergetischen Neutronen der ^{7}Li(p,n)^{7}Be Reaktion durchgeführt. Die hierbei betrachteten Neutronenenergien (der sog. Peakneutronen) decken das Spektrum von 32.7 bis 175.4 MeV ab. Für jedes bestrahlte Target wurden anschließend mit Hilfe sich gegenseitig ergänzender neutronenspektroskopischer Techniken, der Systematik der ^{7}Li(p,n)^{7}Be Reaktion und Monte-Carlo Neutronentransportrechnungen sowohl der individuelle Neutronenfluss als auch das Neutronenspektrum bestimmt. Ferner wurden alle Targets (C, O, Mg, Al, Si, Fe, Co, Ni, Cu, Ag, Te, Pb und U) γ-spektrometrisch untersucht, wobei die Produktionsraten von mehr als 100 relativ kurzlebigen Restkernen bestimmt werden konnten. Zusätzlich zu dieser experimentellen Komponente wurden für die gefundenen Restkerne die Neutronenanregungsfunktionen mittels TALYS 1.0, einer Software zur Simulation von Kernreaktionen, berechnet.

Unter Verwendung dieser drei Ausgangswerte, der spektralen Neutronenflüsse, der Produktionsraten und der TALYS-Berechnungen, konnten die Anregungsfunktionen der gefundenen Restkerne aus den Responseintegralen entfaltet werden. Der hierzu verwendete mathematische Algorithmus basiert auf dem wohlbekannten STAY'SL Formalismus.

Um die Qualität dieses experimentellen Ansatzes zu überprüfen, wurden einige entfaltete Anregungsfunktionen benutzt, um bereits bekannte, experimentell gemessene Produktionsraten aus Dick-Target-Experimenten unserer Arbeitsgruppe neu zu berechnen. Es stellte sich heraus, dass die so ermittelten Produktionsraten in guter

Übereinstimmung mit denen der Dick-Target-Experimente stehen. Diese Ergebnisse bestätigen, dass sich der vorgestellte experimentelle Ansatz zur Bestimmung von Neutronenanregungsfunktionen auf der Basis von Aktivierungsexperimenten mit quasi monoenergetischen Neutronen eignet. Somit wird mit dieser Arbeit nicht nur ein bis dato einzigartiges Set von mehr als 100 experimentellen Neutronenanregungsfunktionen für Energien bis 180 MeV bereitgestellt sondern es werden zusätzlich neue Perspektiven für die experimentelle Bestimmung von Neutronenanregungsfunktionen eröffnet.

Schlagworte: Wirkungsquerschnitte, Restkerne, Neutronen, mittlere Energien

Abstract

Within the framework of investigations into nuclear reactions in extraterrestrial matter our working group has already measured nearly 24,000 cosmochemical relevant cross sections of proton-induced reactions up to 2.6 GeV. The database which originate from these measurements comprises systematic cross section measurements for more than 550 target/product combinations including the targets C, N, O, Mg, Al, Si, Ca, Ti, V, Mn, Fe, Co, Ni, Cu, Rb, Sr, Y, Zr, Nb, Mo, Rh, Ag, In, Te, Ba, La and Pb. Extending these earlier investigations, the present work does not focus on proton-induced but on neutron-induced reactions. To this end, we propose a novel experimental approach which is based on the unfolding of excitation functions from experimental data. In this context, 21 irradiation experiments with quasi mono-energetic neutrons from the ^{7}Li(p,n)^{7}Be reaction were performed. Here, the investigated neutron energies (peak component) cover a spectra from 32.7 up to 175.4 MeV. For each irradiated target the individual neutron flux and neutron spectrum was determined employing complementary neutron spectroscopy techniques, the systematics of the ^{7}Li(p,n)^{7}Be reaction and Monte Carlo neutron transport calculations. All irradiated targets (C, O, Mg, Al, Si, Fe, Co, Ni, Cu, Ag, Te, Pb and U) were examined via γ-spectrometry and the production yields of more than 100 relatively short-lived residual nuclides were determined. In addition to the experimental measurements, the excitation functions of all found neutron induced reactions were calculated using TALYS 1.0, a state-of-the-art software for the simulation of nuclear reactions.

Using the spectral neutron flux, the experimentally measured production yields and the theoretical TALYS calculations it was possible to unfold the excitation functions of the found residual nuclides from their response integrals. The mathematical algorithm used for this purpose is based on the well-known STAY'SL formalism.

In order to examine the quality of this experimental approach several unfolded excitation functions were tested with thick-target experiments of our group. It turned out, that the production rates measured in these thick-targets could be reproduced using the unfolded neutron excitation functions. This tests show that the experimental approach is qualified to determine excitation functions using high current neutron sources of quasi mono-energetic energies. Therefore this work opens new perspectives for the determination of neutron cross sections and additionally provides a unique set of experimental excitation functions for neutron induced reactions up to 180 MeV.

Keywords: cross sections, residual nuclides, neutrons, medium energy

Acknowledgements

1   Introduction

The present work is devoted to the calculation of nuclear reaction cross sections. During the last decades this branch of physics got more and more important for a wide field of technical and scientific applications, including astrophysics, space and environmental sciences, medicine (radionuclide production, dosimetry in mixed nucleon fields, radiation therapy), accelerator technology (activation of detectors, radiation protection, online mass separation), space and aviation technology, accelerator based nuclear waste transmutation and many more (see Table 1.1). With respect to the large number of disciplines with interest in nuclear reaction cross sections, it is not surprising that this work was motivated by a cosmochemical issue, the unsolved issue of neutron-induced activation yields in meteorites.

In general, cosmochemistry focuses on questions regarding the origin and development of the elements and their isotopes. With respect to this focus, cosmochemistry is based on a certain interdisciplinarity which includes nuclear physics or more specifically nuclear reactions in extraterrestrial matter.

Concerning with the origin and development of the substances, cosmochemistry involves direct measurements of isotopic abundance ratios in samples of micrometeorites, meteorites and other extraterrestrial materials. Variation of isotopic abundance ratios measured in cosmochemical samples often can be attributed to naturally occurring nuclear reaction. That is because on their way through space, most of this cosmochem-

Table 1.1: Examples for applications of nuclear data.

Nuclear Physics

· Systematic of Nuclear Reactions

· Pre-equilibrium Model

· Intra-Nuclear Cascade Model

· Pre-equilibrium Decay

· Spallation and Fragmentation

· Fission at Medium Energies

Astronomy

· Element Synthesis
· Remote Sensing of Planetary Surfaces
· Isotope Ratio in the Solar System
· Terrestrial Age of Meteorites

Particle Accelerator Technology

· Activation of Detectors
· Radiation Protection
· Online Mass Separation
· Radioactivity in Beam Pipes

Medicine

· Radionuclide Production
· Radiation Therapy

Space- and Aeronautical Technology

· Radiation Protection
· Materials Science

1

ical samples were directly exposed to cosmic rays, a stream of high-energy charged particles. These cosmic rays induce nuclear reactions that can strongly influence the isotopic abundance in exposed materials. From particular interest for cosmochemists are nuclear reactions that produce radionuclides with half-lifes of more than one month and stable noble gases. In the best case, the exposure history of extraterrestrial matter can be inferred from the abundance of different cosmogenic nuclides within the exposed body. Consequently, the knowledge of the composition and spectra of cosmic rays as well as the reaction cross sections are from major interest for cosmochemists.

1.1 Solar Cosmic Rays

Cosmic rays can be divided by their origin, composition and energy into solar cosmic rays (SCR) and galactic cosmic rays (GCR).

A cosmic ray burst was first time recorded on February the 28 and March 7, 1942 and the sun could be unambiguously identified as the source of high-velocity particles with energies up to $> 10^{10}$ eV. During the following decades ground based and balloon experiments coupled with data from near earth satellites and space probes throughout the heliosphere have greatly increased the understanding of the SCR dynamics. This data and observations show, that the SCR spectrum is mainly determined though the mechanisms of acceleration in solar flares and undergoes a primary change in the corona while the particles escape from the sun. According to the explosive character of solar flares, the observed SCR spectra during a solar particle event (SPE) near the Earth may cover 5 orders of magnitude from > 1 MeV to > 10 GeV and the flux changes may amount to 6-8 orders of magnitude for protons [48, 49]. Furthermore, the generated particle fluence is subject of huge fluctuations and depends strongly on the related solar flare.

From long term SCR observations and from the analysis of the related X-Rays emissions it would appear, that solar flares can be classified into two distinct types: explosive with durations of minutes and gradual with durations of hours and days [55]. In the line with these classification, not only the flux and spectra of the SCR varies but the element abundances change, too (see Table 1.2).

The frequency of occurrence of solar flares is a concomitant of the solar activity and thus, with the 11-year-solar-cycle. During the peak of the 11-year-cycle the Sun is more active and there are typically more sunspots and more solar flares seen. Due to this fluctuations, in particular long time average parameter of the SCR are meaningful.

Table 1.2: Properties of impulsive and gradual events [60]

Properties	Impulsive Events	Gradual Events
Duration	hours	days
Events/year	~ 1000	~ 10
H/He	~ 10	~ 100
He^3/He^4	~ 1	~ 0.0005
O/Fe	~ 1	~ 10

Observations during the three 11-year-solar-cycles ending in 1988 show, that protons dominate the SCR with an average fraction of 98 % followed by a 2 % fraction of α-particles [23, 38]. The mean flux density of protons and alphas was about 100 particles $cm^{-2}s^{-1}$ and about 1 particle $cm^{-2}s^{-1}$ for heavier nuclei [23]. The commonly used model to describe the observed SCR spectra is an exponential law in rigidity

$$\phi(R) = \phi_0 \; e^{-\frac{R}{R_0}} \tag{1.1}$$

where R_0 is a rigidity depending parameter, ϕ_0 is the 4π integral flux density and the rigidity $R = cP/Ze$ is defined by the speed of light c, the particle momentum p, the particle charge Ze.

1.2 Galactic Cosmic Rays

Contrary to SCR, galactic cosmic rays originate in sources outside the solar system, distributed passim in our Milky Way galaxy. In the times before particle accelerators reached very high energies, galactic cosmic rays served as a source of particles for high energy physics investigations, and led to the discovery of subatomic particles, e.g. the muon. Nowadays the main focus of GCR research is rather directed towards astrophysical investigations than to particle physics. However, during the last decades a relatively new field of research was established, the so-called astroparticle physics. Emerging from the intersection of astronomy, particle physics and cosmology astroparticle physics aims to answer where GCR originate, how the GCR constituents can be accelerated to such high energies, what role they play in the dynamics of the Galaxy, and what their composition tells us about matter from outside the solar system. Substantially the GCR include all of the elements in the periodic table but, are domi-

nated by protons (87%) and α-particles (12%). Only 1% of the GCR are heavier nuclei [66]. This composition is significantly different from the composition of the SCR, where α-particles and heavier nuclei together sum up to about 2%. The typical energies of galactic cosmic rays are between 100 MeV and 10 GeV. Nevertheless, cosmic rays have energies far beyond 10 GeV and on rare occasions (< 1 particle km^{-2}year^{-1}) even energies of up to 10^{20} eV were measured [11]. The flux of GCR-particles decreases rapidly for energies beyond 1 GeV. The energy dependence of the GCR proton component can be roughly written [12, 52] as

$$\frac{\mathrm{d}\phi(E)}{\mathrm{d}E} = 1.24 \cdot 10^6 \ \frac{E_P(E_P + 2m_P)(E_P + 780 \cdot e^{-2.510^4 E_P} + M)^{2.65}}{(E_P + M)(E_P + 2m_P + M)} \qquad (1.2)$$

wherein $\mathrm{d}\phi(E)/\mathrm{d}E$ is expressed in cm^{2}s^{-1}MeV^{-1}, E_P [MeV] is the kinetic energy of the GCR protons, m_P [MeV] this the proton mass and M [MeV] is the modulation parameter that describes the energy-loss of an proton on the way reaching the inner solar system. Regarding to the energy per nucleon, similar spectral flux densities apply to α-particles and analogous formulas can be used [12]. The modulation can be attributed to deflection by the interplanetary magnetic field embedded in the solar wind.

Since the solar activity varies over the 11 year solar cycle the modulation and therefore the intensity of cosmic rays at Earth varies, too. Within this period the modulation parameter M may change between 100 and 1000 MeV. The spectral flux den-
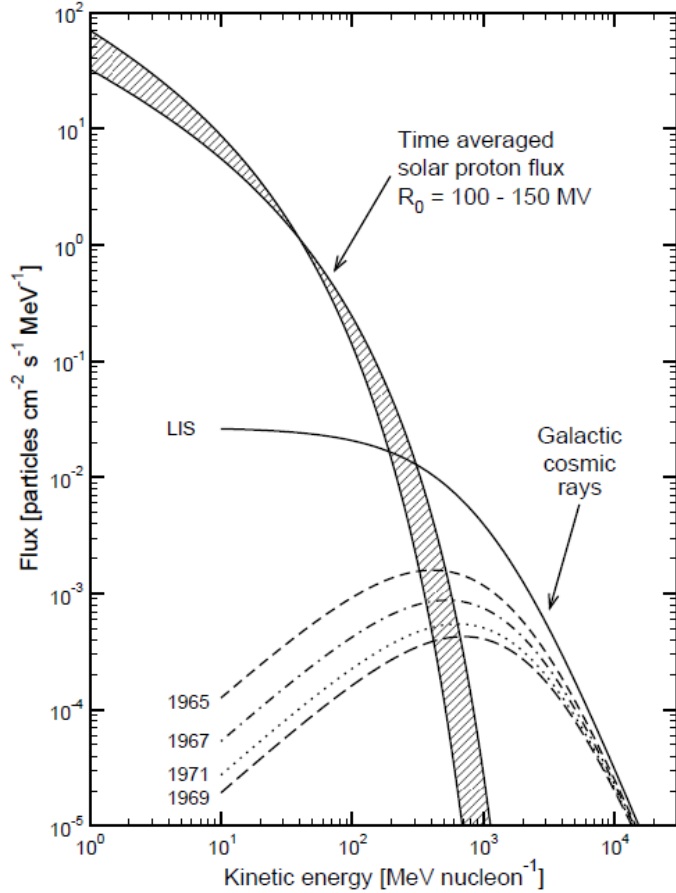

Figure 1.1: GCR proton fluxes near the Earth for solar modulation in the years 1965, 1967, 1971, and 1969 and averaged SCR proton flux. LIS holds for Local Interstellar Spectrum. [45]

sities of the SCR and GCR are shown in Figure 1.1. The GCR flux is plotted for the modulation parameter 470, 680, 880, and 1000 MeV. This values correspond to the modulation measured in the years 1965, 1967,1971 and 1969. It can be seen, that GCR flux is sensitive to changes in the modulation parameter M. This sensitivity applies in particular for energies below a few GeV. The Local Interstellar Spectra (LIS) ploted in Figure 1.1 is calculated using equation 1.2 with $M = 0$.

1.3   Cosmogenic Nuclides

As previously mentioned, the interaction of cosmic rays with the nuclei of exposed material induce nuclear reactions. The isotopes that are produced by this interaction are referred to as cosmogenic nuclides. The production yield of this cosmogenic nuclides is usually inferred from isotope abundance anomalies. Here, the abundance anomalies concern both, existence of stable and radionuclides.

In this context, the cosmogenic nuclides measured in extraterrestrial can be classified by their half-lifes. While stable products, in particular rare gases, integrate over the entire exposure history, radionuclides unveil exposure information about 3 half-lifes [45]. A selection of relevant cosmogenic nuclides with half-lifes above 1 month is shown in table 1.3.

In order to reason from the measured abundance to complex irradiation histories, the

Table 1.3: Some relevant cosmogenic nuclides with half-lifes above 1 month

Nuclide	$t_{1/2}$	Nuclide	$t_{1/2}$	Nuclide	$t_{1/2}$
^{37}Ar	35.04 d	^{39}Ar	269 a	^{53}Mn	3.74 Ma
^{56}Co	77.27 d	^{14}C	5730 a	^{129}I	15.7 Ma
^{22}Na	2.602 a	^{59}Ni	0.076 Ma	^{40}K	1.277 Ga
^{55}Fe	2.73 a	^{41}Ca	0.103 Ma	He	stable
^{60}Co	5.271 a	^{81}Kr	0.229 Ma	Ne	stable
^{3}He	12.33 a	^{36}Cl	0.301 Ma	Ar	stable
^{44}Ti	62 a	^{26}Al	0.717 Ma	Kr	stable
^{32}Si	150 a	^{10}Be	1.51 Ma	Xe	stable

production cross sections are the key quantity.

For this reason, several (thin-target and thick-target) activation experiments were performed during the last decades. Most of those experiments devote to the studies of proton-induced reactions and were carried out at accelerators, where targets of high purity levels were irradiated with monoenergetic particle beams at different energies.

Usually the irradiated targets were thin foils (thin-targets), since this setup allows the particle beam to pass through the target without considerable changes of the differential projectile flux. In contrast, thick-target experiments demand flux corrections according to scattering, isotropy of irradiation, energy loss, the production of secondary particles and the loss of such secondary particles at the target surface. In particular the secondary particle loss complicated the interpretation of thick target experiments. A way out of this problem was the isotropic target irradiation, which simplified the treatment of surface effects. For the first time this experimental approach was applied in series of thick-target experiments at the 600-MeV proton beam of the CERN synchrocyclotron. In the framework of this series three artificial meteoroids made out of diorite and gabbro were isotropically irradiated and the particle flux within these meteoroids successfully modeled [17]. However, except for few isotropic target irradiation most of the thick-target experiments could not come up to expectations [46].

In order to determine the reaction cross sections the activation yields of thin- and thick-target experiments were measured by gamma spectrometry, accelerator mass spectrometry (AMS) or conventional rare gas mass spectrometry. The cross sections $\sigma(E_0)$ were calculated subsequently from the production rates $\dot{N}_{Res.}$ using equation 1.3, where $\phi_P(E_0)$ is the monoenergetic particle flux.

$$\dot{N}_{Res.} = \sigma(E_0)\phi_P(E_0)N_{Target} \tag{1.3}$$

Activation experiments performed by our group reveal essential information about relevant cross sections of proton-induced reactions up to 2.6 GeV on the target elements C, N, O, Mg, Al, Si, Ca, Ti, V, Mn, Fe, Co, Ni, Cu, Rb, Sr, Y, Zr, Nb, Mo, Rh, Ag, In, Te, Ba, La and Pb (e.g. Michel et al [44], Leya et al. [37], Gloris et al [22]). In 2010, the IRS (ZSR) database covers more than 550 target/product combinations with nearly 24,000 cosmochemical relevant cross sections of proton-induced reactions.
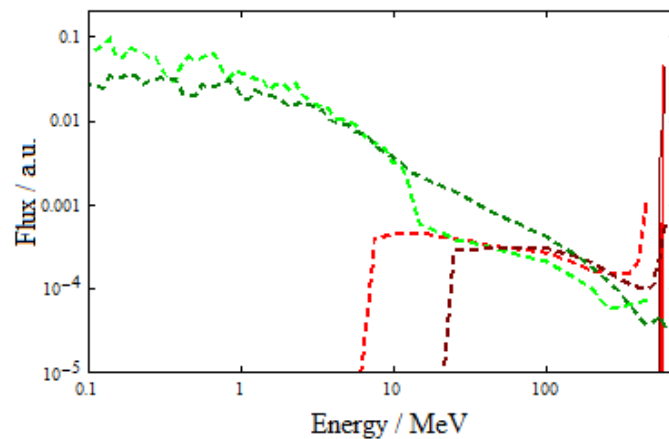
1.4   Cosmic Ray Induced Reactions

Considering the stopping power of the incident protons, it is in principle possible to reveal the exposure history of lunar material and meteoroids using the proton cross sections of the above-mentioned thin-target proton irradiation experiments. However, the exclusive consideration of proton induced reaction limits the analysis of the irradiated

material to the outmost surface, since only in the outer layers nuclear active secondary particles can be widely neglected. This applies evidently only to meteoroids which are relatively bulky, since otherwise the nuclear active secondary particles produced at one side of the irradiated body may pass through the entire meteoroid and induce nuclear reactions at surface of the other side. At the surface (depth ≤ 15 g cm^{-1}) of such bulky exposed bodies the nuclide production is widely dominated by SCR interactions. This dominance can be attributed to the SCR flux, which is (for energies < 200 MeV/A) orders of magnitudes higher than the GCR (see Figure 1.1).

A different situation is given for the nuclide production beyond the surface. Penetration depths of more than ≤ 15 g cm^{-1} are hardly reached by the relatively low energetic SCR, and the nuclide production has to be assigned to the GCR and to secondary particles, in particular neutrons. Already the discovery of the cosmic rays by Victor Francis Hess in 1912 (Nobel laureate in physics in 1936) demonstrated that GCR particles penetrate deep into the earth's atmosphere. Actually GCR interactions and the interactions induced by secondary particles exceed hundreds of g cm^{-1} in depth. The continuing production of secondary particles along the penetration path caused by high energies of the GCR and the related induced

Figure 1.2: The particle flux spectra of a 5cm radius gabbro meteoroid irradiated isotropically with 600 MeV protons calculated with HERMES (see page 43). The plotted flux constituents are primary protons (red solid), secondary protons (red dashed) and secondary neutrons (green dashed) where the graphs darker in tone represent the flux close to the center of the meteoroid and the graphs lighter in tone represent the flux spectra close to surface.

intra- and internuclear cascades makes it much more complicated to reason from the activation yields to the exposure history.

The particular importance of secondary neutrons and their dominance in the particle flux can be seen in Figure 1.2. It shows the differential flux of secondary particles at the surface and in 5 cm depth of a 10 cm diameter artificial gabbro meteoroid

irradiated isotropically with 600 MeV protons.

In spite of the complicated nature of GCR interactions, this medium and high energy interaction are of great interest in cosmochemistry. One reason for this interest is the fact, that meteorites found on earth lost their outer shells due to ablation on their path through the atmosphere. In other cases the atmospheric friction may even cause a break-up of the primary meteoroid into many pieces. In any event cosmogenic nuclides measured in meteorites found on earth are rather produced by GCR interactions than by SCR interactions.

In order to reveal any information from the activation yields found in meteorites, the spectra of primary and secondary GCR particles inside of irradiated object have to be modeled. The general propagation of particles in matter and the cascade evolution can be described by a parameterized Boltzmann equation [53], where the parameter have to be determined experimentally. On account of the stochastically characteristics of the particle transport, the modeled particle spectra are usually based on Monte Carlo simulations, e.g. LAHET [58]. These Monte Carlo simulations require the input of physical quantities like a primary energy spectrum, a primary particle composition, an elemental composition of target material and cross sections.

The GCR production rates can be calculated using the modeled particle transport spectra, if the cross sections for the production of cosmogenic nuclides are known. Cross sections of proton induced reactions are available for many relevant reaction and originate from the above-mentioned thin-target irradiation experiments and are included in the nuclear reaction data library EXFOR [42].

A different situation applies to the cross sections of neutron induced reactions. Whereas experimental cross sections of low energy neutron reactions exist and are stored in evaluated neutron data libraries(see JENDL [65], ENDF [43], JEF [61]), cross sections for energies exceeding about 15 MeV are rare. The deficit of neutron data above 15 MeV can be attributed to the missing electric charge of the neutron. The electrically neutral properties make a direct acceleration of neutrons via electromagnetic fields impossible. Accordingly, the preparation of appropriate experimental setups is challenging and almost all available neutron cross sections above 15 MeV originate from the work of Imamura [28], Uno [72], Kim [32, 33] and Sisterson [68, 69, 67].

However, the missing experimental cross sections, can be achieved alternatively by theoretical modeling calculations. These modeling calculations usually use approximations, simplifications and vary phenomenological models that deal with different

aspects of atomic nuclei and nuclear reactions (see chapter 6). Being ware of the risks and limitations, that are related to the use of such nuclear models, theoretical calculations become a powerful way-out to advance in this branch of research. However, in spite of several improvements achieved by the code systems during the last years, modeling calculations of medium energies activation yields still have at best uncertainties of the order of a factor two [47]. Actually the intercomparison for intermediate energy activation yields between modeling codes and available experimental data demonstrated that average deviations are frequently even much larger than this factor two and individual reaction-wise deviations may go up to three orders of magnitude [47]. This relatively large size of the uncertainties complicate the use modeling calculation in technical and scientific applications including the simulation of nuclide production in meteorites (see table 1.1).

However, the calculation activation yields in meteorites had to use theoretical modeled neutron cross sections for intermediate energy, since a experimental data basis is missing. Hence, the modeling of activation yields in meteorites using theoretical neutron cross sections is either unreliable or very imprecise. In this context, such theoretical calculations of activation yields may have a negative connotation.

Based on the fact that the substitution of experimental cross section by theoretical cross sections is rather unsatisfying, this work is devoted to the calculation of neutron cross sections on the base of experimental data.

1.5 Aim of this Work

The goal of the present work is to provide excitation functions for neutron-induced reactions of medium energies that have a smaller uncertainty than pure predictive theoretical calculations. To this end, this work proposes a new scientific approach which is based on the unfolding of the excitation function $\sigma(E)$ from the response integral $\int \sigma(E)\phi(E)\mathrm{d}E$ of the activation equation 1.4.

$$\dot{N}_{Res.} = N_{Target} \int \sigma(E)\phi(E)\mathrm{d}E. \tag{1.4}$$

The present work describes the entire scientific approach starting from theoretical background and the performed activation experiments until the determination of activation yields, the calculation of theoretical guess functions and unfolding of the excitation

functions.

Further this work discusses the unfolding results and reviews their applicability for activation yield modeling calculation. For this purpose unfolded excitation functions are used to model production rates of experiments performed with artificial meteoroids and the calculated activation yields are compared with experimental data.

2 Experimental Method

In the field of nuclear and particle physics, the probability of a particular interaction between a particle and either another particle or a nucleus is from major interest. It is expressed by a quantity that is called cross section σ, which depends not only on the type of involved particles but also on their kinetic energies[1]. This energy depending function is usually referred to as the excitation function $\sigma(E)$ of a reaction.

Commonly, production cross sections are determined from experiments that are based on a mono-energetic projectile fluence $\phi(E_0)$. In that case, the response integral (see equation 2.1) can be transformed into an ordinary product (see equation 2.2) and the cross section can be calculated directly from the number of produced residual nuclei N , the atomic mass of the target element A_T and the Avogadro number N_A.

$$N = \frac{N_A}{A_T} \int \sigma(E)\phi(E_0)\mathrm{d}E \tag{2.1}$$

$$= \frac{N_A}{A_T} \sigma(E_0)\phi(E_0) \tag{2.2}$$

In the case of neutron-induced reactions, the generation of a proper, monoenergetic projectile-beam of medium energies is not possible, due to a missing neutron charge. Accordingly, the direct calculation of reaction cross sections from the number of residual nuclei N is not feasible.

For this reason, present work proposes an indirect approach to derive the cross sections. This approach is based on the unfolding of the excitation function $\sigma(E)$ from the response integral $\int \sigma(E)\phi(E)\mathrm{d}E$. For this purpose, a set J of irradiation experiments has to be performed and the number of produced nuclei N_j for a desired target-product combination has to be measured (see equation 2.3).

$$N_j = \frac{N_A}{A_T} \int \sigma(E)\phi_j(E)\mathrm{d}E \tag{2.3}$$

For each experiment j the response integral that is taken over the energy has to be decomposed into a sum over discrete energy intervals E_i and the neutron fluence $\phi(E_i)$ has to be determined for each energy interval (see equation 2.4).

$$N_j = \frac{N_A}{A_T} \sum_{i=1}^{I} \sigma(E_i)\phi_j(E_i) \tag{2.4}$$

---

1 cross sections may depend on further quantities e.g. spin

In this manner, a linear system of equations is build. It consists of I variables (fluence intervals $\phi(E_i)$) and J equations (number of produced nuclei N_j). Since this system of linear equations consists of error-prone quantities, it is likely not well conditioned and produces a residual vector $\vec{\chi}$(see equation (2.5)).

$$\vec{\chi} = \begin{pmatrix} \chi_1 \\ \chi_2 \\ \vdots \\ \chi_J \end{pmatrix} = \begin{pmatrix} N_1 \\ N_2 \\ \vdots \\ N_J \end{pmatrix} - \frac{N_A}{A_T} \cdot \begin{pmatrix} \sigma(E_1)\phi_1(E_1) & + & \ldots & + & \sigma(E_I)\phi_1(E_I) \\ \sigma(E_1)\phi_2(E_1) & + & \ldots & + & \sigma(E_I)\phi_2(E_I) \\ \vdots & + & \ddots & + & \vdots \\ \sigma(E_1)\phi_J(E_1) & + & \ldots & + & \sigma(E_I)\phi_J(E_I) \end{pmatrix} \quad (2.5)$$

For the further discussion, equation 2.5 is rewritten to the more clear form of equation 2.6, where $\vec{\chi}$ is again the residual vector, $\vec{N}$ is the vector of the number of produced nuclei, $\vec{\sigma}$ is the desired vector of the cross sections and F fluence matrix with I columns and J rows.

$$\vec{\chi} = \vec{N} - F \cdot \vec{\sigma} \quad (2.6)$$

The uncertainties of the measurements are taken into consideration by the use of the covariance matrix K. Assuming Gaussian probability distributions for the measured experimental number of produced nuclei N_j, a matrix element $K(\vec{N})_{k,l}$ is calculated using the expectation values of these number of nuclei (see equation 2.7).

$$K(\vec{N})_{k,l} = \langle N_k \mid N_l \rangle - \langle N_k \rangle \langle N_l \rangle \quad (2.7)$$

In the same way a second covariance matrix $K(F)$ is calculated. It considers the uncertainties of the neutron fluence. Considering these uncertainties, the desired vector $\vec{\sigma}$ can be calculated by using the method of least-square adjustment. Doing so, the square of the residual vector $\vec{\chi}^2$ has to be minimized (see equation 2.8)

$$\chi^2 = (\vec{N} - F\vec{\sigma})^T V^{-1} (\vec{N} - F\vec{\sigma}) \rightarrow \min \quad (2.8)$$

where $V = K(\vec{N}) + \vec{\sigma}^T K(F)\vec{\sigma}$ is the weighting matrix for the number of produced nuclei and the superscript T indicates the transposition of a matrix or vector, respectively.

In the present work, the systems of equations were underdetermined since the number of performed activation experiments is smaller than the number of fluence intervals. This means, that depending on the examined target-product combinations, up to 155 energy intervals but at most the number of produced nuclei of 20 irradiation experiments were

available. Hence, the fluence matrix F contains more columns than rows ($I > J$) and an ordinary least-square unfolding fails. The required additional information was provided by guess vector $\vec{g}$. This vector contains a priori information about the cross sections and was calculated by the program TALYS, which is software for the simulation of nuclear reactions. The uncertainties of this theoretical guess vector were considered by an additional covariance matrix $K(\vec{g})$. Making use of the guess vector $\vec{g}$, equation 2.8 is rewritten to

$$\chi^2 = (\vec{N} - F\vec{\sigma})^T W^{-1} (\vec{N} - F\vec{\sigma}) + (\vec{\sigma} - \vec{g})^T K(\vec{g})^{-1} (\vec{\sigma} - \vec{g}) \;\rightarrow\; \min \qquad (2.9)$$

where $W = K(\vec{N}) + \vec{g}^T K(F) \vec{g}$ is the new weighting matrix. The insertion of $\vec{g}$ in the weighting matrix (instead of $\vec{\sigma}$) is the so-called linear approximation.
The formal solution of equation 2.9 is found employing a vector $\vec{\lambda}$ of Lagrange multiplier $2\lambda_j$ together with the following boundary condition

$$0 = F(\vec{\sigma} - \vec{g}) + F\vec{g} - \vec{N} - F\vec{\sigma} + \vec{N}. \qquad (2.10)$$

Taking this condition into consideration the final expression for the least-square condition is

$$
\begin{aligned}
\chi^2 \;=\;& (\vec{N} - F\vec{\sigma})^T W^{-1} (\vec{N} - F\vec{\sigma}) + (\vec{\sigma} - \vec{g})^T K(\vec{g})^{-1} (\vec{\sigma} - \vec{g}) \\
+\;& 2\vec{\lambda} \; (F(\vec{\sigma} - \vec{g}) + F(\vec{g} - \vec{\sigma}) - \vec{N} + \vec{N}) \;\rightarrow\; \min.
\end{aligned}
\qquad (2.11)
$$

The quantity χ^2 has to be minimized for the variable $\vec{\sigma}$ and the related vector $F\vec{\sigma}$. Consequently, equation 2.11 has to be derived and set to 0. The derivative leads to

$$\frac{\partial \chi^2}{\partial \vec{\sigma}} \;=\; 0 \;=\; 2 \, (\vec{N} - F\vec{\sigma})^T W^{-1} - 2 \, \vec{\lambda}^T \qquad (2.12)$$

and

$$\frac{\partial \chi^2}{\partial (F\vec{\sigma})} \;=\; 0 \;=\; 2 \, (\vec{\sigma} - \vec{g})^T K(\vec{g})^{-1} + 2 \, \vec{\lambda}^T F \qquad (2.13)$$

In a first step equation 2.13 is rewritten to

$$(\vec{g} - \vec{\sigma}) \;=\; K(\vec{g})^T \, F^T \, \vec{\lambda} \qquad (2.14)$$

and in a second step, equation 2.14 gets multiplied with the matrix F and $\vec{\lambda}W^T$ is added.

$$\vec{\lambda}W^T \ + \ F \ (\vec{g} - \vec{\sigma}) \ = \ \lambda W^T \ + \ F \ K(\vec{g})^T \ F^T \ \vec{\lambda}. \tag{2.15}$$

An conversion of equation 2.12 leads to

$$\vec{\lambda}W^T \ = \ (\vec{N} - F\vec{g}). \tag{2.16}$$

In a third step equation 2.16 is used to substitute the first addend in equation 2.15

$$\vec{N} - F\vec{g} \ + \ F \ (\vec{g} - \vec{\sigma}) \ = \vec{N} - F\vec{\sigma} \ = \ \lambda W^T \ + \ F \ K(\vec{g})^T \ F^T \ \vec{\lambda} \tag{2.17}$$

and the new equation can be solved for $\vec{\lambda}$.

$$\vec{\lambda} \ = \ (W^T \ + \ F \ K(\vec{g})^T \ F^T)^{-1}(\vec{N} \ - \ F \ \vec{\sigma}) \tag{2.18}$$

The calculated expression is used to replace $\vec{\lambda}$ in equation 2.14

$$(\vec{\sigma} - \vec{g}) \ = \ - \ K(\vec{g})^T \ F^T \ (W^T \ + \ F \ K(\vec{g})^T \ F^T)^{-1}(\vec{N} - F \ \vec{\sigma}) \tag{2.19}$$

Finally the method of Lagrange multiplier solves the least-square problem and leads to

$$\vec{\sigma} = \vec{g} - K(\vec{g})F^T X^{-1}(\vec{N} - F\vec{g}) \tag{2.20}$$

where $X = W + FK(\vec{g})F^T$. The resulting covariance matrix, which includes the entire information about the occurring measurement uncertainties is given by equation 2.21.

$$K(\vec{\sigma}) = K(\vec{g}) + K(\vec{g})F^T X^{-1} F K(\vec{g})^T. \tag{2.21}$$

With the deduction of equation 2.20 and equation 2.21 is possible to unfold an neutron excitation function considering experimental data and their variances.

This Least-Squares-Adjustment is the main element of the program STAY'SL which was used in the present work. More details of the unfolding procedure with STAY'SL will be discussed in section 7.

In summary, the excitation functions for the studied neutron induced reactions were unfolded from a set of different response integrals using the last Least-Squares-Adjustment of the STAY'SL formalism. For this purpose, the number of produced nuclei $\vec{N}$,

the differential neutron fluence $\phi(E)$ and a predicted guess functions $\vec{g}$ had to be known. In the next sections it will be discussed how these input quantities were achieved.

3   Activation Experiments

3.1   General Requirements

On the contrary to low energy activation experiments, the preparation of proper medium energy neutron beams encounters difficulties. Actually it is impossible to generate pure monoenergetic neutron, since within this energy range the nuclear behavior permits only a production of quasi-monoenergetic neutrons fields that contain a continuum of lower energy neutrons.

Most conveniently in this context is the bombarding of light elements with protons, since for several light nuclei the neutrons are "loosely" bounded and the energy levels are widely separated. Commonly considered to generate quasi-mono-energetic neutron fields are reactions between protons and ^{2}H, ^{6}Li, ^{7}Li and ^{9}Be. In the present work, the ^{7}Li(p,n)^{7}Be reaction was used to prepare the neutron fields.

The required protons of the ^{7}Li(p,n)^{7}Be are usually generated by particle accelerators. Although plenty of particle accelerator exist, the number of facilities suitable for extensive neutron production is limited. The small number of suitable accelerators can be attributed to the facility layout, which has to consider that the propagation direction of neutrons can not be influenced by electromagnetic fields.

A brief overview of candidate accelerators and their properties are given in Table 3.1. The reliability of quantitative activation analysis is strongly related to the amounts of activated nuclei. Hence, it was necessary to achieve sufficient large numbers of residual

Table 3.1: Particle accelerators and their maximal neutron flux

Particle Accelerator	Proton Energy MeV	Target	Target Size mm	Maximum n-flux 10^7 cm^{-2}h^{-1}
CYRIC	25 and 35	Li	2	$6{,}5 \cdot 10^{-3}$
PSI	$30-70$	^{9}Be	2	3,6
UCL	$20-80$	Li	$3-10$	**470**
TIARA	$45-90$	^{7}Li	$3{,}6-6{,}6$	14
TSL Blue Hall	$50-180$	^{7}Li	$2-10$	3,6
TSL PARTY	$50-180$	^{7}Li	$2-10$	**100**
RIKEN	$80-210$	^{7}Li	10	0,5

nuclei. Since the flux scales linearly with the residual nuclide production rate $\dot{N}_Y$ (see equation 3.1), a high neutron flux ϕ_n was desirable.

$$\dot{N}_Y = \sigma(E)\phi_n N_X - \lambda N_Y \tag{3.1}$$

The importance of a high projectile flux becomes clear considering that the produced neutron flux is up to four orders of magnitude smaller then the flux of the incident protons. In addition to the high flux it was desired, that the performed experiments cover a wide energy spectra. For this reason, the selection of the particle accelerators was based in both selection criteria: the achievable proton flux and the proton energy. Due to this requirements, the experiments were carried out at the particle accelerator in the Université catholique de Louvain (UCL) at Louvain-la-Neuve (Belgium) and at the particle accelerator in The Svedberg Laboratorium (TSL) at Uppsala (Sweden). In this connection the merit of the UCL facility was the high flux, which was about a factor 4 higher than at the Svedberg Laboratorium. In return the maximum proton energy at the TSL was about 180 MeV whereas the proton energies at Louvain were limited to 70 MeV. Therefore, the activation experiments at the UCL and TSL have a complementary character.

Over a 5 year period starting 1997 and ending 2002 a set of 21 activation experiments was carried out at the UCL and TSL, respectively, and 13 different targets, C, O, Mg, Al, Si, Fe, Co, Ni, Cu, Ag, Te, Pb and U were irradiated. The neutron energies were 32.7, 32.9, 45.3, 45.3, 59.9 and 59.9 MeV at the UCL and 46.2, 65.4, 66.4, 73.8, 89.6, 94.3, 95.0, 95.7, 96.1, 96.2, 133.0, 133.7, 144.8, 173.9 and 175.4 MeV at the TSL, where the neutron energies are relate to the high-energy peak of the quasi mono-energetic neutron spectra. Referring to the experimental facility and to the chronological order the nomenclature of the irradiation experiments follows the pattern Louv02,...,Louv07 for the UCL and Uppn0e,....,Uppn0v for the TSL.

3.2   Target Arrangement

Usually targeta are either irradiated in the form of single target foils or directly as a whole target foil piles, the so-called stacked-foil. Both irradiation setups have advantages and disadvantages. The irradiation of single foils allows the widely neglect of unwanted secondary particles in the target. In contrast, secondary particles usually
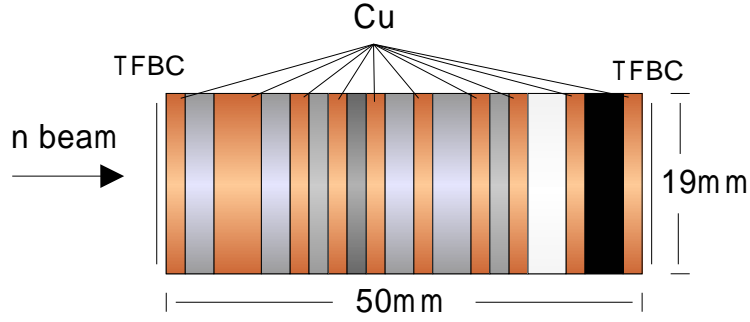
Figure 3.1: Layout of a target stack used in the present work

have to be considered in stacked-foil setups. Nevertheless, parallel irradiation of several targets using one projectile beam that passes through the complete target stack keeps the experiment less time consuming and more economical.

In the present work the stacked-foil irradiation technique was employed at both accelerators, Louvain-la-Neuve and Uppsala. The single targets were piled up to small cylinders of up to 2.5 cm diameter up to 6.6 cm height (see Figure 3.1). All used targets were solids of high purity and natural isotopic ratios. The high purity of the target is insofar necessary as the range of the expected cross section covers 3 orders of magnitude. Thus, impurities of 10^{-3} may cause non negligible influence on the experimental results. Some characteristics of the used targets are given in table 3.2. The arrangement of the targets inside of the stack was chosen, to minimize the energy loss of the

Table 3.2: Target materials and some of their characteristics.

Element	Z	Purity	Manufacturer	Fields of Incidence
C	6	99,95%	Goodfellow	Systematics, Cosmo. Nuclide
O as SiO$_2$	8	Suprasil	Heraeus	Cosmogenic Nuclide
Al	13	99,999%	Goodfellow	ADS, Systematics, Cosmo. Nuclide
Si	14	unknown	Wacker	Semiconductors, Cosmo. Nuclide
Fe	26	99,5%	Goodfellow	ADS, Cosmo. Nuclide, Steal Alloys
Co	27	99,9%	Goodfellow	Systematics, Alloys
Ni	28	99,999%	Goodfellow	Cosmogenic Nuclide
Cu	29	99,9%	electrolyte copper	Monitoring
Ag	47	99,95%	Goodfellow	Monitoring
Te	52	unknown	Johnson Matthey	cosmogenic Nuclide
Pb	82	99,95%	Goodfellow	ADS, Radiation Shielding
U	92	unknown	unknown	ADS, Systematics

neutron beam inside the stack. Therefore the targets with a elements of a high mass number were placed facing the beam, whereas the targets of elements with light masses were put on the opposite side. Between the targets, copper foils were deposited. These copper discs were inserted into the stack in order to monitor of the relative neutron fluence, by comparing changes in the activation yields of products from copper along the stack.

However, it turned out, that spectral changes of the neutron field caused by neutron scattering and by the production of secondary particles, in particular secondary neutrons, had a big influence on the production rate in the monitor foils. Thus, theoretical neutron transport Monte Carlo simulations result better agreements with the production rates than experimental monitoring using copper foils. Accordingly, these theoretical calculations were carried out for all performed activation experiments in order to model the changes of the neuron flux inside of the target stack (see chapter 4.1).

3.3 Uppsala-Accelerator

3.3.1 Accelerator Setup

The irradiation experiments at the The Svedberg Laboratory (TSL) at Uppsala were performed by the former ZSR members S.Neumann [52] and W.Glasser in collaboration with the Gustaf Werner Cyclotron, the Department of Neutron Research at Studsvik and the Department of Nuclear Chemistry of the University of Köln. Figure 3.2 shows the setup of the cyclotron accelerator at the Svedberg Laboratory. The cyclotron was able to work with two different settings, the isochron and the synchrocyclotron Once switch to the first mode, the accelerator produces protons up to 96MeV and
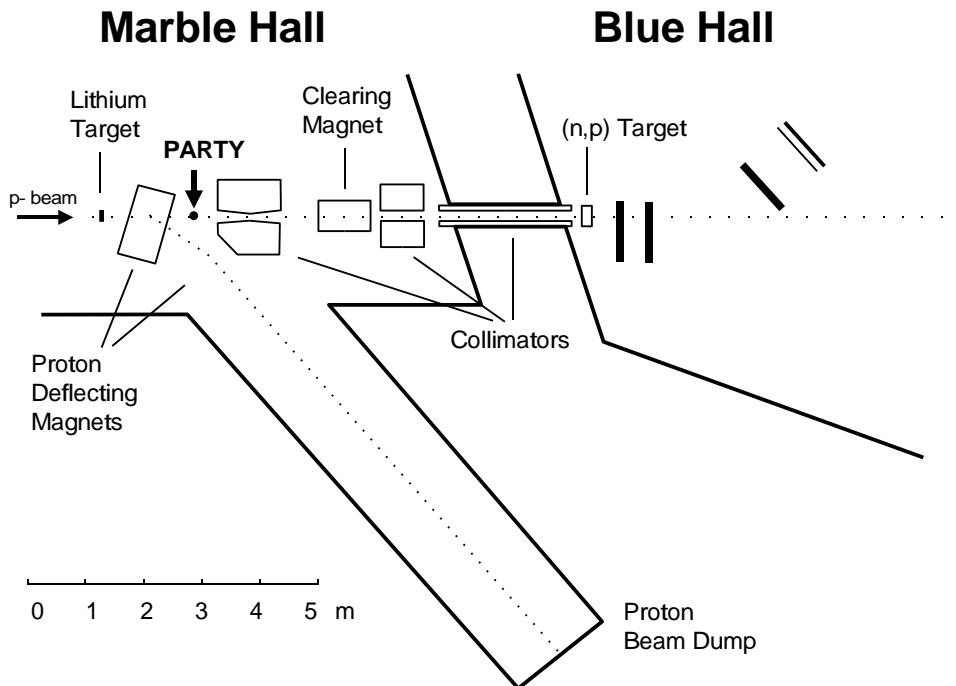
Figure 3.2: Particle Accelerator at the TSL at Uppsala

ions up to $192\frac{Q^2}{A}$MeV, where Q is the charge and A is the mass of the individual ion. In the second mode, the cyclotron, generates protons up to 180 MeV. To create the projectiles three ion sources were available, an internal PIG (Penning Ionization Gauge) in order to produce protons, an ERC (Electron Cyclotron Resonance) for the production of heavy ions and an atom beam ion source to create polarized protons and deuterons. The quasi mono-energetic neutron field was produced by the ^{7}Li(p,n)^{7}Be reaction. The ^{7}Li target was placed in Marble Hall, where it was irradiated by the proton beam. The employed ^{7}Li targets were between 20 and 100 $\frac{mg}{cm^2}$ thick and had

an isotope purity of 99.984 %. The ^{7}Li was inserted into a holder that was made of steal. This holding device was cooled by water and wobbled in an amplitude of 4mm at a frequency of 0.2Hz, in order to avoid a overheating of the target under the high intensity of the proton beam of up to 10 μA. Behind the target, the residual projectile protons and eventually produced charged ejectiles were deflected by a magnetic field towards a beam dump that was located 8 meters far from the ^{7}Li target. The produced neutron beam propagated straight ahead unaffected by the magnetic field. On its way, the created neutron beam was collimated by three collimating devices. The beam vacuum ended behind the first collimating device. While the beam passed through the vacuum limiting diaphragm, charged particles were produced. For this reason, the first collimator was followed by a clearing magnet. The (n,p) targets were arranged 9 meter behind the ^{7}Li target inside of the Blue Hall.

In order to see whether the experimental setup suits the desired purpose or not, a test experiment was performed. This experiment was also designed to find the optimal position for the (n,X) targets. It was found out, that the target stack was well positioned in an angle of 1.55° to the zero axis of the neutron beam. The distance to the ^{7}Li target was 192.0 cm. In this peripheral position, the (p,x) targets were not affecting the central neutron beam. Hence, it was still possible to perform undisturbed (n,p) experiments in the Blue Hall, while the experiments of the present work were using the extant unused neutron beam **par**asi**t**icall**y** (PARTY).
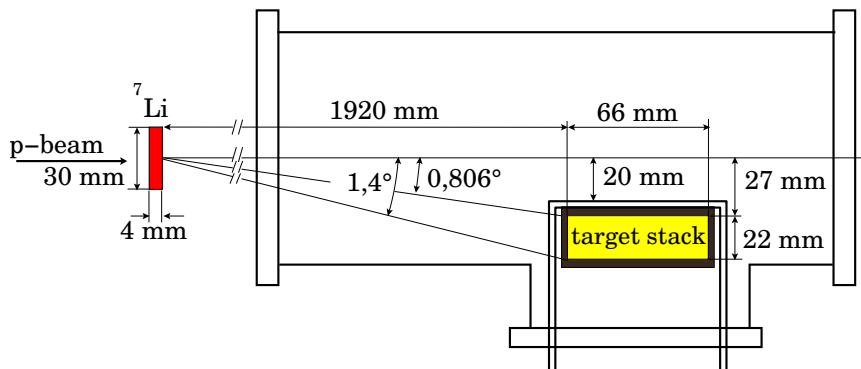
Figure 3.3: Shuttle position at the PARTY-Setup

3.3.2 Buildup of the Target Stacks

As mentioned previously, the targets were irradiated in a piled up arrangement, the so-called stacked-foil setup. To this end the target piles were inserted into an aluminum container, which is referred to as the stack shuttle or more simple shuttle. The diameter of the inner repository of the shuttle was 25 mm. This dimension presupposed a target diameter of a maximum of 25 mm. A scheme is shown in Figure 3.4. Unfortunately not all the targets were available with 25 mm diameter, but smaller. In those cases the target cylinders were inserted into a ring-shaped holder device of aluminum. This ring shaped strickle had an outer diameter of 25 mm and an inner diameter that was of adapted the size of the target. Since during the irradiation it was impossible to enter the room where the experiments were carried out, the shuttle was pneumatically "shot" from outside through a plastic tube to inside the Marble Hall. There it was received by a small hoist which lifted the shuttle into the neutron beam. In this position, the shuttle was placed inside an air containing area
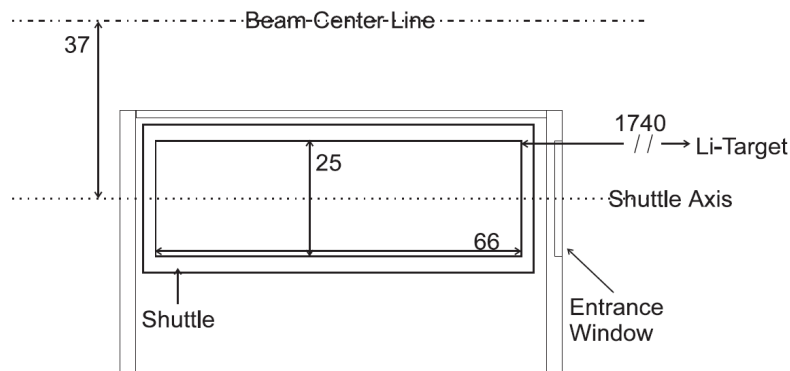
Figure 3.4: The shuttle

of the Marble Hall, but it was directly connected to the vacuum beam from its front side, separated only by a thin aluminum window. This positioning was expected to minimize the influence on the neutron beam by the environment, e.g., scattering loss inside the air.

3.3.3 Flux Monitoring

In order to compute the excitation functions of the neutron induced reaction, information about the neutron fluence and absolute neutron spectra were essential to collect. The monitoring of the neutron beam fluence was performed in collaboration with the

group of V. Eismont from the V.G. Khlopin Radium Institute of Sankt Petersburg, Russia. For this purpose, thin film breakdown counters (TFBC) were employed [70, 19]. A TFBC is basically a capacitor. This capacitor is made of a 3mm thick mono crystalline silicon plate (pole) that is covered by a 100 nm thin layer (isolator) of SiO_2. Upon this coverage a layer (antipole) of 30 nm aluminum is superimposed. In between these two capacitors a fissionable ^{238}U or ^{209}Bi target is inserted. A schematic drawing of the employed TFBC system is shown in Figure 3.5. Each capacitor (TFBC) was charged
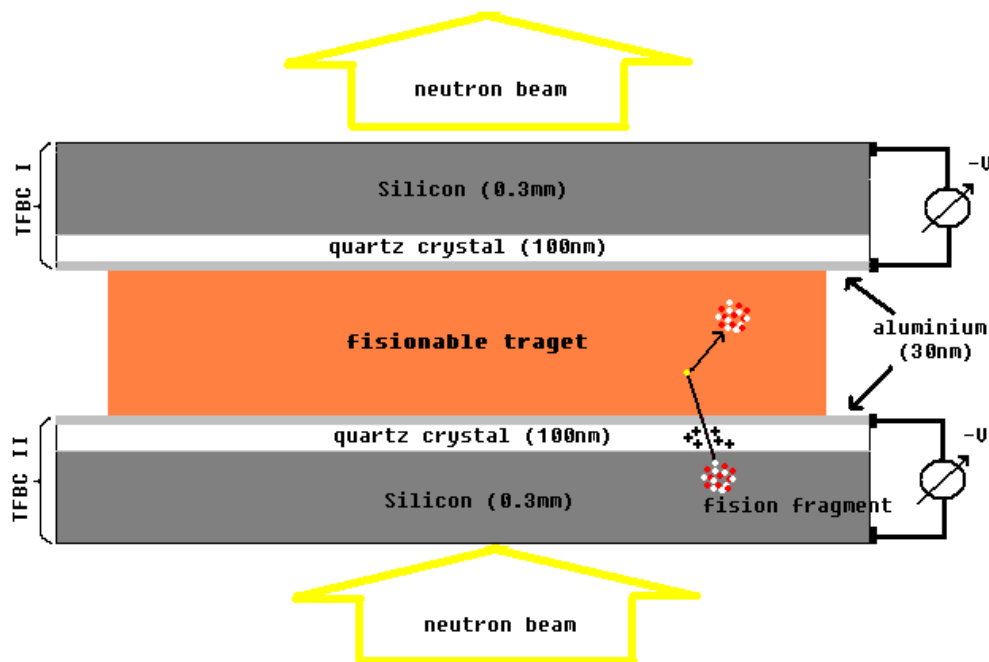
Figure 3.5: Schematically buildup of a employed TFBC system

to a tension between 80 and 100 Volt. When a neutron induced a nuclear fission in the fissionable target, a fragment could pass through the thin Al and SiO_2 layers. Due to its kinetic energy and charge, it ionized the atoms or rather molecules placed in its way. This led to a discharge of the capacitor which could be detected using an appropriate electronic equipment.

The advantages of such a detector are the insensitivity of the TFBC for light weight charged particles, e.g., electrons, the insensitivity for γ-radiation, and the its small dimensions. The former was an essential demand since the examined nuclei were expected to be radioactive, while the letter enabled the detector to be inserted into the neutron beam without an significant change of the passing through neutron field. Four TFBC-Detectors were employed to measure the neutron fluence for almost[1] all exper-

iments. While two of them were using the monitor reaction ^{238}U(n,f) the other both utilized the ^{209}Bi(n,f) fission. The isotopic purity of the ^{238}U targets was 99.999%, whereas the Bi targets consisted of more than 99.995% from the isotope ^{209}Bi. One of each detector type was placed immediately upstream the shuttle while the other two were inserted downstream the shuttle. The distance from the neutron source to the monitors was to 192.0 and 198.3 cm for the upstream and downstream pairs, respectively. The detection efficiency of the TFBCs was measured employing well-characterized ^{252}Cf sources of spontaneous fission fragments. In addition, the relative sensitivity of the monitors was checked in a separate "empty shuttle" run. During this test experiment, no production targets were placed inside the shuttle, while all four neutron monitors were installed in their proper position. The measured neutron fluence Φ_n is the ratio of the registered events and of the detector efficiency. This ratio can be expressed as

$$\Phi_\mathrm{n} = \frac{N_f}{s_0 s_E} \tag{3.2}$$

where N_f is the number of fission events detected by a monitor, s_0 is an energy independent factor, and s_E is energy depending factor on the monitor sensitivity. The energy independent factor $s_0 = \tilde{\varepsilon}\rho_A$ can be written as the product of ρ_A fissionable nuclei per area and the relative efficiency $\tilde{\varepsilon}$. The relative efficiency $\tilde{\varepsilon}$ was experimentally observed employing the well characterized ^{252}Cf source mentioned above.

$$\tilde{\varepsilon} = \frac{n_{sf}}{a_{sf}} \tag{3.3}$$

Here n_{sf} is the counting rate and a_{sf} the known fission activity form the ^{252}Cf source. The energy depending factor s_E can be expressed as

$$s_E = \sigma_f \frac{k_\varepsilon}{k_{low}} \tag{3.4}$$

---

1 For uppn0g and uppn0h only two ^{238}U detector were used

where σ_f is the energy depending fission cross section of the monitor and k_ε is the correction to the detection efficiency due to differences in charge, mass, energy and angular distributions of fission fragments in the ^{252}Cf calibration and beam measurements. k_{low} is the share of monitor events induced by high energy peak neutrons. It has to be added to the equation in order to calculate the high energy peak fluence. Actually, for all experiments, the high energy peak fluence was measured, since based on this information, the full neutron spectra were subsequently reconstructed.

For the given factors, the following uncertainties were assumed: k_{low} around 5%, k_ε around 5%, σ_f of ^{238}U around 5% and σ_f of ^{209}Bi from around 5% for weighted average values to be around 10-13% for the "instantaneous" values. Despite the relatively high uncertainties of cross section of the ^{209}Bi(n,f) reaction, employing ^{209}Bi TFBCs was well-founded, since the ^{209}Bi(n,f) reaction has threshold of about 20 MeV and therefore it was suitable for the high energy peak monitoring. Otherwise the ^{238}U(n,f) cross section has a threshold of about 1 MeV and thus, it is not suitable for the high energy peak monitoring. However, the ^{209}Bi(n,f) cross section is orders of magnitude smaller and not so well studied as the ^{238}U(n,f) reaction, as shown in Figure 3.6. Due to this, the cross section has high relatively uncertainties, in particular in the energy spectra under 50 MeV. In summary, the use of the ^{209}Bi(n,f) reaction was reasonable only for
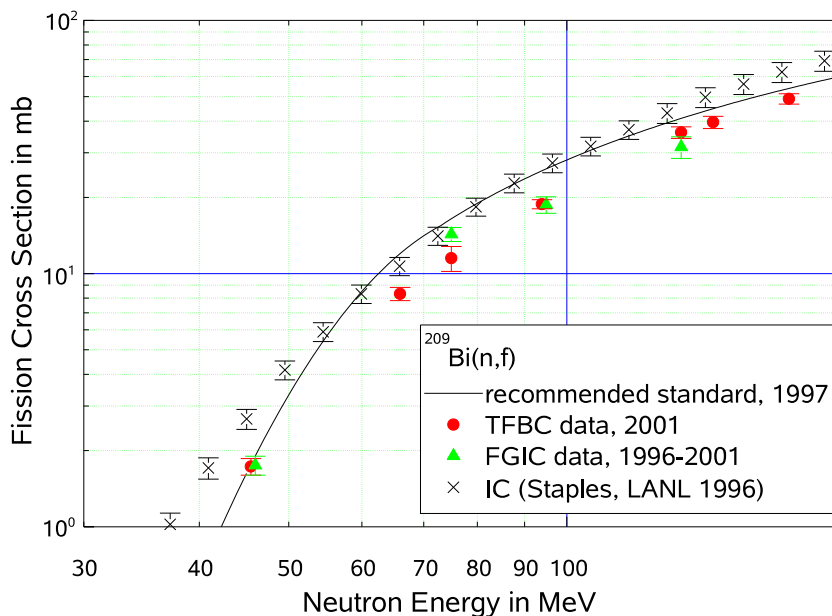
Figure 3.6: Comparing Bi(n,f) cross sections obtained in different experimental facilities

the peak energies above 50 MeV, while the ^{238}U(n,f) reactions were used to monitor

quantitatively the full neutron spectrum.

Furthermore, additional uncertainties of the neutron detectors for counting statistics, e.g., detector calibration, were calculated to be less than 3% [34].

As mentioned above, both the neutron fluence that was discussed in the previous section and the absolute neutron spectra were necessary in order to calculate the excitation functions. The absolute neutron spectra were measured by the Time Of Flight(TOF) method. This technique was successfully employed to characterize the full neutron spectra in other facilities [62]. In the PARTY setup, the distance between the ^{7}Li target and the shuttle was less than 2 m. A neutron of 200 MeV is able to cross this distance in less than 12 ns. However, poor time resolution, the width of the proton beam bunch from the cyclotron and its high pulse frequency made it impossible to measure the full neutron spectra by employing only the PARTY setup. For this reason a third TFBC detector was installed inside the Blue Hall. Due to the longer flight path, it was possible to measure fission events that were induced by the high energy peak of the neutron beam inside of the Blue Hall. Assuming that neutron spectra were identically in both positions, at the Blue Hall and in front of the shuttle, it was possible to compute the high energy peak neutron for the latter by comparing the peak fluence to the total fluence ratio.

The measured peak fluence to total fluence ratios were the basis for the construction of the initial neutron spectra. The construction was done as discussed on page 37 and following. The obtained neutron spectra were the starting point for the calculation on the neutron transport inside of the stack [35].

3.3.4 Time Logging

In order to evaluate the production rate of residual nuclei it was inevitable to monitor the intensity fluctuations of the neutron beam. The monitoring of the time dependent intensity fluctuations over the entire experimental runs is called "time logging". It could be assumed that the neutron production and therefore the neutron flux, was directly correlated to the proton beam intensity. Since protons were, due to their charge, easier to observe, they were employed for an indirect monitoring of the relative neutron beam intensity. Different techniques of observation were tested by V. Ziemann form the Svedberg Laboratory [52]. It turned out to be the most reliable, to employ the standard technique, a frequency counter (FC) of the company ELV GmbH. Under these conditions it was possible to observe the absolute intensity of the proton beam. Nevertheless, the results employing other measurement methods gave information about

the relative proton beam intensity within the specified 5 % deviation of the FC, when normalized. Using the FC, the proton flux was measured at the beam dump, while the output signal was permanently controlled online and synchronized with the data of the cyclotron accelerator. Since the detection technique developed by V. Ziemann was satisfactory, this method was employed in parallel to the FC in order to have a reference signal for the case of a FC malfunction. However, only FC data were used to analyze the experiments, except the experiment uppn0n were no time logging was performed. Due to this an evaluation of residual nuclides with short half-life period was not possible for the targets of uppn0n.

3.4 Louvain La Neuve Accelerator

3.4.1 Accelerator Setup

The irradiation experiments at the CYCLONE (**cyc**lotron de **Lo**uvain-la-**Ne**uve) accelerator at Louvain la Neuve were performed by the former ZSR members (u.o. S.Neumann [52], W.Glasser) in collaboration with the Physikalisch Technische Bundesanstalt (PTB) Braunschweig and Centre de Recherche du Cyclotron at the Université Catholique de Louvain (UCL), Belgium.

CYCLONE is a multiparticle, variable energy, isochronous cyclotron capable of accelerating protons up to 80 MeV, deuterons up to 55 MeV, alpha particles up to 110 MeV and heavier ions up to an energy of $110\frac{Q^2}{A}$ MeV, where Q is the charge and A the mass of the ion. The energy range for heavy ions extends from 0.6 to 27.5 MeV/AMU depending, among other things, on the ion's charge state.

The experiments here were performed in order to complement the Uppsala experiment with energies below 80 MeV. Actually there were experiments performed with less than 80 MeV in Uppsala too, but the expected maximum neutron flux at Louvain la Neuve was 4.7 times higher than that at the TSL, as shown in Table 3.1.

Figure 3.7 shows the setup of the cyclotron at the Université Catholique de Louvain. Down left the cyclotron accelerator is depicted. Starting from there, the beam was heading towards the switching magnet D., which deflected the protons on the Lithium target T. Directly behind the target, a 10 mm thick beam dump made of carbon, was positioned. This dump was decelerating the protons, but the neutrons passed through
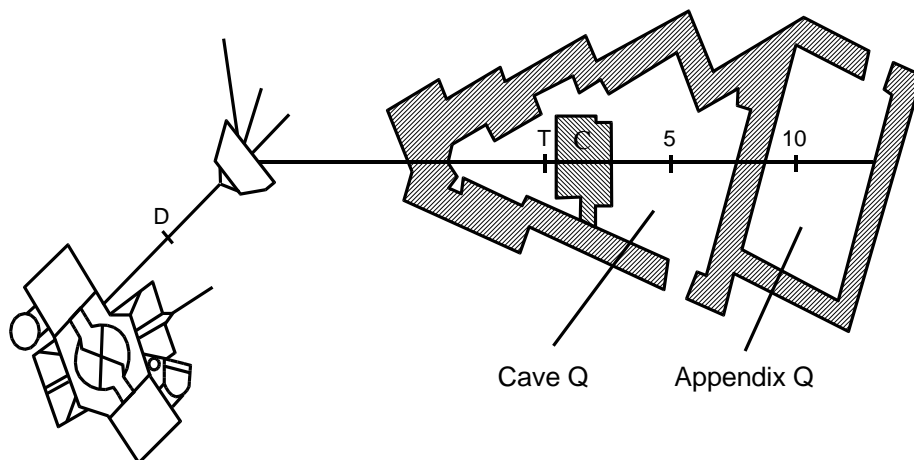
Figure 3.7: Experimental facility at the UCL, Louvain-la-Neuve

it almost unhampered and could enter and run through the beam collimator C. 5 meters behind the position of the lithium target, the materials were irradiated inside of the "Cave Q". After 6 meters more, the TOF measurements on the neutron beam were performed in the "Appendix Q".

3.4.2   Buildup of the Target Stacks

As specified previously, and in analogy with the experiments at the TSL, the targets at the UCL were irradiated using the stacked-foil technique. The target materials were the same at both facilities, Louvain la Neuve and Uppsala and target order followed an identical criteria.

Unlike the experiments in Sweden, the stack was placed directly at the middle of the neutron beam. The diameter of the target cylinders was chosen to be 2.5 cm, while the full width at half maximum of the central neutron beam was due to the collimator reduced to 4 cm. As the slew rate of the neutron beam was relatively large, the beam intensity grew from 0.1 to 0.9 within 1cm, a homogeneous target irradiation was warranted.

During the first two irradiation experiments, LOUV01 (not considered in this work) and LOUV02, the shuttle for the target stack was made of a brazen tube with a bore diameter of 25 mm and a length of 81 mm. During these first two experiments it turned out that the neutron beam changed its profile considerable along the shuttle due to scattering and absorption. Thus, no further experiments, which depended on
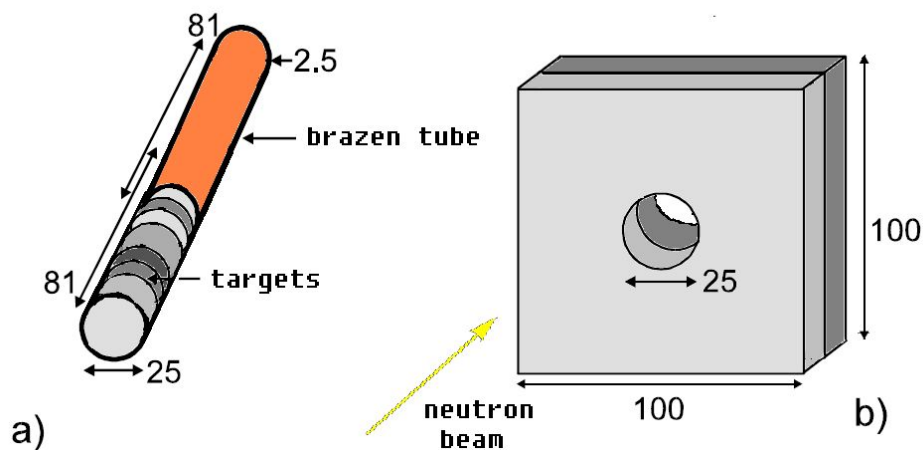
Figure 3.8: Shuttle at UCL Louvain-la-Neuve

the homogeneity of the neutron beam, could be performed beyond the stack. To avoid that inhomogeneity, the brazen tube shuttle was replaced by a set of different $100 \cdot 100$ mm plates, which were made of the same materials as the to be irradiated targets. A drill hole of 25 mm diameter in the center of each of these discs helped to place the corresponding target cylinder that was made of the identical material. Actually, for economical reasons, the $100 \cdot 100$ mm discs were not of high elementary purity and in the cases of silver and tellurium they were made of cadmium and in the cases of cobalt and nickel by iron. Nevertheless, due to these replacements the neutron beam was more uniformly scattered and the unwanted profile change of the neutron beam was reduced. A scheme of both shuttle types is shown in Figure 3.8.

3.4.3 Flux Monitoring

A big advantage of the cyclotron at Louvain la Neuve was that the deflector respectively switching magnet could be also employed to reduce the pulse rate of the beam. The intermittence of the beam was able to last from 500 ns up to 1 μs. Consequently, the shape of the cyclotron pulse was very well defined. In addition, it was possible to perform TOF measurements inside of the appendix C at a distance of 13 meters from the Lithium target. This conditions enabled H. Schuhmacher and coworkers to carry out detailed observations of the neutron field spectra in the UCL accelerator [63]. Since this work was successfully using fission cambers and a plastic scintillation detector (NE102) for the monitoring of the neutron flux and time-logging, respectively, those approved measurement techniques were later repeated during the irradiation of the present work. However, due to data transfer problems the time-logger data of the experiments louv05 and louv06 were not available. Instead for louv05 and louv06 constant neutron flux was assumed.

The lateral profile of the neutron beam behind the collimator was observed by a multi--wire chamber while the energy spectra were analyzed using a ^{238}U fission chamber for energies above 50 MeV a scintillation counter (NE213) for energies under 50 MeV and a proton recoil telescope (PRT) was used to measure the peak neutrons [63, 62, 14].

Under these conditions the obtained neuron spectra were much better resolved than during the TSL experiments. Hence, it was easier to construct the initial neutron spectra for the subsequent neutron transport calculations.

4   Neutron Transport inside the Stack

4.1   Modeling of the Neutron Flux Spectra

The unfolding technique used in the present work requires, among other things, detailed information according to the neutron spectra and neutron flux. In this context it has to be considered that both neutron flux and neutron spectra are changing along the way through the target stack. Therefore it was necessary to know the neutron spectra and flux for each irradiated foil of the stack. To this end, with the help of Daniel Kollár, a former member of the Comenius University of Bratislava, it was possible to carried out neutron transport calculations. These calculations are based Monte Carlo Simulations which model individually each of the performed irradiation experiments [35].

The starting point of the calculations were the primary neutron spectra in front of the stacks. At the UCL this neutron spectra were measured employing the TOF technique. But, as already mentioned in the previous section, at the TSL in Uppsala the experimental determination of neutron spectra were not feasible, since the space distribution at the PARTY facility did not allow to carry out TOF measurements. Hence, the spectra were theoretically constructed for all the TSL experiments.

The construction of the initial neutron spectra in front of the stack was based on two energy regions, the peak and the continuum spectra. This decomposition of the spectra into two regions will be justified and discussed in following sections.

4.1.1   Modeling of the Peak Component

The construction or rather modeling of the neutron spectra is based on the systematics of the ^{7}Li(p,n)^{7}Be reaction. This reaction has a threshold of about 1.881 MeV and can be used to generate monoenergetic neutrons between 0.12 and 0.65 MeV using projectile energies between 1.92 and 2.37 MeV. Applying incident proton energies above 2.37 MeV, the reaction may proceed to the 0.43 MeV first exited state in ^{7}Be and therefore the emitted neutrons are not anymore monoenergetic.

In general the bombarding of ^{7}Li with protons of higher energies may leave the residual ^{7}Be nucleus in the ground-state, in the first excited or in the second excited state.

$$^{7}\text{Li} + \text{p} \longrightarrow \quad ^{7}\text{Be} + \text{n} \qquad \text{Q} = -1{,}646 \text{ MeV} \qquad (4.1)$$

$$\longrightarrow \quad ^{7}\text{Be}^{*} + \text{n} \qquad \text{Q} = -2{,}075 \text{ MeV} \qquad (4.2)$$

$$\longrightarrow \quad ^{7}\text{Be}^{**} + \text{n} \qquad \text{Q} = -6{,}216 \text{ MeV} \qquad (4.3)$$
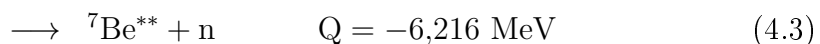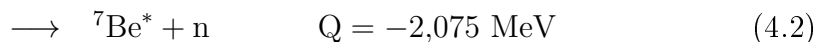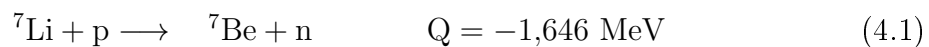
Accordingly, neutrons with three different kinetic energies are produced, since the different excited states are associated with their individual Q-Values.

Apart from this excited state or rather Q-value dependance, the neutron energy E_N is fairly sensitive to the angle of emission. This applies in particular to the bombarding energies used in the present work, which were relatively high compared to the Q-values. For non relativistic proton energies E_P, the neutron energy E_N at the emission angle ϑ is given by

$$E_{\mathrm{n}} = E_{\mathrm{p}} \frac{m_{\mathrm{p}} m_{\mathrm{n}}}{\left(m_{\mathrm{n}} + m_{\mathrm{Be}}\right)^2} \left(2 \cos^2 \vartheta + \alpha\beta \pm 2 \cos \vartheta \sqrt{\cos^2 \vartheta + \alpha\beta}\right) \qquad (4.4)$$

where m_{n}, m_{p} and m_{Be} are the masses of the neutron, the proton and the ^{7}Be nucleus and α and β are defined as

$$\alpha = \frac{m_{\mathrm{Be}} \left(m_{\mathrm{Be}} + m_{\mathrm{n}}\right)}{m_{\mathrm{p}} m_{\mathrm{n}}} \qquad (4.5)$$

$$\beta = \frac{Q}{E_{\mathrm{p}}} + \left(1 - \frac{m_{\mathrm{p}}}{m_{\mathrm{Be}}}\right) \qquad (4.6)$$

, where Q is Q-value of the reaction.

Furthermore, the neutron energy depends in the first place on the energy of the incident particle. This applies self-evidently to all reactions with negative Q-values, since the entire reaction energy summon up to the projectile. In the present work, the protons for the ^{7}Li(p,n)^{7}Be reaction were supplied by cyclotron accelerators. Using this technology the protons have to be synchronized to a high-frequency electric field in order to move along spiral path of the cyclotron beam. Too fast or too slow protons get out of phase with the oscillating electric field and cannot receive any additional acceleration. Hence, the velocity distribution of protons that leave the accelerator is gaussian-shaped, with a rather small full width at half maximum. Thus, proton beam is quasi mono-energetic. When the generated beam gets into the Lithium target, the protons are stopped by elastic and inelastic scattering. The scattering process can be mainly attributed to the coulomb interaction between incident protons and the lithium nuclei. Anderson and Ziegler [1] developed a parameterized formula that describes this stopping, see equation

4.7. This equation is based on the relativistic equation of Bethe and Bloch [7, 5, 6] that describes the energy loss of massive charged particles in matter

$$\frac{\mathrm{d}E_P}{\mathrm{d}x} = \frac{N_T a_1}{\beta^2} \left\{ \ln\left(\frac{a_2 \beta^2}{1-\beta^2}\right) - \beta^2 - \sum_{i=0}^{4} a_{i+3}(\ln E_P)^i \right\} \tag{4.7}$$

where E_P is the proton energy, x is the proton trajectory, N_T is the number of target nuclei and $\beta = v/c$ is the quotient of proton- and light-speed. The seven coefficients a_i were fitted to experimental data.

Originally Anderson and Ziegler restricted the scope of equation 4.7 to energies between 1 and 100 MeV. Later the scope was extended to an energy of 200 MeV. The extension refers to calculations of the program SRIM [77], that showed a good agreement between its calculation result and the Anderson and Ziegler equation for energies far beyond 200 MeV. However, the neutron energies of the present work did not exceed 200 MeV, and therefore equation 4.7 was suitable for the performed experiments.

When the protons penetrate the lithium target, stopping occurs in a statistical process. Fluctuations of this process yield a broadening of the energy peak and tend to result in a Gaussian distribution of the energy spectrum. This process is called energy straggling. Several theories describe the energy straggling of fast moving light ions in matter according to different projectile energies. In the high-energy limit, the energy straggling can be characterized by Bohr's expression [8]

$$\Gamma_B^2 = 4\pi \ Z_1^2 \ Z_T \ e^4 \frac{N_L}{A_T}\xi \left[1 + \frac{4I}{3m_e c^2 \beta^2} \ \ln\left[2m_e c^2 \beta^2 I^{-1}\right] \right] \tag{4.8}$$

where e is the electron charge, Z_1 and Z_T are the atomic numbers of the projectile and target atoms, respectively, A_T is the target mass, N_L is the Avogadro constant, E_1 the energy of the projectile, m_e is the electron mass, ξ is the target density ρ_T multiplied with the penetration depth x and I is the ionization potential. Using this expression, the proton energy spectra can be described by

$$N_P(E_P) \propto N_P \ e^{\frac{(E_P - \bar{E}_P)^2}{2\Gamma_B^2}} \tag{4.9}$$

where $N_P(E_P)$ is the quantity of protons with the energy E_P, N_P is the total number of protons, $\bar{E}_P$ is mean proton energy and Γ_B^2 is Bohr's the energy straggle parameter. An additional effect is the occurring divergence of the proton beam when it passes

through the lithium target. The widening of the beam is described by the divergence angle Θ [40]

$$\Theta^2 = \frac{2\pi Z_1^2 Z_T^2 e^4 N_T \xi}{E_1^2 A_T} \ln\left(\frac{E_1 \, h^2}{4\pi m_e Z_P Z_T^{4/3} e^4}\right) \qquad (4.10)$$

where N_T is the number of the target nuclei and h the Planck-Constant.

The interaction with the lithium target and the related changes in differential proton flux have effect on the generated neutron spectra. In accordance with this changes, the spectral neutron flux $\varphi_{\text{Peak}}(E_\text{n})$ forms a Gaussian curve and looses intensity depending on the angle θ. With respect to the different reaction modes ^{7}Li(p,n)^{7}Be,^{7}Li(p,n)^{7}Be* and ^{7}Li(p,n)^{7}Be** and their related Q-values the neutron spectra contains even three Gaussian peaks. The first two peaks lay so close to each other ($\Delta E_{Peak} = 0{,}429$ MeV), that it was not possible to decompose them (see [13, 3, 62]). Nevertheless, the ratio of the ground-state (eq.4.1) and first-energy-state neutrons (eq.4.2) was estimated to range between 0.3 and 0.4 (see [57, 4]) for energies under 50 MeV, while for higher energies there are no data available in the literature. The emitted neutrons, originating from the reaction that leave the nucleus in second excitation state, appear about 6 MeV shifted. But, experimental measurements showed, that their contribution to the neutron flux is rather small. In the present work, peaks of this neutrons could not be determined in any experimental measured neutron spectra. Hence, the ^{7}Be** neutrons were not considered in the further calculation.

Considering an initial Gaussian energy distribution of the proton beam, the spectral flux density of the corresponding peak neutrons φ_{Peak} was computed as

$$\varphi_{Peak} \propto \int_0^\infty \mathrm{d}E' \int_{E_P - E_{Loss}}^{E_P} \mathrm{d}E_i \int_{E_i - 5\Delta E}^{E_i + 5\Delta E} e^{\frac{(E - E')^2}{2\Delta E^2}} \delta(E - E_n(E')) \mathrm{d}E' \qquad (4.11)$$

where ΔE is the uncertainty of the proton beam with the peak energy E_P, E_i is peak energy of the neutron distribution that refers to the i'th excitation state of the ^{7}Be nucleus, E_{Loss} is the energy loss inside of the ^{7}Li, calculated employing equation 4.7 and $\delta(E - E_n(E'))$ is the Dirac-Function.

This theoretical modeling was compared with the experimental flux spectra from Louvain-la-Neuve in order to see whether the model is in good agreement with the experimental results or not. A comparison is shown is Figure 4.1. Analogous comparisons were also performed for spectra of higher energies, which were measured by different researchers employing the ^{7}Li(p,n)^{7}Be reaction, too [51]. The obtained data in the present work showed a reasonable agreement between experiment and
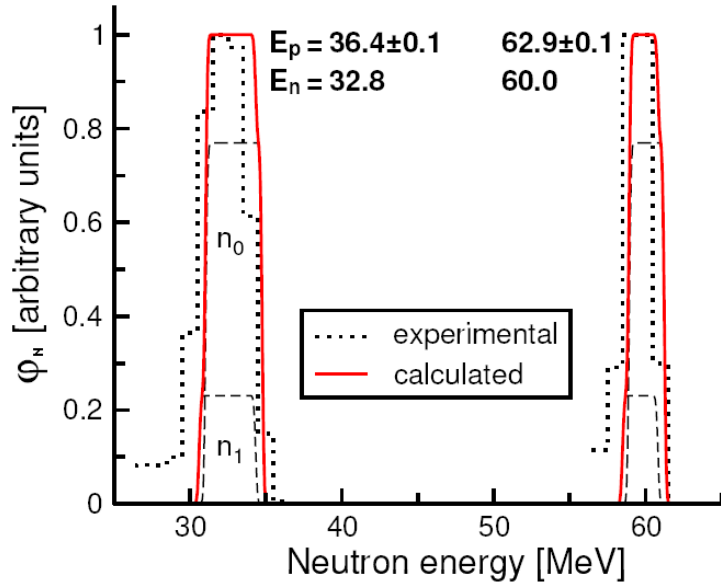
Figure 4.1: Comparison of the theoretical and experimental spectral flux density φ_{Peak} for Louv02 and Louv04. E_p and E_n are the peak energies of the incident proton and the emitted neutron. Here n_0 and n_1 refer to the excitation state of the residual ^{7}Be nucleus.

theory, and therefore, equation 4.11 was used to model the flux density of the peak neutrons φ_{Peak}.

4.1.2   Modeling of the Continuum Component

In addition to reactions shown in equations 4.1, 4.2 and 4.3 there are many-particle and Fermi-Breakup reactions possible. The latter are relevant in particular for light nuclei, were

$$\sum_{i=1}^{N} m_i - m_{\text{Target}} < \frac{T_{\text{projectile}}}{c^2} \qquad (4.12)$$

where N is the nuclei number, m_i is the mass of the nucleon, m_T is the target mass and $T_{\text{Projectil}}$ is the kinetic energy of the projectile. This reactions induce the production of continuum neutrons. Due to the energetics of these reactions, three particle break-ups are preferred. Possible break-ups are

$$^7\text{Li} + \text{p} \longrightarrow \quad ^8\text{Be}^* \quad \longrightarrow \quad \text{n} +^4\text{He} +^3\text{He} \qquad Q = -3{,}23 \text{ MeV} \quad (4.13)$$

$$^7\text{Li} + \text{p} \longrightarrow \quad ^8\text{Be}^* \quad \longrightarrow \quad \text{n} +^6\text{Li} + \text{p} \qquad Q = -7{,}25 \text{ MeV} \quad (4.14)$$
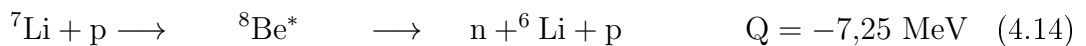
where due to the higher Q-Value, reaction 4.13 is expected to contribute most to the continuum neutrons. This is owing to the probability of a three particle break-up, that is proportional to the kinetic energy E_{Kin}^2 of the involved emitted clusters [10]. Accordingly, the three particle break up reactions, 4.13 and 4.14 have the biggest share in the production of continuum neutrons. This was also shown by N.Nakao et.al [3, 51] in his experimental work about the spectral neutron flux with energies under 90 MeV. The shape of the spectral neutron flux $\varphi_{\mathrm{Cont}}(E_n)$ is proportional to double differentiated cross section, $\frac{\mathrm{d}^2\sigma}{\mathrm{d}\Omega\mathrm{d}E}$, and therefore it can be computed using Fermis Golden Rule [54]

$$\frac{\mathrm{d}^2\sigma}{\mathrm{d}\Omega\mathrm{d}E} = \frac{8\pi^2}{\hbar^2}\frac{\mu_p}{k_p}\langle\mathbf{M}\rangle^2\,\varrho(E_n) \tag{4.15}$$

where μ_p is the reduced mass, $\hbar k_p$ is the relative momentum between projectile and target and $\varrho(E_n)$ is the density of states function. Assuming, that the matrix element $\mathbf{M}^2$ does not depend on the energy of the particles, the relative spectral neutron flux $\varphi_{\mathrm{Cont}}(E_n)$ is fully determined by $\varrho(E_n)$ [54].

$$\varrho(E_n) = \alpha_1\left\{E_n\left(\frac{m_2+m_3}{m_n+m_2+m_3}E_{tot}^c - E_n + 2\alpha\sqrt{E_n}\cos\Theta - \alpha_2^2\right)\right\}^{\frac{1}{2}} \tag{4.16}$$

with

$$\alpha_1 = \frac{2}{h^6}\frac{\sqrt{m_n+m_2+m_3}\,\sqrt{m_n m_2 m_3}^3}{(m_2+m_3)^2} \tag{4.17}$$

$$\alpha_2 = \frac{\sqrt{m_n m_p E_p}}{m_p + m_{\mathrm{Li}\ 7}} \tag{4.18}$$

$$E_{tot}^c = Q + \frac{m_{\mathrm{Li}\ 7}}{m_p + m_{\mathrm{Li}\ 7}}E_p \tag{4.19}$$

and m_2 and m_3 are the fragments in equation 4.13 or 4.14, respectively. Actually $\varrho(E_n)$ reproduces the spectral continuum-neutron flux $\varphi_{\mathrm{Cont}}(E_n)$ satisfactory over a broad energy interval. Nevertheless minor disagreement between experimental and modeled neutron spectra were observed at the low energy tail. These differences were minimized by multiplying the density of states function $\varrho(E_n)$ with an empirical energy depending factor $R(E_n)$ [59]

$$R(E_n) = R_0\frac{1 + R_1 e^{\frac{E_n-E_0}{E_1}}}{1 + e^{\frac{E_n-E_0}{E_2}}} \tag{4.20}$$

where the parameters R_0, R_1, E_0, E_1 and E_2 are fitted to the experimental data (see Figure 4.4).

Using equation 4.16 and the empirical function 4.20 the continuum components of the neutron spectra can be modeled for both reaction modes, $^7\text{Li}(p, ^4\text{He}^3\text{He})n$ and $^7\text{Li}(p, p^6\text{Li})n$. Figure 4.2 shows three different neutron spectra that were computed using equation 4.16 for 75 MeV incident protons. The differences in the spectra arise from the two reaction modes assuming that either only eq. 4.13 contribute or only eq. 4.14 contribute or both equations 4.13 and 4.14 contribute with equal shares. A
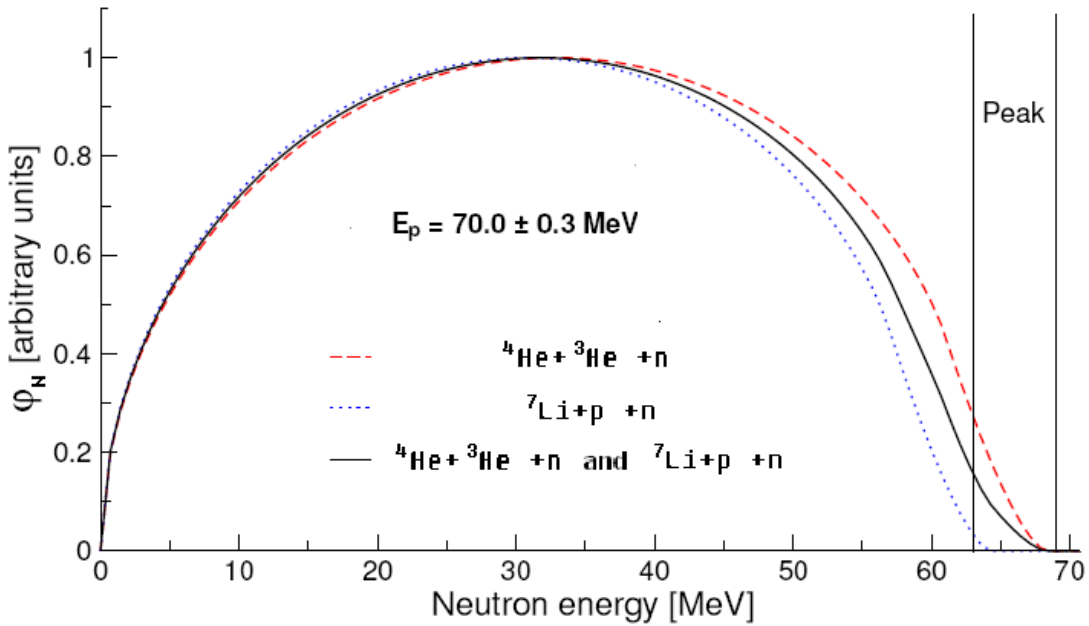
Figure 4.2: Comparison of the theoretical spectral flux density $\varphi_{\text{Con.}}$ using only eq. 4.13, eq. 4.14 or both equations with equal shares. The spectra have been normalized with their maximum value to 1.0

comparison between the calculated spectra shows, that the differences for energies below 15 MeV were approx. 5 % whereas the high energetic part of the spectra shows discrepancies of nearly 40 %. This divergence increase for higher energies of incident protons.

The $^7\text{Li}(p, \alpha + ^3\text{He})n$ reaction is the preferred nuclear reaction, since the probability of a reaction is proportional to the square of the kinetic energy of the involved residual particles. Taking this into account, the discrepancies were reduced discarding the share of equation 4.14 on the continuum neutron spectra. Indeed, the theoretically calculated spectra, that neglects the share of equation 4.14 were in good agreement

with the experimental obtained spectra.

Employing both approaches, for $\varphi_{\text{Peak}}(E_{\text{n}})$ and $\varphi_{\text{Cont}}(E_{\text{n}})$ the initial neutron spectra were modeled, for all cases where no experimental data were available.

4.1.3 Merging of the Spectral Components

The modeled components contain independent information about the high energy peak and the continuum of the neutron spectra, but do not answer the question regarding to their relative proportions in a joint spectrum. However, in order to model the entire experimental neutron spectra it was necessary to merge both components. To this end, the TSL data were compared with the 6 spectra available form the Louvain-la-Neuve irradiation and furthermore with 17 experimental neutron spectra obtained by other researchers [51, 50, 2]. For this comparison the ratio between the peakarea $A_{\text{Peak.}}$ and the continuum area $A_{\text{Con.}}$ was calculated.

$$A_{\text{Peak.}} \quad = \quad \int_{0}^{200} \varphi_{\text{Peak.}} \mathrm{d}E \tag{4.21}$$

$$A_{\text{Con.}} \quad = \quad \int_{20}^{200} \varphi_{\text{Con.}} \mathrm{d}E \tag{4.22}$$

In order to compare the ratios, the spectral flux density $\varphi_{\text{Con.}}$ was limited to energies over 20 MeV. This procedure enabled the consideration of experimental spectra that missed the low energy component, due to their measuring techniques. Figure 4.3 shows the calculated $\varphi_{\text{Peak}}/\varphi_{\text{Con.}}$ ratios. The average ratio of the data inside the box is 0.44. This value is constant for proton energies above 50 MeV. For energies under this cut-off the ratios increase sharply. This increase is explained by the bigger share of the continuum component that lies below cut-off energy of 20 MeV.

Assuming a constant peak to continuum ratio of 0.44 for all energies over 50 MeV, a test modeling was performed. In the case lower neutron energies, the measured ratio of the particular spectra was employed. In this manner the quasi mono-energetic spectral flux density of the UCL irradiations were recalculated. Figure 4.4 shows a selection of the modeled and the measured spectral flux densities for six different proton energies. It turned out, that the model, proposed above, was applicable for energies from 50 MeV up to 90 MeV. Irradiations performed with lower energies showed significant deviations between model and experiment in the low energy tail of the neutron spectrum. This discrepancy was bigger when lower proton energies were used. The opposite behavior
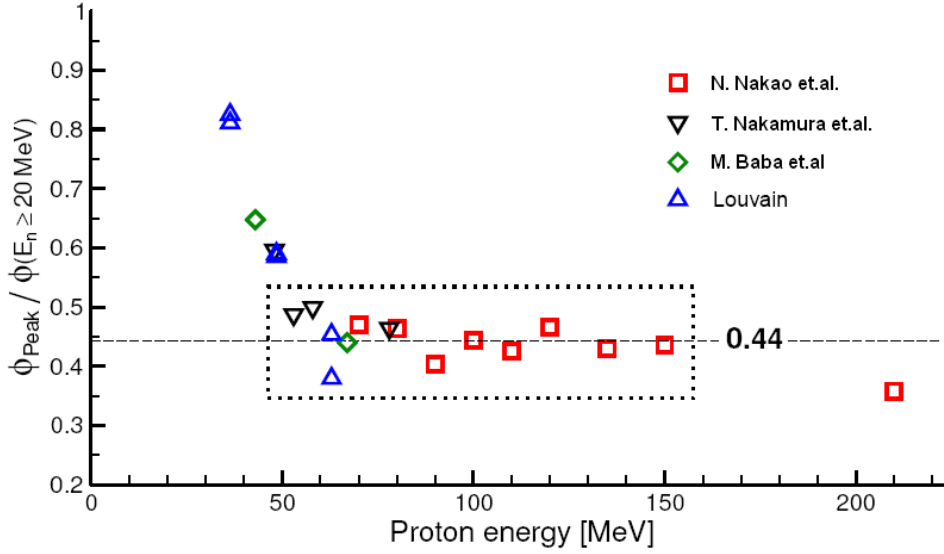
Figure 4.3: The ratio $\varphi_{\mathrm{Peak}}/\varphi_{\mathrm{Con.}}$ for different experiments. The dotted line gives the mean of the points inside of the box. Some of the spectra that were used to calculate the ratio were measured by N.Nakao [51], T.Nakamura [50] and M.Baba [2]

was observed for experiments with a high incident energy. While the low energy area of the spectral flux densities declined with increasing proton energies, the segment besides the peak started rising. The simplifications of the model may explain this behavior. For instance, the increasing contribution of reactions of higher Q-Values could take effect on the rising the fraction of slower neutrons. On the other hand, the importance of the pre-equilibrium reaction channels, that cause an emission of high energetic neutrons in the direction of the neutron beam, could be responsible for spectral changes that occur for higher energies of the incident proton beam.

However, while the model was still acceptable for energies between 50 and 90 MeV, the shape of the continuum fraction was not in agreement with the experimental data at higher energies. Thus, an empirical adjustment was applied in order to fit the modeled spectra to the experimental shape of the spectral neutron flux densities for higher energies. The adjustment was based in the multiplication of the phase space function 4.16 by a increasing linearly energy depending function 4.20, as it was mentioned in chapter 4.1.2. The free parameters of the function 4.20 were fitted separately for each irradiation experiment. The effect of this empirical alignment is depicted by a green dotted line in the flux modeling for energies above 90 MeV in Figure 4.4.

As mentioned before, discrepancies at high energies are observed. Furthermore, the
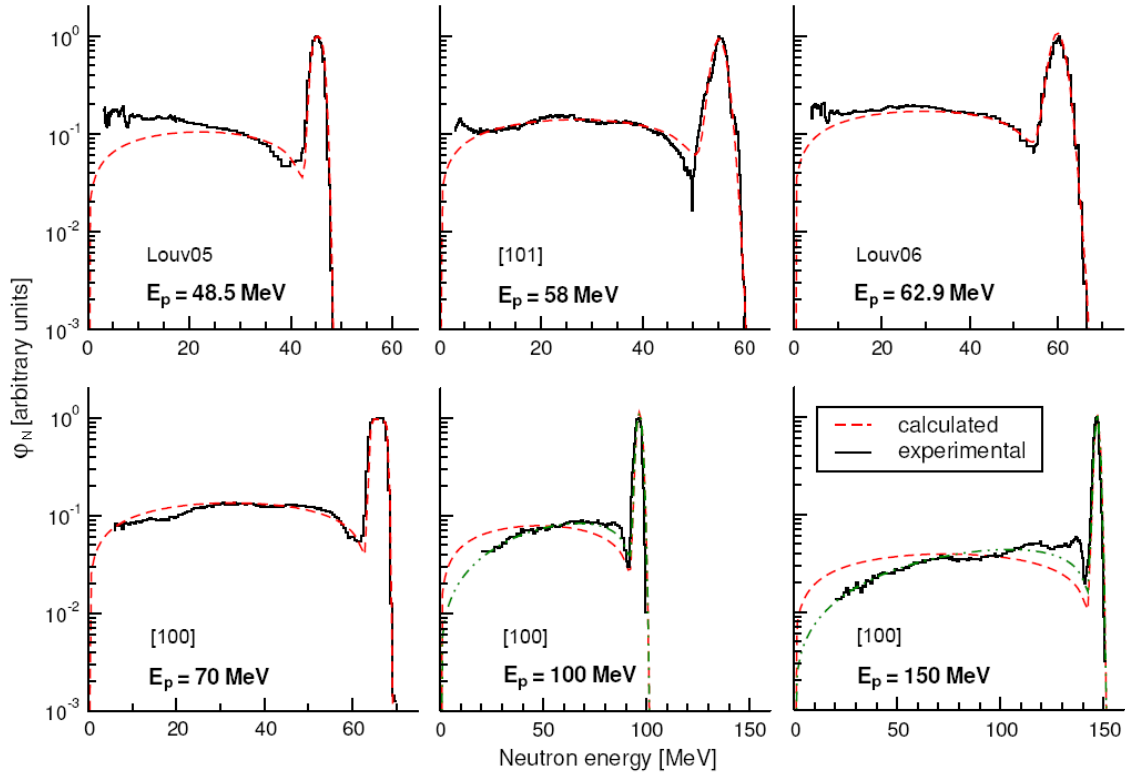
Figure 4.4: Calculated and measured spectral flux densities φ_N for different energies, the green dotted line represents the high energy adjustment of the theoretical flux densities

agreement between the employed model and the experimentally measured neutron fields for energies under 50 MeV were rather poor. Here no empirical adjustments could be applied as it was done for high energies, since the quantity of experimental data did not allowed any assured conclusion about the behavior of the deviations. Thus, data from this kind of experiments were discarded and have not been taken into account for further calculations.

In summary: In case of the irradiation experiments that were carried out at the UCL, the experimentally measured neutron spectra were used as the starting point of the neutron transport calculations. In case of the experiments that were performed at the TSL and had incident proton energies above 50 MeV, semi-empirical neutron spectra were constructed and used as the starting point of the neutron transport calculations. The experiments that were performed at the TSL with incident proton energies under 50 MeV, were could not be considered in the present work.

4.1.4   Transport Calculation Model

Program codes that are employed in order to compute the particle transport inside of a target material are usually based on a Monte Carlo Simulation. This is due to the difficulties that occurred trying to model complex statistical process with computer codes that use deterministic methods. Employing Monte Carlo Simulations individual probabilistic events that represent a process can be simulated sequentially. The probability distributions governing these events are statistically sampled to describe the total phenomenon. In the case of the particle transport, the simulation computes the trajectory of each particle through the target. For this purpose, the nuclear reactions along the path are selected by random numbers. Hence, a detailed knowledge about the occurrence of different nuclear interactions becomes indispensable. The significance of the employed nuclear models gets emphasized, taking into account that not only elastic scattering but inelastic nuclear reactions, which can generate secondary particles, contribute to the change of the incident particle field. The secondary particle could interact with the target material and yield unexpected experimental results. In the present work, it was expected, that neutron scattering and the production of secondary particles resulted in significant changes the neutron field along the target stack.

In order to calculated this changes of the neutron spectra, the LAHET Code System (LCS) was employed. LAHET has the advantage over other Monte Carlo Simulations like HERMES (High Energy Radiation Monte Carlo Elaborate System), that it is based on later nuclear models.

4.2   LAHET

4.2.1   The LAHET Code System

The LAHET (Los Alamos High Energy Transport) Code System had been developed at Los Alamos National Laboratory. Its code system is based on the LANL version of the HETC Monte Carlo code, that was designed in order to compute the transport of nucleons, pions, and muons. In comparison with LANL, the LAHET Code System supports new features, e.g., more elaborated nuclear reaction models, that reproduce the experimental experiences more exact.

The basic idea of the LCS is to link various codes that were programmed for different

physical purposes. In Figure 4.5 an overview of the code linkage and data flow for the LAHET Code System is given. The linking process is based in a local temporary file
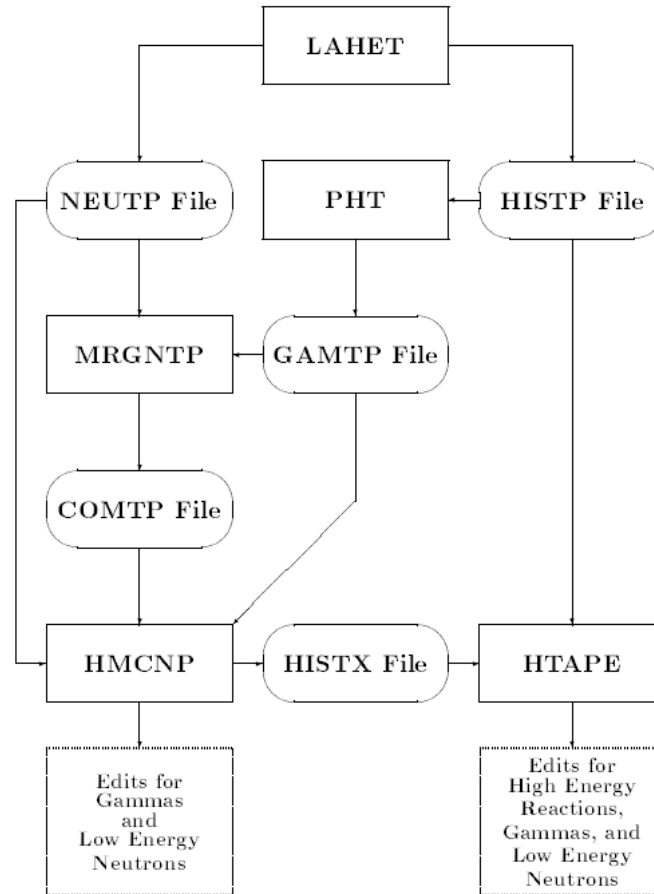
Figure 4.5: Code Linkage and Data Flow for the LAHET Code System

that stores the output data from a particular code in order to provide them as the input file for another code. In this manner most of the common particle interaction problems can be solved. In LAHET the physics of nuclear interactions are calculated employing an intra-nuclear cascade model, that has been adapted from the ISABEL code. The Fermi breakup model has been included in order to model the breakup of light nuclei. Furthermore a multistage pre-equilibrium exciton model has been implemented. To model an intermediate stage between the intra-nuclear cascade and the evaporation phase of a nuclear interaction. In addition, LAHET contained a library of calculated neutron elastic scattering.

The HETC (High Energy Transport Code) and the LAHET code were programmed to

treat all interactions by protons, pions, and muons within HETC respectively LAHET. The treatment of neutron interactions was limited downwards by a threshold energy of 20 MeV at LANL. Each neutron appearing from a nuclear reaction with energy below the threshold has its kinetic parameters recorded on a neutron file (NEUTP) for subsequent transport by a Monte Carlo code using ENDF/B-based neutron cross section libraries.

This subsequent neutron transport is calculated by a modified version of MCNP code (Monte Carlo N Particle) that LAHET resorts, too. The modified code called HMCNP supports the NEUTP file as an input source. MCNP/HMCNP is a general-purpose, continuous-energy, generalized-geometry and time-dependent Monte Carlo transport code. It can be used for neutron, photon, electron, or coupled neutron/photon/electron transport, including the capability to calculate eigenvalues for critical systems. Therefore point wise cross section data are used. In the particular case of neutrons, the ENDF/B database is used as above-mentioned. The usable neutron energy scale ranges from 10^{-11} MeV to 20 MeV. The employment of the ENDF/B database enhanced the reliance of the HMCNP calculation, as neutron capturing and scattering in this energy area was not based on a model but verified by several experiments.

In order to record the description of the events occurring during the LAHET computation, a history file (HISTP) was created. Modified tallies (aspects) of the initial LAHET run are obtained by subsequent processing of the saved data using the HTAPE code. An additional feature of the HMCNP code is the recording of a history file (HISTX). This file can be converted by the HTAPE code as well and therefore the HISTX file is utilized in further calculations.

An important feature of the HETC code is the computation of the neutron induced interactions that results in an emission of a photon, e.g., the deexcitation of residual nuclei after all particle evaporation has ceased. The meaning of this process is evident, since the γ-quanta contribute to the energy loss of the observed system. In order to perform this type of calculations it is necessary to execute the PHT code. PHT code reads it input data from the HISTP file and produces a gamma output file (GAMTP). This file contains a photon source for HMCNP in the same format as NEUTP. Afterwards both files the NEUTP and the GAMTP files are merged with the code MRGNTP in order to act as a source for HMCNP in a coupled neutron-photon interaction that describes the transport of the entire gamma-ray source within the system.

A typical cycle of a LAHET step could be described as follows. The particle its energy and its direction are chosen randomly form a specific source distribution. Considering physical properties like energy loss, ionization effects and nature of interaction, the spot of the interaction between the particle a nucleus is given by a random number. If the interaction yields an excitation of the involved nucleus, then the intra-nuclear cascade will be simulated. In the course, the pre-equilibrium and evaporation model are employed to lose energy and deexcite the nucleus. The information about the particles is stored in a related history file. In the next step, the trajectories and occurring interactions of the evaporated secondary particles or generated photons, are calculated. As the complete history of the LAHET calculation is recorded, the changes of the spectral flux densities φ_N for each target disc inside of the irradiated stack finally are known.

4.2.2   Calculation of the Neutron Flux Spectra with LAHET

Besides the transport calculations, the LAHET Code System was employed to calculate the initial neutron spectra. To perform such a calculation LAHET required additional information about the experimental setup, e.g., the geometry of the irradiated object, their composition and arrangement and a definition of the source of radiation. Furthermore, the input file also had to provide specific parameters for the employed physical models. The LAHET input files written by Daniel Kollár, a former employee of the Comenius University of Bratislava [35].

This spectra were generated for the ^{7}Li(p,n)^{7}Be reaction. Figure 4.6 shows a comparison between the measured spectrum, the theoretical modeled spectrum and the LCS simulated initial neutron spectrum.

The comparison showed, that the LCS spectrum yielded an unsatisfactory description of the spectral flux densities for the entire energy range. Regarding to the creation of the initial neutron spectra it was demonstrated that the applied semi empirical model outmatched the LCS results.

The importance of the intra-nuclear cascade model, that was the main originator of the unsatisfactory description of the initial neutron field, has to be put into perspective. The calculation of the initial neutron field is based on the production of secondary neutron by a direct nuclear reaction. This type of nuclear reaction is not covered by the intra-nuclear cascade model. Even though the LCS did not reproduce the initial neutron spectral flux densities, it was still appropriate for the transport calculation, as the main changes in the spectral shape were due to moderation of the neutrons by
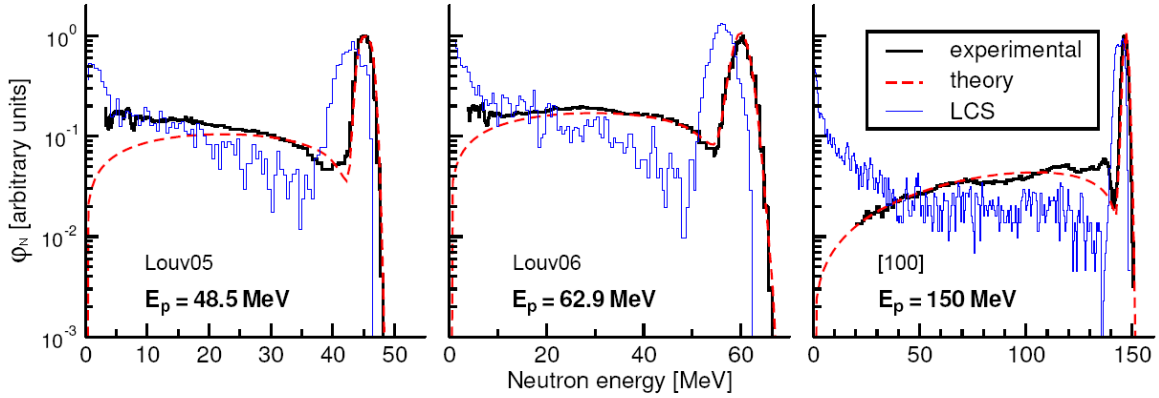
Figure 4.6: Comparison of the measured, theoretical and LCS spectral flux densities φ_N for different energies

elastic scattering and inelastic scattering but not by direct reactions.

The neutron transport calculation inside of the stack showed that the share of the secondary neutrons in the primary neutrons was around 9 %, as shown in Figure 4.7. This calculation was performed for an incident energy of 158 MeV, further simulations showed, that for lower energies the share of secondary neutrons decreased. A spectral analysis of the secondary flux showed, that a big fraction of the secondary neutrons had an energy of less than 20 MeV and was therefore treated employing the fairly reliable ENDF/B database.

4.2.3   LAHET Setup for the Neutron Transport Calculation

The further LAHET calculations were focused on the neutron transport inside of the irradiated target stacks. For this purpose, the experimentally measured neutron spectra of the UCL irradiations were used as the initial LAHET input. For the TSL experiments, the calculated semi-empirical spectra were used. The geometrical setup of the experiments that had to be provided for the transport calculations was discussed and described in chapter 3.4 and 3.3.

A quadratic target assembly was used to fix the circular targets foils for the experiments at Louvain-la-Neuve, as shown in Figure 3.8. The quadratic target holder was also taken into account for the transport calculations. In the experimental setup the squared foils were made of the same materials as the enclosed target foils. But, for reasons of economics the squared foils were not of high isotopic purity and in a few
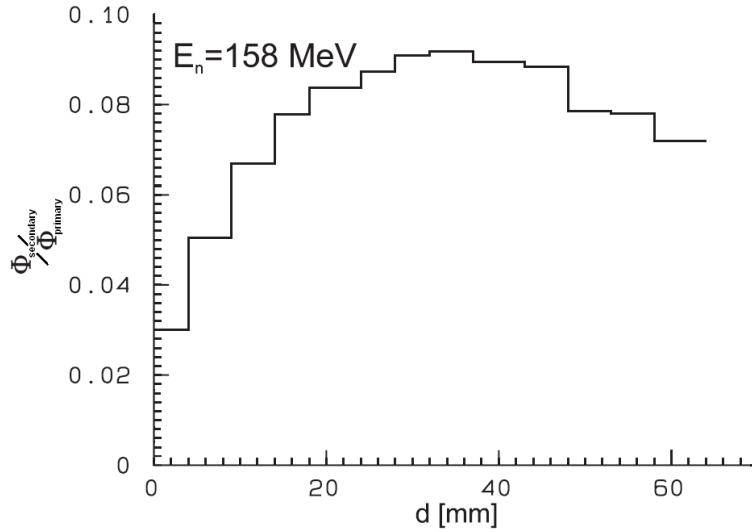
Figure 4.7: The trend of the relative share of the secondary neutron flux in the primary neutron flux $\varphi_{\text{secondary}}/\varphi_{\text{primary}}$ along the target stack for a initial neutron energy of 158 MeV

cases the holder material differed from target foils. Unlike the experiment, in the transport simulation the squared and the corresponding target foil consisted of the identical material. The inputs describing the isotopic composition and densities of the target foils were taken from their manufacturers and are shown in Table 3.2. The modeled neutron beam shared the principal axis with the irradiated stack and was assumed to have a uniformly distributed flux over a circle with a diameter of 5 cm.

The simulations of the irradiations at Uppsala were modeled, allowing for the target discs and the aluminum shuttle. The positioning of the shuttle concerning the principal axis of the neutron beam was shifted, as it is shown in Figure 3.7. For the LAHET calculation this was simplified assuming the energy distribution of the centered neutron beam to be below the angle of the target position, whereas the diameter of the simulated neutron beam was bigger than the shuttle.

Neither for the UCL nor for the TSL simulations neutron backgrounds were considered to contribute to the transport. In order to compute elastic neutron scattering a database called ELSTIN, which was provided by LAHET, was employed. Furthermore, the intra-nuclear cascade model, the pre-equilibrium model and the nuclear evaporation model were activated, whereas the Fermi break-up model was used instead of evaporation model for mass numbers A bigger than 13 and for mass numbers between 14 and 20 for excitation energies over 40 MeV. As above-mentioned,

beneath the downer threshold of 20 MeV the neutron transport calculation was performed by a sub sequential code called HMCNP. This system obtains its nuclear reaction data from libraries, such as ENDF/B-V. For the case of nat.$^{\mathrm{T}}$e no libraries were available. Thus, the $^{127}_{53}$I libraries were used instead. In each modeled experiment the target foils were irradiated by 7×106 neutrons, in this manner, uncertainties in the corresponding flux could were reduced to 5 %. The increment of the neutron energy was set to 1 MeV for energies underneath 130 MeV and it was set to 2 MeV for the energy range from 130 to 180 MeV. Hence, the modeled energy range covered all considered experiments. The reason for the asymmetric settings was related to the STAY'SL code which was used to unfold the neutron flux with the excitation function. In fact STAY'SL could not handle more than 155 energy bins.

5 Evaluation of Production Rates

5.1 Introduction into γ-Spectrometry

As above-mentioned, the biggest share of the produced residual nuclides was expected to be radioactive. This radioactive nuclei usually decayed by β-decay into excited daughter nuclides, which deexcite under the emission of γ-quanta. Due to the specific energy levels of a nucleus, this γ-spectra can be assigned to the emitting radionuclides. Doing so it is possible to identify different radionuclides by their characteristic γ-radiation. Further the intensity of the γ-radiation reveal information about the number of decaying nuclei.

For this reason γ-spectrometer were employed to identify the residual nuclides. The used spectrometer utilized a semi conductor of a high purity germanium crystal (HPGe) or a lithium drifted germanium crystal (GeLi), in which the emitted γ-quanta deposit their energy. The energy deposition of the γ-photons is rooted in the photo electric absorption and Compton scattering. For γ-energies beyond 1024 MeV, electron-positron pair production and annihilation contribute additionally to the energy deposition and can be observed by the production of characteristic 511 keV annihilation radiation.

The mentioned interactions between γ-radiation and the semiconductor result in an excitation of electrons. The Electron-hole pairs are created in the reverse-biased depletion region of the detector. The number of the generated electron-hole pairs is proportional to the energy of the γ-quantum. The accumulation of free charge carriers create an electrical pulse which is amplified and passes an analogue/digital transducer. The obtained digital signal is sorted to a corresponding channel by its intensity using an multi channel analyzer (MCA). In the present work, a 12 Bit analyzer with 4096 channels from ORTEC was employed. For almost all residual nuclides the γ-radiation window of the detector was set to 20 - 2000 keV. Thus, each energy bin was only 0.5 keV wide.

The performance of such a γ-spectrometer depends on the detection efficiency, in particular for samples with low activity. The efficiency is the ratio between the emitted and the detected number of γ-quanta. Two different kinds of efficiencies have to be distinguished. The first, the full energy peak efficiency ϵ_P, or just efficiency ϵ, which describes the detection of γ-quanta that deposit their entire energy in the detector. In other words, the intensity of the generated digital signals represent the entire γ-quanta energy. The second, the total efficiency ϵ_T, includes all interactions between γ-rays and

the detector that cause an electric pulse. Here the electric signal is independent of the share of the photon energy that was deposited in detector.

Apart from the efficiency ϵ, the full width at half maximum (FWHM) of the detected peak determines the performance of the γ-spectrometer. A small FWHM is in particular necessary, when a distinction between two closely adjoining γ-lines has to be made. This work is based in the distinction of different produced residual nuclides and in the estimation of their quantity, therefore neither the significance of the FWHM nor of the efficiency ϵ can be overestimate.

Each irradiated target was examined by up to five different γ-spectrometer. The parallel and sequential use of several spectrometer proved to be useful, since not only biased, detector depending measuring uncertainties were reduced, but also the quantities of samples were processed faster. The latter was advantageous with regard to the nuclear half-life periods of the examined radionuclides. In Table 5.1 some properties of the used γ-spectrometer are given.

The transport of the irradiated targets to Hannover took place within less than 24 hours for most of the cases. Due to the brief time in transit, it was feasible to detect residual nuclides with relatively short half-life periods and it was expected to detect
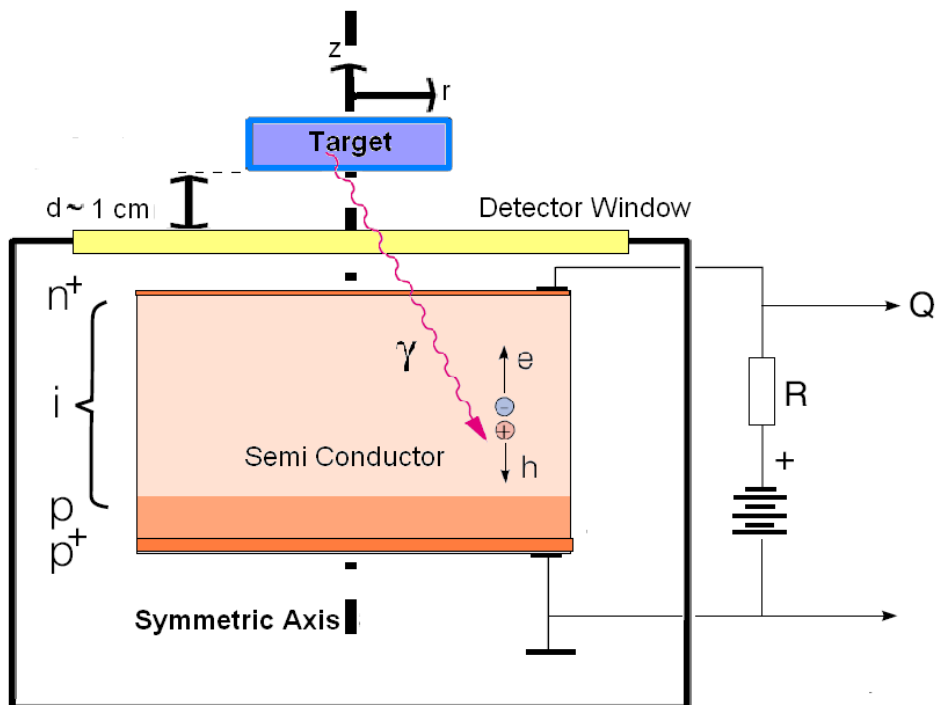
Figure 5.1: Scheme of a γ-spectrometer.

Table 5.1: γ-Spectrometer used in the present work.

Name	Type	Shielding	(former) Location	FWHM at 122/1408 keV	Efficiency ϵ_{P} at 122/1408 keV
Ge_01	HPGe	10cm Pb/Cu	Herrenhausen	0.94/1.90	0.084/0.0069
Ge_02	HPGe	10cm Pb	Herrenhausen	0.87/1.93	0.106/0.0078
GeLiU2	Ge(Li)	5cm Pb	Am kl. Felde	3.02/3.61	0.082/0.0066
GeLiU4	Ge(Li)	5cm Pb	Am kl. Felde	1.44/2.57	0.117/0.0117
GeNeu	HPGe	10cm Pb/Cu	Am kl. Felde	1.22/2.00	0.102/0.0175

radionuclides with half-life periods between 5 hours and 5 years.

In order to perform a proper γ-spectrometry it was necessary to estimate the expected activity of the irradiated targets. Based on the experiences with proton induced reactions data, a wide spectrum of activities was likely probable. In the following argumentation, typical data of proton induced reaction experiments [21] were used as a reference. Assuming the same cross section for a proton and a neutron induced reaction, a relationship between the target nuclei of $N_{\mathrm{TN}}/N_{\mathrm{TP}} \approx 15\mathrm{g}/0.2\mathrm{g} \approx 75$, the irradiation time of $t_{\mathrm{irrN}}/t_{\mathrm{irrP}} \approx 60\mathrm{h}/3\mathrm{h} \approx 20$ and the projectile flux of $\varphi_{\mathrm{N}}/\varphi_{\mathrm{P}} \approx 10^{-5}$ the estimation of the ratio between activities of the neutron induced and the proton induced reactions was calculated using equation 5.40.

$$
\begin{aligned}
N_{\mathrm{j,N}}/N_{\mathrm{j,P}} &\approx 75 \cdot 10^{-5} \cdot 60 \cdot \frac{1 - e^{\lambda t_{\mathrm{irrN}}}}{1 - e^{\lambda t_{\mathrm{irrP}}}} \\
\lim_{\lambda \to 0} N_{j,N}/N_{j,P} &= \frac{3}{10} \\
\lim_{\lambda \to \infty} N_{j,N}/N_{j,P} &= \frac{3}{200}
\end{aligned}
\tag{5.1}
$$

It turned out, that the produced nuclides and their activities are expected to be up to 67 times lower than during the performed proton induced reaction experiments.

According to the low activities, it was necessary to improve the efficiency in comparison to the efficiency of the γ-spectrometer that were used during the proton irradiation experiments. The necessity for the improvement becomes clear, taking into account that the efficiency ϵ_P influences the number of detected decays within a certain period of measurement. This number of detected decays follows the Poisson distribution and therefore the standard deviation is given by the root of the counted events. For this reason a large number of events in the net peakarea NP (see Section 5.2.2) is useful in

order to reduce the relative standard uncertainties.

One possibility to increase the efficiency consists of a modification in the geometry of the spectrometer setup. During the proton induced reactions experiments, the irradiated target foil was usually placed more than 10 cm far form the detector [21]. A shortening of this distance to 1 cm rose the efficiency ϵ_P by a factor which falls between 6 and 10, depending on the particular spectrometer and the γ-energy. The target positioning is illustrated in Figure 5.1. As a consequence of the geometrical modification, some simplifying suppositions concerning the dimensions of the target foil and the neglect of real coincidences were discarded. For this reason a proper analysis of the γ-spectra demanded the correction calculations that are discussed in the Section 5.4.1 and 5.4.2. However, some target foils were outstandingly active and, for this reason, they were measured in other geometries as well.

Apart from the mentioned efficiency improvements, a general prolongation of the measure period is conceivable in order to enlarge the net peakarea. However, the detection period was limited by the quick decay of some residual nuclides and by the large quantities of target foils, which had to be analyzed employing a small number of γ-spectrometer. In fact, each irradiated stacks consisted of up to 21 target foils. Thus, the period of time that was used for the measurements was a compromise between detection precision, were a longer period raised the NP of the examined foil and delectability of short life radionuclides for the pending measurements.

5.2 Calibration

5.2.1 Efficiency Measurement with different Point-Sources

Calibrated point sources were used in order to determine the efficiency of the used γ-spectrometer. The radioactive sources were calibrated by the PTB (Physikalisch Technische Bundesanstalt) and fulfilled the quality standard of DIN EN ISO/IEC 17025. Information of the employed calibrated sources is given in Table 5.2. For each detector the determination of the efficiency was performed for at least four different geometries. Therefore, the different counting rates of the calibrated sources were measured along the axis of symmetry of the cylindrical detector at a distance of 1, 3,

6 and 11 cm to the top of the spectrometer.

For a given geometry the activity A_j of the source j is determined as

$$A_j(t) = \frac{1}{I_\gamma \; \epsilon_P(E_\gamma)} \frac{\mathrm{d}NP}{\mathrm{d}t} \tag{5.2}$$

Here NP is the Gaussian net peakarea (see Section 5.2.2), $\epsilon_P(E_\gamma)$ is full energy peak efficiency at the energy E_γ and I_γ is the probability that the γ-quantum of the energy E_γ is emitted during the nuclear decay.

An example of an obtained efficiency graph is given in Figure 5.2. Here the efficiency $\epsilon_P(E_\gamma)$ was calculated for the detector Ge_02 in the 6 cm geometry. The point sources and the corresponding γ-energies are represented by vary, different colored symbols. The share of the total uncertainty that considers just the uncertainties of the calibrated point sources, e.g., the uncertainty of the emission probability δI_γ, the reference activity $\delta A_j(t_0)$, is likely small compared to the statistical uncertainty of the net peakarea δNP. As above-mentioned, the standard deviation of the NP is given by its root $\sqrt{NP}$ since the counting statistic obeys the Poisson distribution. Hence, it was easy to determine standard uncertainty and in addition to reduce the standard uncertainty of the certain efficiency by a extending the period of the measurement time. Consequently, the calculated uncertainty propagation for all occurring uncertainties including the uncertainty of the net peakarea resulted in less than 0.5 %. Nevertheless, it turned out that such a small measuring uncertainties did not reproduce the experimental reality and rather an uncertainty

Table 5.2: Calibrated sources used in the present work.

Nuclide	Register. No.	Datum	Activity	$\mathbf{T}_{1/2}$
^{241}Am	569-81	01.01.1985	29,20 kBq	432,20 y
^{241}Am	412-94	01.01.1995	37.30 kBq	432,20 y
^{133}Ba	530-83	01.01.1985	29,70 kBq	10,54 y
^{57}Co	173-93	01.01.1995	103,20 kBq	271,80 d
^{57}Co	310-99	01.01.2001	153,50 kBq	271,80 d
^{60}Co	282-77	01.01.1985	38,10 kBq	5,27 y
^{137}Cs	246-83	01.01.1985	29,90 kBq	30,14 y
^{152}Eu	553-78	01.01.1985	27,10 kBq	13,33 y
^{54}Mn	140-91	01.01.1995	22,00 kBq	312,50 d
^{22}Na	247-85	01.01.1985	29,44 kBq	2,60 y
^{226}Ra	408-84	01.01.1985	139,10 kBq	1600,00 y

of 5 % was reasonable. The determination of this 5 % uncertainty is discussed in Section 5.5. On account of this observation, the error bars in Figure 5.2 were set to 5%.

5.2.2 Background Subtraction and Net Peakareas

The net peakarea NP usually overlaps by a background distribution of incomplete collection of charges. This charges are mainly set free by Compton scattering of not fully absorbed γ-photons. The most important origins of the γ-quanta are the local natural background radiation and the detected radiation from the sample that has higher energies than the observed NP photons. The sum of background and net peak form the so-called gross peak, which is represented by the combination of the light and dark green area in Figure 5.3. The gross peak is characterized by the channel number and the height of the peak. In order to obtain the net peakarea, the background distribution had to be subtracted from the gross peak. For this purpose, the background distribution was determined employing the following equation,

$$u_i = u_r + \frac{u_l - u_r}{ar} \sum_{j=i}^{n_r} (K_j - u_r) \tag{5.3}$$
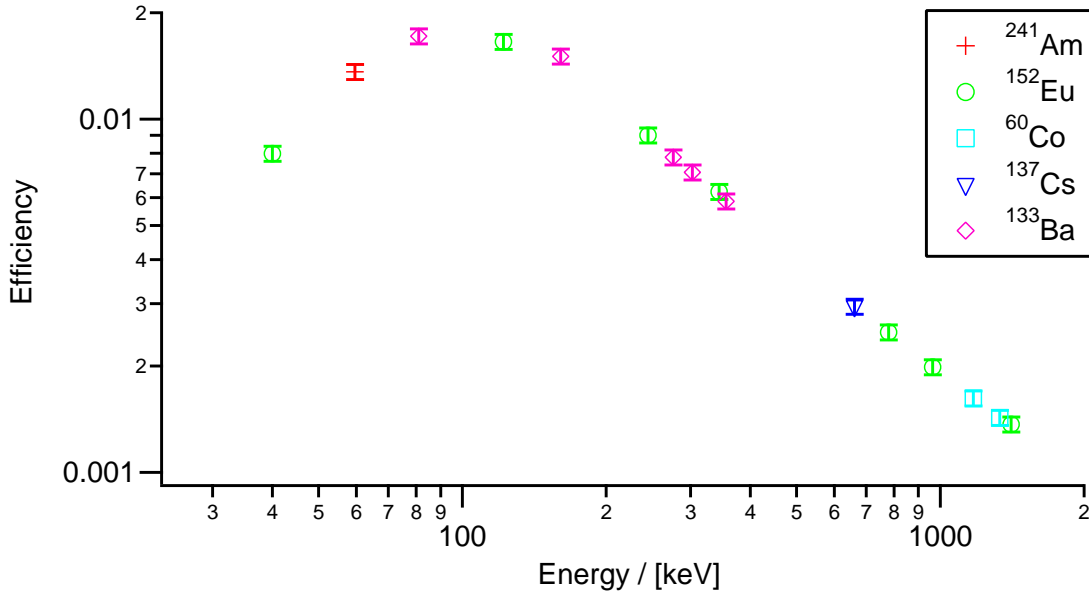
Figure 5.2: Efficiency of the detector Ge_02, measured with several point sources for 6 cm distance geometry.

$$ar \quad = \quad \sum_{i=n_l}^{n_r} K_i - u_r \tag{5.4}$$

Here the area of channels $[n_l \ldots n_r]$ around the peak maxima was selected. u_l and u_r are the number of counts at the left and right boundary of the gross peak. Instead of using the counts of a single channel u_l or u_r the mean value of several boundary channels $\overline{u_l}$ or $\overline{u_r}$ was used.

$$
\begin{aligned}
\overline{u_l} \quad &= \quad \sum_{j=n_l-k}^{n_l} \frac{u_j}{k} \\
\overline{u_r} \quad &= \quad \sum_{j=n_r}^{n_r+k} \frac{u_j}{k}
\end{aligned}
\tag{5.5}
$$

The number of counts K_i in the channel i was used at first to calculate ar (eq.5.4) and afterwards the underground u_i in the channel i. The commercial program GAMMA-W computes the background distribution in a similar manner, but instead of employing a purely channel depending step function is uses smoothed function $f(u_i)$ [73, 74]. This smoothed background determining function $f(u_i)$ is represented by the orange line that divides the light and the dark green area in Figure 5.3.

After the subtraction of the background distribution, the counts of the net peakarea remain. Via least-square fit a Gaussian function can be adjusted to the shape of the NP.

$$\tilde{K}_i = \frac{NP}{\sigma\sqrt{2\pi}} \cdot \exp\left(-\frac{(i-\mu)^2}{2\sigma^2}\right) \tag{5.6}$$

The least-square fit is meaningful, in particular, if two overlapping peaks need to be decomposed. Since the shape of the net peak tends to be asymmetrical, the Gaussian function is extended by an additional factor in order to guarantee the best possible approximation to the peak shape [76].

$$\tilde{K}_i = \frac{NP}{\sigma\sqrt{2\pi}} \cdot \exp\left(-\frac{(i-\mu)^2}{2\sigma^2}\right) \cdot \left(1 - \Theta(\mu - x)\kappa(x-\mu)^5\right) \tag{5.7}$$

The asymmetrical shape of the peak, the so called tailing, is caused by excited free electrons, which were not collected. Therefore, parts of the collected charge might not appear in the appropriate energy channel and the γ-count appears in a lower energy channel.

However, in the present work the analysis of the targets was performed using GAM-

MA-W [75], whereas the efficiency measurement were performed using a self made code. This code is based on the background subtraction as described above, but an implementation of the least-square fit was superfluous, since the radioactive source for the calibration were free of complex overlapping peakarea multiplets.

However, using the self made code and assuming a constant activity of the calibrated source $A_j(t)$ during the measurement, equation 5.2 can be integrated and the efficiency $\epsilon_P(E_\gamma)$ was calculated using equation 5.8.

$$\epsilon_P(E_\gamma) \;=\; \frac{NP}{I_\gamma \; \int_{t_{BoM}}^{t_{EoM}} A_j(t)\mathrm{d}t} \;\overset{A\to const.}{=}\; \frac{NP}{I_\gamma \; A_j(t_{BoM})\cdot(t_{EoM}-t_{BoM})} \tag{5.8}$$

Here t_{BoM} is the moment when the measurement begins and t_{EoM} when it ends.
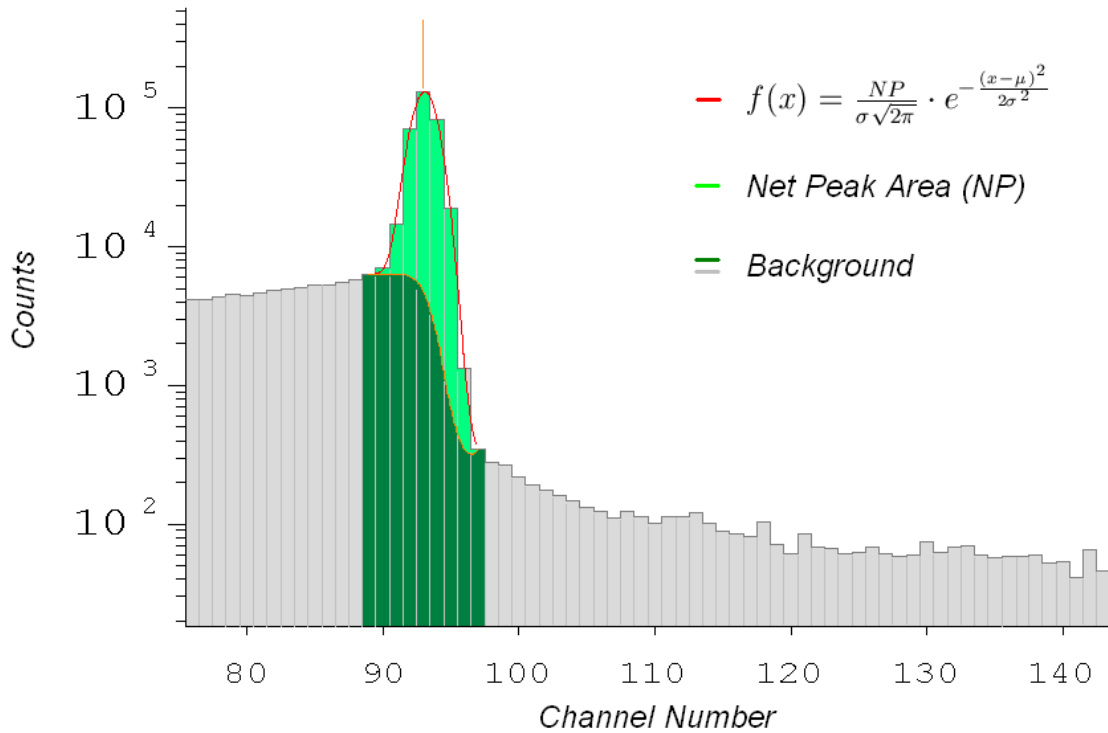
Figure 5.3: The trend of the relative share of the secondary in the primary neutron flux $\varphi_{\text{secondary}}/\varphi_{\text{primary}}$ along the target stack for a initial neutron energy of 158 MeV

5.2.3   Efficiency Functions

After having measurement of the efficiency using the calibrated PTB point sources, it was necessary to find a function that reproduces the graph of the efficiency. For this purpose, several functions are in use. Most of them are purely empirical, since models that are base on physical entities get very difficult and have to be solved using Monte Carlo methods. A characteristica of empirical functions is a set of free parameters that has to be fitted to experimentally measured efficiency data. One of the most common empirical efficiency functions was suggested by Gray and Ahmad [24].

$$\varepsilon(E_\gamma) = \frac{1}{E_\gamma} \sum_{i=1}^{8} a_i \left(\ln \frac{E_\gamma}{E_0} \right)^{i-1} \tag{5.9}$$

The Gray-Function tends to non-physical oscillation for energies above 300 keV. Due to this, the energy range over 300 keV is better reproduced by double logarithmic function.

$$\varepsilon(E_\gamma) = \exp\left(a - b \ln E_\gamma\right) \tag{5.10}$$

The disadvantage of this procedure is that both functions have to be joined. Here a certain mathematical effort is required in order to avoid a point of discontinuity. For this reason it was searched for a function that reproduces the efficiency graph in both, the low and high energetic region. A function that corresponds with the efficiency graph in the low energy region and approaches to a double logarithmic function for high energies was proposed by Wolfgang Glasser, a former researcher of the IRS.

$$\varepsilon(E_\gamma) = \exp\left(b_0 \ln E_\gamma + \sum_{i=1}^{8} \frac{b_i}{E_\gamma^{i-1}} \right) \tag{5.11}$$

This fit contains 9 free parameters, one less than the Gray-Function. Therefore, it is in principle possible to adjust the function employing less boundary condition. Although the Glasser-Function reproduces the efficiency graph satisfactorily it tends to non-physical oscillations, too. In order to avoid this unwanted behavior, the Glasser-Function was adjusted in two steps. Firstly, a modified Glasser-Function

$$\varepsilon(E_\gamma) = \exp\left(b_0 \ln E_\gamma + b_1 + \frac{b_8}{E_\gamma^7} \right) \tag{5.12}$$

was fitted to the efficiency data. This first fit result a very rough reproduction of the efficiency graph. In the second step, a further adjustment was performed employing Glasser-Function 5.11. Here the value of parameter b_8 was not adjusted but taken from result of the first, rough fit.

Figure 5.4 shows a comparison of both functions, the Glasser-Function and the Gray-Function. In order to demonstrate the occurrence of oscillations, the Gray-Fit
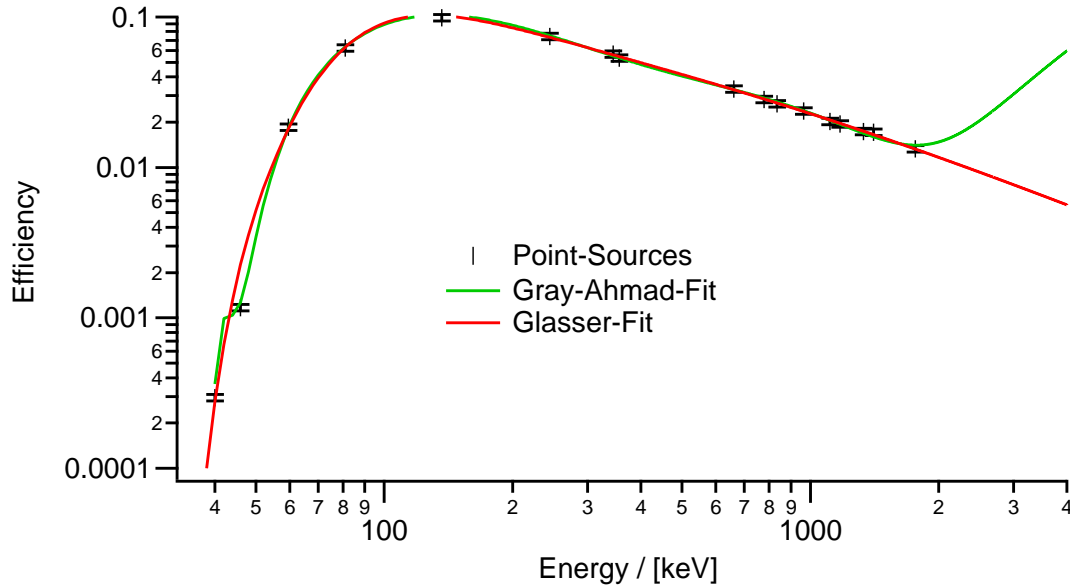
Figure 5.4: Comparison between the Glasser-Fit and the Gray-Fit on Ge_Neu in 1cm distance to the detector top.

is not merged from two functions. It can be observed, that the Gray-Fit makes an unphysical turn at around 46 keV. However, in the present work all efficiencies graphs were reproduced employing the Glasser-Function, where the free parameters were achieved using the mentioned 2-step fitting.

5.3   Analysis of the Targets

The γ-spectra of the target stacks were analyzed using the commercial software Gamma-W. Gamma-W is a high sensitivity, high precision code for the analysis of gamma ray spectra from Ge(Li) and HPGe detectors. Gamma-W determines peakareas through algorithms that fit mathematical shape functions to experimental counts after the subtraction of the analytical background distribution. The underlying gaus-

sian-functions and background distribution are described above (see page 56). These particular calculation of net peakareas was central to the determination of production rates, since the occurring complex overlapping peakarea multiplets could be easily analyzed.

Gamma-W features both manual operations by the user and automatical code executions via the use of codewords. This codewords and their associated parameters are elements of a highly flexible meta-language, which can be even used to create batch files for fully automatic γ-spectra analysis. Although the use of batch files allows to program simple and fast analysis sequences, in the present work manual operations were used. This was due to the rather complex experimental situation, where a manual, step-by-step analysis allowed a better overview on the relation between γ-spectra, γ-detector and irradiation experiments. Nevertheless, the net peakarea calculation were performed using the "automatic high precision spectrum analysis". This automated peak analysis has two advantages over the manual operation. For one thing the automated peakarea calculations are much faster and for another thing the used algorithm detects even small peaks that easily overlooked. In addition, the automated peakarea calculations yields fully reproducible data.

The output file of a "automatic high precision spectrum analysis" contained among others information according to the name of the spectra, the used γ-spectrometer, the measuring geometry, the starting time, the measuring time, the used background blank, the found net peakareas and their corresponding γ-energies and uncertainties.

The Gamma-W output files were analyzed on the base of the Evaluated Nuclear Structure Data File (ENSDF) of March 2008. For this purpose, a self written computer code scanned the Gamma-W output file for nuclide specific γ-spectra. It appeared, that this exclusively γ-spectra based analysis yielded huge numbers possible residual nuclides. However, most of the identified nuclides could not be related to the irradiation experiments. For instance, when the identified residual nuclide was much heavier than the target or had half lifes of milliseconds. For that reason further nuclide filter were implemented.

The most important nuclide filter originated from the reaction modeling calculation. The predictions of these calculations were anyway indispensable for unfolding of the excitation functions. Therefore, only predicted reaction products were of interest, whereas any other nuclide could be neglected.

A further nuclide filter was related to the half lifes $t_{1/2}^{N_i}$ of the supposed reaction products N_i. Since the intensity of the emitted radiation reduces exponentially with time,

the detection probability changes for the worse, too. Hence, the detection of a nuclide becomes rather unlikely after a certain number of half lifes had passed between the end of the irradiation t_{EoI} and the beginning of the γ-spectrometry t_{BoG}. In the present work it was assumed, that after 10 half lifes the radiation intensity of a certain radionuclide would very likely fall below detection threshold. For that reason, a net peakarea was not assigned to a radionuclide N_i when the following condition held: $t_{1/2}^{N_i} < 10 \, (t_{BoG} - t_{EoI})$.

Apart from this filters, the used algorithm marked all peak that might have suffered interference with either background radiation or peaks from other potential residual nuclides. Such marked peak were, as far as possible, not considered for the calculation of the production rates.

Using this filter the peaks in the γ-spectra were identified and assigned to corresponding radionuclides.

However, in order to calculate the activation yields it was necessary to correct the measured net peakarea for so called "real coincidences", the geometrical properties of the γ-spectrometer setup and for the nuclei which already decayed before the γ-spectrometry started.

5.4 Corrections

5.4.1 Coincidence Correction

A γ-spectrometer requires a certain time to process the electric pulse caused by an incident γ-quantum, dead-time. If two or more events happen within one read out cycle they cannot be decomposed into single events. Hence, multiple events seem to appear coincident and the collected charge is proportional to the energy of two or more γ-quanta. The collected charge affects a correct classification of the γ-ray, which cause an assignment to a wrong energy channel. In the experimental setup two different coincident events can be distinguished, the "random" and "real" the coincidence.

Random Coincidences

Random coincidence summing occurs when two or more different radioactive nuclei emit γ-quanta which reach the γ-detector quasi simultaneously. Hence, the random summations occur always. The frequency of their incidence scales with both, activity of the analyzed sample and detection efficiency. The latter is in particular related to

solid angle where the detector is placed. This is intelligible, since at least two γ-quanta have to be quasi simultaneously emitted within this direction. As above-mentioned, the analyzed targets were not very active and the solid angle of the detector at the used experimental geometry was rather small. Nevertheless, some few spectra showed slight random coincidence effects. These effects manifest themselves in the appearance of a summation peak. One of the biggest summation peak that was observed during the analysis is shown in Figure 5.5. The considered nuclide ^{54}Mn has only one γ-line at
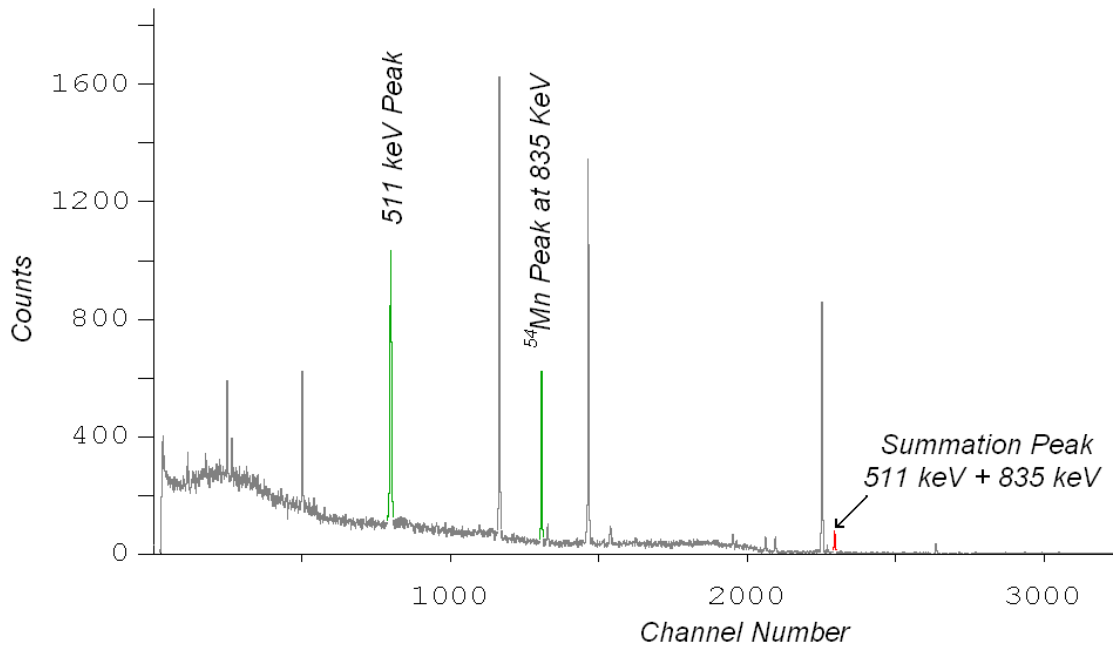
Figure 5.5: Random coincident that occurred in a Fe-Target foil.

835 keV and decays by electron capturing and thus, it does not contribute to the 511 keV peak. Despite of this, there is a visible peak at the sum of the 511 keV and 835 keV at 1346 keV, although no nuclide of such an energy is expected to be present in the analyzed target foil. This is a good indication for a random coincidence summing. In order to correct such an effect, the number of counts which refer to the net peakarea of the summation peak has to be added to each coincidence peak. In this context, number of counts are not related to the efficiency $\epsilon_P(1346 keV)$ at the summation peak, instead each γ-quantum is detected with it proper efficiency at 511 keV and 835 keV.

A proper consideration of these random coincidences in complex γ-spectra is rather impossible. Further, in the present work, random coincidences played a tangential

role. Hence, for the evaluation of production rates the random coincidence summing was not considered.

Real Coincidences

In contrast to the random coincidence, the real coincidence does not depend on the activity of the sample and can cause both, an enlargement or a reduction of the measured net peak. Accordingly, the summation effects are also distinguished by summing-in or summing-out effects. In both cases, all coincident γ-quanta are emitted by the same nucleus. This is possible, since the relaxation of the nucleus may occurs gradually via the emission of several γ-quanta. The number of γ-quanta emitted during such a gradual relaxation depend on the number of intra-nuclear energy level and the selection rules, e.g., the β^+ decay of ^{152}Eu to ^{152}Sm passes 23 intra-nuclear energy levels and emits γ-quanta with 148 different energies. The time scale of such a deexcitation ranges usually between 10^{-12} and 10^{-9} seconds. Therefore a common γ-spectrometer is unable to resolve two or more of these immediately consecutive events.

Just like in the case of random coincidences at least two of these emitted photons must reach the γ-detector to cause summation effects. Therefore they have to be emitted within the solid angle where the detector is placed. It is clearly evident that this critical solid angle and thus, the summation effects decrease with an increasing distance between detector and sample. In the present work, at measuring distance of more than 5 cm real coincidence were practically absent. However, most of the analyzed targets were measured at close to detector geometries, where real coincidences could not be neglected. On this account the summing effects were corrected for all analyzed targets and residual nuclides, respectively.

The approach to the correction of real coincidences is based on a theoretical modeling of the net peakarea $NP_{i,k}$ for a certain intra nuclear transition $i \rightarrow k$. Actually two different theoretical net peakareas have to be modeled. The first model describes the desired, coincidences free peakarea, whereas the second model describes the experimentally measured peak, which includes "real" coincidences.

The ratio of both modeled peaks κ can be used to subtract out the influence of the coincidences from experimentally measured activities.

The theoretical modeling of the net peakarea $NP_{i,k}$ starts with a simple intra nuclear

transition from the nuclear energy level i to the level k. Assuming, that during this transition a γ-quantum is emitted, the net peakarea $NP_{i,k}$ can be expressed by

$$NP_{i,k} \;=\; \rho_i \; \chi_{i,k} \; \varepsilon_{i,k} \; \int A(t)\mathrm{d}t \tag{5.13}$$

where $A(t)$ is the activity of the sample, ρ_i is the occupation probability of the i-th nuclear excitation level (directly after the preceding α or β-decay), $\varepsilon_{i,k}$ is the detector peak efficiency at the energy $E_{i,k}$ and $\chi_{i,k}$ is the transition probability $i \to k$ out of the total transition probability from level i to any level. If internal conversion is considered, the following equation holds

$$NP_{i,k} \;=\; \rho_i \; \chi_{i,k} \; \frac{\varepsilon_{i,k}}{1 + \alpha_{i,k}} \; \int A(t)\mathrm{d}t \tag{5.14}$$

where $\alpha_{i,k}$ is the conversion coefficient.

The stated occupation probability ρ_i does not consider transitions from above lying levels to the i'th level. However, if such above lying levels exist, they have to be taken into account. To this end, the occupation probability ρ_i has to be replaced by an entity that considers this intra nuclear transitions. Assuming m energy levels, ρ_i can be replaced by

$$\tilde{\rho}_i \;=\; \rho_i \;+\; \sum_{n=i+1}^{m} \tilde{\rho}_n \; \chi_{n,i} \tag{5.15}$$

$$NP_{i,k} \;=\; \tilde{\rho}_i \; \chi_{i,k} \; \frac{\varepsilon_{i,k}}{1 + \alpha_{i,k}} \; \int A(t)\mathrm{d}t \tag{5.16}$$

This model does not consider summing effects and therefore represents the first of the previously mentioned peakarea models.

In contrast to the rather simple first model, the consideration of "real" coincidences demands a more complex approach. Whereas the first peakarea model focuses on the total occupation probability $\tilde{\rho}_i$, the second model uses a virtual occupation probability P_i. Compared with $\tilde{\rho}_i$, P_i additionally considers the unwanted detection of γ-quanta that are emitted during the transition from above lying levels. The probability of such a detection is usually refered to as the total efficiency $\varepsilon_{n,k}^{tot}$. What makes the difference between peak efficiency $\varepsilon_{n,k}$ and total efficiency $\varepsilon_{n,k}^{tot}$ is the energy transfer to the detector. In this connection $\varepsilon_{n,k}$ is the probability that a γ-quantum transfers its complete energy to detector, whereas $\varepsilon_{n,k}^{tot}$ is the probability that the quantum transfers either its entire energy or just a share of it. Evidently any additional energy transfer interferes

with the correct assignment of the detector signal to the intra nuclear transition $i \rightarrow k$. Hence, the virtual occupation probability P_i is expressed by

$$P_i = \rho_i + \sum_{n=i+1}^{m} P_n \, \chi_{n,i} \left(1 - \frac{\varepsilon_{n,i}^{tot}}{1 + \alpha_{n,i}} \right), \tag{5.17}$$

, where $1 - \varepsilon_{n,i}^{tot} \cdot (1 + \alpha_{n,i})^{-1}$ is the probability that the γ-quantum of a transition $n \rightarrow k$ is not detected.

Assuming that the intra nuclear transition does not stop at the energy level k, the subsequent emission of γ-quanta from below lying levels (level $k-1$ to level 0) has to be considered, too. In analogy to the emission of γ-quanta from above lying levels, this additional γ-quanta are considered via their transition- and detection probability. To this end a new variable M_k is introduced.

$$M_k = \sum_{j=0}^{k-1} M_j \, \chi_{k,j} \left(1 - \frac{\varepsilon_{k,j}^{tot}}{1 + \alpha_{k,j}} \right) \quad \text{with } M_0 = 1 . \tag{5.18}$$

In case that the intra nuclear level i and k are no neighbor-levels, additional transitions from i to k via intermediate level may occur. Such a transition cascade may involves the emission of several γ-quanta, where the sum over the energy of this quanta is very likely equal to the energy of the $E_{i,k}$. Therefore the coincidental detection of all γ-quanta emitted during such a transition cascade results in a false positive detection of the $i \rightarrow k$ transition.

For this reason, the gradual transitions from i to k via intermediate nuclear level have to be considered. In the present work, this is done by a sum $A_{i,k}$ over all transition paths which start at level i and end at level k. The individual addends of this sum were weighted by their detection probability.

$$A_{i,k} = \chi_{i,k} \, \frac{\varepsilon_{i,k}}{1 + \alpha_{i,k}} + \sum_{j=k+1}^{i-1} \chi_{i,j} \, \frac{\varepsilon_{i,j}}{1 + \alpha_{i,j}} \, A_{j,k} \tag{5.19}$$

Apart from this intra nuclear transitions, two further issues have to be considered. At first the metastable energy levels and in second place positron emission at β^+ decays. In the context of real coincidence every nuclear excitation state that last longer than the time resolution of the γ-detector can be considered metastable. In such cases the detector can measure at least two distinct signals. The first signal refers to transitions towards the metastable level and the second refers to transitions starting from the

metastable level. Therefore P_i, M_k and $A_{i,k}$ had to be corrected for "metastable" energy levels.

In the present work the time resolutions of the used γ-spectrometers were about 10^{-6} seconds. In the case of P_i this value was considered via a function $\delta^P(t_{1/2}(k))$, with

$$\delta^P(t_{1/2}(k)) \;=\; \begin{cases} 1, & t_{1/2}(k) \leq 10^{-6} \\ 0, & t_{1/2}(k) > 10^{-6} \end{cases} \tag{5.20}$$

where $t_{1/2}(k)$ is the half-life of the nuclear excitation level k. The correction of the variable M_k used a similar function $\delta^M(t_{1/2}(i))$, with

$$\delta^M(t_{1/2}(i)) \;=\; \begin{cases} 1, & t_{1/2}(i) \leq 10^{-6} \\ 0, & t_{1/2}(i) > 10^{-6} \end{cases} \tag{5.21}$$

and the half-life $t_{1/2}(i)$ of the excitation level i. $A_{i,k}$ was rectified using the function $\delta^A(t_{1/2}(i,k))$

$$\delta^A(t_{1/2}(i,k)) \;=\; \begin{cases} 1, & t_{1/2}(i) \leq 10^{-6} \text{ or } t_{1/2}(k) \leq 10^{-6} \\ 0, & t_{1/2}(i) > 10^{-6} \text{ or } t_{1/2}(k) > 10^{-6} \end{cases} \tag{5.22}$$

where $t_{1/2}(i)$ and $t_{1/2}(k)$ are the half-life excitation level i and k, respectively.

The positron emission during β^+ decays causes 511 keV annihilation radiation which can be detected by the γ-spectrometer. Thus, positron emissions have to be considered since the annihilation radiation may cause summing effects. For this purpose a function $\delta(\beta^+)$ was defined as

$$\delta(\beta^+) \;=\; \begin{cases} (1 - \varepsilon_{511}^{tot})^2, & \beta^+ \text{ decay with positron emission} \\ 1, & \text{decay without positron emission} \end{cases} \tag{5.23}$$

where $(1 - \varepsilon_{511}^{tot})^2$ is the probability that non of both 511 keV annihilation photons interacts with the γ-detector. Using this equations the net peakarea $NP_{i,k}^{Real}$ of the transition $i \rightarrow k$, which includes real coincidences, can be written as

$$NP_{i,k}^{Real} \;=\; \tilde{P}_i \; \tilde{M}_k \; \tilde{A}_{i,k} \int A(t)\mathrm{d}t \tag{5.24}$$

where $\tilde{P}_i$ is

$$\tilde{P}_i \;=\; \rho_i \; \delta(\beta^+) \;+\; \sum_{n=i+1}^{m} \; \tilde{P}_n \; \chi_{n,i} \; \delta^P(t_{1/2}(i)) \; \left(1 - \frac{\varepsilon_{n,i}^{tot}}{1 + \alpha_{n,i}}\right), \qquad (5.25)$$

$\tilde{M}_k$ is

$$\tilde{M}_k \;=\; \sum_{j=0}^{k-1} \; \tilde{M}_j \; \chi_{k,j} \; \delta^M(t_{1/2}(k)) \; \left(1 - \frac{\varepsilon_{k,j}^{tot}}{1 + \alpha_{k,j}}\right) \quad \text{with } \tilde{M}_0 \;=\; 1 \qquad (5.26)$$

and $\tilde{A}_{i,k}$ is

$$A_{i,k} \;=\; \chi_{i,k} \; \frac{\varepsilon_{i,k}}{1 + \alpha_{i,k}} \;+\; \sum_{j=k+1}^{i-1} \chi_{i,j} \; \delta^A(t_{1/2}(i,j)) \; \frac{\varepsilon_{i,j}}{1 + \alpha_{i,j}} \; A_{j,k}. \qquad (5.27)$$

Dividing equation 5.16 and 5.24 the coefficient $\kappa_{i,k} = NP_{i,k}/NP_{i,k}^{Real}$ is found. The multiplication of $\kappa_{i,k}$ with the corresponding measured net peakarea corrects the summation effect of the transition $i \to k$ for the given geometry and detector. The nuclear data ($\chi_{i,k}$, $\alpha_{i,k}$, $t_{1/2}(i,k)$, $\delta(\beta^+)$ and ρ_i) used for the peak modeling were taken from the Evaluated Nuclear Structure Data File (ENSDF) of March 2008.

The used detector efficiencies $\varepsilon_{i,k}$ and $\varepsilon_{i,k}^{tot}$ were measured in the context of the detector calibration. However, the described correction method demands priori efficiency data and thus, was not qualified to perform the summing effect corrections for the detector calibration.

Therefore the detector efficiency had to be determined with coincidence-free radionuclides. This is ensured by the use of nuclides, which emit only a single γ-quantum of one well defined energy during their decay (so-called one line nuclides). However, apart from the use of the one-line nuclides ^{241}Am, ^{137}Cs and ^{54}Mn, it was inevitable to the employ further nuclides for the efficiency calibration since the available one line nuclides covered a rather small energy spectra. To this end, the two-line nuclides ^{57}Co and ^{60}Co were used chosen since they are recommended to be employed for the detector calibration as long as no sufficient number of one-line nuclides is available [16].

In addition to the peak efficiency $\varepsilon(E)$, the total efficiency $\varepsilon(E)^{tot}$ had to be recorded, too. For this propose the same radioactive sources were used.

Although the measured peak and total efficiency $\varepsilon(E)^{tot}$ was calculated based on

few measured points, it was possible to perform a first correction of the coincidence summing using a set of nuclide specific approximation formulas which were suggest for calibration purposes by Debertin and Schötzing [16]. This formulas were available for commonly used calibration nuclides like ^{152}Eu, ^{133}Ba or ^{226}Ra. Thus, it was possible to perform a second peak efficiency calibration using more radionuclides.

Figure 5.6 shows the performed summing effect corrections of the calibration nuclides. Further it shows the graphs of the total and peak efficiencies of the detector GeLiU4 at the 1 cm geometry. The error bars of the efficiency points were set to 5 %. It can be noticed that the applied summation effect corrections show good agreement with the graph of the efficiency.
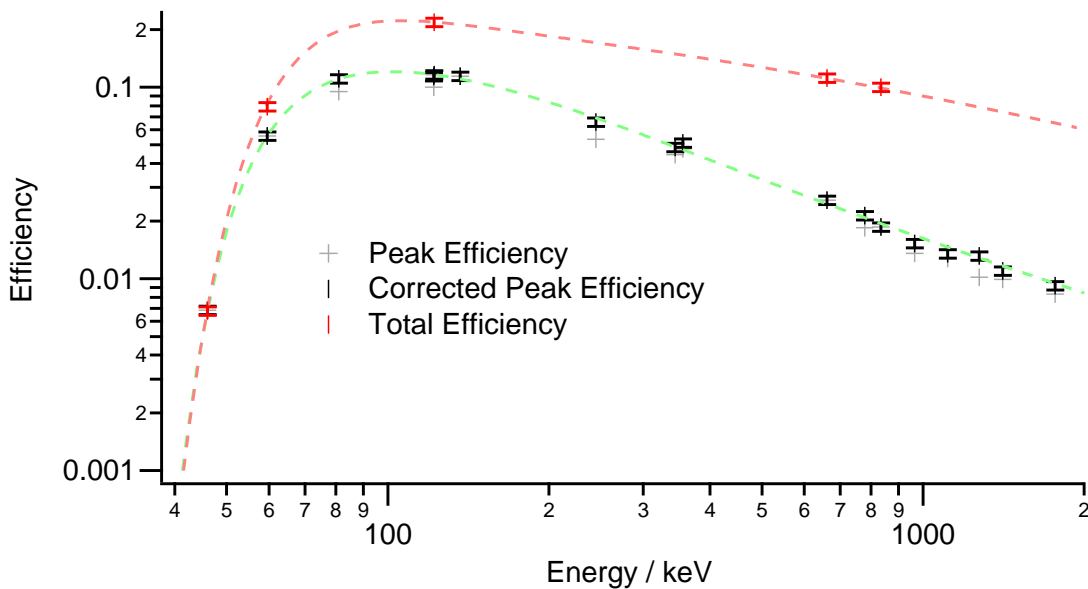
Figure 5.6: Correction of the Coincidence Summing

Table 5.3 shows the correction coefficient κ which corresponds to the ^{152}Eu-lines in Figure 5.6. The table emphasizes the importance of the coincidence correction, since it demonstrates that some net peakareas need to be corrected by more than 20 %. In fact ^{22}Na had to be corrected by almost 30 % in the same detector and setup. Hence, is was possible to calculate a "corrected" efficiency function which covered a wide energy range between about 40 and 1768 keV. This efficiency function allowed the determination of activation yields including the correction of summing effects via the calculation of κ.

Employing the "corrected" efficiency functions, the total efficiencies and the nuclear

Table 5.3: Coincidence Correction Coefficient κ for ^{152}Eu on GeLiU4 in the 1cm geometry

Energy/keV	121.8	244.7	344.3	778.9	964.1	1112.0	1408.0
κ	1.12	1.22	1.09	1.16	1.13	1.09	1.11

data from the Evaluated Nuclear Structure Data File it was possible to calculate $\kappa_{i,k}$. The reliability of the calculated $\kappa_{i,k}$ values was tested using the program ETNA (Efficiency Transfer for Nuclide Activity measurements). ETNA was developed by the Laboratoire National Henri Becquerel (LNHB) in France and is Monte Carlo Simulation of a entire γ-spectrometer. Consequently, ETNA is not only able to compute the coincidence summing but to simulate the efficiency transfer and geometrical corrections in γ-ray spectrometry. In order to use the MC features it would have been necessary to enter several data according to the geometrical and physical properties of the employed detectors. This information were not available, since the used detectors were manufactured at a time, where these data were of no interest. Nevertheless, ENTA offers the possibility of entering measured efficiency data. Using this option the correction coefficient κ could be calculated for several of radionuclides. An extended comparison between the results of ETNA and the used $\kappa_{i,k}$ values showed excellent agreement, which indicates a good reliability of the performed summation effect corrections.

5.4.2   Geometrical Correction

A further factor that affected the efficiency and had to be considered is based in the geometrical extent of the target foils. In contrast to the cylindrical shape of the targets, the calibration sources were point-shaped. In order to calculate the volume-efficiency ϵ_V, the point-efficiency ϵ_{Point} was integrated over the dimensions of the target foil. A certain share of the emitted γ-quanta gets absorbed on the trajectory $s(z,r)$ within target material. This self absorption is considered in terms of the attenuation factor $exp(-\mu s)$. In this connection $\mu = \mu(E_\gamma)$ is the energy depending absorption coefficient.

For a target of the radius R a thickness h and a distance to the detector d, ϵ_V can be written as [15]:

$$\epsilon_V(d,E_\gamma) = \frac{2\pi}{h\pi R^2} \int_d^{d+h} \mathrm{d}z \int_0^R e^{-\mu E_\gamma s(z,r)} \epsilon_{Point}(r,z,E_\gamma) r \mathrm{d}r. \tag{5.28}$$

Assuming that the integral 5.28 can be factorized into a radius independent attenuation factor $u(z,E_\gamma)$, a radius depending function $v(r,E_\gamma)$ and a thickness depending function $w(z,E_\gamma)$, equation 5.28 can be expressed like in equation 5.29. Hence, a simple correction of the point efficiency can be performed.

$$\epsilon_V(d,E_\gamma) = \epsilon_{Point}(d,E_\gamma) \int_d^{d+h} u(z,E_\gamma)\mathrm{d}z \int_0^R v(r,E_\gamma)\mathrm{d}r \int_d^{d+h} w(z,E_\gamma)\mathrm{d}z \tag{5.29}$$

The decomposition of the integral 5.28 was already applied for the diploma thesis of Carsten Kaftan and the PhD Thesis of Sonja Neumann [29, 52]. In the cited works the procedure is discussed in more detail.

The Radius Depending Function $v(r,E_\gamma)$

In order to determine the radius depending function $v(r,E_\gamma)$ and to find out if the small target diameter of maximum 25 mm had an influence on the detection efficiency, a calibration source of exactly the above mentioned diameter was build. For this purpose, a 25 mm disk of blotting paper was moistened with a calibrated standard solution (QCY). Subsequently the efficiency of the detectors were recorded in a distance of 1 cm employing both, the disk source and the point sources. A comparison of the obtained efficiency functions is shown in Figure 5.7. The result of the comparison shows two, within the estimated 5 % uncertainty, identical graphs of the efficiency. Both efficiency function overlap in the energy area of 90 keV and they cross each other at about 600 keV. Since the behavior of the detector efficiency did not show any significant change according to the diameter of 25 mm at 1 cm distance, all influences of the target diameter concerning the calculated activity of the residual nuclei were discarded.

In consequence, the integral over the radius depending function $\int v(r)\mathrm{d}r$ was set to 1
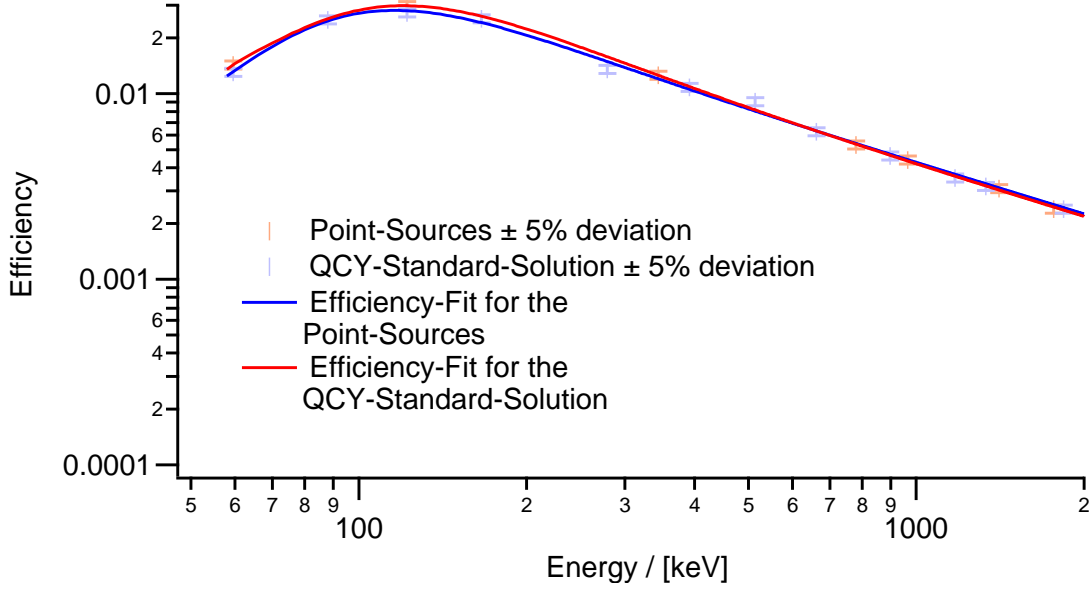
Figure 5.7: The detector efficiency measured in 1 cm distance to the top of the detector with the 25 mm diameter QCY disk and with the point sources.

and the function of the volume-efficiency ϵ_V could be simplified. This updated function is shown in equation 5.30.

$$\epsilon_V(d,E_\gamma) = \epsilon_{Point}(d,E_\gamma) \int_d^{d+h} u(z,E_\gamma)\mathrm{d}z \int_d^{d+h} w(z,E_\gamma)\mathrm{d}z \qquad (5.30)$$

The Thickness Depending Function $w(z,E_\gamma)$

Besides the diameter of the target foils, their thickness of up to 5 mm was considered to have a geometrical influence on the efficiency. This effect was expressed in the thickness depending function $w(z)$. Neglecting the radius dependency of the geometrical influence, $w(z)$ reproduces the dependency of the point-efficiency $\epsilon_{Point}(d,E_\gamma)$ on the distance between the radioactive sample and the detector. In a first approximation $w(z,E_\gamma)$ is proportional to the solid angle α in which the sample "sees" the detector. This angle is determined by equation 5.31. Equation 5.31 considers the third dimension

of the geometry via the exponent 2 in the arcus tangent function. This is possible due to the cylindrical symmetry of the system.

$$w(z,E_\gamma) \propto \alpha = ArcTan^2(\frac{d}{z + d_0})$$ (5.31)

Here r is the radius of the semi conducting crystal, d_0 the distance between the top of the detector and the crystal, and d the distance between the detector and the radioactive source.

In order to determine $w(z,E_\gamma)$, the efficiency function $\epsilon_{Point}(d,E_\gamma)$ was measured for several distances d. The thickness function, which depends not only on the distance z to the detector but also on the energy of the γ-quanta was fitted to these measured efficiency functions. Doing so it was possible to calculate individual thickness functions for each γ-energy, γ-spectrometer and the target thickness. It turned out, that the individual thickness functions $w(z,E_\gamma)$ reproduced the behavior of the efficiency $\varepsilon(d,E_\gamma)$ satisfactory, in particular for small changes of d. An example of this adjustment is shown in Figure 5.9. Here the efficiency functions of the detector Ge_02 are plotted in blue for the distances of 1, 3, 6, 10 and 11 cm. Perpendicularly to the set of efficiency function $\epsilon_{Point}(d = \{1,3,6,10,11\},E_\gamma)$ the fitted thickness functions $w(z,E_\gamma =$
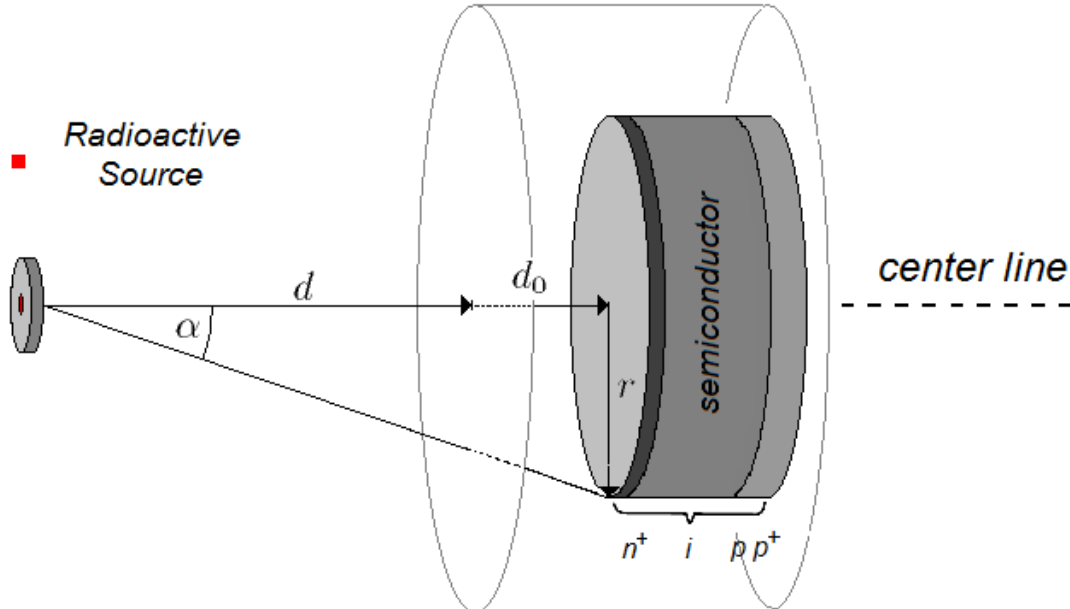
Figure 5.8: Illustration of the relation between the thickness depending function $w(z)$, the solid angle α and the arctan-function.

200,...,1800keV) are displayed. The latter are plotted in green.

Since the nuclear decay is a statistical process, its location in the target foil is only predictable in terms of statistics. Thus, for a sufficiently high number of nuclear decays their spatial distribution can be seen as homogeneous. Hence, the mean distance between decaying nuclei and detector is $\bar{z} = d_0 + d + h/2$. Here h is the thickness of the target foil. Therfore the mean contribution of the thickness function is calculated as follows,

$$\int_d^{d+h} \frac{w(z,E_\gamma)}{h}\mathrm{d}z \tag{5.33}$$

Considering equation 5.33, the correction of the efficiency can be expressed as

$$\epsilon_V(d,E_\gamma) = \epsilon_{Point}(d,E_\gamma) \int_d^{d+h} u(z,E_\gamma)\mathrm{d}z \int_d^{d+h} \frac{\beta \ ArcTan^2(\frac{r}{z+d_0})}{h} \ \mathrm{d}z \tag{5.34}$$

Here β, r and d_0 are parameters that were obtained by the above mentioned fitting procedure.

Self Absorption Correction $u(z,E_\gamma)$

The attenuation of a γ-line due to the absorption of γ-quanta inside of the target foil is considered in the factor $\exp(-\mu s)$. The values of the attenuation coefficients $\mu = \mu(E_\gamma)$
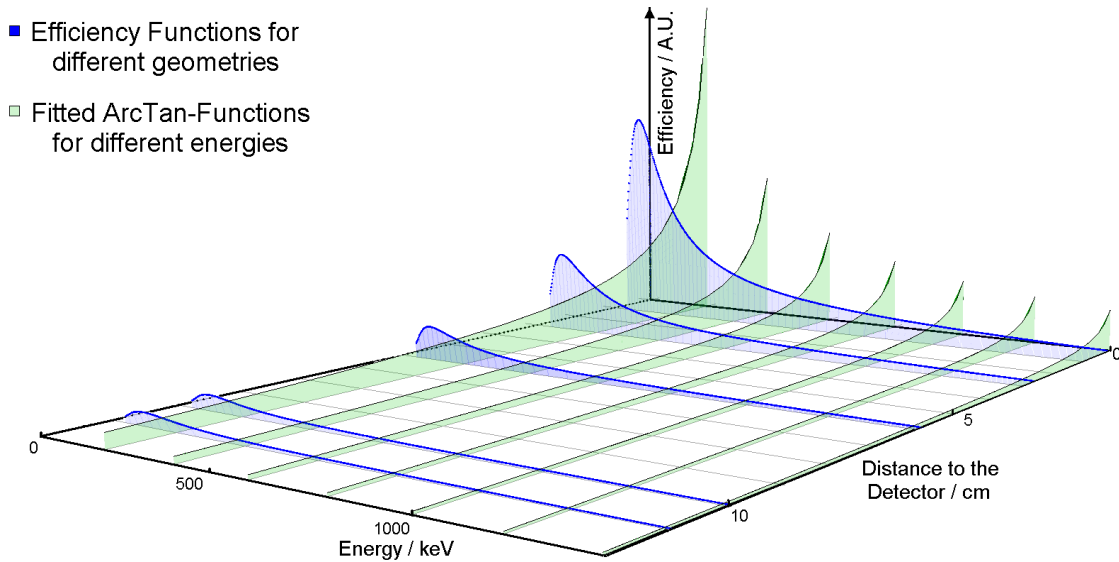
Figure 5.9: The trend of the relative share of the secondary in the primary neutron flux $\varphi_{\mathrm{secondary}}/\varphi_{\mathrm{primary}}$ along the target stack for a initial neutron energy of 158 MeV
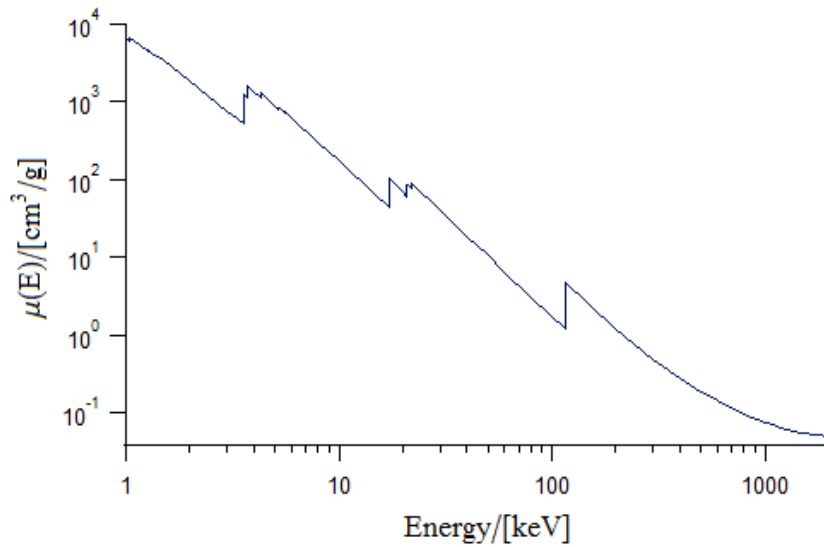
Figure 5.10: Energy dependent attenuation coefficient of uranium.

differ for each irradiated material and can be taken from the database of Storm and Israel [71]. The trajectory $s = s(r,h)$ of the γ-quantum had to be calculated for the dimensions of the corresponding target foil.

However, in this work the self absorption was calculated using the program XCOM. This program can generate cross sections and attenuation coefficients for any element, compound or mixture at energies between 1 keV and 100 GeV. Apart from the total cross sections and attenuation coefficients the XCOM output includes partial cross sections for incoherent scattering, coherent scattering, photoelectric absorption, and pair production in the field of the atomic nucleus and in the field of the atomic electrons. Although the XCOM database pertain only isolated neutral atoms, the XCOM calculation are qualified for the present work, since the neglected molecular effects which may modify the cross sections occur mainly in the vicinity of absorption edges. These absorption edges, however, are negligible in the energy region of γ-radiation. Further XCOM calculations omitted is the nuclear photoeffect. This interaction is relevant for the giant-dipole resonance in energy regions from about 5 MeV to 30 MeV, but for the present work any significant contribution can be ruled out.

The energy grid of the XCOM calculations can be fully adapted to individual demands. For this reason it was possible to calculated individual, energy depending attenuation coefficients $\mu = \mu(E_\gamma)$ for all used target materials. Figure 5.10 shows the attenuation coefficient $\mu = \mu(E_\gamma)$ of uranium. The clearly visible sawtooth pattern of the

attenuation graph can be related to the photoelectric effects on the inner electrons. For the evaluation of the production yield only γ-quanta with energies beyond these photoelectric effects were considered, since in the vicinity of such a sawtooth the attenuation coefficient is subject to huge changes. These fluctuations would make any calculation of self-absorption unreliable. However, in the present work this limitations were only relevant for the targets made from lead and uranium. Thus, when possible, only γ-quanta with energies beyond 100 keV were considered for lead targets and only γ-quanta with energies beyond 200 keV were considered for uranium targets.

In order to evaluate the targets, the obtained attenuation function $u(z,E_\gamma)$ was integrated into the correction of the efficiency.

$$\epsilon_V(d,E_\gamma) = \epsilon_{Point}(d,E_\gamma) \int_d^{d+h} \frac{\kappa \cdot \exp(-\mu(z,E_\gamma) \cdot s(h))}{\kappa \cdot h} \mathrm{d}z \int_d^{d+h} \frac{\beta \; ArcTan(\frac{r}{z+d_0})}{h} \; \mathrm{d}z \tag{5.35}$$

The importance of the performed geometrical and coincidence correction is clearly evident from table 5.4. It shows, that the discussed correction increase the activation yield of the isotope ^{52}Mn in the irradiated iron targets by more than 50%.

Table 5.4: Activity Correction on the 744 keV γ-line of ^{52}Mn in iron targets

^{52}Mn/Mol without corr.	Thickness	Self Absorption	Coincidence	^{52}Mn/Mol with corr.
$4.57 \cdot 10^8 \pm 10.2\%$	≈ 16 %	≈ 8 %	≈ 20 %	$6.87 \cdot 10^8 \pm 13.6\%$

Time-Logger Correction

In order to infer production rates from the net peakarea, the half lifes of the measured radionuclides have to be considered additionally to the mentioned coincidence and geometrical corrections. This additional data treatment is based on the evaluation of the Time-Logger files which were recorded during the irradiation experiments (see chapter 3.3.4). The general case of such a Time-Logger correction is discussed hereinafter.

The aim of the performed activation experiments was to induce nuclear reactions on target nuclides. In this context, the production rate P_j of the isotope j is given by

$$P_j = N_i \; \sigma_{j,i,k}(E') \; \varphi_k(E') \tag{5.36}$$

where is the N_i number of a target nuclei of the isotope i with the cross section $\sigma_{j,i,k}(E')$ which gets irradiated by a projectile k with energy E' and the projectile flux $\varphi_k(E')$. In the present case, the irradiated targets consist of only one element but of in some cases of several isotopes. This was due to the fact that all targets were made from elements with natural isotopic abundance. Therefore the equation of production rate must be extended in order to include several isotopes and their particular cross sections,

$$P_j = \sum_i N_i \ \sigma_{j,i,k}(E') \ \varphi_k(E') \tag{5.37}$$

In equation 5.37, mono-energetic projectiles are presumed, but as it was mentioned in the previous chapters, the experimental neutron spectra followed a complex, energy depending distribution. Taking this into account, it is necessary to integrate out the energy dependence. Therefore the integration has to be performed over the product of the neutron flux and the cross section, excitation function respectively.

$$P_j = \sum_i N_i \ \int_0^\infty \sigma_{j,i,k}(E) \ \varphi_k(E) \ dE \tag{5.38}$$

If the produced isotope is radioactive the number of nuclei in the sample will be reduce with time. The velocity of this process is usually characterized by a specific decay constant λ_j. The change of the existing quantity of produced nuclei $\dot{N}_j$ depends congruously on both, the activity $A_j = \lambda_j N_j(t)$ and the production rate P_j of the isotope.

$$
\begin{aligned}
\dot{N}_j &= \sum_i N_i \ \int_0^\infty \sigma_{j,i,k}(E) \ \varphi_k(E) \ dE - \lambda_j N_j(t) \\
\dot{N}_j &= P_j(t) - \lambda_j N_j(t)
\end{aligned}
\tag{5.39}
$$

The differential equation 5.39 can be solved, assuming a constant number of target atoms during the irradiation time and further an absence of activates at a time $t = 0$. The integration results in the activation equation.

$$N_j(t) = \frac{P_j(t)}{\lambda_j}(1 - e^{-\lambda_j t}) \tag{5.40}$$

Considering the presence of the examined isotope at a time t_{l-1}, equation 5.39 can be integrated for $t_l > t_{l-1}$. The expanded activation equation gives the number of nuclei $N_j(t_l)$ at the moment t_l.

$$N_j(t_l) = \frac{P_j(t_l)}{\lambda_j} \left(1 - e^{-\lambda_j t_l}\right) + N_j(t_{l-1}) \, e^{-\lambda_j (t_l - t_{(l-1)})} \tag{5.41}$$

Employing this equation the irradiation period was divided into small time segments. Doing so it was possible to integrate the data of the time logger measurements which provided information about fluctuations in the neutron flux intensity.

In the further course of the discussion the time dependent neutron flux $\varphi_N(E, t_l)$ represents the measured average neutron flux in the time interval t_l. Defining $t_{EoI} = \tau$ as the end of the irradiation, equation 5.41 can be used to derive

$$A_j(\tau) = N_i \sum_{l=1}^{EoI} \int_0^\infty \sigma_j(E) \, \varphi_N(E, t_l) \, dE \, \left(1 - e^{-\lambda_j t_l}\right) + \lambda_j N_j(t_{l-1}) \, e^{-\lambda_j (t_l - t_{(l-1)})}. \tag{5.42}$$

Here $\lambda_j N_j(\tau)$ is equivalent to the activity $A_j(\tau)$ of the residual nuclide at the EoI (End of Irradiation).

This recursive equation could be solved in a simplified form, where

$$\int_0^\infty \sigma_j(E) \, \varphi_N(E, t_l) \, dE \to \sigma_j \cdot \varphi_N(t_l) \tag{5.43}$$

was replaced. In addition, the different target isotopes were combined to one target material $N_T = \sum N_i$. Thus, the total cross section σ_j was calculated using the initial condition $N_j(t_0) = 0$, the number of target nuclei N_T and the measured time dependent neutron flux $\varphi_N(t_l)$.

Usually the examined residual nuclei j were not only produced directly by the nuclear reaction between the incident neutron and the target, but also either by nuclear β-decay along the isobar chain, or by α-decay for heavier nuclei. This additional production brunch requires the production (e.g. by a neutron induced reaction during the irradiation) and presence of a proper mother nuclide. Taking this into account, a system of two coupled differential equations is found.

$$\begin{aligned}
\dot{N}_{mot} &= \sigma_{mot} \varphi N_T - \lambda_{mot} N_{mot} \\
\dot{N}_j &= \sigma_j \varphi N_T - \lambda_j N_j + \lambda_{mot} N_{mot}
\end{aligned} \tag{5.44}$$

In this context the number of mother nuclei is called N_{mot} to avoid a mix-up of indices. Depending on the number of considered isobars respectively mother nuclides, larger systems of coupled differential equations can be found. However, the consideration of more mother nuclides would complicated the following equations without providing additional information.

This differential equation system can be solved using the following ansatz

$$N_j(t) = f(t)\, \mathrm{e}^{-\lambda_j t}$$

With the initial conditions $N_i = const.$ equation 5.45 can be written as follows,

$$
\begin{aligned}
N_j(t_l) \;=\; & \varphi(t_{l-1})N_i \left\{ (\sigma_{mot} + \sigma_j) \frac{1 - \mathrm{e}^{-\lambda_j(t_l - t_{l-1})}}{\lambda_j} + \sigma_{mot} \frac{\mathrm{e}^{-\lambda_{mot}(t_l - t_{l-1})} - \mathrm{e}^{-\lambda_j(t_l - t_{l-1})}}{\lambda_{mot} - \lambda_j} \right\} + \\
& N_{mot}(t_{l-1}) \frac{\lambda_{mot}}{\lambda_{mot} - \lambda_j} \left(\mathrm{e}^{-\lambda_j(t_l - t_{l-1})} - \mathrm{e}^{-\lambda_1(t_l - t_{l-1})} \right) + \\
& N_j(t_{l-1}) \mathrm{e}^{-\lambda_j(t_l - t_{l-1})}
\end{aligned}
\tag{5.45}
$$

In order to solve this recursive equations it is necessary to determine the activity $\lambda_{mot} N_{mot}$ of the mother nuclide. In the present work this was impossible for most of the considered residual nuclei, since their mothers had relatively short half-life periods. For this reason the calculated excitation functions included the nuclear production information of the superior branch of the isobar chains for the specific neutron induced reactions.

Caused by the experimental difficulties related to the determination of short living nuclides, it is widely used to state this so-called "cumulative" cross sections. The drawback for applications is rather small, since most of them use "cumulative" cross sections anyway. However, in this work the "cumulative" excitation functions were unfolded with the help of modeled excitation functions. The latter were based on "individual" cross sectionsand had to be recalculated to cumulativ excitation functions in order to be compatible with the measured production rates (see page 99).

5.5   Uncertainty Propagation

In the present work, the uncertainty propagation and the calculation of the total measurement uncertainties were performed following the recommendations of the

ISO-GUM [20]. In the context of activity uncertainties two sources were considered, the efficiency uncertainty and the counting statistics.

Uncertainty of the Efficiency

The reliability of the calculated efficiency function $\varepsilon(E_\gamma)$ depends mainly on the accuracy of the measured efficiency points. The standard uncertainties of these points are in principle known. They consist of both, the poison uncertainty of the counting statistic and of the calibration (activity) uncertainty. Both uncertainties ranged between 1 % and 5 %. Unfortunately it was not possible to incorporate this measurement uncertainties into the efficiency function fitting procedure. Hence, a measured point with a big uncertainty got the same weight during the adjustment of the efficiency function as a point with a small uncertainty. In this manner only a rough estimation of the uncertainties of the efficiency functions was possible by estimating the distribution of the unweighted measured points around the graph of the efficiency function. However, these estimations were not suitable for a proper uncertainty propagation.

Driven by this reason, the uncertainty estimation of the efficiency function was performed by statistical measurements. For this purpose, a calibrated point source
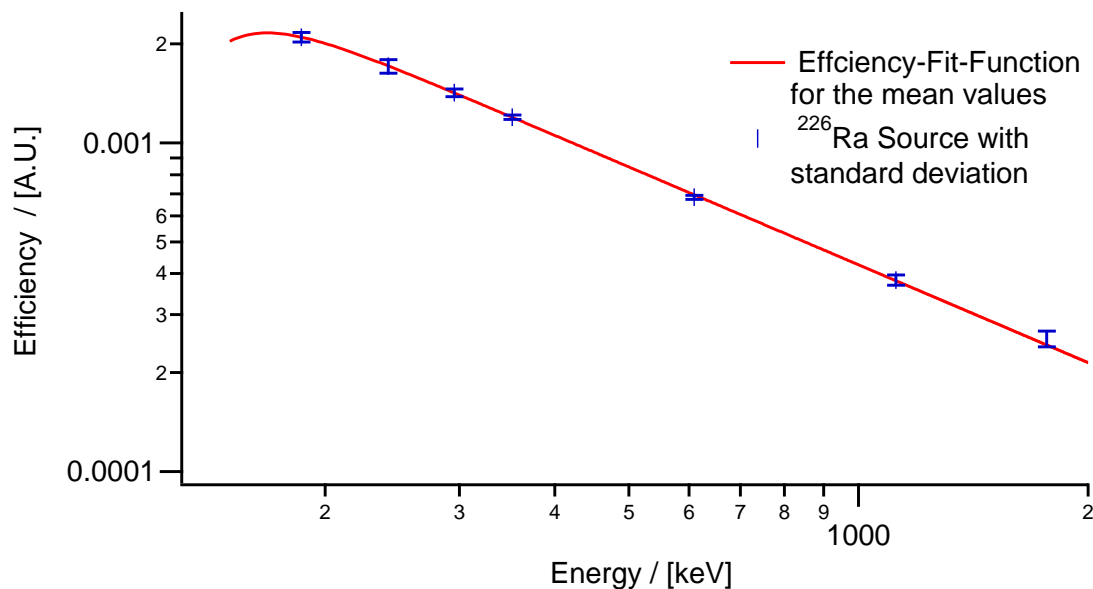
Figure 5.11: Estimation of the Standard-Deviation of the Efficiency Function $\varepsilon(E_\gamma)$ by statistical measurements
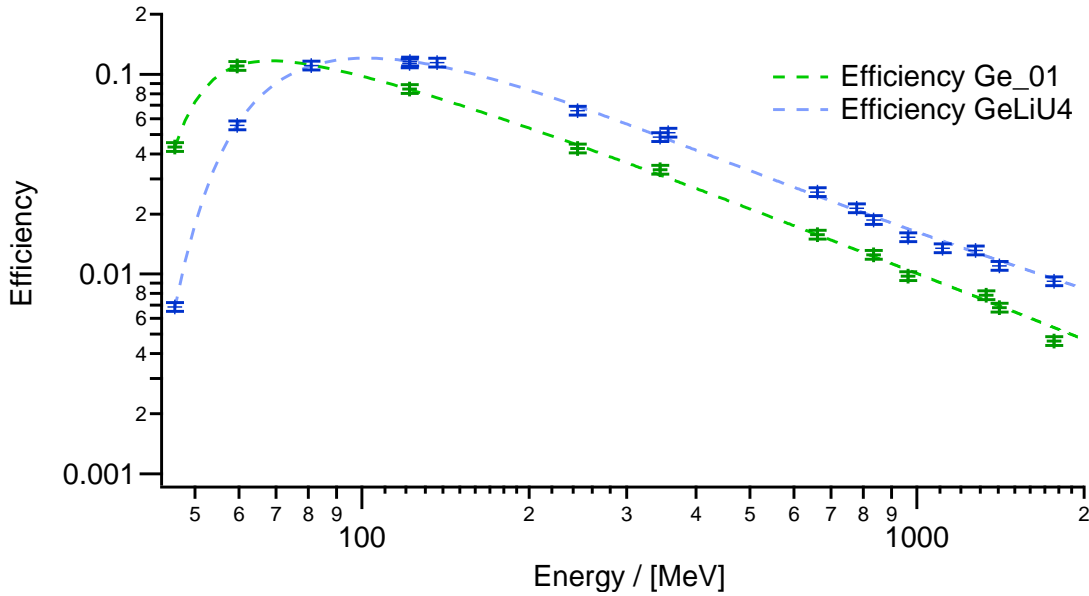
Figure 5.12: The efficiency of Ge_01 and GeLiU4 in direct comparison, both for the 1 cm geometry

was employed in order to measure the efficiency of a detector. This procedure was repeated 6 times and the fit of the efficiency function $\varepsilon(E_\gamma)$ was performed using the mean values of the measurement. The result of this procedure is shown in Figure 5.11. It turned out that the maximum difference between a mean value and the corresponding value of the efficiency function $\varepsilon(E_\gamma)$ was 4.4 %. In order to be on the safe side, the standard deviation of the efficiency was rounded to 5 %. These 5 % were assumed to be the uncertainty contribution of the efficiency and were added to the uncertainty propagation.

In this context, the uncertainties of the calibration sources were set to 5 % in all Figures that show measurements which include such sources.

Further individual differences according to the efficiency properties of the used detector became clear, when comparing the efficiency of the different detectors. Figure 5.12 shows the plot of the efficiency corresponding to the detector Ge_01 and GeLiU4, both for the 1 cm geometry. It is evident that the Ge_01 detector is more suitable for the detection of lower energy γ-rays than the GeLiU4 detector. For a γ-energy of 40 keV the efficiency of Ge_01 outdoes GeLiU4 by a factor of seven. On the other hand, GeLiU4 detects high energetic γ-quanta twice as good as Ge_01. The difference in the detection probability influences directly the uncertainties occurring
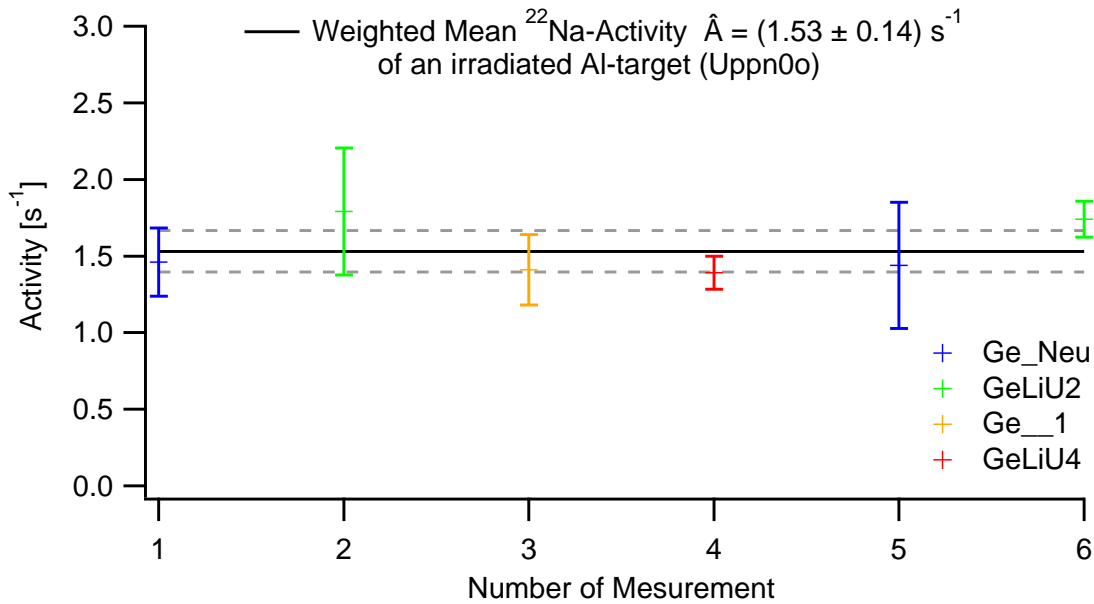
Figure 5.13: ^{22}Na activity of the ^{27}Al target foil that was irradiated during the Uppn0o-Experiment in the TSL with 73.8 MeV neutrons. The activity was measured 6 times with different γ-spectrometer.

during the analysis of the target foils. In principle, the specific properties of a detector could be used to optimize the detection quality for nuclides with certain energy-lines, but due to the amount of target foils that had to be analyzed in a short time, such optimisations were impossible.

Uncertainty of the Counting Statistics

Apart from the efficiency uncertainties, the uncertainties of the counting statistics of the residual nuclides were considered, too. They were automatically calculated by GAMMA-W and consist of two sources, of the poison statistic of the measured counts and on an mathematical treatment that considers the background substraction. Due to the low activities of the targets, their contribution was even bigger than the contribution of the efficiency uncertainties.

A typical set of measured activities is shown in Figure 5.13. It shows the activity of ^{22}Na measured for the 1275 keV γ-line which occurred in the ^{27}Al target foil. The target was irradiated during the Uppn0o-Experiment in the TSL with neutrons of 73.8 MeV energy. The analysis of the ^{27}Al target was performed with four different γ-spectrometer. Altogether six measurements were done within the period of 34 hours

for 86 days after the irradiation. The measure time was between 4.8 hours and 8.1 days. With respect to this long analysis periods, different measure times and different detector properties, the variation of activities and their uncertainties are evidentially observable in Figure 5.13. In order to obtain the best estimation of the real activity, the activities A_i were weighted with their relative standard uncertainties σ_i/A_i. The weighted mean activity $\overline{A}$ and its standard uncertainty $\sigma(A)$ was calculated as follows.

$$\overline{A} = \frac{\sum\limits_{1=1}^{n}(A_i^3/\sigma_i^2)}{\sum\limits_{1=1}^{n}(A_i^2/\sigma_i^2)} \tag{5.46}$$

$$\sigma(A) = \sqrt{\frac{n}{\sum\limits_{1=1}^{n}(1/\sigma_i^2)}} \tag{5.47}$$

The calculation of the standard deviation and the uncertainty propagation were carried out in agreement with the recommendations of the ISO-GUM [20].

6 Calculations of Nuclear Reactions

6.1 Theoretical Background

The following chapter will focus on the reactions that may happen between a neutron of the used projectile beam and an atom of the irradiated target. In order to induce any nuclear reaction the incident particle must interact with the nucleons in the target. In this context a huge problem exists, since even at these days no exact and reliable theory of a basic nucleon-nucleon interaction exist. This applies even more to such a complex process like a nuclear reaction. For this reason, the several models have to be used to describe interaction between projectile and target. Commonly, this nuclear reactions models are divided according to their energies and reaction times into compound nucleus reactions, pre-equilibrium reactions, spallation reactions, fragmentation reactions and direct reactions. The limits of these models and of the transitions between them are rather smooth and may differ between particular applications.

However, any nuclear reaction is based on the absorption of a part of the incoming flux by a scattering potential. This absorption can be understood in analogy to the scattering of light from a partially absorbing (cloudy) crystal ball. In classical physics the imaginary reflection coefficient is used to describe this problem. The nuclear counterpart of this reflection coefficient is a complex scattering potential known as the optical model potential. This optical model potential is usually composed of two components, a Coulomb potential and a nuclear potential. Whereas the Coulomb part is based on the projectile and target charges, the nuclear part contains volume, surface, and spin-orbit parts. The parameters of the optical model potential are determined by fitting calculated physical observables to the experimental results.

Using a properly parameterized optical model potential it is possible to calculate the absorbtion probability of an incident particle. Beyond the absorbtion probability and the optical model, the generic mechanism of nuclear reactions models is related to the energy dependence of the projectile wavelength. Referring to the performed irradiation experiments, Figure 6.1 shows the particular case of a neutron, which changes its wavelength according to its kinetic energy within the range of 1 to 200 MeV. In addition to the neutron wavelength the nuclear radii of carbon, iron and uranium are shown. These radii belong to the smallest, a medium and the biggest nucleus that was irradiated in the present work. Furthermore, the typical radius for a

nucleon-nucleon interaction is shown.

Just like in classical optics, the resolution of the incident neutron depends on its wavelength. Therefore a neutron with low kinetic energy may have a wavelength that corresponds to the dimensions of the target nucleus. The interaction between such a neutron and the target will rather involve the entire target nucleus than a single nucleon, since the neutron does not "see" this nuclear substructure. In this case the neutron will be absorbed and its kinetic and binding energy will be (uniformly) distributed to the degrees of freedom of the activate. Subsequently the collectively excited compound nucleus will start to de-excite. This process is based in an statistical redistribution of kinetic energy among the nucleons, where in one moment a nucleon or a cluster of nucleon receives enough momentum to leave the nucleus. Supporting the assumption of a statistical process, the spectra of the isotropic ejected particles are in agreement with the Maxwell-Boltzmann distribution of a corresponding nuclear temperature. Further, the typical duration of this process, between 10^{-19} and 10^{-16} seconds (a single, strong nuclear force dominated interaction happens in about 10^{-24} seconds), supports a long lasting nuclear rearrangement, too. As a consequence of this thermodynamical properties, the ejected particles are often referred to as evaporated. The theoretical description of this process was already formulated in 1936 by Nils Bohr [Bo36]. Based on the ideas of Bohr, Victor Frederick Weisskopf developed the
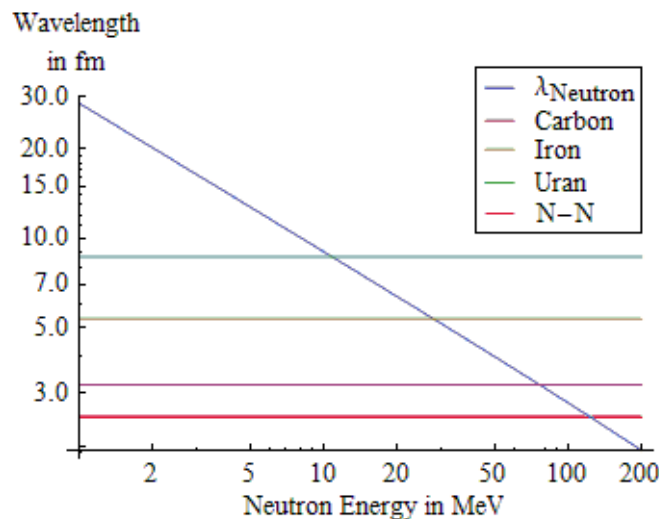
Figure 6.1: The radius of a carbon-, iron- and uranium nucleus and the radius of a nucleon-nucleon interaction compared with the energy depending wavelength of an incident neutron.

still used model of this so-called compound nuclear reaction [Wei37,Wei40].

When the projectile has a higher kinetic energy and shorter wavelength it starts "seeing" and interacting with the nuclear substructures. This type of reaction, which is referred to as spallation reaction, may be described by a two-step process [64].

During the first step of the reaction, the nucleons inside of the target nucleus are treated like a confined ideal gas and individual energy levels are not considered. When an incident particle, which may have a kinetic energy of several hundred MeV, enters this ideal gas, it can interact with one of this quasi-free nucleons. In this case the energy transfer will be most likely high enough to exceed the binding energy of the nucleon, while the remaining kinetic energy of the projectile is more than enough to leave the nucleus again. The accelerated nucleon will either directly leave the nucleus as an ejectile or interact with further nucleons. The latter way of interaction may start an intranuclear cascade (INC). Due to this cascade, not only the initial projectile but also several secondary particles can leave the target nucleus. In contrast to the compound nuclear reaction, where the continuing redistribution of energy inside of the compound nucleus result in an isotropic emission of secondary particles, here the primary reaction and the subsequent cascade is dominated by the momentum of the projectile. Therfore the ejectiles are mainly emitted in forward direction. The ejectiles that leave the nucleus during the INC cause an energy-loss. After a number of intranuclear interaction the energy transferred among the remaining nucleons will be less than their binding energies and a direct ejection of a particle becomes impossible. This moment is referred to as the end of the intranuclear cascade.

During the second step of the reaction, the nucleus is considered to be energetically equilibrated. Based on this assumption, the ejection of nucleons goes according to the evaporation process of the compound nuclear reaction.

However, the use of a two step spallation model is problematic, since a proper connection between the quasi free nucleons of the first step and the equilibrated compound nucleus of the second step does not exist. A solution for this problem is provided by the so-called pre-equilibrium models. The historically first, and physically most transparent is the exciton model for pre-equilibrium reactions [25, 26]. This model refers in particular to the time span between the first step of the spallation reaction and the equilibrated nucleus. For this purpose and in contrast to the two step spallation model, it considers individual nuclear levels. Accordingly, scattering processes during the INC do not inevitably cause particle emissions but nuclear excitations. In this context the exciton model introduces the existence of particle-hole

pairs which are created at the Fermi level. This particle-hole pairs, the so-called excitons, can interact with nucleons or further excitons. Their interactions lead, with certain probabilities, to the creation of new excitons, to the recombination of excitons or to the emission of nucleons. This probabilities depend on quantities like the occupation numbers, nuclear level densities, nuclear level energies and transition probabilities. The determination proper values for this interaction cross sections, which goes hand in hand the parametrization of the effective squared transition matrix are still subject of an extensive debate.

The pre-equilibrium reaction model that was used for the present work is based on a proposal of Kalbach, which in contrast to the ordinary exciton model distinguishes between neutron and protons. Hence, it is called two-component excitation model [30, 31].

With a further increase of the projectile momentum, the energy transferred to the target or rather to a single nucleon of the target is enlarged. This higher energy triggers the ejection of a large number of nucleons during the INC. Due to the velocity of the INC, there is not enough time to rearrange the nucleon inside of the target and the large number of ejected particles causes huge local variations in the nuclear density. In this case the range of the nucleon-nucleon interaction may be not enough to bridge the generated density gap and the adjacent nucleons can not anymore interact with all their neighbors. This detached nucleons and their remaining neighbors approach and build clusters. Doing so they gain binding energy which will be expressed by increasing momenta of the clusters. In consequence, the subnuclear clusters become even more independent from each other and from the rest of the nucleus. Finally the kinetic energy, the missing attractive nuclear force and the repulsive coulomb field can cause a decomposition of the target nucleus into single nucleons and clusters. This type of reaction is referred to as multifragmentation and subject of recent nuclear research [9, 18].

When the incident particle has energies of several GeV or more, the induced reaction become more related to the field of particle physics than to nuclear physics, since the involved resolutions and energy densities trigger the interaction with substructures of nucleons and the generation of "exotic" particles.

Beside this high energy reactions, reactions that can not be described by a statistical model, the so-called direct reactions occur within the entire projectile spectra. An example for this type of reaction is the $^{7}\text{Li(p,n)}^{7}\text{Be}$ reaction. This reaction was from huge interest for the present work, since it was used to generate the quasi mono-energetic
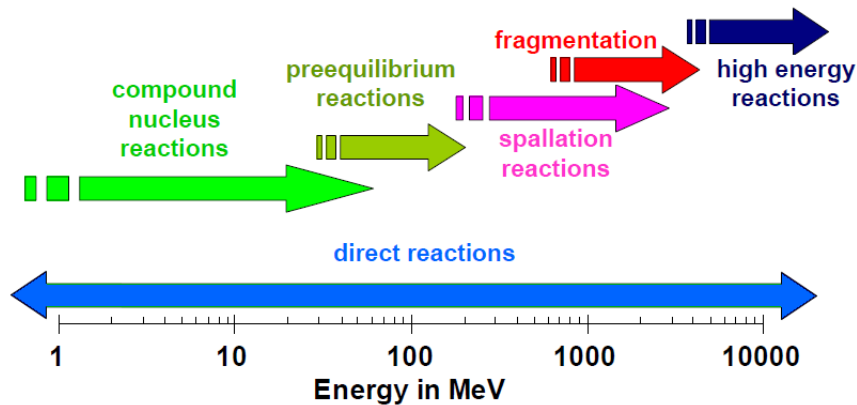
Figure 6.2: Regime of nuclear reaction

neutron fields.

Due to the energy of the incident neutron of at most 180 MeV the production of residual nuclides is neither related to multifragmentation reactions nor to high energy reactions (see also Figure 6.1). Further, an major role of direct reactions which produce residual targets can be ruled out, too. Actually the investigated nuclide production is widely dominated by compound reactions and spallation reactions and pre-equilibrium reactions, respectively.

Since the unfolding formalism required additional information about the graph of the neutron excitation function, it was necessary to find a code system that supported involved nuclear reactions and to model the excitation function.

6.2   TALYS

The software that was used for this objective is called TALYS, which was created at NRG Petten (Netherlands) and CEA Bruyères-le-Châtel (France). In the code system of TALYS many state-of-the-art nuclear models are included to cover all main reaction mechanisms encountered in light particle-induced nuclear reactions (see Table 6.2). This self-evidently includes compound reactions models and pre-equilibrium reactions models.

Beyond the application related to this work, the TALYS software package is applicable to simulate nuclear reactions that meet the following requirements. The projectiles are neutrons, photons, protons, deuterons, tritones, ^{3}He- or alpha-particles with kinetic energies that ranges between 1 keV and 200 MeV and the target is a nucleus with mass numbers between 12 and 339. In this manner TALYS evaluates plenty of nuclear

reactions from the unresolved resonance range up to intermediate energies.

The simulations are based on recent nuclear physics and include modern nuclear models for the optical model, level densities, direct reactions, compound reactions, pre-equilibrium reactions and from particular interest for heavy nuclei fission reactions. In addition to the nuclear models TALYS uses a large nuclear structure database.

The output of TALYS include several reaction properties like the total and partial cross sections, energy spectrum angular distributions, double-differential spectra, residual production cross sections and recoils.

The simulations of TALYS allow a fine tuning the adjustable parameters of the various reaction models to available experimental data. However, this option was not used in the present work, an TALYS was run with its default settings.

Table 6.1: Nuclear models and structure information implemented in TALYS 1.0 (released 21.December.07)

Optical Model:

- Optical model potential (OMP) calculations are performed with ECIS-06
- Neutrons/protons: Koning-Delaroche phenomenological spherical OMP (local / global), Soukhovitskii deformed OMP for actinides, and user-defined OMP's
- Complex particles: Simplified Watanabe folding approach

Direct Reactions:

- Direct reaction calculations are performed with ECIS-06
- DWBA for (near) spherical nuclei
- Coupled-channels for deformed nuclei (symmetric rotational / harmonic vibrational / vibration-rotational / asymmetric rotational)
- Weak-coupling model for odd nuclei
- Giant resonances (Kalbach macroscopic phenomenological model)

Compound Reactions:

- Hauser-Feshbach
- Width-fluctuation models (Moldauer / GOE triple integral / HRTW)
- Blatt-Biedenharn formalism for angular distributions
- Astrophysical reaction rates by Maxwellian folding of the cross sections
- Initial excited nucleus with excitation energy population

Pre-equilibrium Reactions:

- Two-component exciton model
- Photon exciton model (Akkermans and Gruppelaar)
- Continuum stripping, pick-up and knock-out (Kalbach phenomenological model)
- Angular distribution (Kalbach systematics)

Multiple Emission:

- Multiple pre-equilibrium emission for any number of particles
- Multiple Hauser-Feshbach emission for any number of particles

Fission:

- Hill-Wheeler transmission coefficients
- single / double / triple humped barriers
- Class II (III) states
- Experimental barrier parameters
- Rotating-Liquid-Drop model
- Rotating-Finite-Range model
- Microscopic barrier parameters
- Fission fragment mass distributions (Multi-Model Random-Neck-Rupture model)
- Fission fragment charge distributions (scission-point model)

Gamma-Ray Transmission Coefficients:

- Brink-Axel Lorentzian
- Kopecky-Uhl Generalized Lorentzian
- photoabsorption cross sections: (GDR + quasi-deuteron (Chadwick)

Nuclear Structure Database (based on RIPL-2):

- Abundances
- Discrete levels
- Deformations
- Masses
- Level density parameters
- Resonance parameters
- Fission barrier parameters
- Thermal cross sections
- Microscopic level densities
- Precision shapes

Recoils:

- Exact approach
- Method of average velocity

Further information about specific features of TALYS and a full description of all implemented nuclear models are given by A.J. Koning, S. Hilaire and M. Duijvestijn [36].

7   Unfolding of Excitation Functions

7.1   STAY'SL

The unfolding of the desired excitation function $\vec{\sigma}$ was performed using equation 7.1

$$\vec{\sigma} = \vec{g} - K(\vec{g})F^T X^{-1}(\vec{N} - F\vec{g}) \tag{7.1}$$

and the measurement uncertainties were considered via the covariance matrices $K(\vec{\sigma})$ of equation 7.2.

$$K(\vec{\sigma}) = K(\vec{g}) + K(\vec{g})F^T X^{-1} F K(\vec{g})^T. \tag{7.2}$$

These equations were already derived in chapter 2 where further information can be found.

These equations are integrated in the programm STAY'SL. Its first version was programmed by F.G. Perey and released in 1977 [56]. Originally, STAY'SL was not designed to unfold excitation functions, on the contrary it was used to calculate differential fluxes. For this purpose, STAY'SL uses the already known[1]symmetric routine which considers the entire statistic of the input data. The symmetry of the STAY'SL code allows the exchange of cross sections and flux data and therefore the unfolded quantities can be changed, too. The bases of the formalism, Least-Squares-Adjustment, stays untouched, and the excitation function can be unfolded using known neutron spectra and experimentally measured activities.

The modifications of the program code, that were required for this reverse use of STAY'SL, were performed in 1990 by M. Matzke [41]. The modifications concern mainly the assignment of memory space and the input-output routines. In 1994, I. Leya optimized the STAY'SL code [39] for experiments that were carried out at the ZSR and adapted the data input and output routine to the formats used at the ZSR. This modified version of STAY'SL was named STAYSL94. In the present work, STAYSL94 was used.

In order to perform the best possible unfolding, STAYSL94 contains free parameters that can (and have to) be adjusted to the individual requirements. These free parameters refer to the covariance of the performed experiments and to the "bending strength" of the unfolded excitation function. All of them are determined in the input files of

---

1   The algorithm introduced chapter 2 shows, referring to the goal of the present work, the unfolding of excitation functions and not the unfolding of particle fluxes.

STAYSL94.

Overall STAYSL94 requires 3 input files with data related to the number of produced nuclides, the neutron spectra and the guess function. In addition STAYSL94 uses a file that contains nothing but the name of the analyzed reaction (e.g. Ag(n,x)^{96}Tc) and a file that contains the names of all involved input files. The general input and output structure of STAYSL94 is shown in Figure 7.1.

The following paragraphs describe the layout of this input files of STAYSL94. Further effects of different free parameter settings on the unfolded excitation function will be discussed.
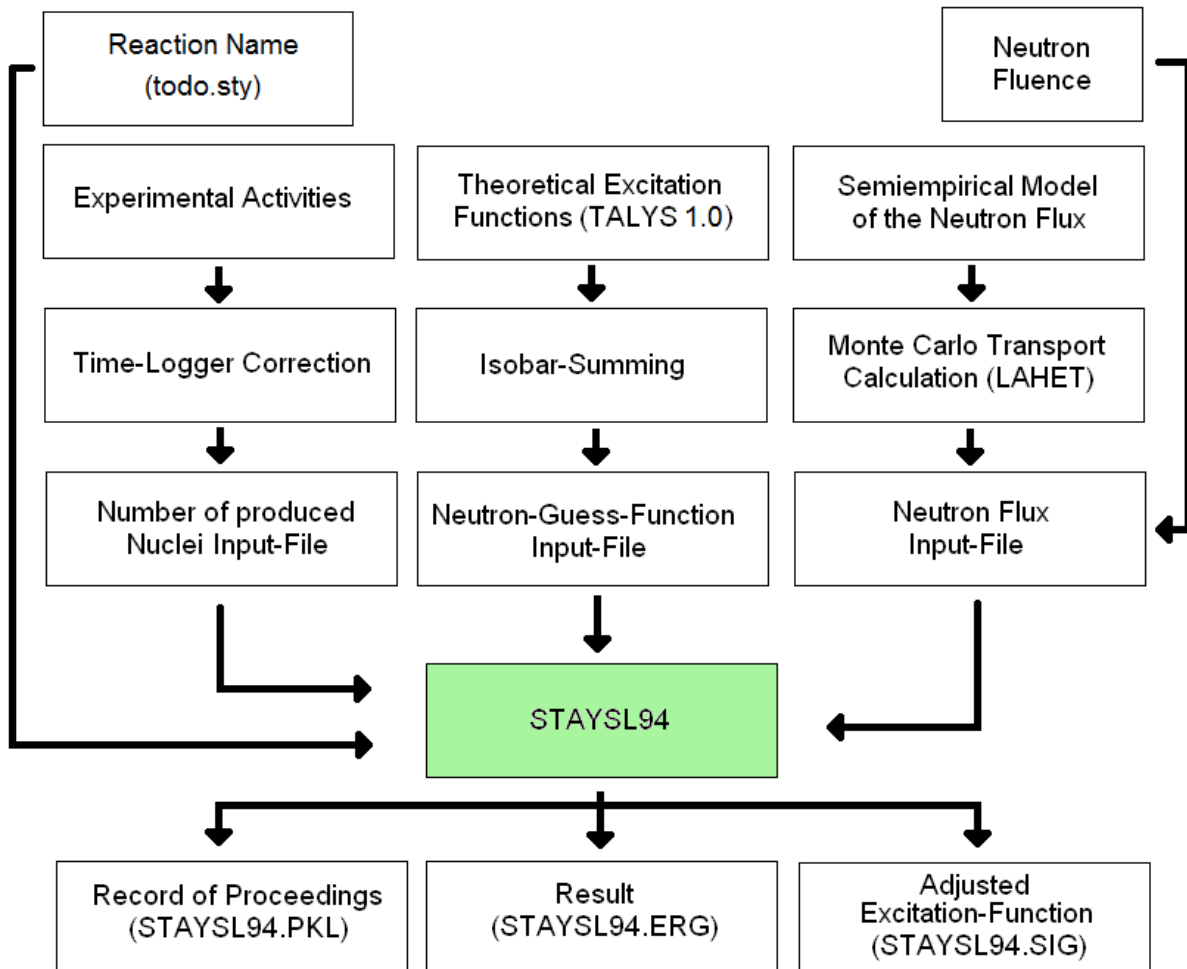
Figure 7.1: The general unfolding procedure using STAYSL94

7.2 Configuration of STAY'SL

7.2.1 The Activity Input-File

The first input file refers to the measured activities of the produced residual nuclides. However instead of the measured activities A the input file demanded the number of nuclei N that were produced during the irradiation. Consequently, the activities A had to be transformed into numbers of nuclei N. For this propose, the simple identity $A = \lambda N$ can be used, where $\lambda = \ln 2/t_{1/2}$ is the decay constant and $t_{1/2}$ the half life time.

The activities or rather the related numbers of nuclei N had to be corrected by the numbers of nuclei that decayed during the irradiation. This correction was carry out using the time-logger data and was in particular meaningful for nuclides with half life times which were short in comparison to the irradiation time. The mathematical treatment of this correction is described in chapter 5.42.

The next step was to put the numbers of nuclei N into the STAYSL94 input format. Here, it has to be considered that the vector $\vec{N}$ in conditional equation $\vec{\sigma} = \vec{g} - K(\vec{g})F^T X^{-1}(\vec{N} - F\vec{g})$ does not refer to the absolute number of produced nuclei, but to the relative number of produced nuclei. This relative number is expressed by N/N_{Target} where N is derived from the measured activities and N_{Target} is the number of target nuclei. N_{Target} can be calculated using the mass and the nuclear mass of the target. For instance:

At the uppn0p experiment, a $m_{target} = 8.873$ g iron target with the natural nuclear mass, $m_n = 55.85 \cdot 1.66054 \cdot 10^{-24}$g was irradiated. Assuming an activity, $A = 20.33$ s^{-1} for ^{54}Mn with a half life time, $t_{1/2} = 312.2$ days, the number of produced ^{54}Mn nuclei per number of target nuclei is calculated as follows:

$$N_{Res} = \frac{A \ t_{1/2}}{\text{Ln}(2)} \cdot \frac{m_n}{m_{target}} = N \cdot \frac{m_n}{m_{target}} = 4.983 \cdot 10^{-15} \qquad (7.3)$$

All experimental activities and their uncertainties were measured and calculated, respectively as shown in equation 7.3. Table 7.1 shows an example of a complete "activity" input file for STAYSL94. At the right side of the table, a short form of the irradiation experiment and the irradiated target belonging to the number of produced nuclei is given. The variable (string) that saves this value has only 6 digits. Hence, the short form is build in the following way:

Experiment: **uppn0e** Target: **fe** Number of Target-Foil: **01** Short Form: **uefe01**

The same abbreviation also appears in the neutron flux files. Here it indicates the differential neutron flux spectra that belongs to the target foil. Thus, these abbreviations link the produced nuclei with the neutron flux in the target.

The parameter "#covariance" appearing in the bottom of the table determines the degree of consideration for the non-diagonal elements of the covariance matrix $\mathbf{K}$, see page 11 and following. A smaller covariance value stands for less correlation between the irradiation experiments. In order to determine the size of this parameter no directive exists, but by trial and error it turned out, that values between 0 and 0.001 seemed to be reasonable, since in some cases higher covariances caused unphysical oscillations of the unfolded excitation function. Finally the covariance was set to 0.0009. This value considers on the one hand that the experiments are correlated, since they were carried out using similar experimental setups and on the other hand it is to small to cause oscillations of the unfolded excitation function.

However, the influence of this covariance settings was rather negligible compared to the setting of the "bending strength" and standard uncertainties of the guess function which will be discussed in the next paragraph.

Table 7.1: Format of the Input file for the produced nuclei (STAYSL94)

```
          Input STAYSL94

          Sigma[barn] Fehler Reaction Beam


          #activities
[    1]    1.00000E-15  ±   5.000%    FE(N,)MN-54   uefe01
[    2]    2.00000E-15  ±   6.000%    FE(N,)MN-54   l2fe01
[    3]    3.50000E-15  ±   7.325%    FE(N,)MN-54   l3fe01
[    4]    4.00000E-16  ±  17.325%    FE(N,)MN-54   upfe01


   #covariance=0.0009
```

7.2.2   The Guess Function Input-File

The input of STAYSL94 includes the file of the neutron guess function. This file is based on theoretical predicted cross section that were calculated with TALYS 1.0. The outputs of TALYS contain information about individual production cross sections, but the experimental measured activities attribute to both, the individual production reaction and to the α and β decay of existing progenitors. Figure 7.2 shows the β^+ branch of the 51 isobar chain (red). Here it becomes evident, that, for example, the measured activities for ^{51}Cr depend not only on its production rate but also on the production rate of ^{51}Mn, ^{51}Fe and all other progenitor. With respect to this "cumulative" activities, it was necessary to build up theoretical cumulative cross sections $\sigma_{n,cum}$ by considering the individual cross sections σ_{n-x} of the progenitors.

 In case, that an observed nuclide n has a progenitor n-1, its activity can not be written anymore like in equation 1.4. In fact, the consideration of it mother nuclide leads to the system of coupled differential equations (see equations 7.4) which has to be solved.

$$\begin{aligned}
\frac{dN_{n-1}}{dt} &= \sigma_{n-1}\varphi N_T - \lambda_{n-1}N_{n-1} \\
\frac{dN_n}{dt} &= \sigma_n\varphi N_T - \lambda_n N_n + \lambda_{n-1}N_{n-1} \ , \quad t \leq t_{EoI}
\end{aligned} \tag{7.4}$$

Ni51	**Ni52** 38 ms 0+ ECp	**Ni53** 45 ms 7/2- ECp	**Ni54** 0+ EC	**Ni55** 212.1 ms 7/2- EC	**Ni56** 6.077 d 0+ EC	**Ni57** 35.60 h 3/2- EC	**Ni58** 0+ 68.077	**Ni59** 7.6E+4 y 3/2- EC	**Ni60** 0+ 26.223	**Ni61** 3/2- 1.140
Co50 44 ms 6+ ECp	**Co51**	**Co52** 18 ms EC	**Co53** 240 ms 7/2- EC	**Co54** 193.23 ms 0+ EC	**Co55** 17.53 h 7/2- EC	**Co56** 77.27 d 4+ EC	**Co57** 271.79 d 7/2- EC	**Co58** 70.82 d 2+ EC	**Co59** 7/2- 100	**Co60** 5.2714 y 5+
Fe49 70 ms 7/2- ECp	**Fe50** 150 ms 0+ ECp	**Fe51** 305 ms (5/2-) EC	**Fe52** 8.275 h 0+ EC	**Fe53** 8.51 m 7/2- EC	**Fe54** 0+ 5.8	**Fe55** 2.73 y 3/2- EC	**Fe56** 0+ 91.72	**Fe57** 1/2- 2.2	**Fe58** 0+ 0.28	**Fe59** 44.503 d 3/2- β-
Mn48 158.1 ms 4+ ECp	**Mn49** 382 ms 5/2- EC	**Mn50** 283.88 ms 0+ EC	**Mn51** 46.2 m 5/2- EC	**Mn52** 5.591 d 6+ EC	**Mn53** 3.74E+6 y 7/2- EC	**Mn54** 312.3 d 3+ EC,β-	**Mn55** 5/2- 100	**Mn56** 2.5785 h 3+ β-	**Mn57** 85.4 s 5/2- β-	**Mn58** 3.0 s 0+ β-
Cr47 500 ms 3/2- EC	**Cr48** 21.56 h 0+ EC	**Cr49** 42.3 m 5/2- EC	**Cr50** 1.8E+17 y 0+ ECEC 4.345	**Cr51** 27.702 d 7/2- EC	**Cr52** 0+ 83.789	**Cr53** 3/2- 9.501	**Cr54** 0+ 2.365	**Cr55** 3.497 m 3/2- β-	**Cr56** 5.94 m 0+ β-	**Cr57** 21.1 s 3/2-,5/2-,7/2- β-
V46 422.37 ms 0+ EC	**V47** 32.6 m 3/2- EC	**V48** 15.9735 d 4+ EC	**V49** 330 d 7/2- EC	**V50** 1.4E+17 y 6+ EC,β- 0.250	**V51** 7/2- 99.750 β-	**V52** 3.743 m 3+ β-	**V53** 1.61 m 7/2- β-	**V54** 49.8 s 3+ β-	**V55** 6.54 s (7/2-) β-	**V56**

Figure 7.2: An example for the nuclides (red colored) that contribute to the measured activity of ^{51}Cr

Here, dN_{n-1}/dt is the activity of the progenitor, dN_n/dt is the activity of the observed nuclide and $t \leq t_{EoI}$ indicates that this formulas are valid during the time that both nuclides are activated. The integration of equations 7.4 result in the modified equation of nuclear activation (see equation 7.5)

$$N_n(t) = \varphi N_T \left(\sigma_n \frac{1 - e^{-\lambda_n t}}{\lambda_n} + \sigma_{n-1} \left(\frac{1 - e^{-\lambda_n t}}{\lambda_n} + \frac{e^{-\lambda_{n-1} t} - e^{-\lambda_n t}}{\lambda_{n-1} - \lambda_n} \right) \right) \tag{7.5}$$

where $N_n(t)$ is the number of nuclei at the time t before the end of the irradiation t_{EoI}. For the evaluation of produced residual nuclides via offline γ-spectrometry this expression has to be rewritten for the time after the period of activation has finished $t > t_{EoI}$ (see equation 7.6).

$$N_n(t) = \varphi N_T \left(\left(\sigma_n + \sigma_{n-1} \frac{\lambda_{n-1}}{\lambda_{n-1} - \lambda_n} \right) \frac{1 - e^{-\lambda_n t_{EoI}}}{\lambda_n} + \sigma_{n-1} \frac{1 - e^{-\lambda_{n-1} t_{EoI}}}{\lambda_n - \lambda_{n-1}} e^{-\lambda_{n-1} t} \right)$$
$$\tag{7.6}$$

In case that the half-life of the nuclide n is big in comparison to the half-life of its progenitor n-1 ($\lambda_n << \lambda_{n-1}$), the moment of activity determination can be chosen in a way, that the nuclei of the progenitor are almost entirely decayed. Doing so, the second addend of the in brackets enclose sum can be neglected. A comparison of equation 7.6 with equation 7.5 shows, that the cumulative cross section can be expressed like in equation 7.7.

$$\sigma_{n,cum} = \sigma_n + \sigma_{n-1} \frac{\lambda_{n-1}}{\lambda_{n-1} - \lambda_n} \tag{7.7}$$

However, an observed nuclide may have several progenitors and not every progenitor decays with a probability of μ=100% into the observed nuclide. Both possibilities have to be considered for a proper calculation of the cumulative cross section. Assuming a very short half-life of pre-progenitors n<n-1 the cumulative cross section can be expressed by equation 7.8

$$\sigma_{n,cum} = \sigma_n + \frac{\lambda_{n-1}}{\lambda_{n-1} - \lambda_n} \sum_{i=1}^{n-1} \mu_i \, \sigma_i \tag{7.8}$$

where σ_i are the progenitor cross sections and μ_i are the branching probabilities.

In the following, the calculated cumulative guess function was reformatted to the STAYSL94 input format. Since the unit of the TALYS output is millibarn, but the desired excitation function was given in barn, the TALYS output had to be rewritten to barn. The layout of the input file is shown in Figure 7.2. In the first section of

Table 7.2: Format of the Input-File for the guess function (STAYSL94)

```
Energies in[MeV]
# energy
0 1 2 3 4 5 6 7 8 9 10
11 12 13 14 15 16 17 18 19 20
.

.
152 154 156 158 160 162 164 166 168 170
172 174 176 178 180


cross sections in barn

#cross CO(N,)MN-54
#deviation = 50 %
[   1]     4.60636E − 06
[   2]     8.95752E − 04
[   3]     7.42642E − 03
.

.
[154]     8.95752E − 04
[155]     7.42642E − 03
#correlation
#0.95*Exp( − 0.001*(
```

the input file, the energy grid was entered. In the present work, the grid consisted of 155 + 1 entries. Starting from zero, the energy-steps were 1 MeV until 130 MeV and changed to 2 MeV in the energy range from 130 MeV until 180 MeV. The reason for this scaling is given by the limited capacity of STAYSL94 which cannot handle vectors with more than 156 entries. In fact, STAYSL94 permits only 155 free energy parameters, since the first entry has to be zero.

The second section of the file contains only one entry, the reaction, e.g., "#cross CO(N,)MN-54". The same information was provided in an additional file, which is usually called "todo.sty". This "to do" file includes only the latter line that defines the reaction and is used by STAYSL94 to link the guess function and the nuclear reaction.

The third entry, "#deviation = 50 %", determines the standard uncertainty of the

corresponding guess function. In the present work, the uncertainty was set to 50 %. This value is taken from the international codes and model intercomparison for intermediate energy activation yields [47], where it was stated that modeling calculations of medium energies activation yields may still have uncertainties of the order of a factor 2. As a consequence of this rather big standard uncertainty the unfolded excitation may differ significantly from the shape of the guess function. Figure 7.3 shows, that the result of the unfolding can depend on size of this uncertainties. It shows the result of unfolding, where the deviation value of the guess function was set to 5 %. It is

L2	L3	L4	UE	UM	UO	UP	UQ
32.7	45.3	59.9	96.1	133	73.8	175.4	144.8
MeV	MeV	MeV	MeV	MeV	MeV	MeV	MeV
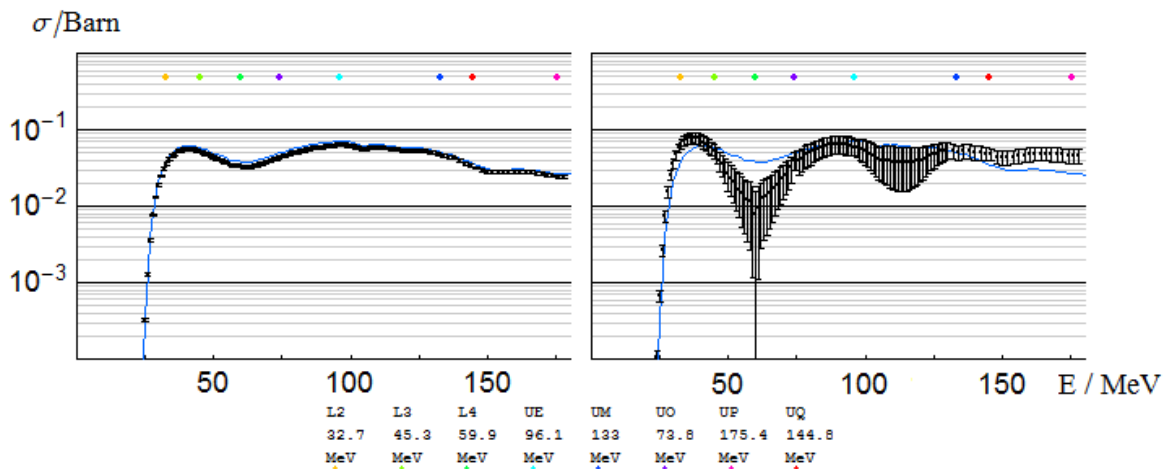
Figure 7.3: The production of ^{54}Mn from natural cobalt, with a standard deviation of the guess function set to 5 % on left side, and to 95 % on the right side

evident that the obtained excitation function follows the graph of the guess function and does not use the information that is provided by the experimental data.
The entry of the standard uncertainty is followed by the entries of the guess function. Here each line starts with a number of the energy grid and is followed by the corresponding value of the guess function.

The two final lines in the input file refer to the correlation between the entries of the guess function. This correlation determines how much the adjustment of a certain value influence adjoining data points of unfolded function. Since this parameter influences the pliability of the unfolded function, it is refered to "bending strength" parameter. In the present setup, the correlation between two data points decays exponential with the increasing number of entries existing between them. Despite this exponential correlation decrease the setting of bending strength is very important. To give evidence for this assertion, Figure 7.4 shows the production of ^{54}Mn from natural
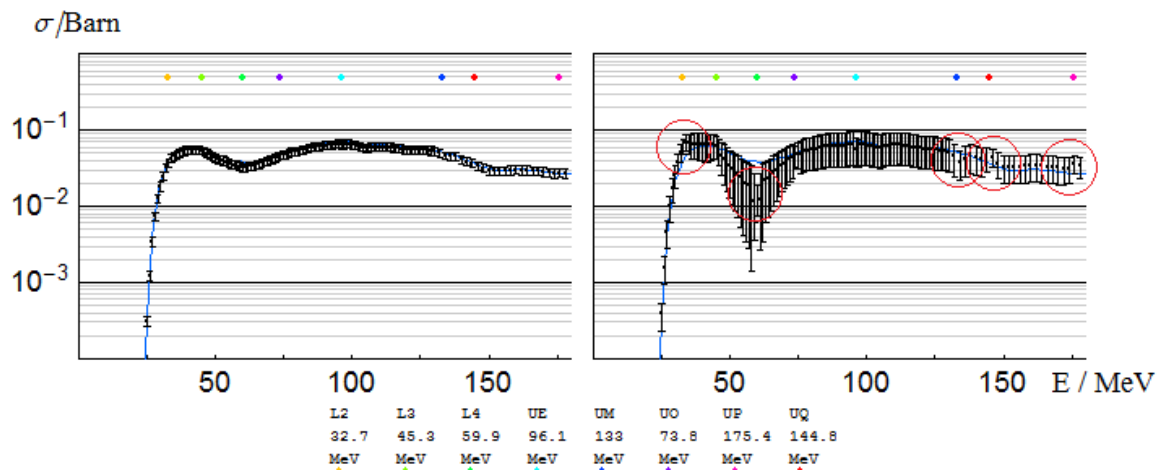
Figure 7.4: The production of ^{54}Mn from natural cobalt with high "bending strength" on the left and very flexible on the right.

cobalt. For both unfolded functions, the STAYSL94 input files are identical except from the bending strength parameter. The consequences on the uncertainties and the behavior of the excitation function are evident.

In order to determine the best possible bending strength setting, STAYSL94 was run with different correlation parameters. It turned out, that for some experiments the unfolded excitation function tended to "jump" for too low settings. This behavior is shown in the red marked areas of Figure 7.4. A contrary behavior was found for to high correlation parameters. Here the unfolded excitation function overlapped completely with the guess function and the information about the measured activities were not considered, since bending was not allowed.

Consequently, the chosen correlation settings had to be small in order to consider the measured activities, but big enough to avoid the jumping of the unfolded excitation function. In the present work the value of the correlation was set to "# 0.95*Exp(-0.001*(", considering a good compromise between the discussed behaviors.

7.2.3   The Neutron Flux Input-File

In the third step of the unfolding procedure the neutron flux functions were formatted to the STAYSL94 input format. For this purpose, the relative differential neutron flux spectra, which were calculated with LAHET, were normalized to the experimentally measured neutron fluence. In the case of the experiment uppn0l, the neutron fluence

Table 7.3: Format of the Input-File for the differential neutron fluence (STAYSL94)

```
Energies in[MeV]
# energy
0 1 2 3 4 5 6 7 8 9 10
11 12 13 14 15 16 17 18 19 20
.

.
152 154 156 158 160 162 164 166 168 170
172 174 176 178 180


cross sections in 1/barn

   #beam l2cu01
   #standard deviation = 10.00 %
[   1]    4.60636E − 30     6.32 %
[   2]    8.95752E − 28     6.52 %
[   3]    7.42642E − 27     6.92 %
.

.
[154]    0.00000E + 00
[155]    0.00000E + 00


   #beam l2pb01
   #standard deviation = 10.00 %
[   1]    4.60636E − 30     6.27 %
[   2]    8.95752E − 28     6.45 %
.

.
[154]    0.00000E + 00
[155]    0.00000E + 00
```

was not directly measured. Here the fluence was calculated by comparing the activity of the monitor foils of uppn0l and uppn0f. This comparison was possible, since both experimental runs, uppn0f and uppn0l were carried out under almost identical conditions referring to the proton energy and the thickness of the ^{7}Li target (see Appendix). Therfore, the differential neutron fluence was known for each irradiated

target foil.

The layout of the input file for the neutron fluences is shown in Figure 7.3. Its format is similar to the input file of the guess function. It starts with the definition of the used energy grid. The energy grid has to be the same as in the input file of the guess function. The definition of the energy is followed by the determination of the irradiated target foil and the correlated neutron fluence. In order to define the target foils, the same abbreviations as in the input file for the number of produced nuclei were used.

The neutron fluence has to refer to the same dimension as the guess function. In other words the fluence has the dimension of barn^{-1}.

7.2.4   Linking the Input-File

When STAYSL94 is executed, it needs a file that contain the information were to find the latter three files about numbers on produced nuclei, the guess function and the neutron fluence. This information was stored in a file named "options.sta". Table 7.4 shows the layout of the "options.sta" file. In the first line of the file it is determined whether STAYSL94 starts the unfolding directly after the execution or it has to wait for a further confirmation in order to start the calculation. The following three lines link the STAYSL94 input files. The fourth line links the STAYSL94 output file. It contains both, the unfolded excitation function and the correlation matrix. Additionally, the excitation function and the guess function are stored in a second output file called "staysl94.sig". The entry "0" in the fifth line determines whether the entire guess function is multiplied by a coefficient in order to obtain a better adjustment. Here "1"

Table 7.4: Format of the options.sta file (STAYSL94)

```
Proceed immediately?  Y
C:\spec\nuclei.sty
C:\spec\fluence.sty
C:\spec\talys.sty
C:\spec\staysl94.erg
0
C:\spec\TODO.sty
```

disables this scaling and "0" enables it. In the present work, this coefficient was always set to "0". In the final line the TODO file is linked.

With the described input files and correlation setting all excitation functions were unfolded. The results of the unfolding are discussed in the next section.

8 Results and Discussion

The goal of this work was to provide excitation functions which are based on experimental measured activation yields from neutron-induced reactions of medium energies. To this end, this work uses a novel experimental approach which is based on the unfolding of neutron excitation functions from experimental data. Within the frame of this approach activation yields of more than 100 relatively short-lived residual radionuclide from 13 different target elements (C, O, Mg, Al, Si, Fe, Co, Ni, Cu, Ag, Te, Pb and U) were determined. Using this activation yields, their corresponding spectral neutron fluxes and supplementary modeling calculations it was possible to unfold more than 100 excitation functions from their response integrals. In this context, this work shows not only that it is possible to infer excitation functions from a set of activation experiments with known activation yields and spectral neutron fluxes, but also provides a unique set of experimental excitation functions for neutron-induced reactions of medium energies up to 180 MeV.

All unfolded excitation functions are plotted in the appendix (see page 157 and following). Due to its extend, a detailed table of the underlying data is not present, but can be found on the webpage of the IRS (http://www.zsr.uni-hannover.de/wirkung.htm). The discussion of this results focuses on two different aspects of the unfolded excitation functions. At first, the results of this work are compared with already existing cross sections of neutron- and proton-induced nuclear reactions. In this context, not only the agreement and disagreement but also unfolding artifacts will be exemplarily discussed. In the second part, it is tested to what extent the unfolded excitation function can predict the production of residual nuclides, in particular in meteorites. For this, the excitation function were folded with neutron fluxes calculated for former irradiation experiments.

8.1 Results compared with existing Data

The comparison of the unfolded excitation function with reference data of other authors is limited by the few data existing. This applies in particular to cross section of medium energy reactions. However, during the last decade few activation experiments were carried out. Some of this experiments state the energy integrated activation cross section which is also called integral or effective cross section (e.g. J.C. Hill et al. [27]). Normally this integral cross sections are measured in spallation experiments and may

answer questions according to the production rates of very particular setups. Due to the setup depending, unique character of integral cross sections, they are not suitable for a direct comparison with our unfolded excitation function unless supplementary information about the spectral neutron flux are available. For such cases, the neutron flux could be folded with our excitation function. The resulting activation yield could be used to calculate the integral activation cross section which could be compared with the original data. Unfortunately, data sets with both, the integral cross section and their corresponding neutron flux were not available. Hence, the unfolded excitation function could be only compared with the few existing "true" cross sections.

Apart from this work, mainly two further techniques of medium energy neutron cross section measurements were introduced within the last years. One goes back to the work of Kim et al.[33]. The experimental approach of Kim used an incremental measurement of the cross section. For this purpose a quasi mono-energetic neutron beam was generated, and the differential neutron flux was measured. For a first experiment, the kinetic energy of the peak neutrons was chosen to be a little bit above the threshold of the investigated reaction. Doing so, the cross section can be directly calculated from the production rates, were the energy uncertainty of reaction cross section is given by the FWHM of the peak neutrons. In a next activation experiment the energy of the peak neutrons was shifted by a few MeV (about the FWHM of the peak) to a higher energy. Knowing the neutron spectra and the first cross section it was possible to calculate the share of nuclei which was produced by the peak neutrons of the second experiment and thus, the a further cross section. Repeating this procedure it was possible to measure reaction cross sections for increasing energies. Based on this idea Kim calculated several cross sections of neutron induced nuclear reactions of medium energies up to 120 MeV.

The second experimental approach goes back to the work of Sisterson et al. [68]. The experimental technique is based in a comparison of the production rates measured for two identical, simultaneous irradiated targets. To this end, a neutron field was generated using the Beryllium plus proton reaction. Behind the Beryllium-Neutron source the neutron spectra contains both, a continuum part and a high-energy (quasi-monoenergetic) peak. This high-energy peak is very pronounced at an angle 0° to the incident proton beam but decreases rapidly at increasing angle, while the continuum part of the spectra shows isotropic behavior. Considering the different neutron spectra the targets were aligned at an angle of 0° and 16° to the proton beam. The yield of any product radionuclide from an (n,x) reaction, produced by
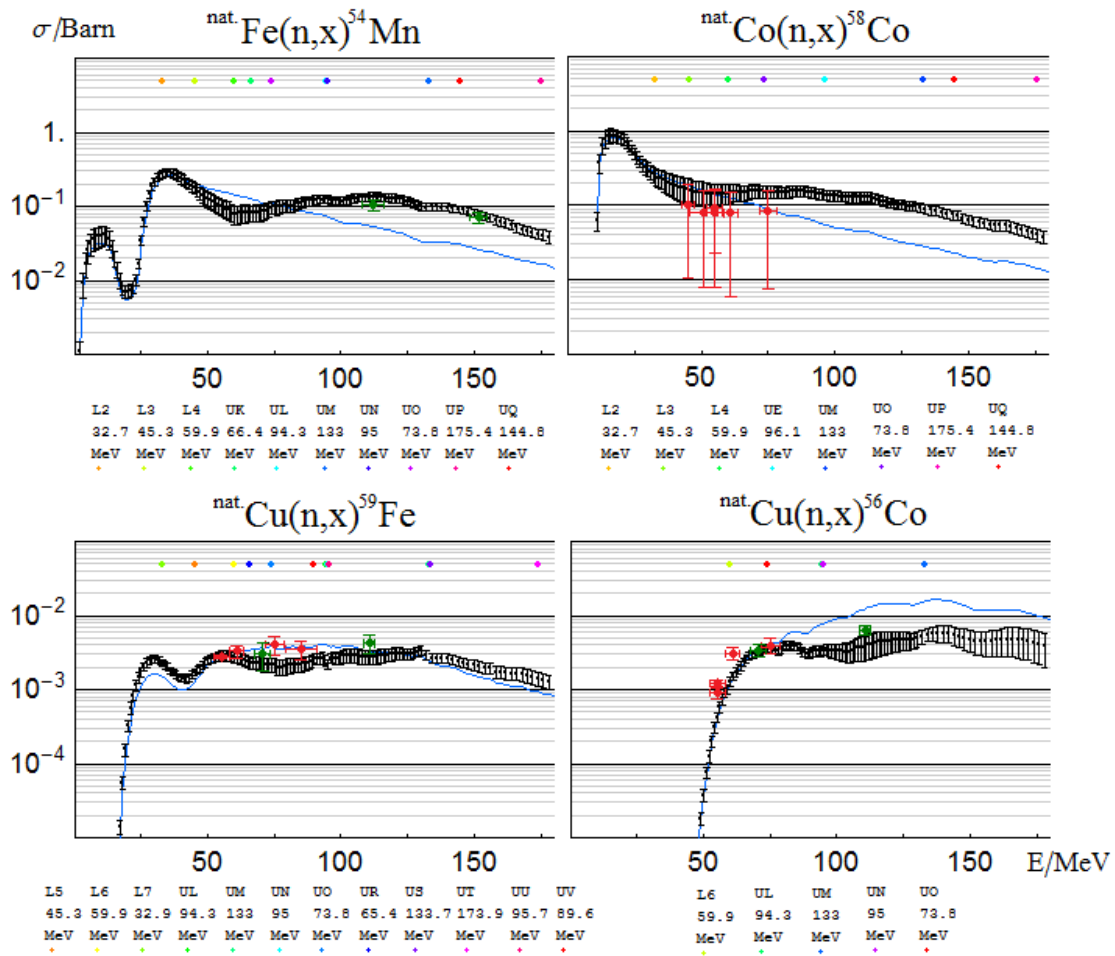
Figure 8.1: Unfolded excitation functions (black) and their corresponding guess function (blue) in comparison with cross sections by Kim et al.(red) and Sisterson et al.(green). The colored dots represent the high-energy peaks of the underlying neutron spectra where the corresponding abbreviations used in the legend are explained at page 157

irradiation in the 0° beam position, therefore included components due to reactions initiated by both the high-energy peakneutrons and the continuum, while the yield resulting from irradiation in the 16° beam was dominated by reactions initiated by the continuum of the neutron spectra. Thus, the substraction of the production rate in the 16° beam (after appropriate normalization) from the production rates in the 0° beam results in production rate of the peak neutrons and consequently allows the calculation of the production cross section for the high-energy peak. Using this setup Sisterson calculated several cross sections of neutron induced nuclear reactions of medium energies up to 152 MeV.
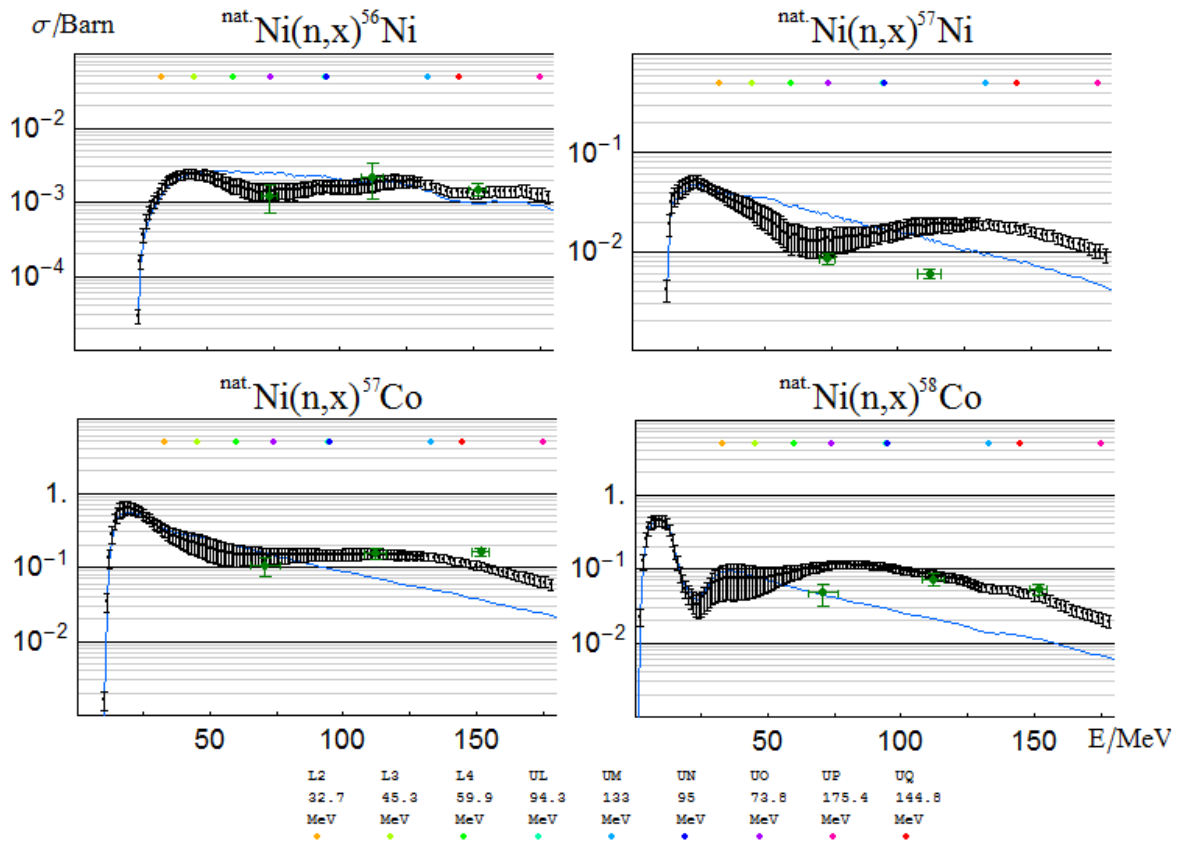
Figure 8.2: Unfolded excitation functions (black) and their corresponding guess function (blue) in comparison with cross sections Sisterson et al.(green). The colored dots represent the high-energy peaks of the underlying neutron spectra where the corresponding abbreviations used in the legend are explained at page 157

A exemplary comparison of 8 different unfolded excitation functions with cross sections of Kim and Sisterson are shown in Figure 8.1 and 8.2. From the Figures can be concluded that the unfolded functions are in good agreement with the existing data. Nevertheless minor inconsistencies exist with respect to the $Cu(n,x)^{59}Fe$ cross section of Kim et al. at 75 MeV and the $Ni(n,x)^{57}Co$ cross section of Sisterson et al. at 152 MeV. According to the $Cu(n,x)^{59}Fe$ reaction the course of the unfolded excitation function shows a slight local minimum between 60 and 90 MeV while the course of cross sections of Kim show a contrary behavior. Actually, neither a minimum nor a maximum make sense in this energy range. The existence of non justified, slight minima/maxima is related to the correlation parameter of the TALYS input file (see page 102). The setting of this correlation parameter causes a certain "bending strength" during the unfolding of the excitation function. The "bending strength"

becomes problematic when the guess function (locally) under/over estimates the slope of the "true" excitation function. The under/over estimation together with the limited flexibility of the unfolded function provoke wrong local courses of the unfolded function that creates this unwanted local minima/maxima. The "bending strength" effect is illustrated in Figure 8.3.

According to the inconsistent data point that occurs in the Ni(n,x)^{57}Co reaction it is assumed that the difference between the unfolded function and the cross section can be explained with the same mechanism. Unfortunately this unfolding artifacts can not be easily reduce, since changes in the "bending strength" lead to oscillations in the excitation functions (see page 102). Apart from the "bending strength" problem it can not ruled out that the inconsistencies may fully or partially originate from other sources. For instance, the improbable case of wrongly measured ^{57}Co γ-counting rates of the Uppsala "P" activation experiment (with 178 MeV) could cause the observed inconsistence. At last it has also to be considered that the inconsistencies could originate from the experiments of Kim and Sisterson. However, further activation experiments with different neutron energies and/or better guess functions would improve the situation.

In addition to this relatively small discrepancies, the reaction cross sections of
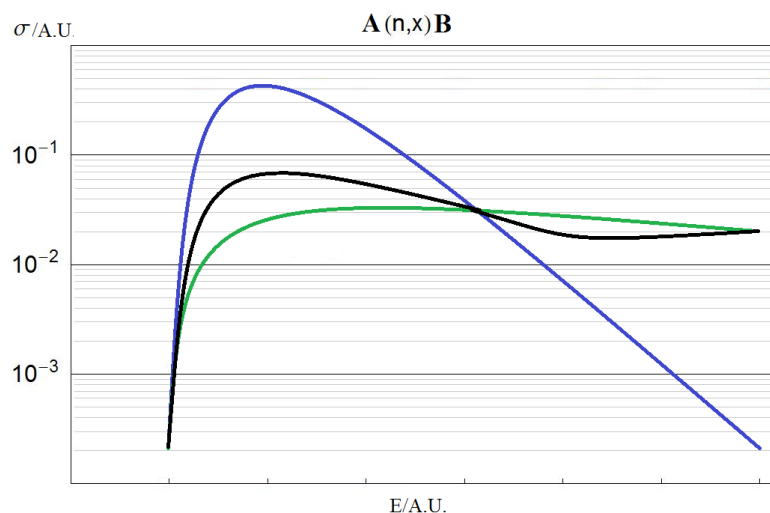
Figure 8.3: Illustration of the creation of slight local minima/maxima due to over/under estimation of the slope of the "true" excitation function, where the "wrong estimating" guess function is plotted in blue, the "true" excitation function is plotted in green and the unfolded excitation function is plotted in black.

Ni(n,x)^{57}Ni and Ni(n,x)^{58}Co show much bigger inconsistencies. This deviations between unfolded excitation functions and independently measured cross sections can only be lead back to the "bending strength" problem if the course the guess function differs strongly from the "true" excitation functions. But, generally, model calculations are, regarding to their course, to some extent reliable. Exceptions of this general reliability occur for certain nuclear reactions, for instance reactions that involve magic or doubly magic nuclei where the binding energy of the first ejected nucleon is significantly different from next one. Actually nickel is such a magic nuclei and ^{57}Ni is even the next neighbor of the doubly magic nuclei ^{56}Ni. The difference between unfolded excitation function and independent measured cross section is indeed the biggest for the Ni(n,x)^{57}Ni reaction. Based on this facts, the discrepancies in the data can be explained using once more the "bending strength" hypothesis. Nevertheless, it applies again that the inconsistencies may originate from other sources, although the magic nuclei problem appears to be reasonable.

Aside from the mentioned medium energy cross sections, further data exist for neutron energies below 14.5 MeV. They originate from various fusion experiments which generate monoenergetic neutron beams and so allow the direct calculation of the cross sections from the production rates. This experimental cross sections are stored in different data bases. A rather extensive data library is the EAF, the **E**uropean **A**ctivation **F**ile, which is prepared for the European Activation System (EASY). The latest EAF library, EAF-2007, contains a neutron data library with 65565 excitation functions involving 816 different targets from ^{1}H to ^{257}Fm in the energy range 10^{-5} eV to 60 MeV. The extent of the EAF already indicates that the EAF includes several data banks. Actually the present EAF library is based JEFF-3.0, EFF-2.4, ENDF/B-VI, JENDEL-3.2 and IRDF-90.2. In addition, the shape of the stated excitation functions are extended to energy regions beyond the experimental limits using model calculations.

Although the EAF contains data for various energies the comparison between EAF and unfolded excitation function will focus only on the 14.5 MeV cross section. This 14.5 MeV was chosen, since most likely experimental data of the deuterium-tritium reaction exist for this energy.

Figure 8.4 shows exemplarily a comparison between unfolded excitation functions and EAF cross sections. The left side of the Figure shows two excitation functions (Al(n,x)^{24}Na and Ni(n,x)^{54}Mn) that were unfolded using both, the known neutron spectra and supplementary information based on the 14.5 MeV cross sections. The

right side of the Figure shows the same excitation functions, which were unfolded without considering the 14.5 MeV cross sections. In addition the right side shows the EAF 14.5 MeV cross sections (red) including their standard deviations.

Comparing the left and right side of Figure 8.4 it can be conclude that the supplementary cross sections does not change the course of the unfolded excitation functions. Further the right side of the Figure shows, that the EAF cross section and the unfolded function are in good agreement.

Figure 8.5 shows an further comparison between two unfolded excitation function. The left side of the Figure 8.5 shows the $Pb(n,x)^{203}Pb$ reaction including additional EAF information and whereas the right side of Figure 8.5 shows the $Pb(n,x)^{203}Pb$ reaction without any EAF information. Further the right side of Figure 8.5 shows the 14.5 MeV EAF cross section (red). A closer look to the plot shows inconsistencies between the courses of the unfolded functions at the local maximum below 25 MeV. This inconsistencies can be attributed to the consideration of the 14.5 MeV EAF cross section at left side of the Figure 8.5.

The local maximum between 8 and 25 MeV goes back to a compound nuclear reaction $^{204}Pb(n,2n)^{203}Pb$, where ^{204}Pb is a stable lead isotope with the natural abundance of only 1.4%. The increase of the excitation function above 25 MeV originates from the reaction $^{206}Pb(n,4n)^{203}Pb$, where ^{206}Pb with a natural abundance of 24.1% occurs about 17 times more frequently than ^{204}Pb. Due to the abundance ratio of this both lead isotopes, the production of ^{203}Pb is, beyond the 24 MeV reaction threshold, strongly dominated by the $^{206}Pb(n,4n)^{203}Pb$ reaction. Unfortunately, the present work does not include any activation experiment with neutron energies (peak neutrons) below this 24 MeV reaction threshold. Instead, the activation experiment with the lowest neutron energy was Louvain 2, where the peak neutrons had an kinetic energy of 32.7 MeV. This means, that even for the activation experiment with the lowest neutron energy about 50% of the fluence (which add up to the peak neutrons) was beyond the 24 MeV threshold. Consequently, a rather small fraction of the measured ^{203}Pb yield arises from ^{204}Pb and a large fraction from ^{206}Pb. In addition, the constantly occurring problem of a low counting rates complicated the determination of the exact activation yields via γ-spectrometry. In case of the Louvain 2 $Pb(n,x)^{203}Pb$ yield the measurement uncertainties are about 19.6%. The rather big measurement uncertainties together with used spectral neutron flux and the abundance ratio demonstrate, that the performed activation experiments are not suitable for a proper determination of the $Pb(n,x)^{203}Pb$ excitation function below 24 MeV and explains the
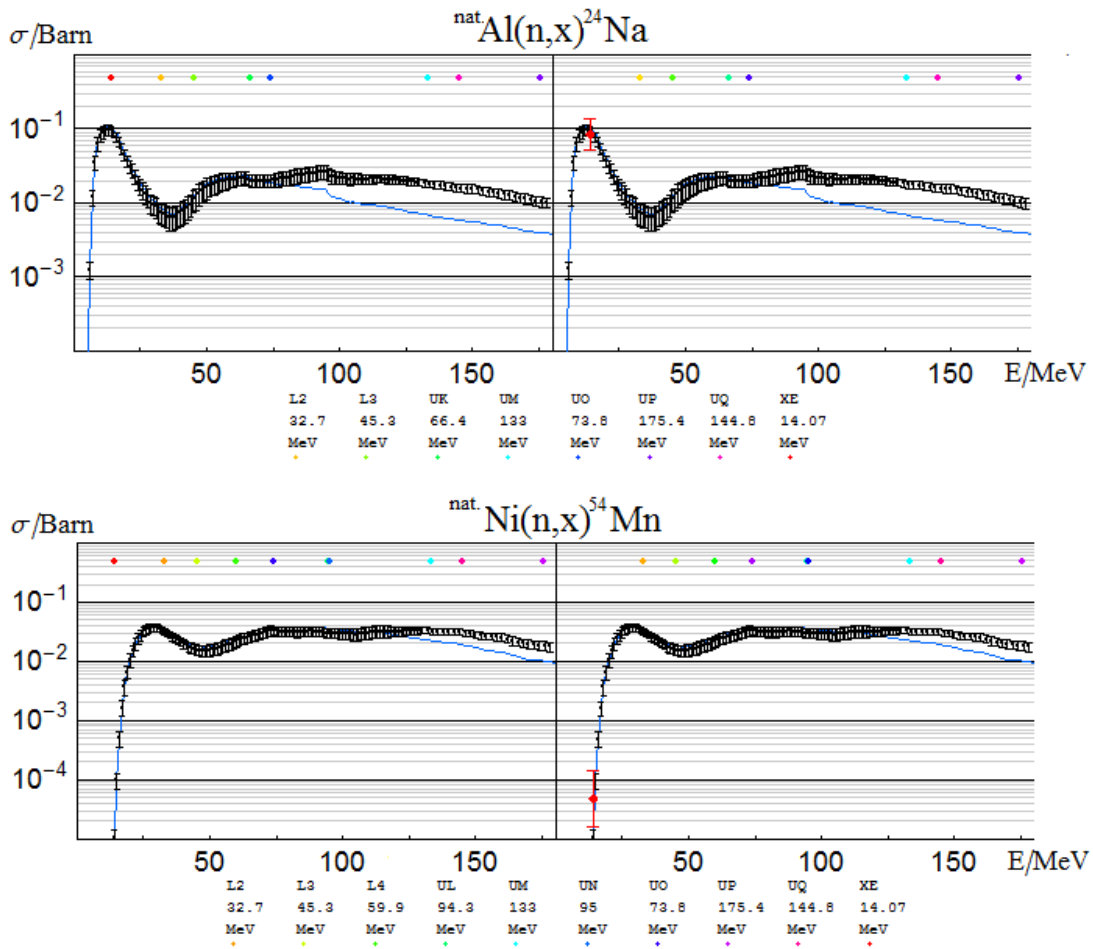
Figure 8.4: left: Unfolded excitation functions (black) which were unfolded including supplementary information about the EAF cross section at 14.5 MeV. right: Unfolded excitation functions (black) and their corresponding guess function (blue) in comparison with 14.5 MeV EAF cross section (red). The colored dots represent the high-energy peaks of the underlying neutron spectra where the corresponding abbreviations used in the legend are explained at page 157

inconsistencies of the plotted excitation functions.

The given example shows clearly the limitations of the experimental method and demonstrates that the unfolded excitation functions have always to be interpreted in the context of the underlying neutron spectra. Furthermore, from the example can be deduced that additional activation experiments would help to improve the quality and reliability of the unfolded excitation functions. Nevertheless it has to be emphasized that the integration of the 14.5 MeV EAF cross section into the unfolding procedure does not significantly affect the course of the unfolded $Pb(n,x)^{203}Pb$ excitation function
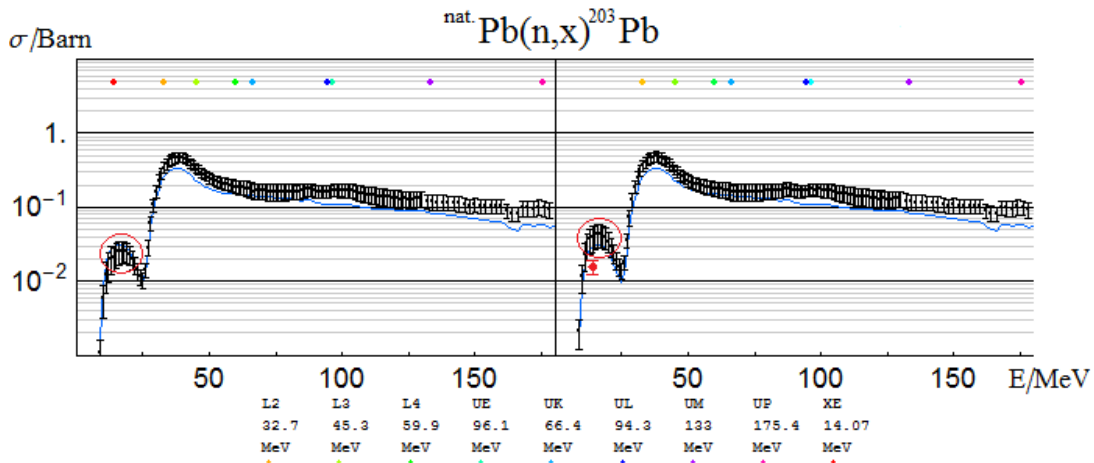
Figure 8.5: left: Unfolded excitation function (black) which is unfolded including supplementary information about the EAF cross section at 14.5 MeV. right: Unfolded excitation function (black) and its corresponding guess function (blue) in comparison with 14.5 MeV EAF cross section (red). The colored dots represent the high-energy peaks of the underlying neutron spectra where the corresponding abbreviations used in the legend are explained at page 157

above 24 MeV and that most of the unfolded excitation functions are in outstanding agreement with the 14.5 MeV EAF cross sections.

Apart from the comparison with neutron cross sections the unfolded data can also be interpreted with respect to proton cross sections. In the preceding pages different formation modes of neutron- and proton-induced reaction exemplarily discussed.

Figure 8.6 shows the n- and p- induced production of ^{58}Co from nickel on the left side and the n- and p- induced production of ^{96}Tc from silver on the right side.

 The plot on the left shows clear differences between the p- and n- induced production of ^{58}Co. For energies below 25 MeV the p-induced production cross sections form a pronounced local maxima which goes back to the Ni(p,α)^{58}Co reaction. The binding energy of the α-particles shifts the reaction threshold of the ordinary Ni(p,2p2n)^{58}Co reaction by -29.3 MeV. This α channel is missing for neutron-induced production of ^{58}Co from nickel. Beyond the reaction threshold of the Ni(p,2p2n)^{58}Co and Ni(n,p3n)^{58}Co, respectively, in the energy range between 55 and 180 MeV, the p-induced reaction shows cross sections which are between two and four times bigger than the cross sections of the neutron mode. In this energy interval the slopes of the excitation functions show similar behaviors, with a slightly faster decrease of the neutron cross sections. In summary it may be said, that excitation functions of the

115
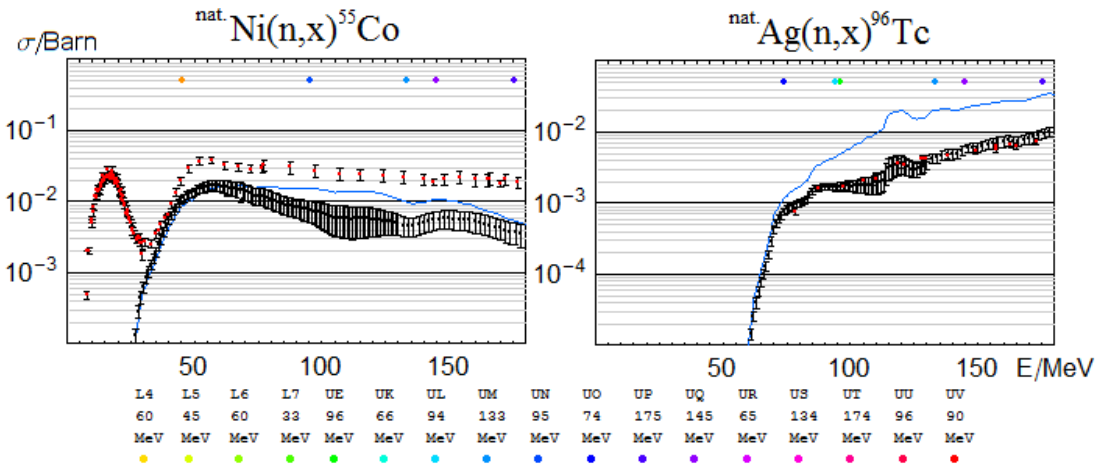
Figure 8.6: left: neutron-induced production of ^{58}Co from natural nickel (black) and proton-induced production of ^{58}Co from natural nickel (red). right: neutron-induced production of ^{96}Tc from natural silver (black) and proton-induced production of ^{96}Tc from natural silver (red). The colored dots represent the high-energy peaks of the underlying neutron spectra where the corresponding abbreviations used in the legend are explained at page 157. Proton cross sections are taken from [45]

p- and n-induced production of ^{58}Co from nickel do not have much in common, since neither their reaction threshold nor the values of their excitation functions concur.

With respect to the differences between the p- and n-induced production modes, the production of ^{96}Tc from silver shows the opposite behavior. Over the entire energy range from 75 to 180 MeV the excitation functions of the p- and n-induced production modes show good agreement.

Originating from the deficit of neutron data, it was and may is a common procedure for calculations of activation yields to replace missing neutron cross sections by proton cross sections. This was in particular practice for projectile energies which were large in comparison to reaction threshold and for products which consist of much less nucleons than the target. In this context the discussed examples show, that a universal interchangeability of proton- and neutron-induced reaction cross sections does not exist. The comparison of further p- and n-induced production modes (not shown) within the evaluation of the present work corroborate this point of view. Hence, it is concluded, that the cross section interchange method is may good enough for rough estimation of the order of magnitude of an activation yield, but it is advised not to use it for more ambitious calculations.

Except for reaction modes related to spallation and compound nuclear reactions, the
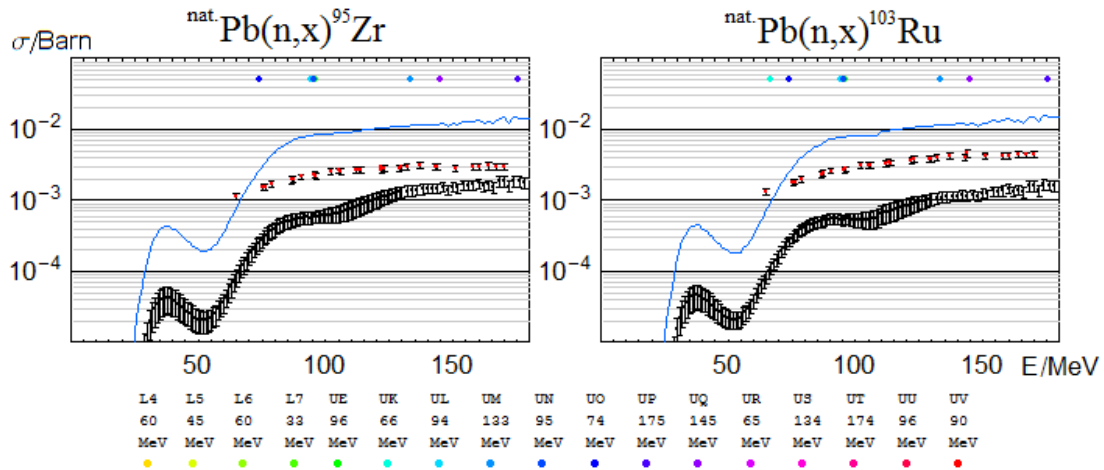
Figure 8.7: Unfolded excitation functions of neutron-induced fissions of natural lead (black) including the related TALYS guess functions (blue). Cross sections of proton-induced fissions of natural lead (red) [44]. The colored dots represent the high-energy peaks of the underlying neutron spectra where the corresponding abbreviations used in the legend are explained at page 157

present work also includes excitation functions which originate from medium energy neutron-induced fission reactions. Figure 8.7 shows unfolded excitation functions of neutron- and proton-induced fissions of lead and the related TALYS guess functions. It is conspicuous that the unfolded functions differ significantly from the predicted guess functions. This differences occur only for fission modes of lead whereas the predicted fission cross sections of uranium are in better agreement with the unfolded excitation functions (see Figure 8.8). It can be supposed, that the prediction accuracy of TALYS is affected by shell structure of the lead, since it consists of 72 protons and therefore, is a magic nucleus. Furthermore, the most abundant (52.4%) lead isotope ^{208}Pb has even a double magic nucleus.

Problems that occur in the prediction of activation yields are not limited to fission modes. The production of ^{96}Tc from silver in Figure 8.6 illustrates a comparable gap between experiment and theoretical calculation. Further examples can be found in the appendix of this work, where the complete set of unfolded excitations is plotted together with their corresponding guess functions. The given examples and the Figures in the appendix demonstrate, that modeling calculations of medium energy neutron-induced activation yields can not yet replace experimental measurements.

Apart from prediction problems that Figure 8.7 illustrates, it shows that the unfolded excitation functions starts slightly to increase (faster) at about 100 - 120 MeV. The
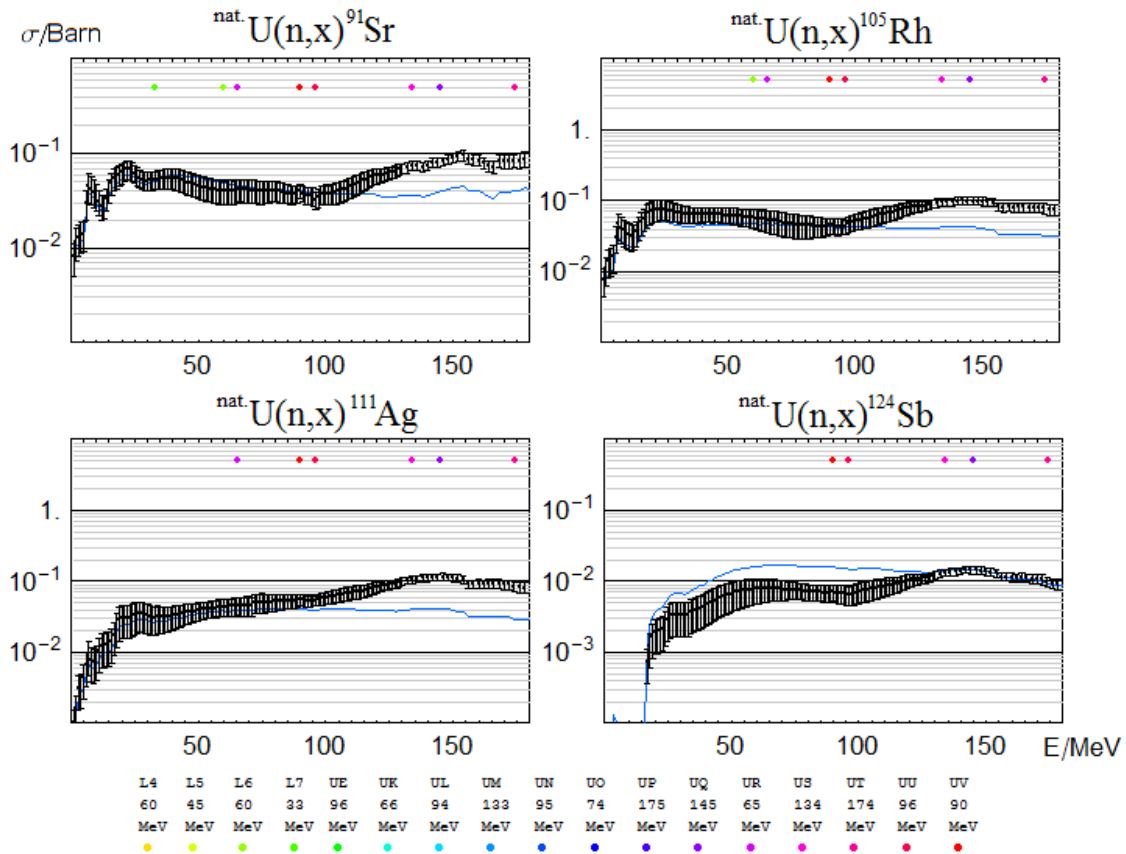
Figure 8.8: Unfolded excitation functions of neutron-induced fissions of natural uranium (black) including the related TALYS guess functions (blue). The colored dots represent the high-energy peaks of the underlying neutron spectra where the corresponding abbreviations used in the legend are explained at page 157

same behavior can be observed in the excitation functions of Figure 8.8. This behavior could go back to different fission modes, which are related to the projectile energy and where observed in proton-induced fission reaction [22]. Unfortunately, the low counting rates during the evaluation of the irradiated targets caused activation yield uncertainties of up to 30%. Furthermore, the rather complex γ-spectra (up to 250 peaks), and the accompanying peak interferences, did not allow to determine all predicted residual nuclides.

In conclusion the unfolded excitation functions of lead and uranium may indicate the existence of distinct modes for neutron-induced fission at medium energies, but the present work is not appropriate for a further, detailed analysis of the activation yields or of the phenomenology of isobaric distributions.

8.2   Meteorite Experiments

A main motivation of the present work was to generate excitation functions of medium energy neutron reactions in order to model the production of cosmogenic nuclides in stony and iron meteorites as well as in lunar samples. In this context it makes sense to validate the unfolded functions using activation yields from irradiation experiment which simulate the interaction of galactic cosmic-ray protons with meteoroids.

To this end data of two irradiation series were available. These experiments were carried out under experimental conditions which are hardly correlated to the performed neutron experiments. Thus, both series offer independent sets of activation yields and are qualified for testing the unfolded neutron excitation functions.

The first experimental series includes the activation of two spherical targets made of gabbro with a radius of 25 cm and of steel with a radius of 10 cm. Both were irradiated isotropically with 1600 MeV protons at the SATURNE synchrotron at Laboratoire National Saturne (LNS)/CEN Saclay, where the proton energy corresponds to the mean spectra of galactic cosmic-rays during the Maunder Minimum.

The second series consist of three experiments with stony meteoroid models at the CERN synchrocyclotron. The meteoroids with radii of 5, 15 and 25 cm were isotropically irradiated with 600 MeV protons.

For both series the depth and size depending spectra of primary and secondary nucleons available. They were determined by Monte Carlo calculations using the high-energy transport code HETC (High Energy Transport Code) within the HERMES (High Energy Radiation Monte Carlo Elaborate System) code system.

All experiments supply depth-dependent production rate data of both radionuclides and rare gases from a wide range of target elements. The measured production rates differ significantly with respect to both, target-product combination and depth-dependencies. Both differences are important for the calculations performed in the present work, since they are strongly correlated to the neutron cross section. This interrelation is explained by the generation of huge amounts of secondary particles, in particular to secondary neutrons which are preferred evaporated in compound reactions. Further neutrons are in contrast to protons not stopped by coulomb interactions, and propagate quasi unhampered through the target. Figure 8.9 shows two double logarithmic plots of the particle spectra inside of the gabbro meteoroid which was irradiated with 1600 MeV protons. The left side of the Figure depicts the spectra close to the surface of the meteoroid whereas the right side shows the spectra in the center. In both plots

the secondary neutrons add up to more than 99% of the secondary particles for energies below 10 MeV. Their dominance in the particle spectra continues up to about 200 MeV. Above 200 MeV the secondary particle flux consists of around 50% neutrons and 50% protons. At about 1.6 GeV the peak of the primary protons appears. Comparing the flux at the surface and at the center of the meteoroid it turns out, that the number of secondary particles, above all secondary neutrons, grows with increasing penetration depths while the high energy peak of the primary protons decreases. The spectra implies, that products with strong increasing activation yields over the range of the radius, are low-energy products and are mainly activated by neutrons whereas decreasing production rates indicate high-energy products which are mainly activated by primary protons.

Therefore, products with strong increasing production rates were from particular interest for the present work, since neutron modes were dominant in the performed activation yield calculations. On the other side the spectra shows a high neutron flux for energies below 1 MeV and this energy region is not properly considered in the unfolded excitation functions. For this reason only reactions with reaction thresholds above 1 MeV can be considered.

In the following section the results of the folding will be exemplarily discussed. The entire set of calculated depth-dependent production rates is shown in the appendix (see page 189). Figure 8.10 shows two typical calculation results. Both were performed
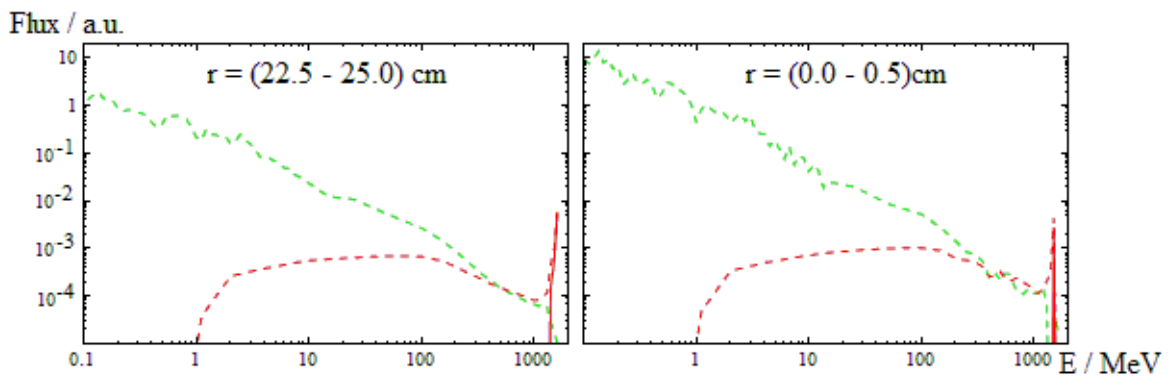
Figure 8.9: The particle flux spectra of the gabbro meteoroid with 25cm radius irradiated isotropically with 1600 MeV protons calculated with HERMES (see page 43). The plotted flux constituents are primary protons (red solid), secondary protons (red dashed) and secondary neutrons (green dashed). left: Particle flux spectra close to the surface of the meteoroid. right: Particle flux spectra close to center of the meteoroid.

for the 50cm diameter gabbro meteoroid which was irradiated with 1600 MeV protons. The abscissa of the plots represent the radius of the meteoroid, where 0 determines the center. The ordinates determine the production rates. Both Figures include separately information about the production induced by primary protons (red solid), secondary protons (red dashed), secondary neutrons (green dashed) and a sum of this three production modes, the total production rate (black solid). The grey area around total production rate define the production uncertainties. The blue markers represent experimental measured production rates. The results of the calculations are in good agreement with the measured production rates. This agreement is partially attributed to the relatively large calculation uncertainties. However, the uncertainties are determined via conventional error propagation and include nothing but the uncertainties of the proton cross sections, neutron cross sections and the uncertainties of the particle flux. Thus, the size of the uncertainties which is far from being satisfactory illustrates clearly the precision limits of activation yield modeling calculations of nowadays.

The examination of further depth-dependent production rates confirm, that the calculated production most closely correspond to measured data. Notwithstanding this overall agreement, some calculated activation yields differ significantly from the corresponding experimental measurements. This applies most notably the production of ^{22}Na from aluminium and silicon and to the production of ^{57}Co from nickel. Figure 8.11
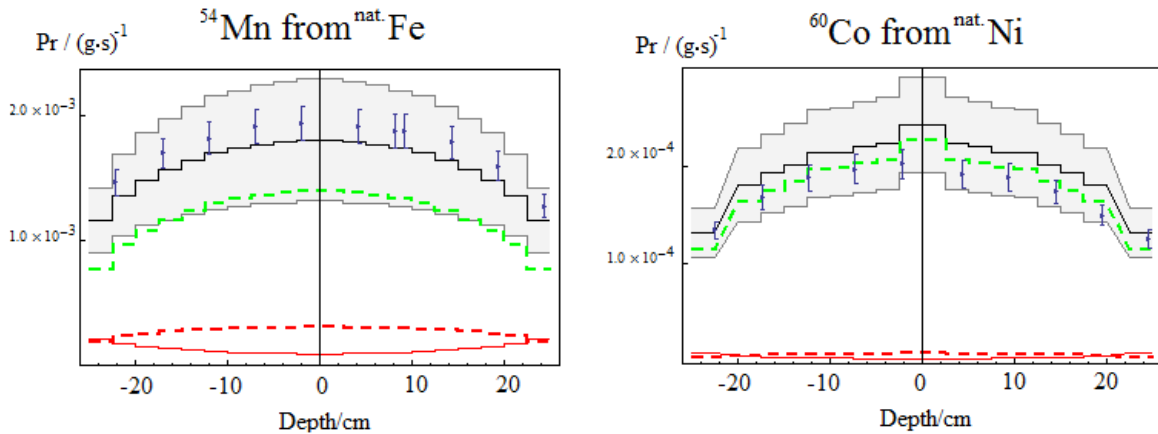
Figure 8.10: The production of ^{54}Mn from natural iron (left) and ^{60}Co from natural nickel (right) in the stony meteorite with a radius of 25cm irradiated with 1600 MeV protons. Both Figures show production induced by primary protons (red solid), by secondary protons (red dashed), by secondary neutrons (green dashed) and the total production rate (black solid) with its uncertainties as well as experimental production rates (blue).
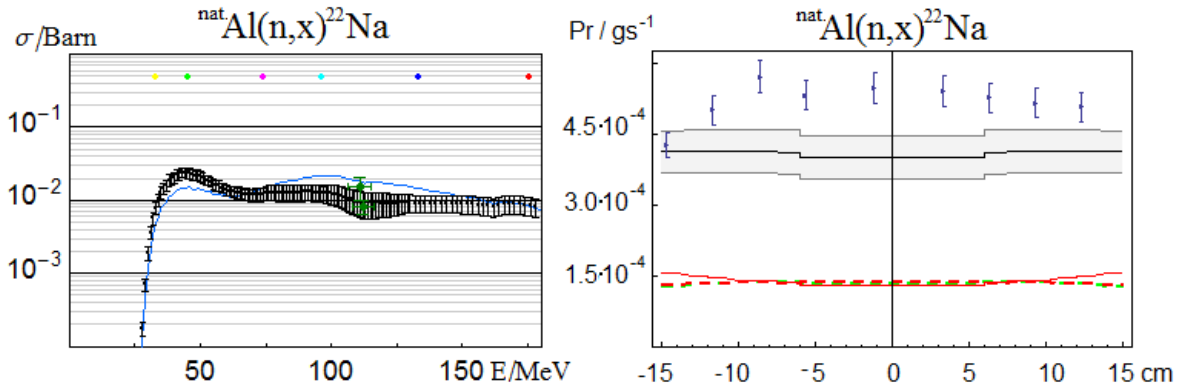
Figure 8.11: Production cross sections of ^{22}Na from natural aluminium (left) and the depth-dependent production of ^{22}Na from natural aluminium in the stony meteorite with a radius of 15cm irradiated with 600 MeV protons (right). Both Figures show production induced by primary protons (red solid), by secondary protons (red dashed), by secondary neutrons (green dashed) and the total production rate (black solid) with its uncertainties as well as experimental production rates (blue).
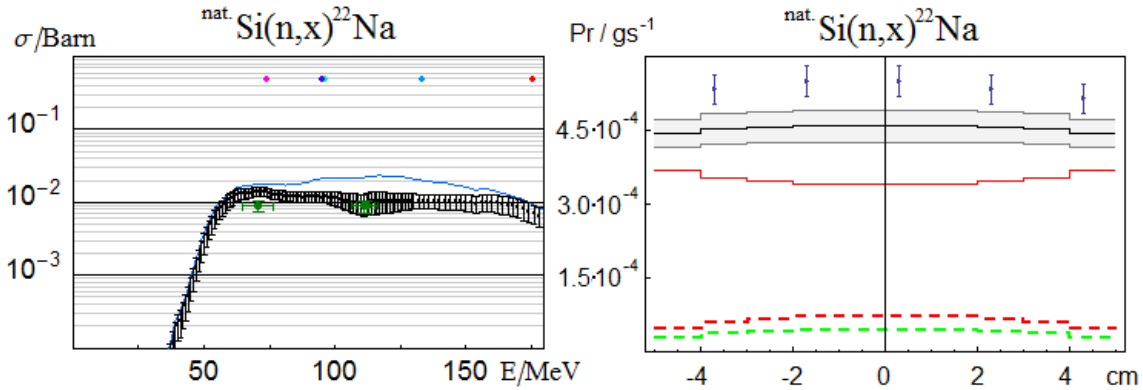
Figure 8.12: Production cross sections of ^{22}Na from natural silicon (left) and the depth-dependent production of ^{22}Na from natural silicon in the stony meteorite with a radius of 5cm irradiated with 600 MeV protons (right). Both Figures show production induced by primary protons (red solid), by secondary protons (red dashed), by secondary neutrons (green dashed) and the total production rate (black solid) with its uncertainties as well as experimental production rates (blue).

and Figure 8.12 show the depth-dependent activation yields of ^{22}Na from aluminium and silicon, respectively. Additional the Figures 8.11 and 8.12 show the corresponding unfolded excitation function.

The Figures 8.11 and 8.12 show, that in non of both meteoroids the production of ^{22}Na is dominated by the neutron mode. This applies in particular to the production from

silicon in the 10 cm diameter meteoroid. In consequence of the small contribution of the n-production mode it seems to be questionable to attribute the relatively big gab between calculated and measure activation yield only to the unfolded neutron excitation functions. However, neglect further error sources implies, that the unfolded excitation functions underestimates the production of ^{22}Na by about a factor of 2. This factor two appears rather big considering, that the excitation functions show good agreement with neutron cross sections calculated by Sisterson [67], as it is shown on the left sides of Figure 8.11 and 8.12.

A different situation is given for the production of ^{57}Co from nickel (see appendix page 198, 205, 214 and 222), were problems of the excitation function are known and were already attributed to the "bending strength" (see page 111). In this case it is very likely, that the problems which occur modeling the activation yields in the meteoroids go back to unfolded excitation function.

By all means the source of the problems that occur in the production of ^{22}Na from aluminium and silicon stays undetermined. Notwithstanding, the calculation of activation yields in meteoroids remain successful. They verify independently from the performed unfolding procedure the reliability and therefore quality of the unfolded excitation functions. Further they demonstrate, that the use of unfolded neutron cross sections opens a new approach to applied activation yield calculations. In this context the large uncertainties are may inconvenient, but compared to uncertainties that would occur using theoretical modeled cross sections they are reduced by about 50%.

Even though some small and also some bigger problems occurred during performed calculations, this work showed that the unfolding of cross sections from the response integral is feasible and provides more than 100 neutron excitation functions. This excitation functions represent the best available data of neutron induced reaction of medium energies nowadays. Further the comparison of the unfolded excitation functions with already existing neutron cross sections of other authors and the production rate calculations for the meteoroids verify the quality of the unfolding. In summary, even if some unfolded excitation functions have to be reviewed when new guess functions are available, the results of the present work exceed all expectations.

9   Conclusions

This work proposes a novel experimental approach which is based on the unfolding of neutron excitation functions from experimental data. Within the frame of this experimental approach 21 irradiation experiments with well-characterized, quasi mono-energetic neutrons of energies between 32.7 and 175.4 MeV were performed at the UCL/Louvain-la-Neuve and TSL/Uppsala. The abundances of relatively short-lived residual radionuclide from 13 different target elements (C, O, Mg, Al, Si, Fe, Co, Ni, Cu, Ag, Te, Pb and U) were determined by γ-spectrometry. More than 100 excitation functions of neutron-induced reactions were calculated from the response integrals with an unfolding formalism which uses the neutron spectra, the radionuclide abundances and the aid of additional information that was provided by "guess" excitation functions computed by the TALYS 1.0 code.

Comparisons between the results of the present work and available existing neutron cross sections show good agreements within the limits of the examined energy spectra. Calculations of activation yields in artificial meteorites, determined by folding experimental excitation functions with the spectral flux of primary protons, secondary protons and secondary neutrons, most closely correspond to experimental measured activation yields. This results prove that the experimental approach is applicable to determine excitation functions using high current neutron sources of quasi mono-energetic energies. Therefore, this novel approach opens new perspectives for the determination of neutron cross sections.

Except for the proof of concept, the work yields fundamental, physical findings. Based on the unfolded functions it could be see, that there are distinct differences between the n- and p- induced production modes of residual nuclides. Moreover, the excitation functions of lead and uranium indicate, that, by analogy to proton-induced reactions, distinct modes for neutron-induced fission at medium energies exist. Further unfolded functions show, that the prediction of reliable nuclear excitation functions via modeling calculations of medium energy neutron-induced reactions is not possible, yet.

According to this fundamental findings, further excitation functions for n- induced production of residual nuclides are needed in order to validate and improve theoretical modeling calculations and to understand the differences between n- and p- induced reaction modes. This includes not only the determination of radio nuclides but also of stable products, e.g. rare gases which are important for the field of cosmochemistry.

In the short term the collection and integration of existing experimental neutron cross sections into the unfolding procedure and the recalculation of guess functions using recently released TALYS 1.2 would help to improve the quality of neutron excitation function. In the medium-term, the continuation of irradiation experiments would be very promising, since recent technologies enable extended neutron energy ranges and higher neutron fluxes, where the latter improves the counting rates and therefore the quality of the entire unfolding procedure. This experiments could answer the question of the existence of distinct fission modes of neutron-induced fission at medium energies and further experimental data would as well benefit to the numerous application given in Table 1.1 including a more precised modeling of activation yields in meteorites.

References

[1] H.H. Andersen and J.F. Ziegler. *Hydrogen stopping powers in all elements*. Pergamon Press, New York, 1977.

[2] M. Baba, T. Kiyosumi, T. Iwasaki, M. Yoshioka, et al. Characterization and application of 20-90 MeV ^{7}Li(p, n) neutron source at TIARA. *Nucl. Data for Sci. and Technology Conf. Proc.*, pages 90–92, 1994.

[3] M. Baba, Y. Nauchi, T. Iwasaki, T. Kiyosumi, N. Nakao, et al. Characterization of 40-90 MeV ^{7}Li(p,n) Neutron Source at TIARA using a Proton Recoil Telescope and a TOF Method. *Nucl. Instrum. Methods*, A428:454–465, 1999.

[4] C. J. Batty, B. E. Bonner, E. Friedman, C. Tschalar, L. E. Williams, A. S. Clough, and J. B. Hunt. ^{6}Li(P,N) ^{6}Be and ^{7}Li(P,N) ^{7}Be Reactions at Intermediate Proton Energies. *Nuclear Physics A*, A120(2):297, 1968.

[5] H. Bethe. Zur Theorie des Durchgangs schneller Korpuskularstrahlen durch Materie. *Annals of Physics*, 3:325, 1930.

[6] H. Bethe. Bremsformel für Elektronen relativistischer Geschwindigkeit. *Zeitschrift für Physik*, 76:293, 1932.

[7] F. Bloch. Zur Bremsung rasch bewegter Teilchen beim Durchgang durch Materie. *Annals of Physics*, 16:285, 1933.

[8] N. Bohr. On the decrease of velocity of swiftly moving electrified particles in passing through matter. *Philosophical Magazine*, 30:581–612, 1915.

[9] J. P. Bondorf, A. S. Botvina, A. S. Iljinov, I. N. Mishustin, and K. Sneppen. Statistical Multifragmentation of Nuclei. *Physics Reports-Review Section of Physics Letters*, 257(3):133–221, 1995.

[10] A. S. Botvina, A. S. Iljinov, I. N. Mishustin, J. P. Bondorf, et al. Statistical simulation of the breakup of highly excited nuclei. *Nucl. Phys. A*, 475:663–686, 1987.

[11] D. A. Bryant, G. I. Powell, and C. H. Perry. The Origin of High-Energy Cosmic-Rays. *Nature*, 356(6370):582–583, 1992.

[12] G. Castagnoli and D. Lal. Solar Modulation Effects in Terrestrial Production of C-14. *Radiocarbon*, 22(2):133–158, 1980.

[13] H. Conde, S. Hultqvist, N. Olsson, T. Ronnqvist, R. Zorro, J. Blomgren, G. Tibell, A. Hakansson, O. Jonsson, A. Lindholm, L. Nilsson, P. U. Renberg, A. Brockstedt, P. Ekstrom, M. Osterlund, F. P. Brady, and Z. Szeflinski. A Facility for Studies of Neutron-Induced Reactions in the 50-200 Mev Range. *Nuclear Instruments and Methods in Physics Research Section a-Accelerators Spectrometers Detectors and Associated Equipment*, 292(1):121–128, 1990.

[14] V. Dangendorf, R. Nolte, F. Roos, H. Schuhmacher, B. R. L. Siebert, and M. Weyrauch. Proton recoil telescopes for fluence measurement in neutron beams of 20-200 MeV energy. *Nuclear Instruments and Methods in Physics Research Section a-Accelerators Spectrometers Detectors and Associated Equipment*, 469(2):205–215, 2001.

[15] K. Debertin. *Gamma- and X-Ray Spectrometry with Semiconductor Detectors*. North Holland, Amsterdam, Oxford, New York, Tokio, 1988.

[16] K. Debertin and U. Schötzig. PTB-Bericht. Technical Report PTB-Ra-24, Physikalisch-Technische Bundesanstalt, 1990.

[17] B. Dittrich, U. Herpers, T. Schiffmann, R. Michel, P. Cloth, P. Dragovitsch, D. Filges, J. Beer, and W. Wolfli. Production of Cosmogenic Nuclides in Meteoroids - Simulation Experiments and Modeling. *Analyst*, 114(3):295–301, 1989. T8952 Times Cited:11 Cited References Count:36.

[18] R. Donangelo, K. Sneppen, and S. R. Souza. A computer program for statistical multifragmentation of nuclei. *Computer Physics Communications*, 140(3):405–411, 2001.

[19] V. P. Eismont, A. V. Prokofyev, and A. N. Smirnov. Thin-Film Breakdown Counters and Their Applications (Review). *Radiation Measurements*, 25(1-4):151–156, 1995.

[20] International Organization for Standardization (ISO). *Guide to the Expression of Uncertainty in Measurement (GUM)*. ISO, Genf, 1995.

[21] M. Gloris. *Protonen-induzierte Restkernproduktion in schweren Elementen bei mittleren Energien*. Dissertation, University of Hanover, 1998.

[22] M. Gloris, R. Michel, F. Sudbrock, U. Herpers, P. Malmborg, and B. Holmqvist. Proton-induced production of residual radionuclides in lead at intermediate energies. *Nuclear Instruments and Methods in Physics Research Section a-Accelerators Spectrometers Detectors and Associated Equipment*, 463(3):593–633, 2001.

[23] J. N. Goswami, R. E. Mcguire, R. C. Reedy, D. Lal, and R. Jha. Solar-Flare Protons and Alpha-Particles during the Last 3 Solar-Cycles. *Journal of Geophysical Research-Space Physics*, 93(A7):7195–7205, 1988.

[24] P. W. Gray and A. Ahmad. Linear Classes of Ge(Li) Detector Efficiency Functions. *Nuclear Instruments and Methods in Physics Research Section a-Accelerators Spectrometers Detectors and Associated Equipment*, 237(3):577–589, 1985.

[25] J. J. Griffin. Statistical Model of Intermediate Structure. *Physical Review Letters*, 17(9):478, 1966.

[26] G. D. Harp, J. M. Miller, and B. J. Berne. Attainment of Statistical Equilibrium in Excited Nuclei. *Physical Review*, 165(4):1166, 1968.

[27] J. C. Hill, D. G. Shirk, R. F. Petry, and K. H. Wang. Effective Cross-Sections for (N,2pn), (N,2p), and (N,3pn) Reactions Using Intermediate-Energy Neutrons. *Physical Review C*, 12(6):1978–1982, 1975. Az357 Times Cited:6 Cited References Count:13.

[28] M. Imamura, H. Nagai, M. Honda, K. Kobayashi, K. Yoshida, H. Yoshikawa, and T. Kobayashi. Measurements of the Long-Lived Radionuclides in Environmental-Samples by Accelerator Mass-Spectrometry. *Journal of Radioanalytical and Nuclear Chemistry-Articles*, 138(2):261–270, 1990.

[29] Carsten Kaftan. *Ueber die Produktionradioaktiver Restkernedurch schnelle Neutronen*. Diploma thesis, University Hanover, 1994.

[30] C. Kalbach. 2-Component Exciton Model - Basic Formalism Away from Shell Closures. *Physical Review C*, 33(3):818–833, 1986.

[31] C. Kalbach. Consistent Exciton Model-Calculations with Shell Structure, Pairing and Isospin Effects. *Journal of Physics G-Nuclear and Particle Physics*, 21(11):1519–1538, 1995.

[32] E. Kim, T. Nakamura, A. Konno, Y. Uwamino, N. Nakanishi, M. Imamura, N. Nakao, S. Shibata, and S. Tanaka. Measurements of neutron spallation cross sections of C-12 and Bi-209 in the 20- to 150-MeV energy range. *Nuclear Science and Engineering*, 129(3):209–223, 1998.

[33] E. J. Kim, T. Nakamura, Y. Uwamino, N. Nakanishi, M. Imamura, N. Nakao, S. Shibata, and S. Tanaka. Measurements of activation cross sections on spallation reactions for Co-59 and Cu-nat at incident neutron energies of 40 to 120 MeV. *Journal of Nuclear Science and Technology*, 36(1):29–40, 1999.

[34] J. Klug, J. Blomgren, A. Atac, B. Bergenwall, S. Dangtip, K. Elmgren, C. Johanasson, N. Olsson, S. Pomp, A. V. Prokofiev, J. Rahm, U. Tippawan, O. Jonsson, L. Nilsson, P. U. Renberg, P. Nadel-Turonski, A. Ringbom, A. Oberstedt, F. Tovesson, V. Blideanu, C. Le Brun, J. F. Lecolley, F. R. Lecolley, M. Louvel, N. Marie, C. Schweitzer, C. Varignon, P. Eudes, F. Haddad, M. Kerveno, T. Kirchner, C. Lebrun, L. Stuttge, I. Slypen, A. N. Smirnov, R. Michel, S. Neumann, and U. Herpers. SCANDAL - a facility for elastic neutron scattering studies in the 50-130 MeV range. *Nuclear Instruments and Methods in Physics*, 489a(1-3):282–303, 2002.

[35] Daniel Kollar. *Neutron Cross Sections and Interactions of Cosmic Ray Particles with Terrestrial and Extraterrestrial Matter*. Dissertation, Comenius University Bratislava, 2003.

[36] A. J. Koning, S. Hilaire, and M. Duijvestijn. TALYS-0.72 A nuclear reaction program. Technical report, NRG - Nuclear Research and Consultancy Group, NRG, 1755 ZG Petten, The Netherlands, 2006.

[37] I. Leya, H. Busemann, H. Baur, R. Wieler, M. Gloris, S. Neumann, R. Michel, F. Sudbrock, and U. Herpers. Cross sections for the proton-induced production of He and Ne isotopes from magnesium, aluminum, and silicon. *Nuclear Instruments and Methods in Physics Research Section B-Beam Interactions with Materials and Atoms*, 145(3):449–458, 1998.

[38] I. Leya, H. J. Lange, and R. Michel. Model calculations for production rates of cosmogenic nuclides in iron meteoroids: The influence of trace elements on production rates. *Meteoritics and Planetary Science*, 32(4):A78–A79, 1997.

[39] Ingo Leya. *Modellrechnungen zur Beschreibung der Wechselwirkungen galaktischer kosmischer Teilchenstrahlung mit Stein und Eisenmeteoriten - Dünntargetbestrahlungen und Dicktargetexperimente.* Dissertation, University of Hanover, 1997.

[40] P. Marmier and E. Sheldon. Physics of Nuclei and Particles. *Academic Press, New York and London*, 1969.

[41] M. Matzke. private communication to R. Michel. about the STAY'SL program code, 1990.

[42] V. McLane. EXFOR basics - A short guide to the nuclear reaction data exchange format. Technical report, International Atomic Energy Agency, 2000.

[43] V. McLane et al. ENDF-201, ENDF/B-VI summary documentation supplement. Technical report, International Atomic Energy Agency, 1991.

[44] R. Michel, R. Bodemann, H. Busemann, R. Daunke, M. Gloris, H. J. Lange, B. Klug, A. Krins, I. Leya, M. Lupke, S. Neumann, H. Reinhardt, M. SchnatzButtgen, U. Herpers, T. Schiekel, F. Sudbrock, B. Holmqvist, H. Conde, P. Malmborg, M. Suter, B. DittrichHannen, P. W. Kubik, H. A. Synal, and D. Filges. Cross sections for the production of residual nuclides by low- and medium-energy protons from the target elements C, N, O, Mg, Al, Si, Ca, Ti, V, Mn, Fe, Co, Ni, Cu, Sr, Y, Zr, Nb, Ba and Au. *Nuclear Instruments and Methods in Physics Research Section B-Beam Interactions with Materials and Atoms*, 129(2):153–193, 1997.

[45] R. Michel, I. Leya, and L. Borges. Production of cosmogenic nuclides in meteoroids: Accelerator experiments and model calculations to decipher the cosmic ray record in extraterrestrial matter. *Nuclear Instruments and Methods in Physics Research Section B-Beam Interactions with Materials and Atoms*, 113(1-4):434–444, 1996.

[46] R. Michel, M. Lupke, U. Herpers, R. Rosel, D. Filges, P. Dragovitsch, W. Wolfli, B. Dittrich, and H. J. Hofmann. Simulation of the Interactions of Galactic Cosmic-Ray Protons by Irradiation of a Thick Stony Target with 1.6 GeV Protons. *Journal of Radioanalytical and Nuclear Chemistry-Articles*, 169(1):13–25, 1993.

[47] R. Michel and P. Nagel. International codes and model intercomparison for intermediate energy activation yields. *International Conference on Nuclear Data for Science and Technology*, 59:879–883, 1997.

[48] L. I. Miroshnichenko. Empirical model for the upper limit spectrum for solar cosmic rays at the Earth's orbit. *Radiation Measurements*, 26(3):421–425, 1996.

[49] L. I. Miroshnichenko. *Solar Cosmic Rays*, volume 260. Astrophysics and Space Science Library / Kluwer Academic Publishers, Dordrecht, Boston, London, 2001.

[50] T. Nakamura, M. Takada, N. Nakao, M. Baba, et al. Quasi mono-energetic neutron fields for neutron cross section and shielding experiments in the energy range of 20 to 200 MeV. *Nuclear Data for Science and Technology Conference Proceedings*, 59:1508–1512, 1997.

[51] N. Nakao, Y. Uwamino, T. Nakamura, et al. Development of a quasi-monoenergetic neutron field using the ^{7}Li(p,n)^{7}Be reaction in the 70 to 210 MeV energy range at RIKEN. *Nuclear Instruments and Methods*, A420:218–231, 1999.

[52] Sonja Neumann. *Aktivierungsexperimente mit Neutronen mittlerer Energien und die Produktion kosmogener Nuklide in extraterrestrischer Materie*. Dissertation, University Hanover, 1999.

[53] K. Obrien. Secular Variations in the Production of Cosmogenic Isotopes in the Earths Atmosphere. *Journal of Geophysical Research-Space Physics*, 84(Na2):423–431, 1979.

[54] G.G. Ohlsen. Kinematic relations in reactions of the form A+B–>C+D+E. *Nuclear Instruments and Methods*, 37:240 – 248, 1965.

[55] R. Pallavicini, S. Serio, and G. S. Vaiana. Survey of Soft-X-Ray Limb Flare Images - Relation between Their Structure in Corona and Other Physical Parameters. *Astrophysical Journal*, 216(1):108–122, 1977.

[56] F.G. Perey. Least-squares dosimetry unfolding: The program STAY'SL. Technical report, ORNL report ORNL/TM-6062, ENDF-254, NEA Data Bank, 1977.

[57] C. H. Poppe, J. D. Anderson, J. C. Davis, S. M. Grimes, and C. Wong. Cross-Sections for Li-7(P,N)Be-7 Reaction between 4.2 and 26 Mev. *Physical Review C*, 14(2):438–445, 1976.

[58] R. Prael and H. Lichtenstein. User guide to LCS: The LAHET Code System. Technical report, Los Alamos Rep. UR-89-3014, 1989.

[59] A. Prokofiev, M. Chadwick, S. Mashnik, N. Olsson, and L. Waters. Development and validation of the 7Li(n,p) nuclear data library and its application in monitoring of intermediate energy neutrons. *Journal of Nuclear Science and Technology*, 2:112, 2002.

[60] D. V. Reames. Energetic particles from solar flares and coronal mass ejections. *High Energy Solar Physics*, 374:35–44, 1996.

[61] J. Rowlands. The JEF-2.2 nuclear data library - OECD/NEA Data Bank. Technical report, Nuclear Energy Agency, 2000.

[62] H. Schuhmacher, H. J. Brede, V. Dangendorf, M. Kuhfuss, J. P. Meulders, W. D. Newhauser, and R. Nolte. Quasi-monoenergetic neutron beams with energies from 25 to 70 MeV. *Nuclear Instruments and Methods in Physics Research Section a-Accelerators Spectrometers Detectors and Associated Equipment*, 421(1-2):284–295, 1999.

[63] H. Schumacher, H. J. Brede, V. Dangendorf, M. Kuhfuss, J. P. Meulders, W. D. Newhauser, R. Nolte, and U. J. Schrewe. Quasi-monoenergetic reference neutron beams with energies from 25 MeV to 70 MeV. *International Conference on Nuclear Data for Science and Technology*, 59:388–392, 1997.

[64] R. Serber. Nuclear Reactions at High Energies. *Physical Review*, 72(11):1114–1115, 1947.

[65] K. Shibata, T. Nakagawa, T. Asami, T. Fukahori, et al. JENDL-3. Technical report, Japan Atomic Energy Agency, 1990.

[66] J. A. Simpson. Elemental and Isotopic Composition of the Galactic Cosmic-Rays. *Annual Review of Nuclear and Particle Science*, 33:323–381, 1983.

[67] J. M. Sisterson. Cross section measurements for neutron-induced reactions off C, Al, SiO2, Si and Au producing relatively short-lived radionuclides at neutron energies between 70 and 160 MeV. *Nuclear Instruments and Methods in Physics Research Section B-Beam Interactions with Materials and Atoms*, 261(1-2):993–995, 2007.

[68] J. M. Sisterson, F. D. Brooks, A. Buffler, M. S. Allie, D. T. L. Jones, and M. B. Chadwick. Cross-section measurements for neutron-induced reactions in copper at neutron energies of 70.7 and 110.8 MeV. *Nuclear Instruments and Methods in Physics Research Section B-Beam Interactions with Materials and Atoms*, 240(3):617–624, 2005.

[69] J. M. Sisterson and M. B. Chadwick. Cross section measurements for neutron-induced reactions in Ti, Fe and Ni at several neutron energies ranging from 70.7 to 151.6 MeV. *Nuclear Instruments and Methods in Physics Research Section B-Beam Interactions with Materials and Atoms*, 245(2):371–378, 2006.

[70] A. N. Smirnov and V. P. Eismont. Thin-Film Breakdown Counters (Review). *Instruments and Experimental Techniques*, 26(6):1249–1258, 1983.

[71] E. Storm and H.I. Israel. Photon cross sections from 1 keV to 100 MeV for elements Z = 1 to Z = 100. *Nucl. Data*, A7:565–581, 1970.

[72] Y. Uno, Y. Uwamino, T. S. Soewarsono, and T. Nakamura. Measurement of the neutron activation cross sections of C-12, Si-30, Ti-47, Ti-48, Cr-52, (CO)-C-59, and Ni-58 between 15 and 40 MeV. *Nuclear Science and Engineering*, 122(2):247–257, 1996.

[73] W. Westmeier. Background Subtraction in Ge(Li) Gamma-Ray Spectra. *Nuclear Instruments and Methods*, 180(1):205–210, 1981.

[74] W. Westmeier. The Fitting of Solid-State Detector Spectra. *Nuclear Instruments and Methods in Physics Research Section a-Accelerators Spectrometers Detectors and Associated Equipment*, 242(3):437–442, 1986.

[75] W. Westmeier. commercial software GAMMA-W, 2006.

[76] W. Westmeier. *GAMMA-W 18.03 Manual.* Gesellschaft für Kernspektrometrie mbH, Ebsdorfergrund-Mölln, Germany, February 2006.

[77] J.F. Ziegler, J.P. Biersack, and U. Littmark. *The Stopping and Range of Ions in Solids.* Pergamon Press, New York, 1985.

A   Irradiation Data

The following pages contain the data of the irradiation experiments. The name of the irradiation experiment is given by the abbreviation: uppn0e, uppn0f,.., uppn0q for the experiments that were performed in Uppsala and louv01, louv02,.., louv04 for the experiments that were performed in Louvain-la-Neuve.

BoI : **B**egin **o**f **I**rradiation (UTC+1)

EoI : **E**nd **o**f **I**rradiation

$\mathbf{E_p}$: The energy of the incident protons in MeV.

$\mathbf{E_n}$: The mean energy of the peakneutrons in MeV.

$\mathbf{\Phi_1}$: The fluence of the peak neutrons in front of the target stack.

$\mathbf{\Phi_2}$: The fluence of the peak neutrons behind the stack.

$\mathbf{d_{Li}}$: The thickness of the Li-Target.

The given tables contain information about the target elements, the mass of the targets and the radius of the target foils. The tables are followed by a plot of the corresponding time logger data.

A.1   louv02

BoI	11.10.1997, 13:15	E_p	36,4 MeV
EoI	13.10.1997, 07:00	E_n	$(32,7\pm2,0)$MeV
Φ_1	$(1,33\pm0,08)\cdot10^{10}$ cm^{-2}	d_{Li}: 5 mm	
Φ_2	N/A		

Foil	Mass/g	d/mm	Ø/mm	Block	Foil	Mass/g	d/mm	Ø/mm	Block
cuv2000	4,31128	1	25	cu2001	cuv2005	8,48482	2	25	cu2006
pbv2001	11,13895	2	25	pb2001	alv2001	5,12303	4	25	al2001
cuv2001	17,26017	4	25	cu2002	cuv2006	8,73090	2	25	cu2007
agv2001	20,54678	4	25	ag2001	quv2001	4,31927	4	25	qu2001
cuv2002	8,52881	4	25	cu2003	cuv2007	8,61427	2	25	cu2008
niv2001	17,36789	4	25	ni2001	ccv2001	3,40107	4	25	cc2001
cuv2003	8,64946	2	25	cu2004	cuv2008	8,73408	2	25	cu2009
cov2001	18,19061	4	25	co2001	tev2001	1,94160	1	25	te2001
cuv2004	8,65309	2	25	cu2005	$\sum$ 18		56		18
fev2001	14,38738	4	25	fe2001					

Data of the Time−Logging
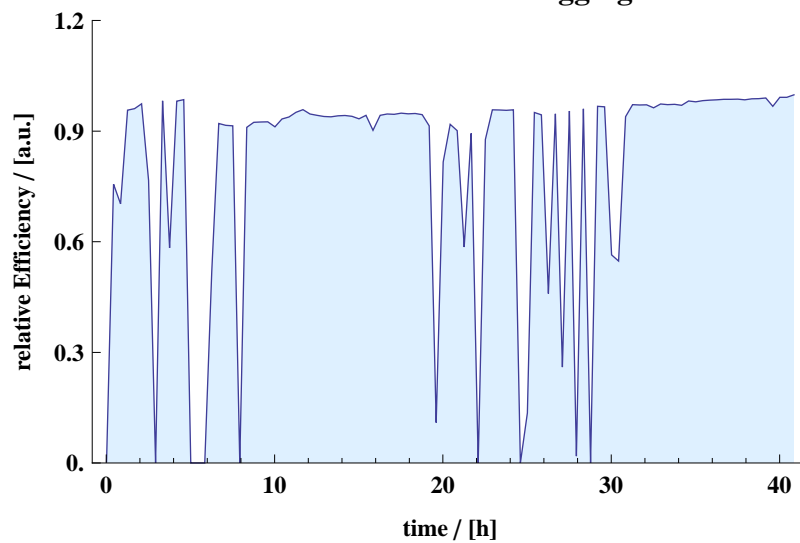
A.2   louv03

BoI   04.04.1998, 17:27 E_p 48,5 MeV
EoI   06.04.1998, 07:32 E_n (45,3±1,6) MeV
Φ_1 $(1{,}16 \pm 0{,}07) \cdot 10^{10}$ cm^{-2} d_{Li}: 5 mm
Φ_2 N/A

Foil	Mass/g	d/mm	Ø/mm	Block
cu2529	8,74127	2	25	cu3001
pb2505	5,59002	1	25	pb3001
pb2506	5,54766	1	25	
cu2521	8,71253	2	25	cu3002
cu2530	8,77087	2	25	
te20v	1,8987	1	20	te3001
cu2528	8,66835	2	25	cu3003
ag2506	5,11314	1	25	ag3001
ag2507	5,14212	1	25	
ag2508	5,13907	1	25	
ag2511	5,13043	1	25	
cu2522	8,60384	2	25	cu3004
ni2505	4,35008	1	25	ni3001
ni2506	4,32784	1	25	
ni2508	4,35317	1	25	
cu2526	8,67175	2	25	cu3005
co2505	4,51791	1	25	co3001
co2507	4,55318	1	25	
co2510	4,56507	1	25	
cu2533	8,68833	2	25	cu3006
fe2505	3,59256	1	25	fe3001
fe2509	3,85089	1	25	
fe2510	3,84483	1	25	

Foil	Mass/g	d/mm	Ø/mm	Block
cu2525	8,70437	2	25	cu3007
si	4,35339	4	25	si3001
cu2524	8,66447	2	25	cu3008
al2505	1,28700	1	25	al3001
al2509	1,28674	1	25	
al2510	1,27965	1	25	
cu2523	8,74813	2	25	cu3009
qu2505	1,05479	1	25	qu3001
qu2506	1,07402	1	25	
qu2509	1,07145	1	25	
cu2527	8,62380	2	25	cu3010
cc2505	0,85444	1	25	cc3001
cc2513	0,85405	1	25	
cc2512	0,84954	1	25	
cc2511	0,85322	1	25	
cc2514	0,85356	1	25	
cu2520	8,58397	2	25	cu3011
$\sum$ 40		55		21

Data of the Time–Logging
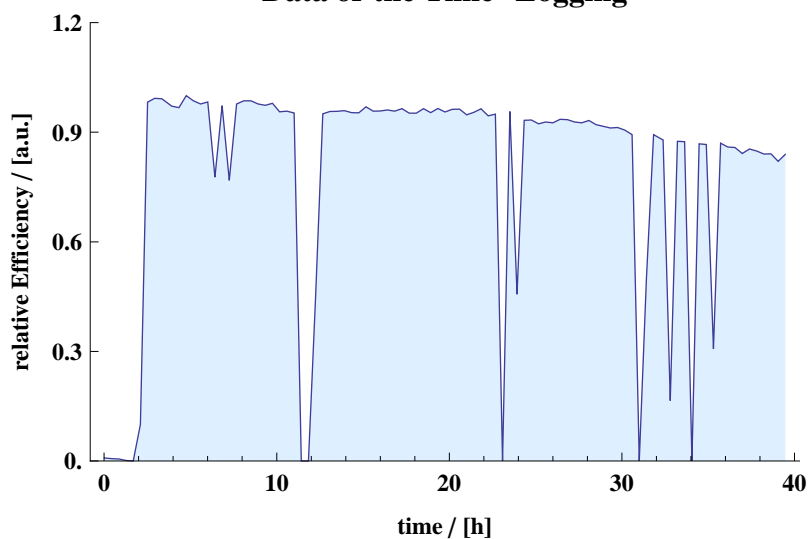
A.3   louv04

BoI	14.11.1998, 16:32	E_p	62,9 MeV
EoI	16.11.1998, 06:57	E_n	$(59,9\pm1,3)$ MeV
Φ_1	$(1,19 \pm 0,07) \cdot 10^{10}$ cm^{-2}	d_{Li}:	5 mm
Φ_2	N/A		

Foil	Mass/g	d/mm	Ø/mm	Block
cu2531	8,61913	2	25	cu4001
pb2507	5,65404	1	25	pb4001
pb2508	5,61160	1	25	
cu2534	8,65488	2	25	cu4002
cu2535	8,71345	2	25	
te30v	1,67790	1	20	te4001
cu2536	8,62876	2	25	cu4003
ag2509	5,14431	1	25	ag4001
ag2510	5,11798	1	25	
ag2512	5,13364	1	25	
ag2514	5,13579	1	25	
cu2537	8,75155	2	25	cu4004
ni2507	4,33257	1	25	ni4001
ni2509	4,33114	1	25	
ni2510	4,36070	1	25	
cu2538	8,65213	2	25	cu4005
co2506	4,53928	1	25	co4001
co2508	4,55549	1	25	
co2509	4,52232	1	25	
cu2539	8,73856	2	25	cu4006

Foil	Mass/g	d/mm	Ø/mm	Block
fe2506	3,84438	1	25	fe4001
fe2507	3,82744	1	25	
fe2508	3,84154	1	25	
cu2540	8,65800	2	25	cu4007
si	4,34634	4	25	si4001
cu2541	8,66765	2	25	cu4008
al2506	1,28354	1	25	al4001
al2507	1,28743	1	25	
al2508	1,28766	1	25	
cu2542	8,63705	2	25	cu4009
qu2507	1,06323	1	25	qu4001
qu2508	1,06540	1	25	
qu2510	1,06869	1	25	
cu2543	8,63628	2	25	cu4010
cc2506	0,90788	1	25	cc4001
cc2507	0,86386	1	25	
cc2508	0,76681	1	25	
cc2509	0,90385	1	25	
cc2510	0,85438	1	25	
cu2544	8,63680	2	25	cu4011
$\sum$ 40		56		21

Data of the Time−Logging

138
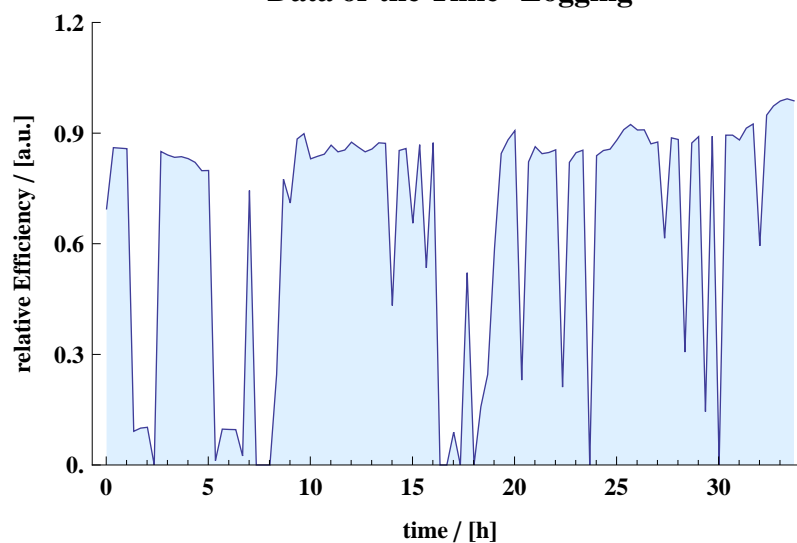
A.4   louv05

BoI   06.12.2000, 13:22 E_p 48,5 MeV
EoI   09.12.2000, 07:19 E_n $(45{,}3\pm1{,}6)$ MeV
Φ_1 $(1{,}17 \pm 0{,}07) \cdot 10^{10}$ cm^{-2} d_{Li}: 5 mm
Φ_2 N/A

Foil	Mass/g	d/mm	Ø/mm	Block
cu5001	8,68209	2	25	cu5001
cu5003	8,67424	2	25	
uu5001	1,38659	0,16	25	
uu5003	1,38251	0,16	25	uu5001
uu5005	1,39100	0,16	25	
uu5007	1,40140	0,16	25	
cu5005	8,64775	2	25	cu5002
cu5007	8,67467	2	25	
$\sum$ 8		4,64		3

Time−Logging of the Neutron−Flux
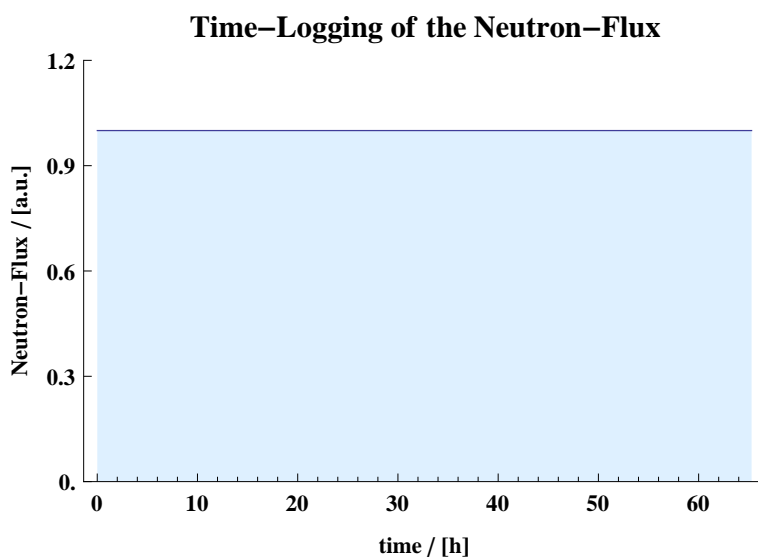
A.5   louv06

BoI	18.05.2001, 04:50	E_p	62,9 MeV	
EoI	20.05.2001, 11:00	E_n	$(59,9\pm1,3)$ MeV	
Φ_1	$(1,46 \pm 0,10) \cdot 10^{10}$ cm^{-2}	d_{Li}: 5 mm		
Φ_2	N/A			

Foil	Mass/g	d/mm	Ø/mm	Block
cu6001	8,65460	2	25	cu6001
cu6003	8,67853	2	25	
uu6001	1,39953	0,16	25	uu6001
uu6003	1,39911	0,16	25	
uu6005	1,40656	0,16	25	
uu6007	1,41048	0,16	25	
cu6005	8,66820	2	25	cu6002
cu6007	8,68609	2	25	
$\sum$ 8		4,64		3

Time−Logging of the Neutron−Flux

140
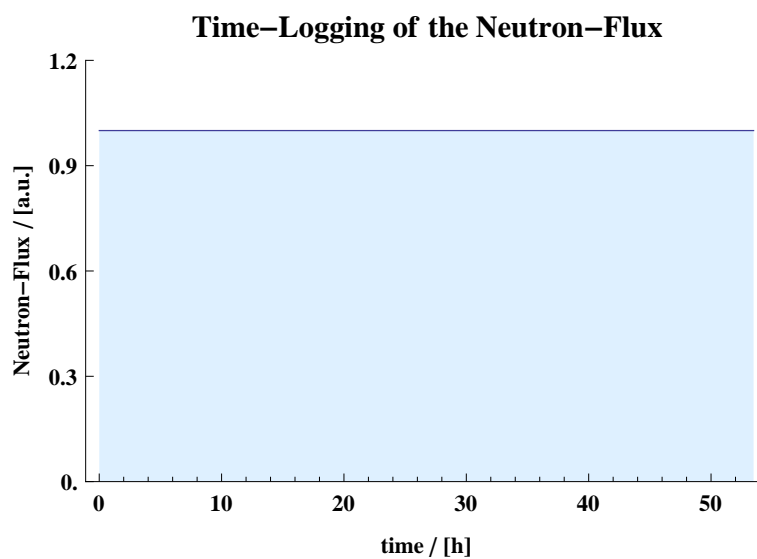
A.6 louv07

BoI	27.11.2001, 07:06		E_p	36,4 MeV
EoI	29.11.2001, 08:00		E_n	$(34,0\pm2,0)$ MeV
Φ_1	$(9,62\pm0,56)\cdot10^9$ cm^{-2}		d_{Li}:	5 mm
Φ_2	N/A			

Foil	Mass/g	d/mm	Ø/mm	Block
cu7001	8,68821	2	25	cu7001
cu7003	8,64673	2	25	
uu7001	1,41380	0,16	25	
uu7003	1,38965	0,16	25	uu7001
uu7005	1,41229	0,16	25	
uu7007	1,38315	0,16	25	
cu7005	8,63177	2	25	cu7002
cu7007	8,70301	2	25	
$\sum$ 8		4,64		3

141
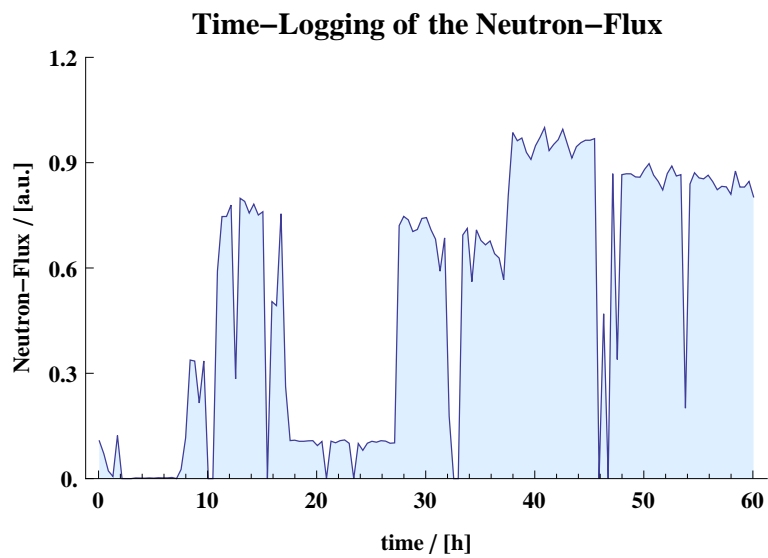
A.7   uppn0e

BoI	21.01.1998, 11:20	E_p (98,5±0,3) MeV
EoI	24.01.1998, 13:45	E_n (96,1±0,8) MeV
Φ_1	$(1{,}23 \pm 0{,}16) \cdot 10^{11}$ cm^{-2}	d_{Li}: 4 mm
Φ_2	$(8{,}45 \pm 0{,}80) \cdot 10^{10}$ cm^{-2}	

Foil	Mass/g	d/mm	Ø/mm	Block
cu1708	3,9697	2	17	
	+0,9591		+2	cue001
cu1709	3,9621	2	17	
	+0,9536		+2	
cu1003	1,3506	2	10	
	+3,5779		+9	cue002
cu1007	1,3441	2	10	
	+3,5392		+9	
ag008	2,96639	1	19	
ag019	2,96617	1	19	
ag012	3,01008	1	19	age002
ag021	3,00947	1	19	
cu1004	1,3334	2	10	
	+3,5820		+9	cue008
cc2017	0,94785	2	19	
cc2010	1,02464	2	19	cce001
cu1005	1,3445	2	10	
	+3,5637		+9	cue007
pb1	3,6013	1	20	
pb2	3,5232	1	20	pbe001
cu1009	1,3406	2	10	
	+3,5674		+9	cue004
co2008	5,23131	2	19	coe001

Foil	Mass/g	d/mm	Ø/mm	Block
cu1711	3,9422	2	17	
	+0,9691		+2	cue005
si2002	1,20821	2	19	
si2004	1,21597	2	19	sie001
cu1001	1,3292	2	10	
	+3,5773		+9	cue006
qu2012	1,36137	2	20	
qu2010	1,35985	2	20	que001
cu1710	3,9486	2	17	
	+0,9244		+2	cue003
ag020	3,00748	1	19	
ag014	2,96996	1	19	
ag016	2,96878	1	19	age001
ag025	3,00020	1	19	
cu1712	3,9604	2	17	
	+0,9286		+2	cue009
cu1704	3,9733	2	17	
	+0,9433		+2	
cu1010	1,3446	2	10	
	+3,5778		+9	cue010
cu1008	1,3395	2	10	
	+3,5929		+9	
$\sum$ 31		50		17

Data of the Time−Logging
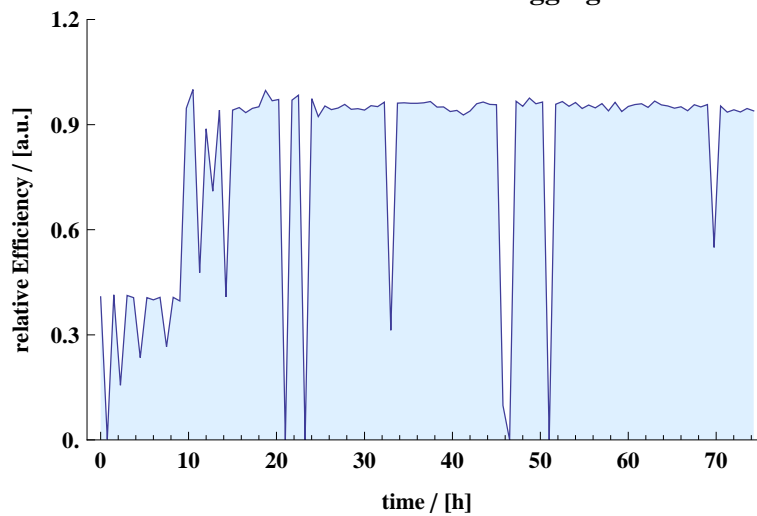
A.8   Uppn0f

BoI	15.06.1998, 19:05		E_p	(98,6±0,3) MeV
EoI	18.06.1998, 21:48		E_n	(96,2±0,8) MeV
Φ_1	$(1{,}54 \pm 0{,}21) \cdot 10^{11}$ cm^{-2}		d_{Li}: 4 mm	
Φ_2	N/A			

Foil	Mass/g	d/mm	Ø/mm	Block
cu1011	4,97893	2	19	cuf001
ag026	2,97022	1	19	
ag027	2,99493	1	19	agf001
ag030	2,97243	1	19	
ag029	3,00084	1	19	
cu5019	12,41029	5	19	cuf002
Dose6	3,78506	8	19	tef001
cu1010	4,97963	2	19	cuf003
si1003	0,59865	1	19	sif001
si1005	0,54163	1	19	
cu1007	4,98615	2	19	cuf004
al2013	1,54811	2	19	alf001
cu1002	4,98970	2	19	cuf005

Foil	Mass/g	d/mm	Ø/mm	Block
mg2008	0,97794	2	19	mgf001
cu1014	4,98797	2	19	cuf006
Dose9	6,17782	11	19	tef002
cu2017	5,01105	2	19	cuf007
si1002	0,50583	1	19	sif002
si1004	0,57166	1	19	
cu2025	4,98087	2	19	cuf008
al2002	1,55016	2	19	alf002
cu2024	4,97579	2	19	cuf009
mg2010	0,98037	2	19	mgf002
cu2015	4,88146	2	19	cuf010
$\sum$ 24		58		19

Data of the Time−Logging

143
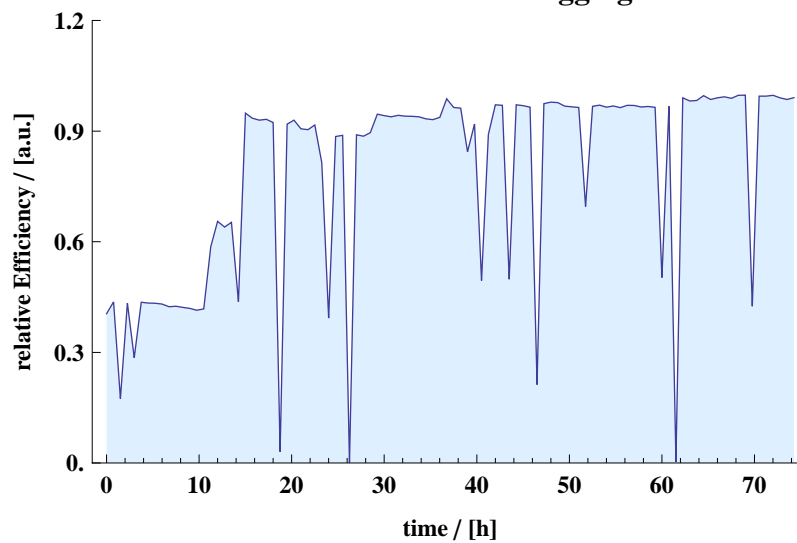
A.9 uppn0h

BoI	09.09.1998, 19:22		E_p	(49,2±0,1) MeV
EoI	10.09.1998, 14:00		E_p	(46,2±1,3) MeV
Φ_1	$(5,48 \pm 0,49) \cdot 10^{10}$ cm^{-2}		d_{Li}: 4 mm	
Φ_2	$(3,43 \pm 0,31) \cdot 10^{10}$ cm^{-2}			

Foil	Mass/g	d/mm	Ø/mm	Block
cu2035	4,89095	2	19	cuh001
pbI	3,57014	1	20	pbh001
pbII	3,51835	1	20	
cu2031	5,01433	2	19	cuh002
cu2021	5,00362	2	19	
ag010	2,99188	1	19	
ag017	2,98892	1	19	agh001
ag006	2,99156	1	19	
ags002	2,99751	1	19	
cu2028	4,99529	2	19	cuh003
co2004	5,24575	2	19	coh001
co2003	5,29582	2	19	
cu2034	5,01140	2	19	cuh004
fe2014	4,22604	2	19	feh001
fe2011	4,43542	2	19	
cu2022	4,99040	2	19	cuh005

Foil	Mass/g	d/mm	Ø/mm	Block
si5004	3,25875	5	19	sih001
cu2018	5,04404	2	19	cuh006
al2010	1,54067	2	19	alh001
cu2030	5,01235	2	19	cuh007
qu2011	1,35680	2	20	
qu1001	0,67933	1	20	quh001
qu1013	0,69372	1	20	
cu2032	5,00837	2	19	cuh008
cc2015	0,94184	2	19	cch001
cc2012	0,93967	2	19	
cus001	4,97908	2	19	cuh009
nis027	2,56629	1	19	
nis028	2,56615	1	19	nih001
nis030	2,54299	1	19	
$\sum$ 30		52		18

Data of the Time−Logging

144
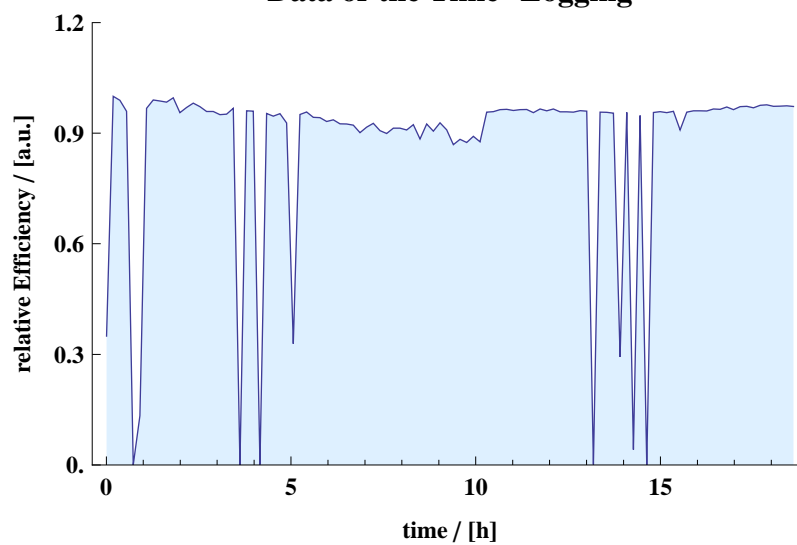
A.10   uppn0k

BoI	10.09.1998, 21:45	E_p (69,1±0,2) MeV
EoI	12.09.1998, 14:00	E_n (66,4±1,0) MeV
Φ_1	$(8,49 \pm 0,82) \cdot 10^{10}$ cm^{-2}	d_{Li}: 4 mm
Φ_2	$(5,00 \pm 0,49) \cdot 10^{10}$ cm^{-2}	

Foil	Mass/g	d/mm	Ø/mm	Block
cu2023	5,01242	2	19	cuk001
pb$\overline{\text{III}}$	3,52970	1	20	pbk001
pb$\overline{\text{IV}}$	3,55770	1	20	
cu2027	5,08498	2	19	cuk002
cus023	4,87616	2	19	
ags001	2,98452	1	19	agk001
ags005	2,99394	1	19	
ags006	2,99743	1	19	
ags007	2,96524	1	19	
cus013	4,98858	2	19	cuk003
co2006	5,30436	2	19	cok001
cos001	2,67073	1	19	
cos003	2,69224	1	19	
cus015	4,88024	2	19	cuk004
fe2006	4,38930	2	19	fek001
fe2017	4,43250	2	19	
cus009	4,96190	2	19	cuk005

Foil	Mass/g	d/mm	Ø/mm	Block
si5003	3,29002	5	19	sik001
cus008	4,88859	2	19	cuk006
al2001	1,59322	2	19	alk001
cus007	4,88575	2	19	cuk007
qu1012	0,69572	1	20	quk001
qu1014	0,69630	1	20	
qu1006	0,70612	1	20	
qu1011	0,69078	1	20	
cus027	4,89824	2	19	cuk008
cc2005	0,94171	2	19	cck001
cc2009	0,94673	2	19	
cus017	4,88324	2	19	cuk009
nis022	2,53952	1	19	nik001
nis023	2,56130	1	19	
nis024	2,56640	1	19	
$\sum$ 32		52		18

Data of the Time−Logging

145
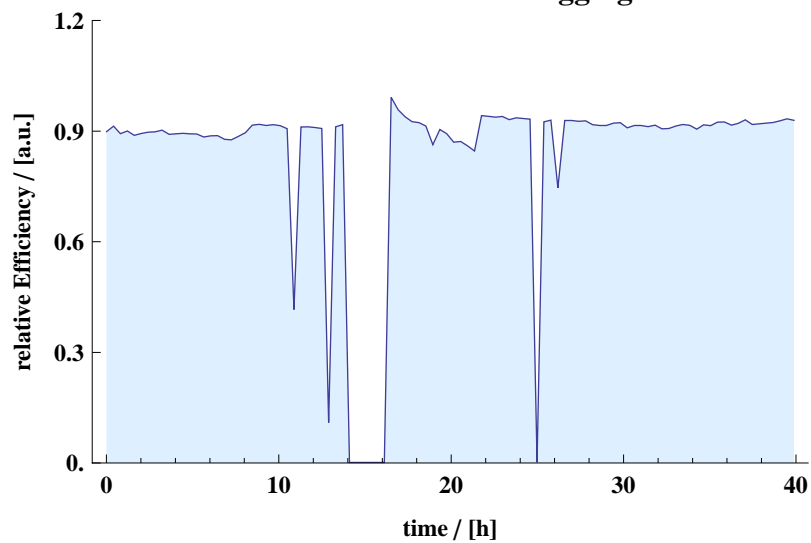
A.11 uppn0l

BoI	20.10.1998, 13:40		E_p	(96,8±0,3) MeV
EoI	24.10.1998, 13:54		E_n	(94,3±0,8) MeV
Φ_1	$(2{,}10 \pm 0.21) \cdot 10^{11}$ cm^{-2}		d_{Li}: 4 mm	
Φ_2	N/A			

Foil	Mass/g	d/mm	Ø/mm	Block
cus024	4,95687	2	19	cul001
ags003	2,99611	1	19	
ags010	2,97830	1	19	agl001
ags004	2,95567	1	19	
ags011	2,99674	1	19	
cus014	12,51632	5	19	cul002
ted5	4,71682	8	19	tel001
cus012	4,89385	2	19	cul003
mg2003	0,97391	2	19	mgl001
cus025	4,92735	2	19	cul004
pbVII	3,56448	1	20	pbl001
pbVIII	3,54706	1	20	
cus021	4,92725	2	19	cul005
nis005	2,56046	1	19	
nis016	2,53401	1	19	nil001
nis013	2,56480	1	19	
nis014	2,55979	1	19	

Foil	Mass/g	d/mm	Ø/mm	Block
cus019	4,90866	2	19	cul006
fe2020	4,39034	2	19	fel001
fe2009	4,51494	2	19	
cu2016	5,01070	2	19	cul007
al2017	1,55719	2	19	all001
cus016	4,90629	2	19	cul008
qu1010	0,70388	1	20	
qu1005	0,68198	1	20	qul001
qu1008	0,70484	1	20	
qu1002	0,68999	1	20	
cus020	4,87552	2	19	cul009
cc1010	0,46276	1	19	
cc1003	0,46379	1	19	ccl001
cc1005	0,46084	1	19	
cc1001	0,46119	1	19	
cus011	4,92746	2	19	cul010
$\sum$ 33		57		19

Data of the Time−Logging
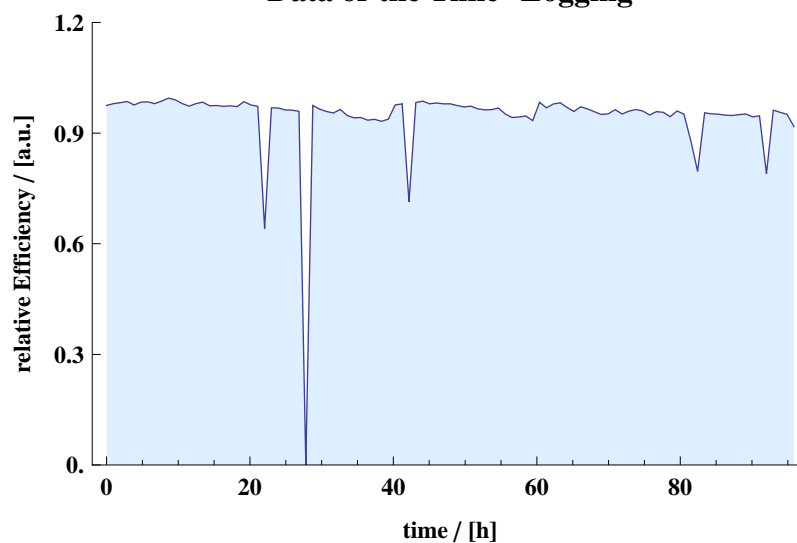
A.12 uppn0m

BoI	26.05.1999, 10:18			E_p	$(136{,}7{\pm}1{,}0)$ MeV	
EoI	29.05.1999, 14:00			E_n	$(133{,}0{\pm}2{,}2)$ MeV	
Φ_1	$(5{,}76 \pm 0{,}51) \cdot 10^{10}$ cm^{-2}			d_{Li}: 15 mm		
Φ_2	$(4{,}07 \pm 0{,}37) \cdot 10^{10}$ cm^{-2}					

Foil	Mass/g	d/mm	Ø/mm	Block	Foil	Mass/g	d/mm	Ø/mm	Block
cu1301	4,95483	2	19	cum001	cu1313	4,88660	2	19	cum007
ag1301	2,99791	1	19		fe1301	4,22274	2	19	fem001
ag1303	2,99874	1	19	agm001	fe1303	4,23300	2	19	
ag1305	2,96503	1	19		cu1315	5,01228	2	19	cum008
cu1303	12,62191	5	19	cum002	al1301	1,54914	2	19	alm001
co1301	2,66993	1	19		cu1317	5,00233	2	19	cum009
co1303	2,69174	1	19	com001	qu1301	0,69048	1	20	
co1305	2,67806	1	19		qu1303	0,70487	1	20	
cu1305	4,87200	2	19	cum003	qu1305	0,69500	1	20	qum001
mg1301	0,98029	2	19	mgm001	qu1307	0,68755	1	20	
cu1309	4,91091	2	19	cum005	cu1319	4,99506	2	19	cum010
pb1301	3,12965	1	19		cc1301	0,45988	1	19	
pb1303	3,14439	1	19	pbm001	cc1303	0,46039	1	19	
cu1311	4,93214	2	19	cum006	cc1305	0,45344	1	19	ccm001
ni1301	2,55206	1	19		cc1307	0,45784	1	19	
ni1303	2,56026	1	19	nim001	cu1321	4,96982	2	19	cum011
ni1305	2,56477	1	19		$\sum$ 33		50		19

Data of the Time−Logging

147
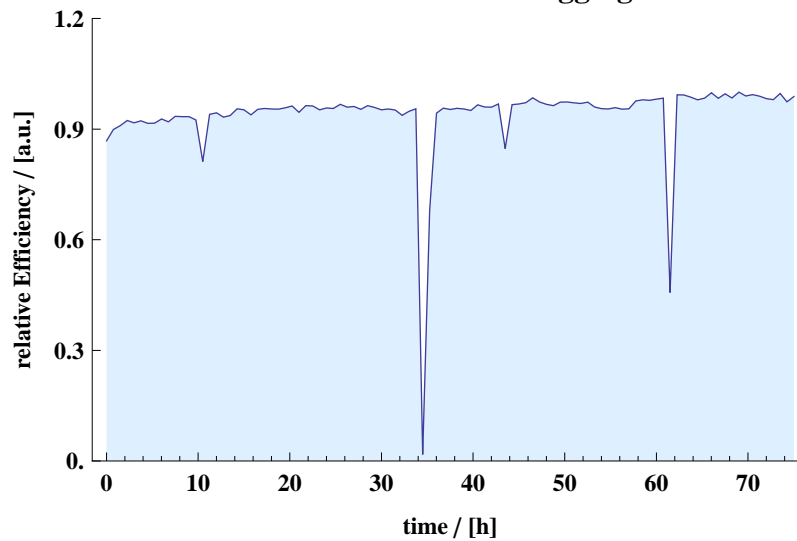
A.13 Uppn0n

BoI	02.11.1999, 16:48		E_p	$(98{,}0 \pm 2{,}0)$ MeV
EoI	05.11.1999, 14:00		E_n	$(96{,}0 \pm 2{,}0)$ MeV
Φ_1	$(3{,}3 \pm 0{,}4) \cdot 10^{11}$ cm^{-2}		d_{Li}:	4 mm
Φ_2	N/A			

Foil	Mass/g	d/mm	Ø/mm	Block	Foil	Mass/g	d/mm	Ø/mm	Block
cu1307	4,97373	2	19	cun001	cu1409	4,97405	2	19	cun006
te1401	4,74736	10	19	ten001	cc1401	0,50165	1	19	
cu1401	12,62455	5	19	cun002	cc1403	0,45702	1	19	
mg1401	0,97171	2	19	mgn001	cc1405	0,45654	1	19	ccn001
cu1403	5,00687	2	19	cun003	cc1407	0,46055	1	19	
pb1403	3,13990	1	19		cu1411	4,99500	2	19	cun007
pb1401	3,10694	1	19	pbn001	qu1401	0,38315	1	15	
cu1405	4,95474	2	19	cun004	qu1403	0,38700	1	15	
ni1403	2,56254	1	19		qu1405	0,38381	1	15	qun001
ni1401	2,56137	1	19	nin001	qu1407	0,38174	1	15	
cu1407	4,97779	2	19	cun005	cu1413		2	19	cun008
fe1405	2,18651	1	19		$\sum$ 25		46		15
fe1403	2,18520	1	19	fen001					
fe1401	2,18428	1	19						

Data of the Time−Logging
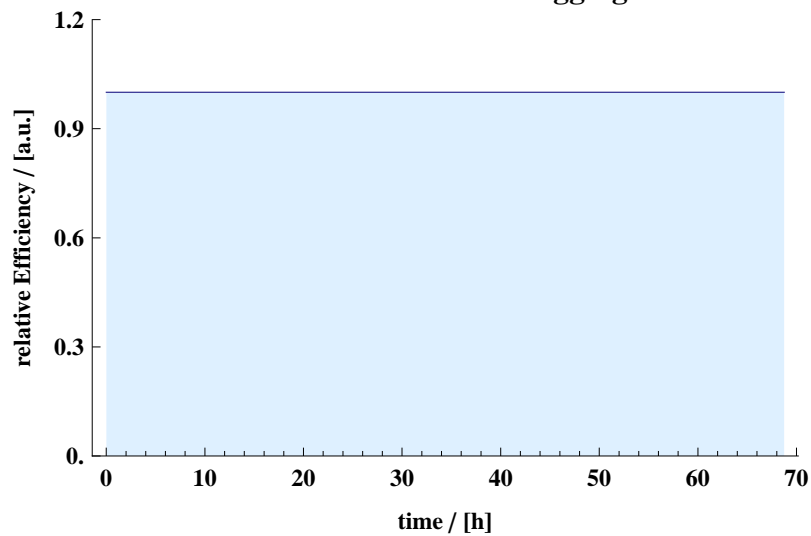
A.14 uppn0o

BoI	14.12.1999, 11:00		E_p	$(76{,}40\pm0{,}20)$ MeV
EoI	18.12.1999, 13:58		E_n	$(73{,}8\pm1{,}0)$ MeV
Φ_1	$(4{,}31\pm0{,}57)\cdot10^{11}$ cm^{-2}		d_{Li}: 4 mm	
Φ_2	$(2{,}67\pm0{,}35)\cdot10^{11}$ cm^{-2}			

Foil	Mass/g	d/mm	Ø/mm	Block	Foil	Mass/g	d/mm	Ø/mm	Block
cu1501	4,95682	2	19	cuo001	cu1511	4,96919	2	19	cuo006
ag1307	2,98545	1	19		fe2007	4,38174	2	19	feo001
ag1501	2,98764	1	19	ago001	fe2015	4,28840	2	19	
ag1503	2,99333	1	19		cu1513	5,01100	2	19	cuo007
cu1503	12,62021	5	19	cuo002	al1020	0,82905	1	19	alo001
co1307	2,67240	1	19		cu1515	4,98327	2	19	cuo008
co1501	2,66862	1	19	coo001	cc1501	0,46200	1	19	
co1503	2,67291	1	19		cc1503	0,46078	1	19	cco001
cu1505	4,96637	2	19	cuo003	cc1505	0,45585	1	19	
mg1501	0,97260	2	19	mgo001	cc1507	0,46105	1	19	
cu1507	4,96263	2	19	cuo004	cu1517	4,97734	2	19	cuo009
pb1501	3,09564	1	19	pbo001	qu1501	0,38473	1	15	
pb1503	3,10990	1	19		qu1503	0,38000	1	15	quo001
cu1509	4,96758	2	19	cuo005	qu1505	0,38507	1	15	
ni1307	2,54552	1	19		qu1507	0,39048	1	15	
ni1501	2,53472	1	19	nio001	cu1519	4,95765	2	19	cuo010
ni1503	2,56083	1	19		$\sum$ 33		50		19

Data of the Time−Logging
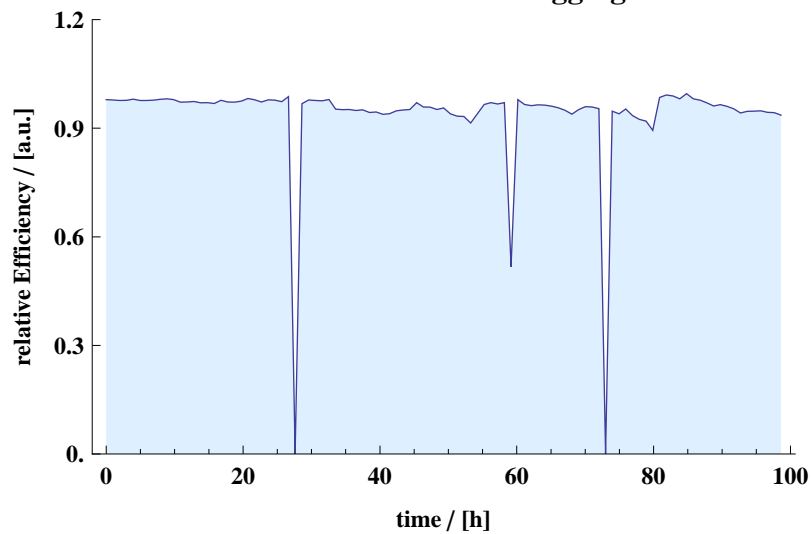
A.15   Uppn0p

BoI   09.05.2000, 18:57 E_p (178,8±0,8) MeV
EoI   14.05.2000, 06:00 E_n (175,4±2,0) MeV
Φ_1 $(5,20 \pm 0,46) \cdot 10^{10}$ cm^{-2} d_{Li}: 15 mm
Φ_2 $(3,72 \pm 0,33) \cdot 10^{10}$ cm^{-2}

Foil	Mass/g	d/mm	Ø/mm	Block	Foil	Mass/g	d/mm	Ø/mm	Block
Cu1601	4,99213	2	19	cup001	cu1611	4,96250	2	19	cup006
ag1601	2,98919	1	19		fe2012	4,28326	2	19	fep001
ag1603	2,97995	1	19	agp001	fe1603	4,58982	2	19	
ag1605	2,99619	1	19		cu1613	4,99869	2	19	cup007
cu1603	12,62400	5	19	cup002	al2020	1,55848	2	19	alp001
co1601	2,66724	1	19		cu1615	4,98924	2	19	cup008
co1603	2,65963	1	19	cop001	cc1601	0,45700	1	19	
co1605	2,67317	1	19		cc1603	0,45517	1	19	ccp001
cu1605	4,98430	2	19	cup003	cc1605	0,46018	1	19	
mg1601	0,97048	2	19	mgp001	cc1607	0,45344	1	19	
cu1607	5,00365	2	19	cup004	cu1617	4,99718	2	19	cup009
pb1601	3,11347	1	19	pbp001	qu1601	0,38660	1	15	
pb1603	3,11735	1	19		qu1603	0,38414	1	15	qup001
cu1609	4,98955	2	19	cup005	qu1605	0,38473	1	15	
ni1601	2,45387	1	19		qu1607	0,38270	1	15	
ni1603	2,44209	1	19	nip001	cu1619	4,99995	2	19	cup010
ni1605	2,56387	1	19		$\sum$ 33		50		19

Data of the Time−Logging
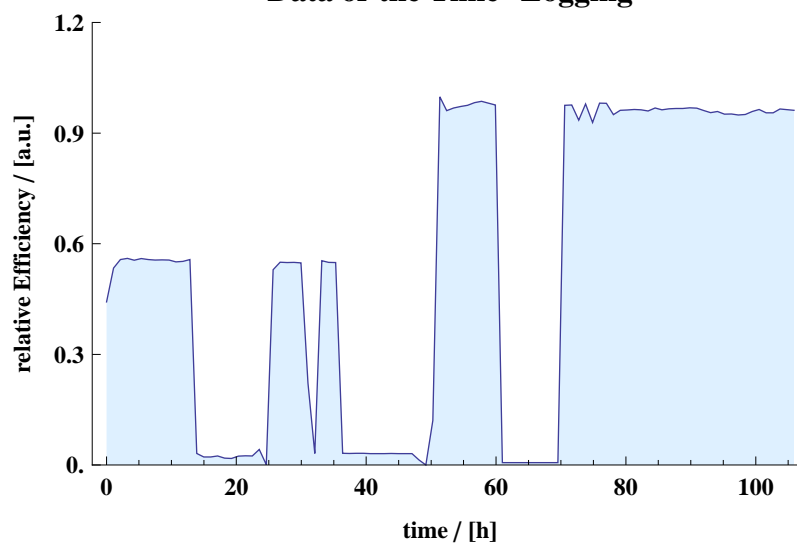
A.16 Uppn0q

BoI   03.10.2000, 11:52 E_p (148,4±0,6) MeV
EoI   07.10.2000, 14:00 E_n (144,8±2,1) MeV
Φ_1 $(1,06 \pm 0,08) \cdot 10^{11}$ cm^{-2} d_{Li}: 15 mm
Φ_2 $(7,38 \pm 0,54) \cdot 10^{10}$ cm^{-2}

Foil	Mass/g	d/mm	Ø/mm	Block	Foil	Mass/g	d/mm	Ø/mm	Block
cu1701	5,00417	2	19	cuq001	cu1711	4,96976	2	19	cuq006
ag1701	2,99506	1	19		ni1701	2,46404	1	19	
ag1703	2,99917	1	19	agq001	ni1703	2,43625	1	19	niq001
ag1705	2,98926	1	19		cu1713	4,99946	2	19	cuq007
cu1703	12,60810	5	19	cuq002	fe1701	4,59854	2	19	
co1701	2,55115	1	19		fe1703	4,58548	2	19	feq001
co1703	2,64404	1	19	coq001	cu1715	4,96463	2	19	cuq008
co1705	2,68670	1	19		al1701	1,53905	2	19	alq001
cu1705	4,99638	2	19	cuq003	cu1717	4,99181	2	19	cuq009
mg1701	0,97016	2	19	mgq001	cc1701	0,44539	1	19	
cu1707	5,01160	2	19	cuq004	cc1703	0,44994	1	19	ccq001
pb1701	3,11426	1	19		cc1705	0,44116	1	19	
pb1703	3,10713	1	19	pbq001	cu1719	5,00852	2	19	cuq010
cu1709	4,98551	2	19	cuq005	qu1701	0,38100	1	15	
uu1701	0,80330	0,15	19		qu1703	0,38753	1	15	quq001
uu1703	0,80632	0,15	19		qu1705	0,37892	1	15	
uu1705	0,80096	0,15	19		cu1721	4,97640	2	19	cuq011
uu1707	0,81608	0,15	19	uuq001	$\sum$ 33		50,12		21
uu1709	0,79746	0,15	19						
uu1711	0,81475	0,15	19						
uu1713	0,81017	0,15	19						

Data of the Time−Logging

151
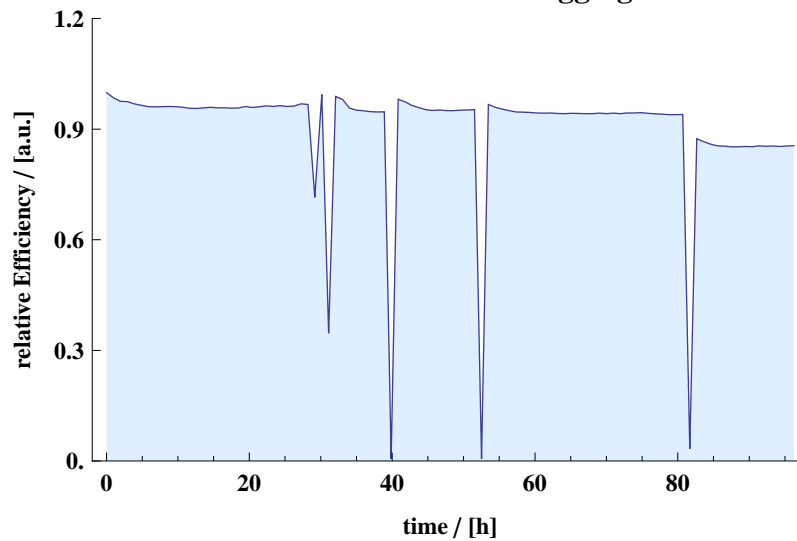
A.17   Uppn0r

BoI	28.02.2001, 23:03	E_p	(68,1±0,2) MeV
EoI	03.03.2001, 14:00	E_n	(65,4±1,1) MeV
Φ_1	$(2{,}82 \pm 0{,}27) \cdot 10^{11}$ cm^{-2}	d_{Li}:	4 mm
Φ_2	$(1{,}65 \pm 0{,}16) \cdot 10^{11}$ cm^{-2}		

Foil	Mass/g	d/mm	Ø/mm	Block
cu1801	4,98642	2	19	cur001
uu1801	0,81149	0,15	19	
uu1803	0,80739	0,15	19	
uu1805	0,81635	0,15	19	
uu1807	0,80437	0,15	19	uur001
uu1809	0,80584	0,15	19	
uu1811	0,80515	0,15	19	
uu1813	0,79075	0,15	19	
cu1803	5,53766	2	20	cur002
$\sum$ 9		5,05		3

Data of the Time−Logging
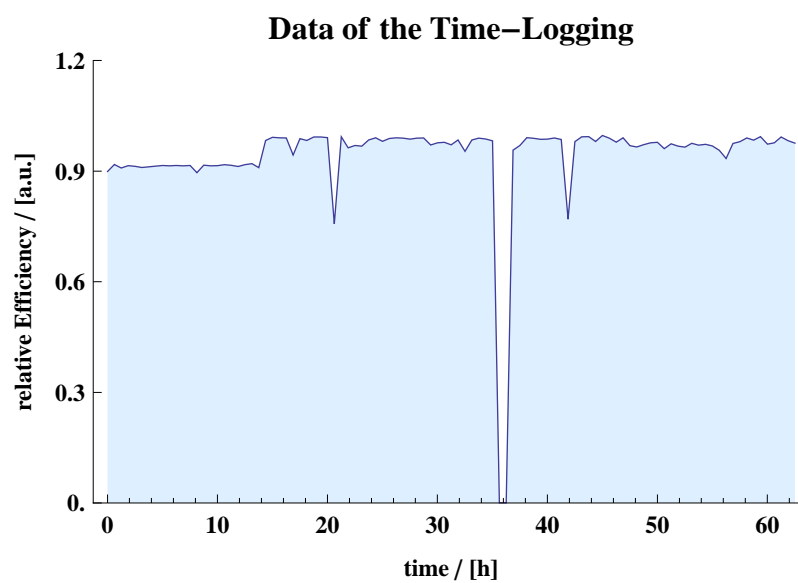
A.18   Uppn0s

BoI   06.06.2001, 09:51 E_p (137,4±1,0) MeV
EoI   10.06.2001, 10:54 E_n (133,7±2,4) MeV
Φ_1 $(1,15 \pm 0,094) \cdot 10^{11}$ cm^{-2} d_{Li}: 15 mm
Φ_2 $(8,04 \pm 0,66) \cdot 10^{10}$ cm^{-2}

Foil	Mass/g	d/mm	Ø/mm	Block
cu1901	5,52731	2	20	cus001
uu1901	0,80354	0,15	19	
uu1903	0,80301	0,15	19	
uu1905	0,81100	0,15	19	uus001
uu1907	0,79181	0,15	19	
uu1909	0,80260	0,15	19	
uu1911	0,80924	0,15	19	
cu1903	5,53827	2	20	cus002
$\sum$ 8		4,90		3

Data of the Time−Logging
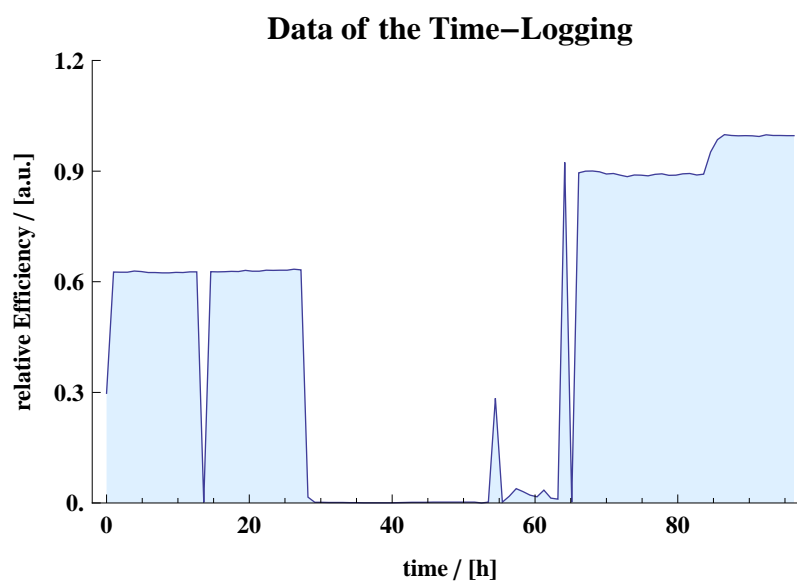
A.19 Uppn0t

BoI	25.09.2001, 21:00		E_p	(177,3±1,0) MeV
EoI	29.09.2001, 14:00		E_n	(173,9±2,1) MeV
Φ_1	$(5,42 \pm 0,48) \cdot 10^{10}$ cm^{-2}		d_{Li}: 15 mm	
Φ_2	$(3,77 \pm 0,53) \cdot 10^{10}$ cm^{-2}			

Foil	Mass/g	d/mm	Ø/mm	Block
cu2001	5,00810	2	19	cut001
uu2001	0,85356	0,15	19	uut001
uu2003	0,86843	0,15	19	
uu2005	0,82725	0,15	19	
uu2007	0,81163	0,15	19	
uu2009	0,83084	0,15	19	
uu2011	0,80495	0,15	19	
uu2013	0,87896	0,15	19	
cu2003	4,98126	2	19	cut002
$\sum$ 9		5,05		3

Data of the Time−Logging
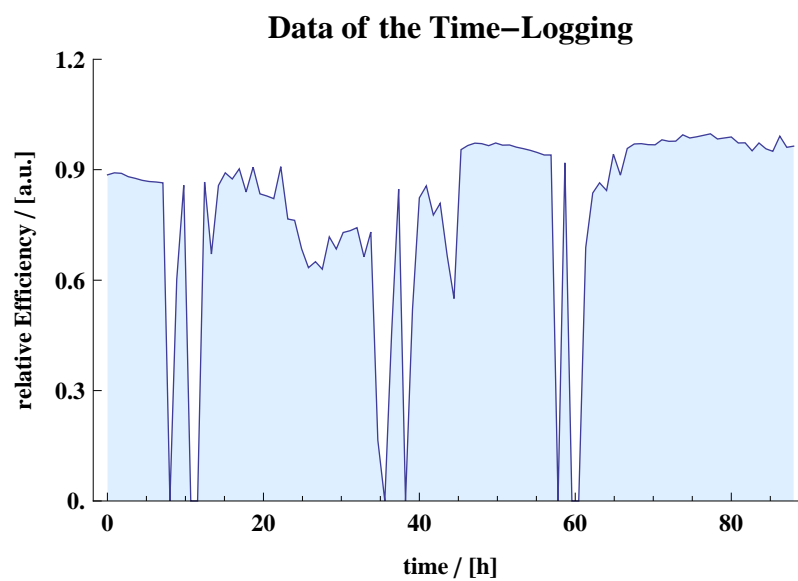
A.20   Uppn0u

BoI   04.02.2002, 23:04 E_p (98,1±0,3) MeV
EoI   10.02.2002, 14:03 E_n (95,7±0,9) MeV
Φ_1 $(6{,}54 \pm 0{,}46) \cdot 10^{11}$ cm^{-2} d_{Li}: 4 mm
Φ_2 $(4{,}08 \pm 0{,}28) \cdot 10^{11}$ cm^{-2}

Foil	Mass/g	d/mm	Ø/mm	Block
u1	4,99075	2	19	cuu001
c1	0,84974	0,15	19	
c2	0,87263	0,15	19	
c3	0,86670	0,15	19	
c4	0,87058	0,15	19	uuu001
c5	0,80946	0,15	19	
c6	0,81584	0,15	19	
c7	0,81829	0,15	19	
u2	5,00268	2	19	cuu002
$\sum$ 9		5,05		3

Data of the Time–Logging
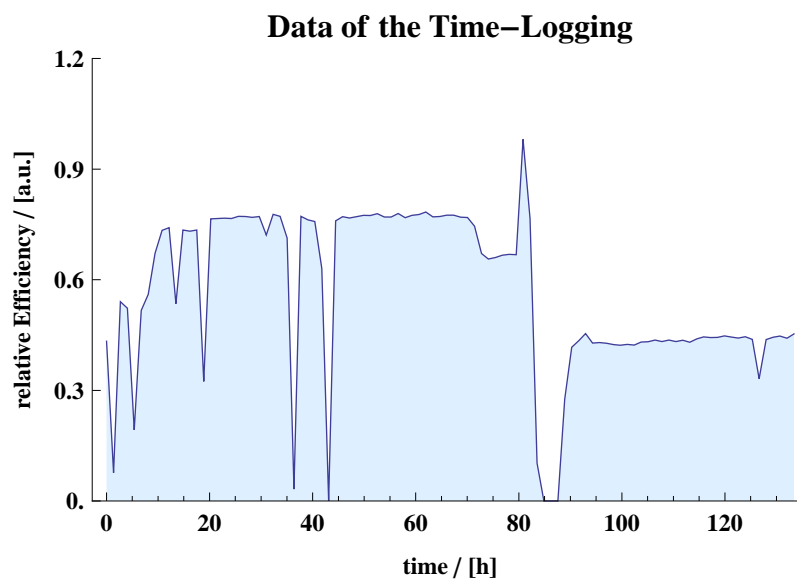
A.21 Uppn0v

BoI	21.09.2002, 05:35		E_p	(92,08±0,3) MeV
EoI	23.09.2002, 08:00		E_n	(89,6±0,9) MeV
Φ_1	$(1,69 \pm 0,14) \cdot 10^{11}$ cm^{-2}		d_{Li}: 4 mm	
Φ_2	$(9,96 \pm 0,81) \cdot 10^{10}$ cm^{-2}			

Foil	Mass/g	d/mm	Ø/mm	Block
cuu3	4,97589	2	19	cuv001
uuv1	0,86124	0,15	19	
uuv2	0,89370	0,15	19	
uuv3	0,81316	0,15	19	
uuv4	0,88173	0,15	19	uuv001
uuv5	0,88525	0,15	19	
uuv6	0,80580	0,15	19	
uut8	0,87912	0,15	19	
cuu4	4,95700	2	19	cuv002
$\sum$ 9		5,05		3

Data of the Time−Logging

156
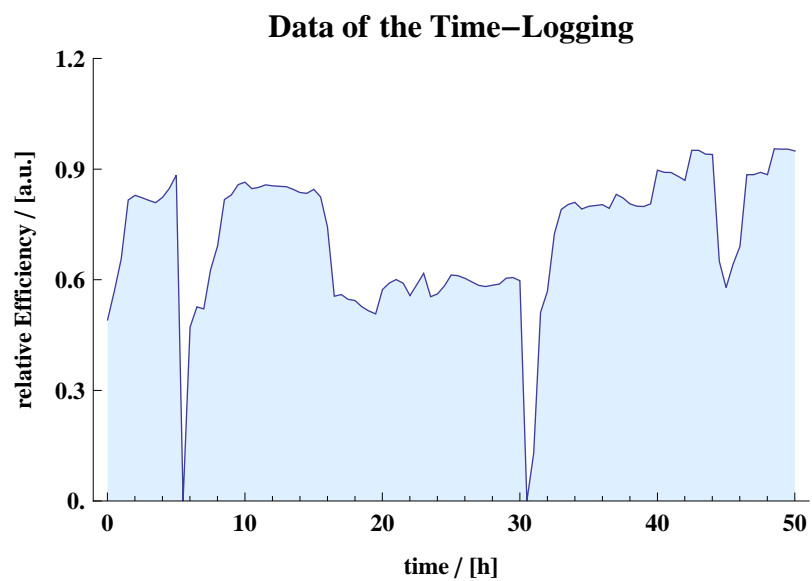
B Excitation Functions

The following chapter contains figures of all excitation functions that were unfolded in the connection with the present work. Due to its extend, a detailed table of the underlying data is not present, but can be found on the webpage of the IRS (http://www.zsr.uni-hannover.de/wirkung.htm). The images are arranged corresponding to an increasing target mass. All figures contain the unfolded guess function (black), the Talys "guess" function (blue) and colored dots which indicate the positions of the high-energy peaks of the underlying neutron spectra. The colors of this dots correspond to the legend shown in figure B.1. The used abbreviation follow the following pattern: **UE 96 MeV** correspond to the irradiation experiment **u**ppn0**e** with high-energy neutron peak at **96 MeV**

L4	L5	L6	L7	UE	UK	UL	UM	UN	UO	UP	UQ	UR	US	UT	UU	UV
60	45	60	33	96	66	94	133	95	74	175	145	65	134	174	96	90
MeV	MeV	MeV	MeV	MeV	MeV	MeV	MeV	MeV	MeV	MeV	MeV	MeV	MeV	MeV	MeV	MeV

Figure B.1: Legend of the following figures.
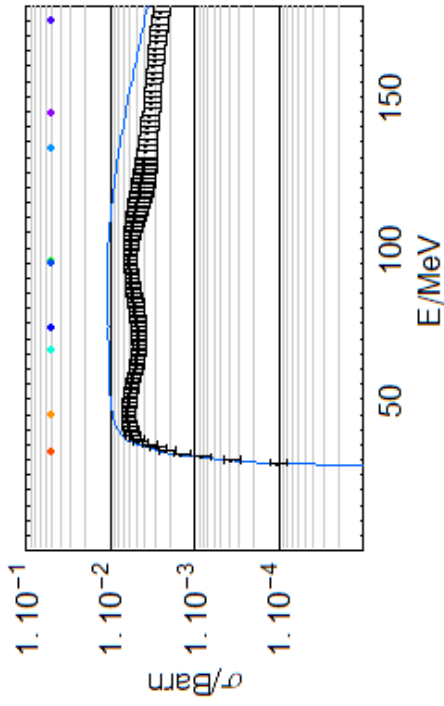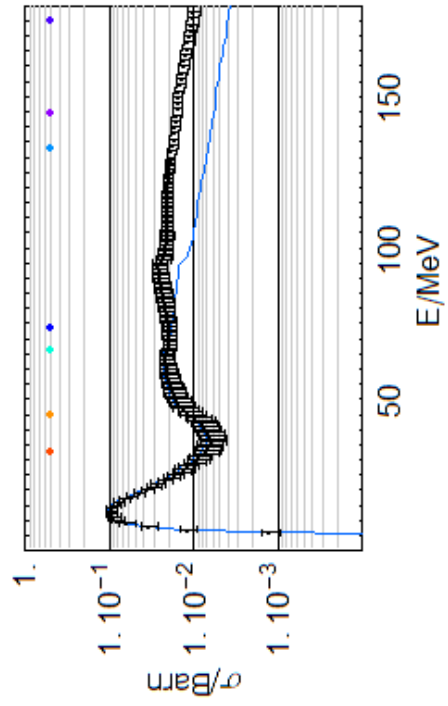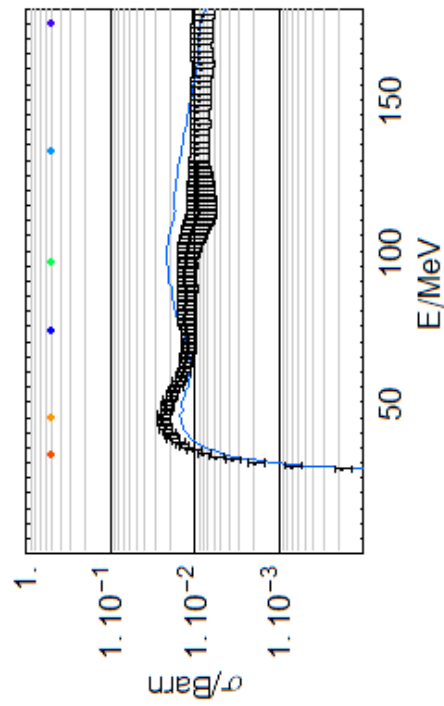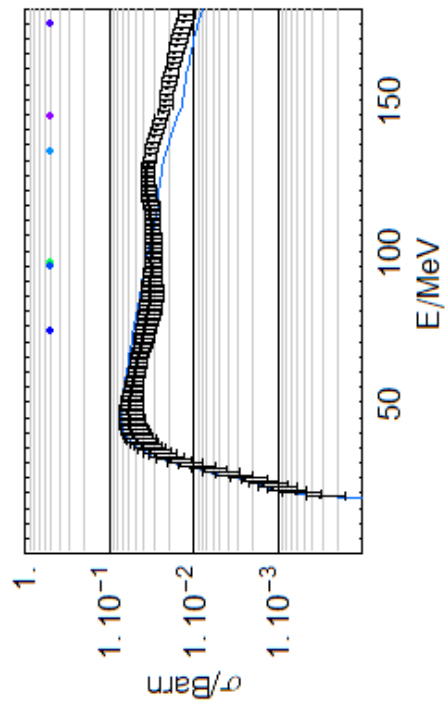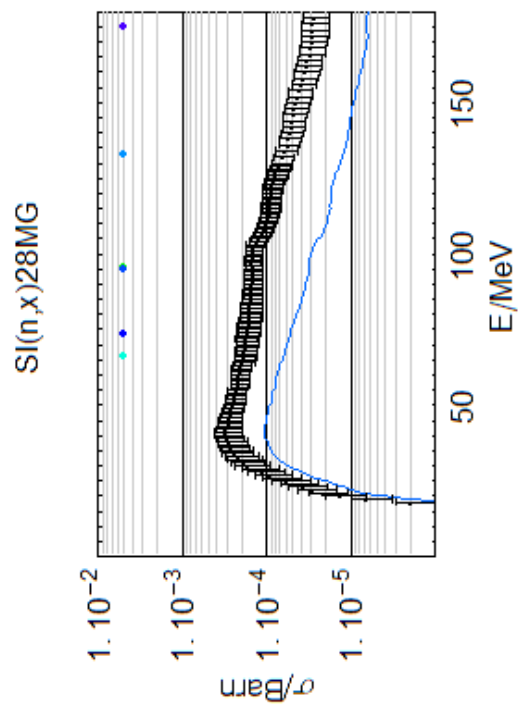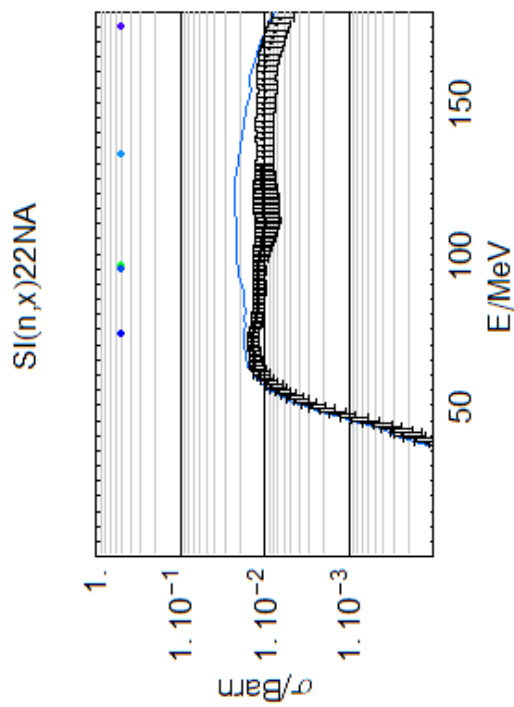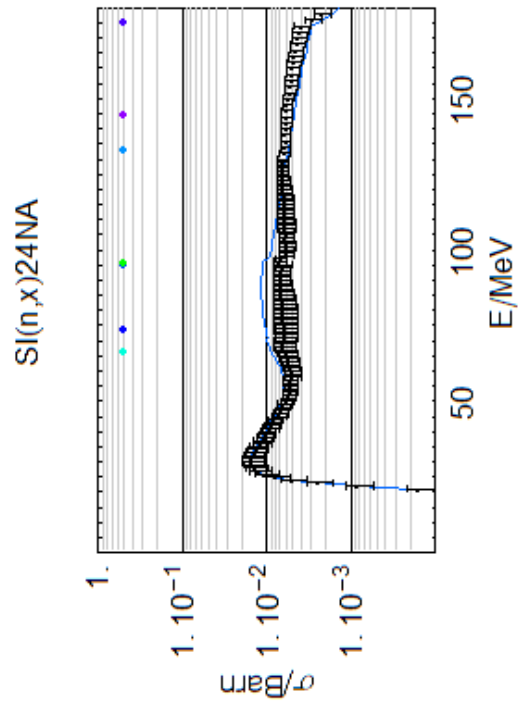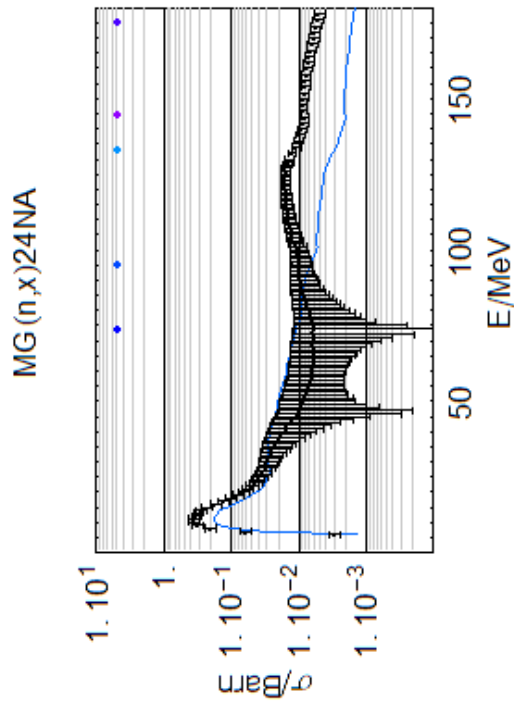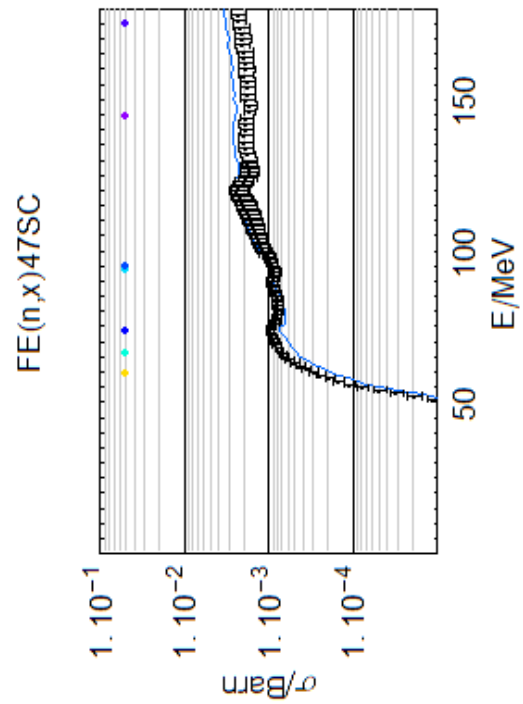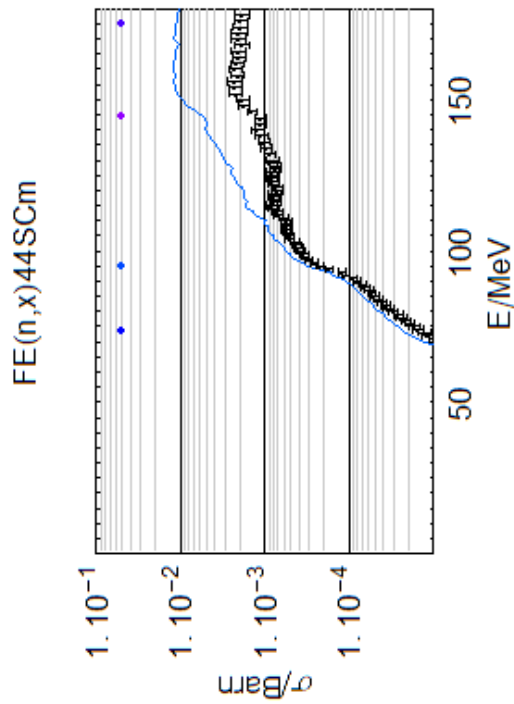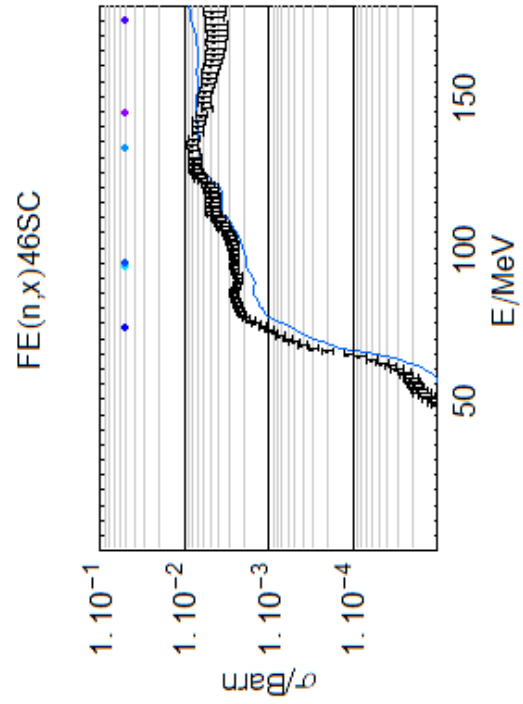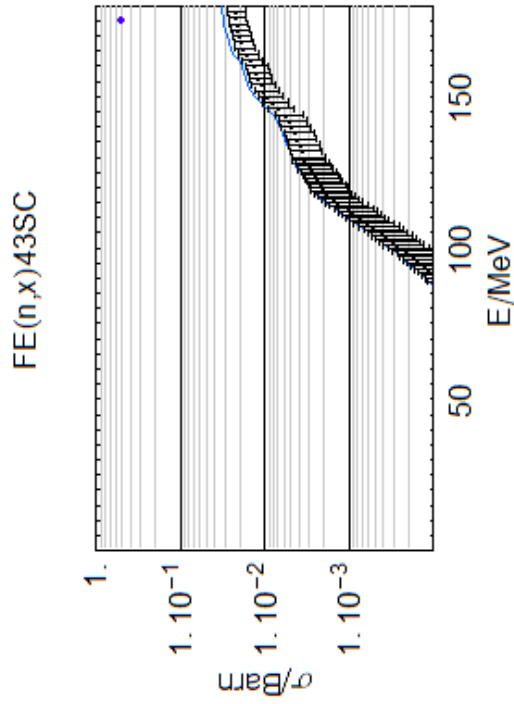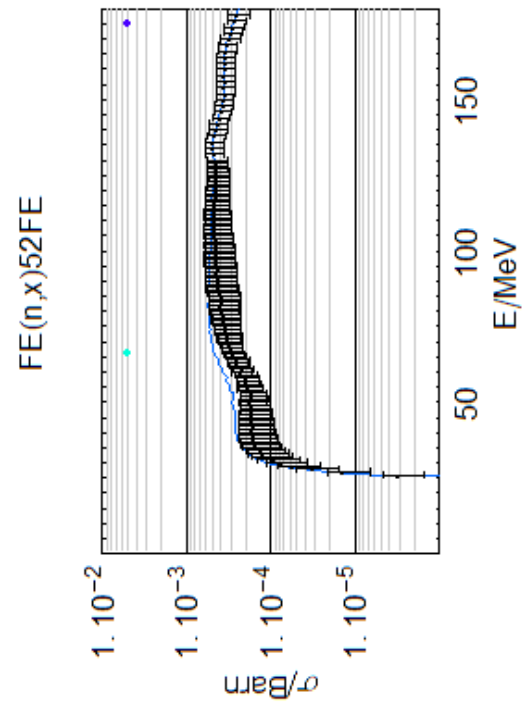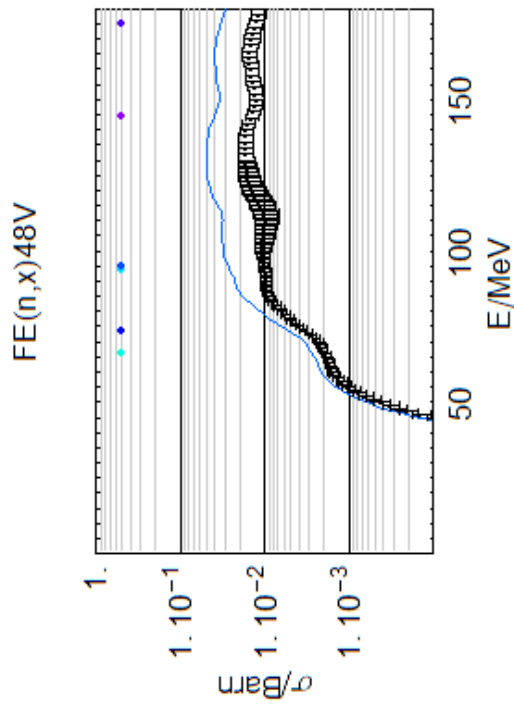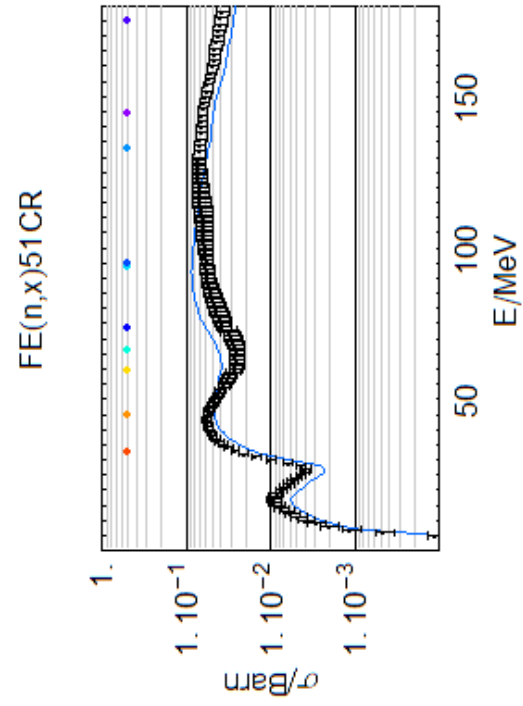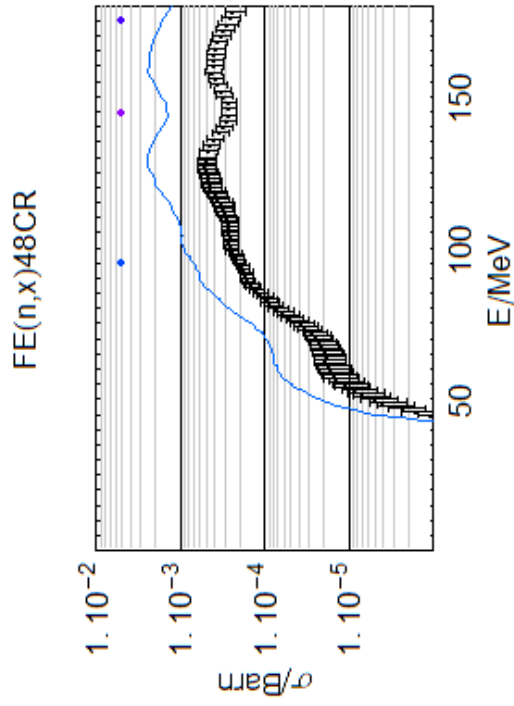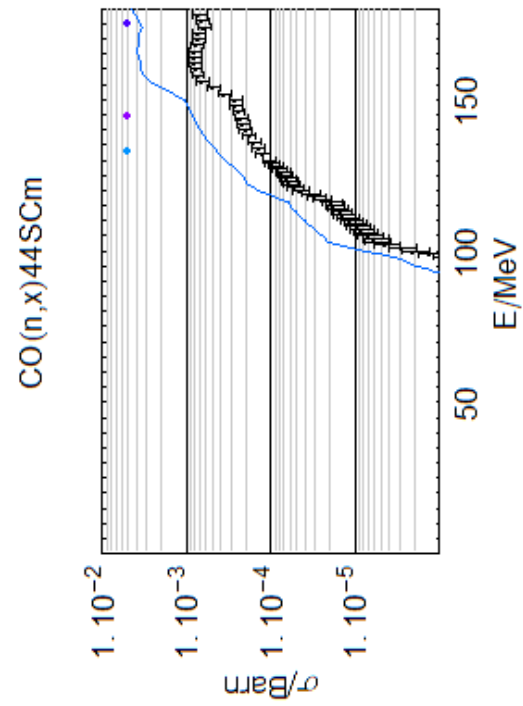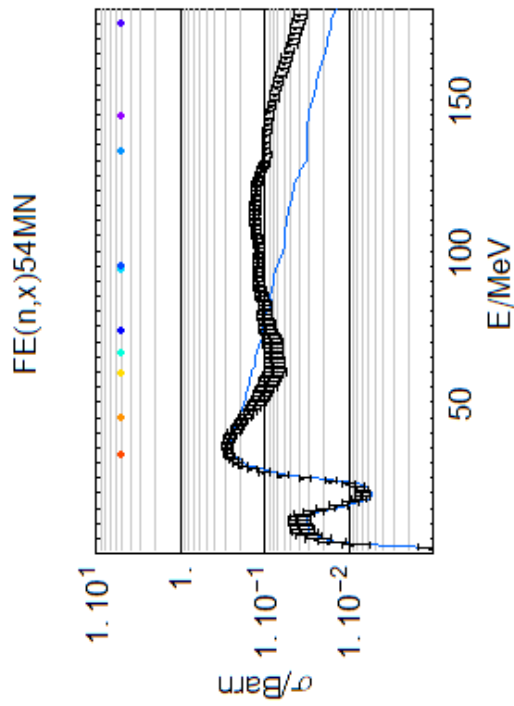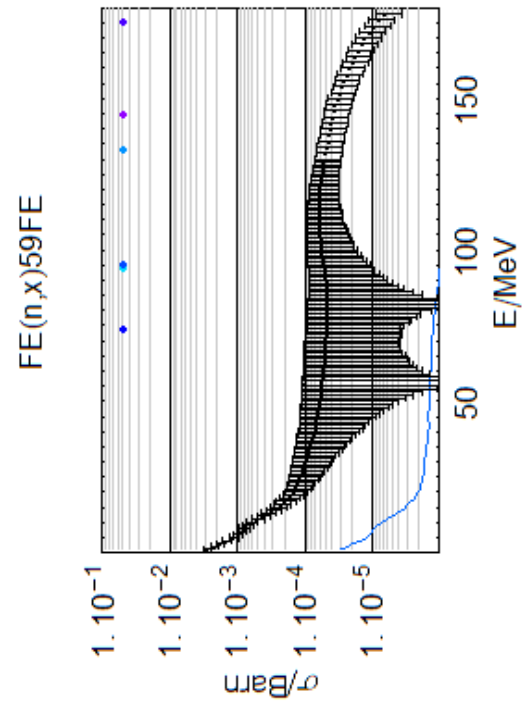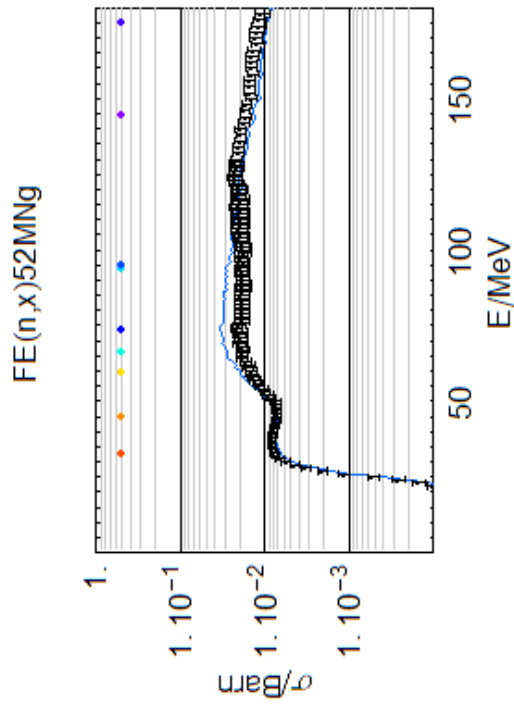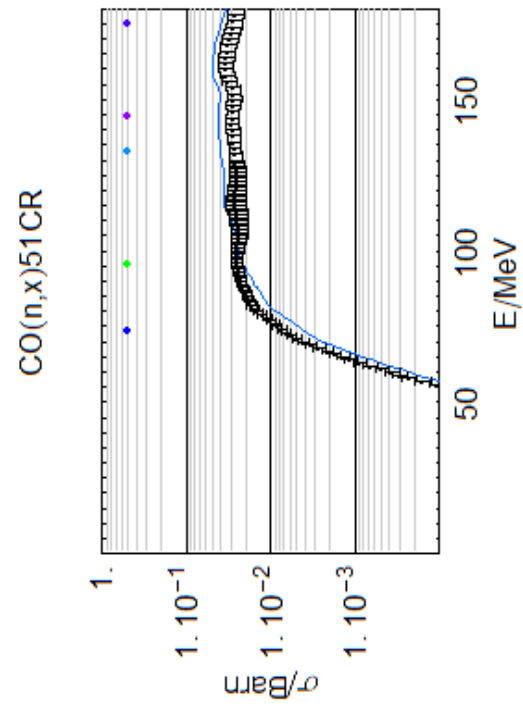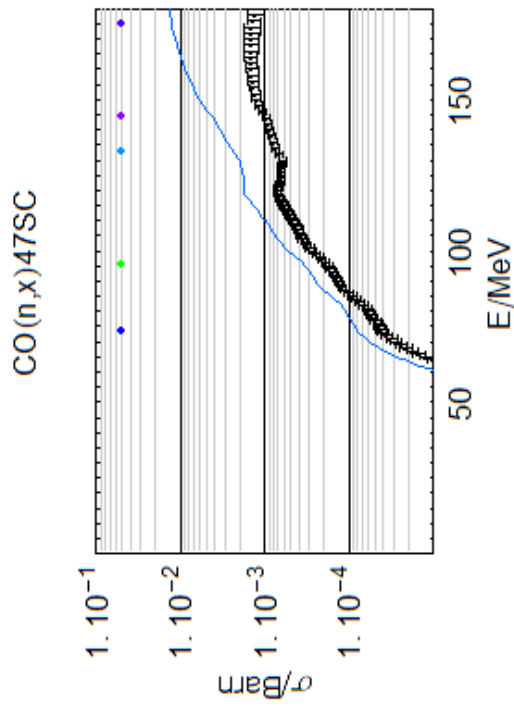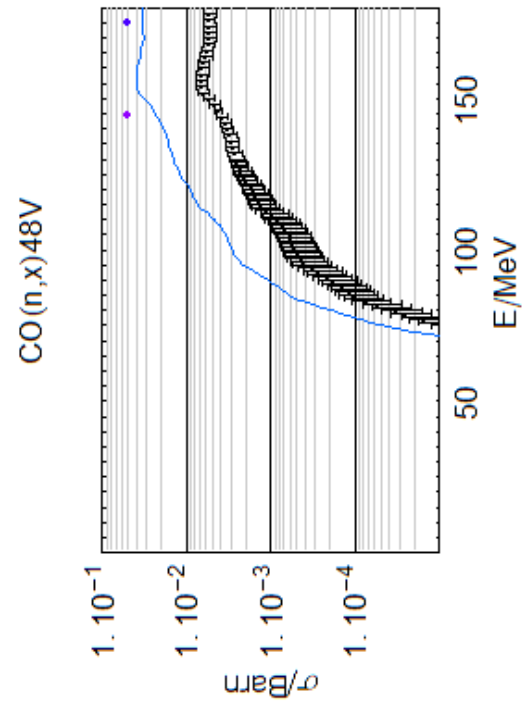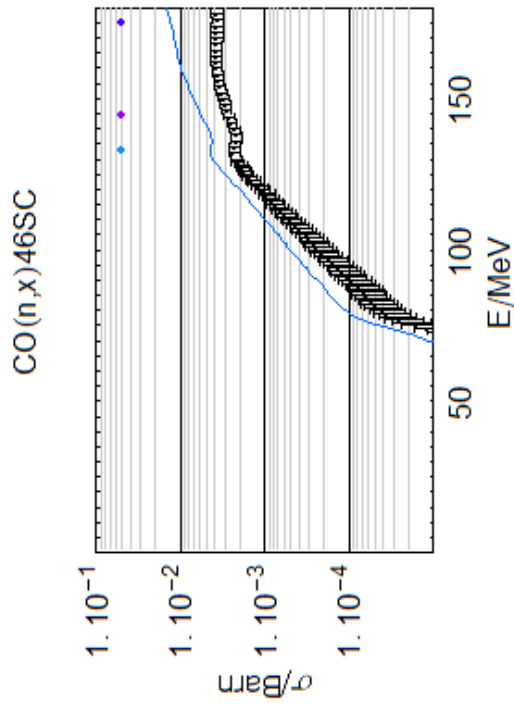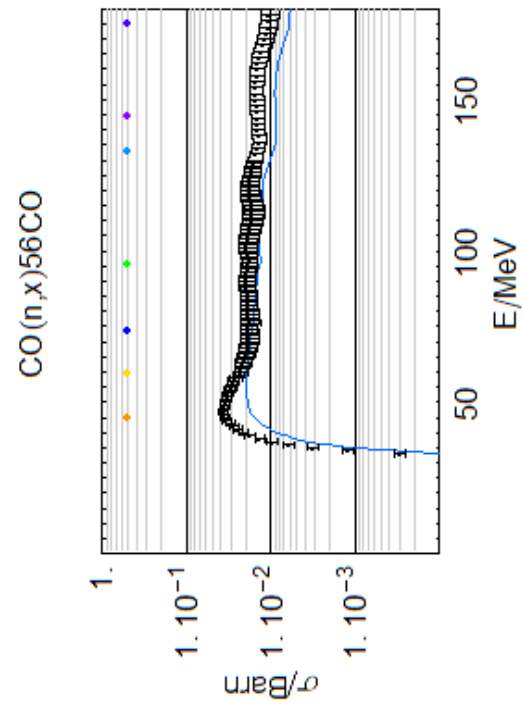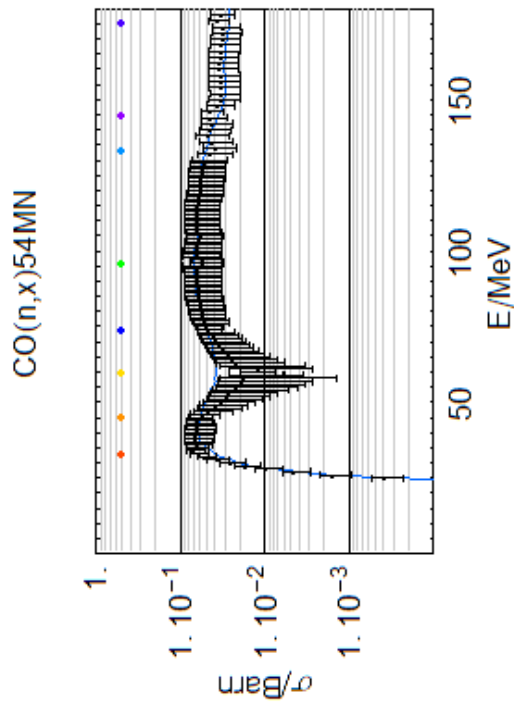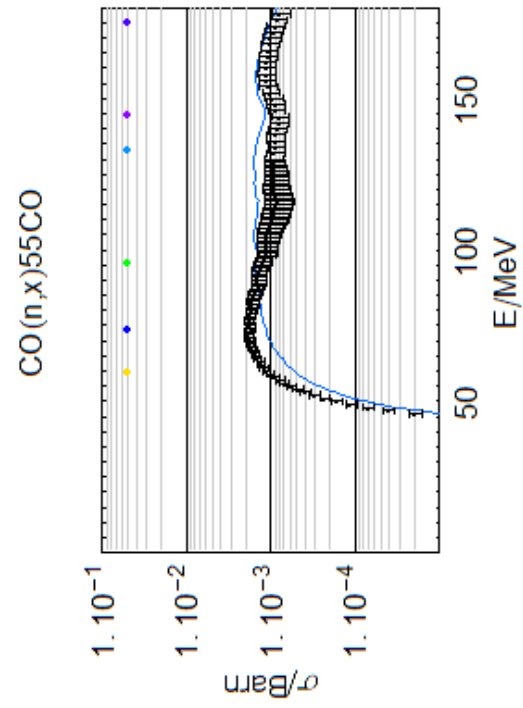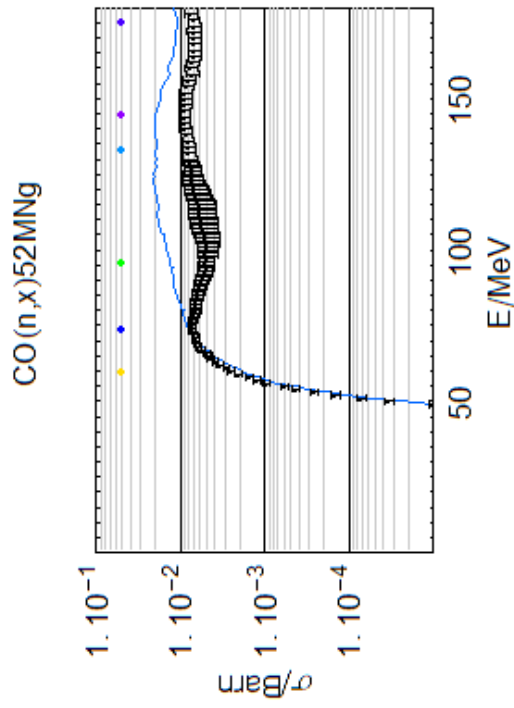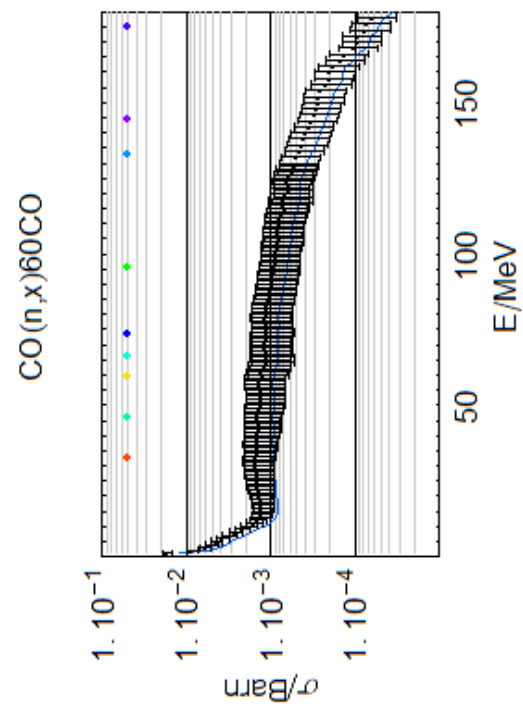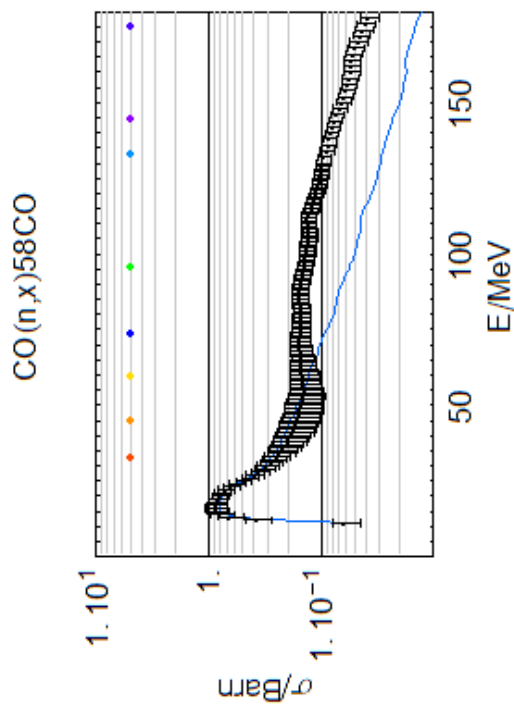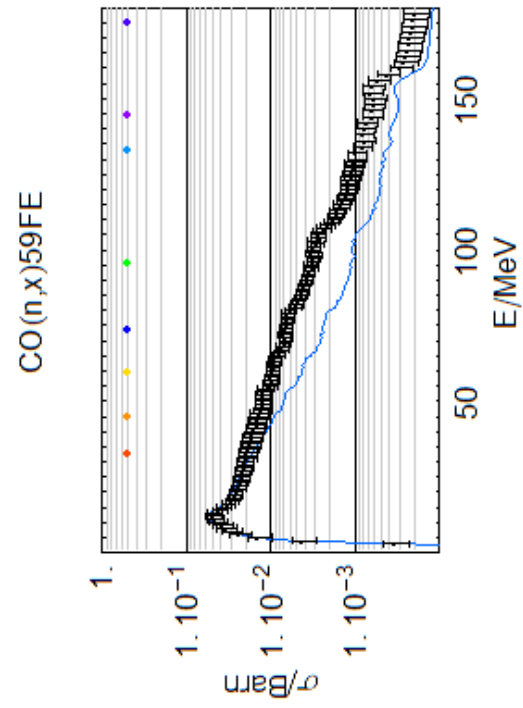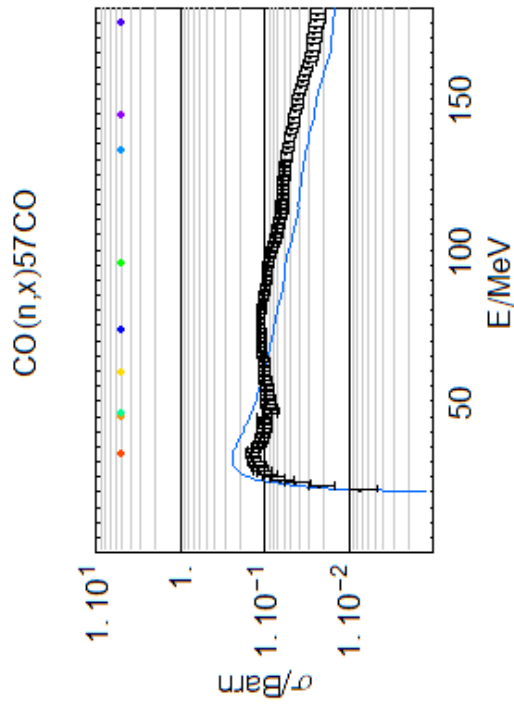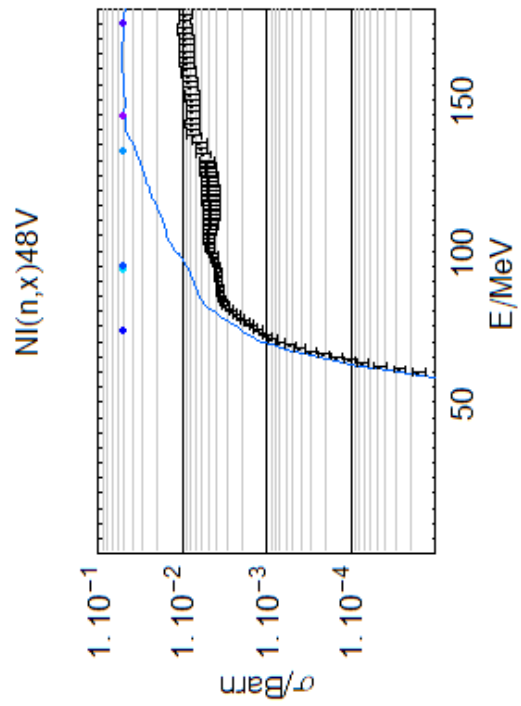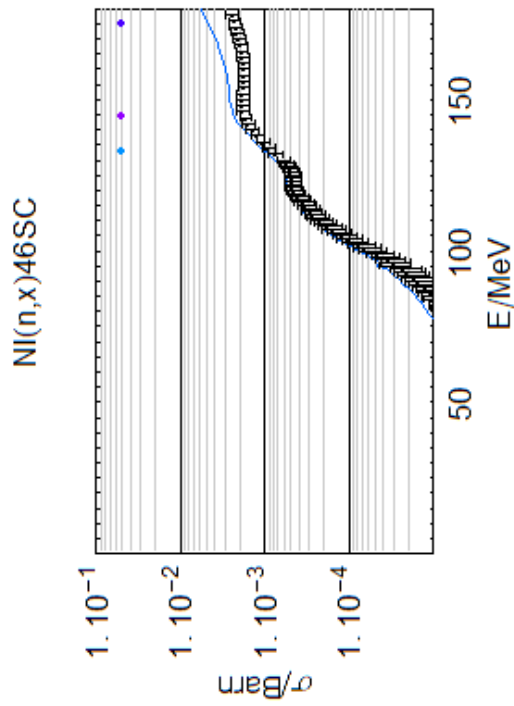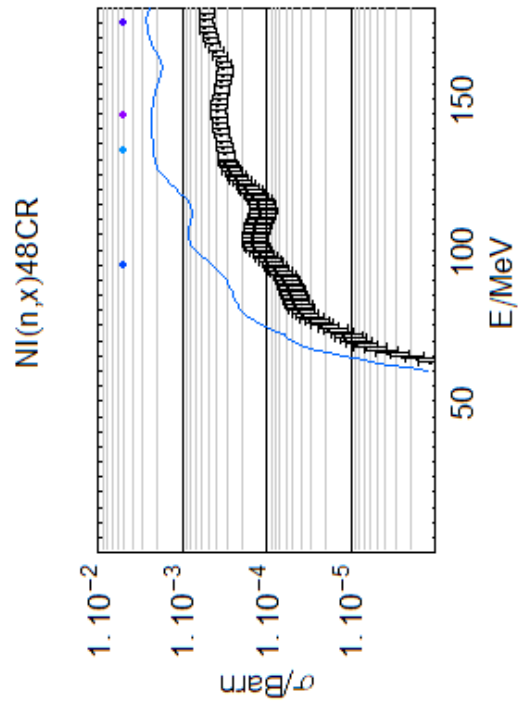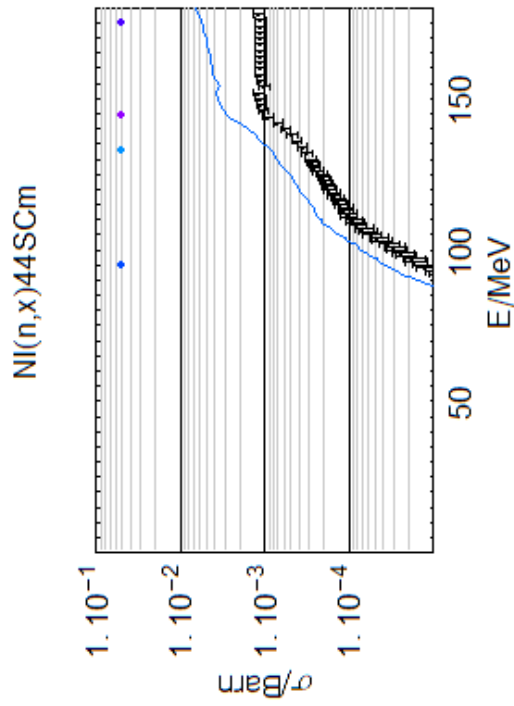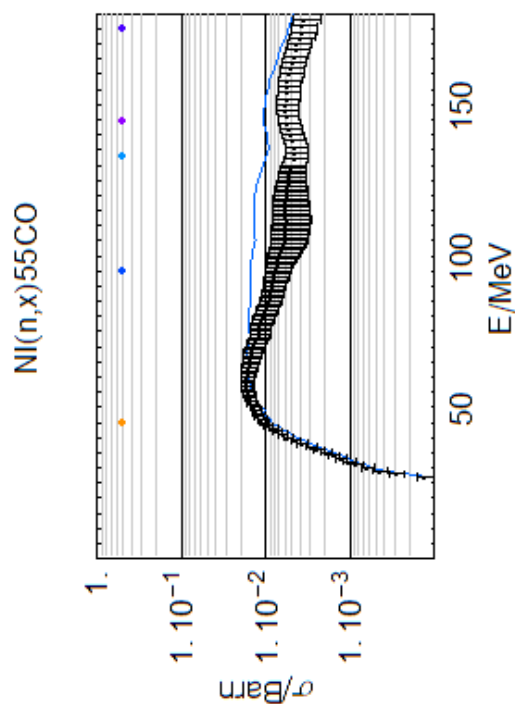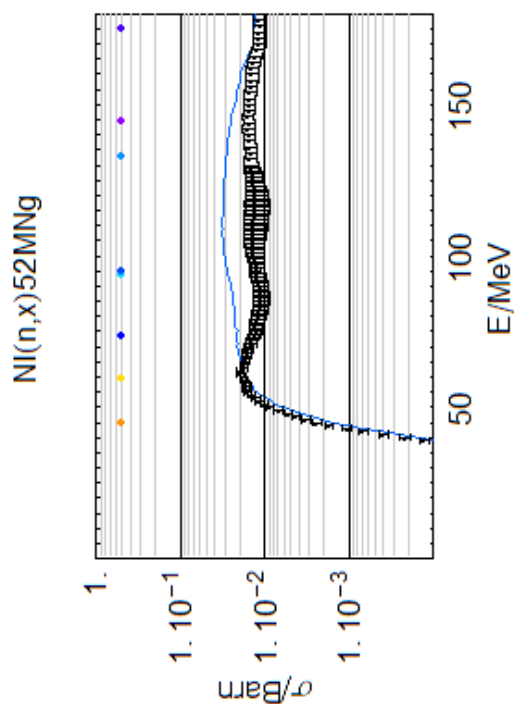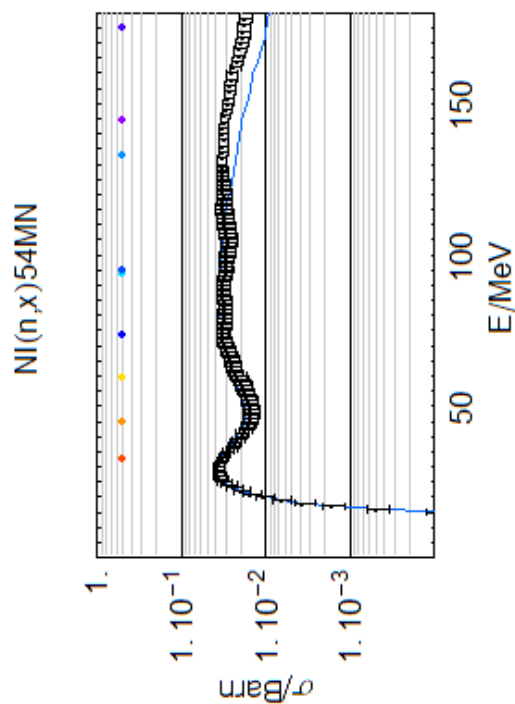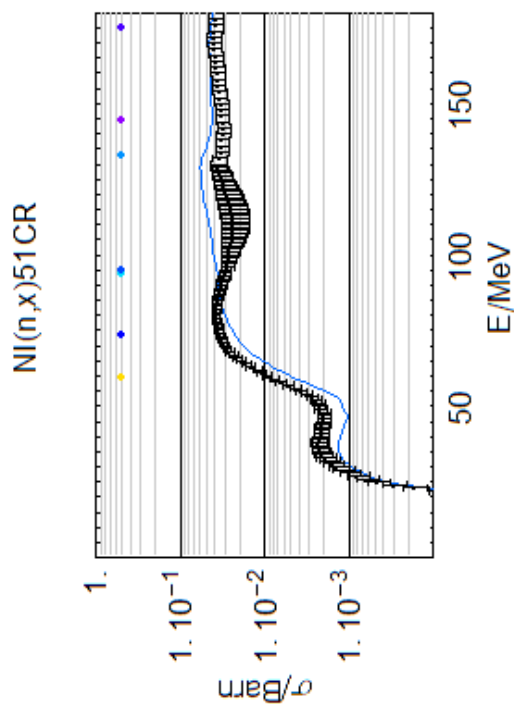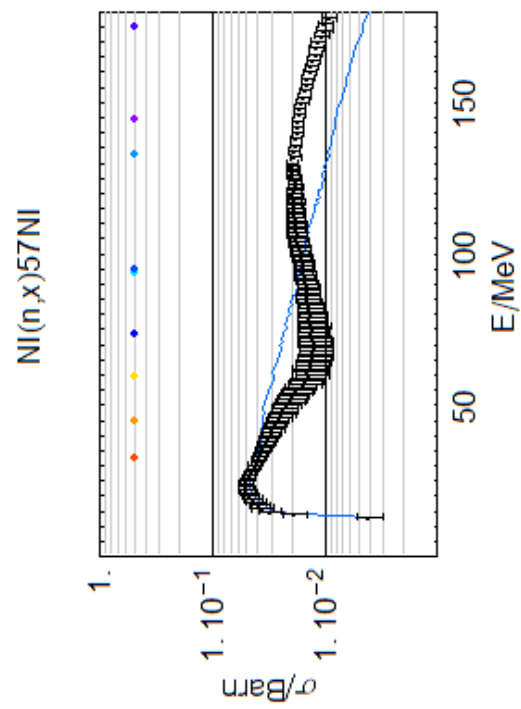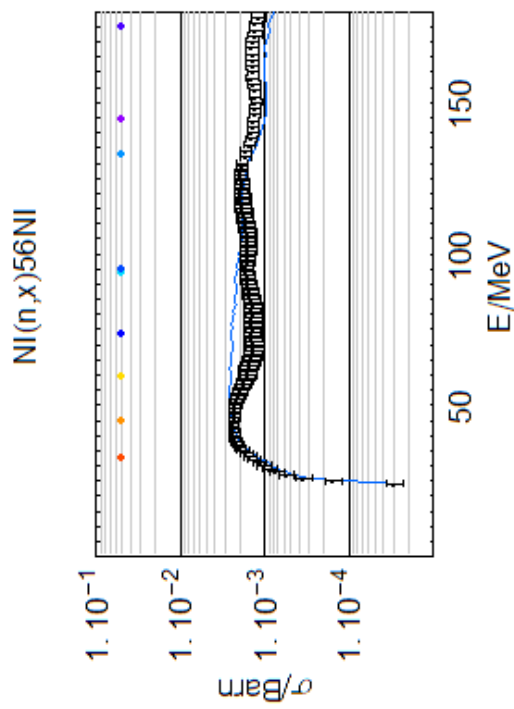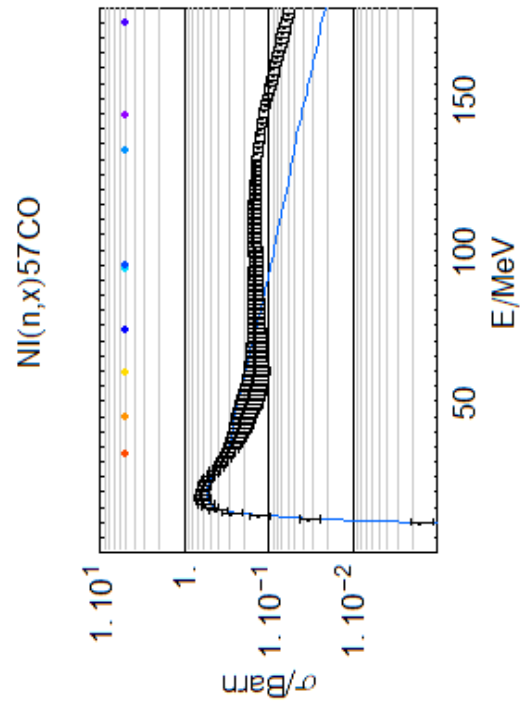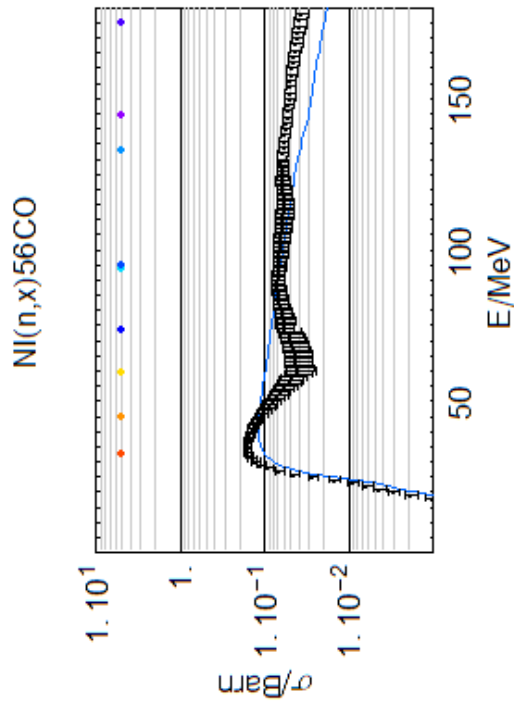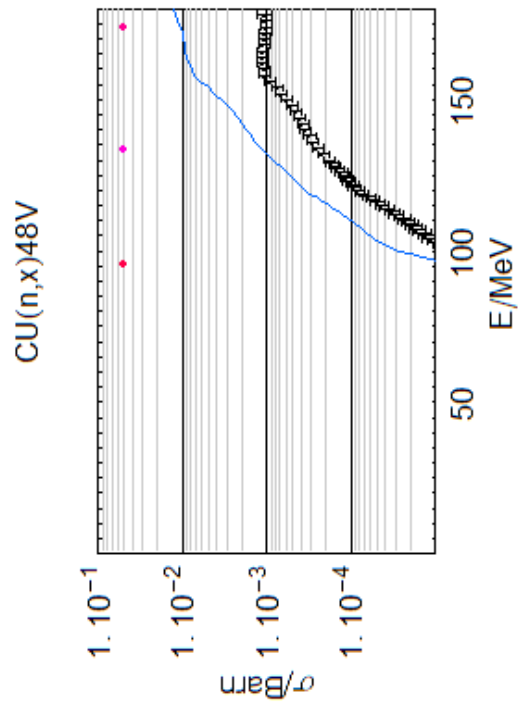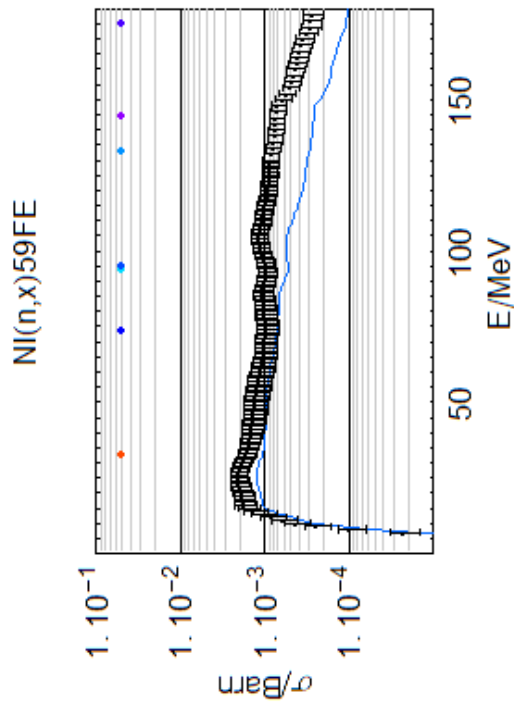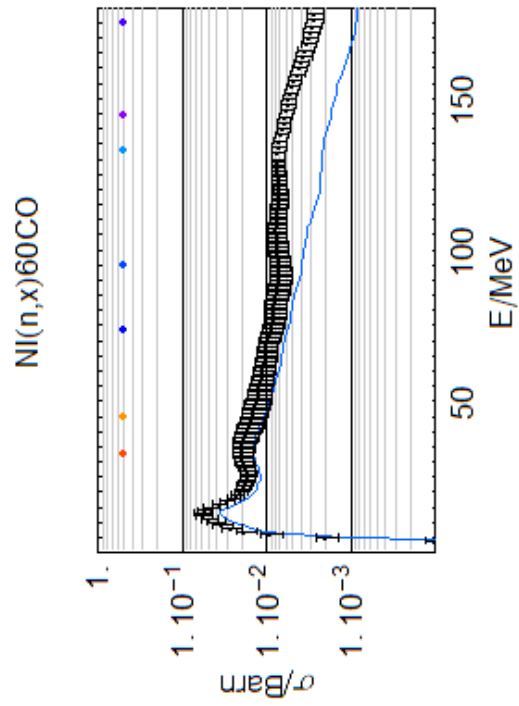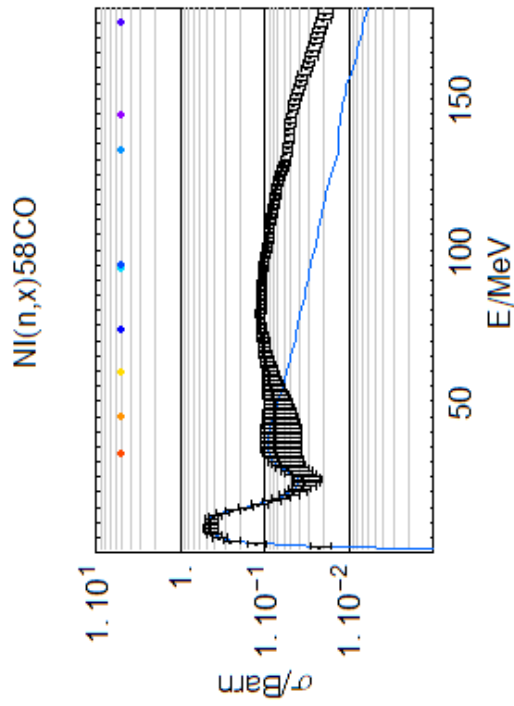
FE(n,x)43SC

FE(n,x)46SC

FE(n,x)44SCm

FE(n,x)47SC

FE(n,x)48V

FE(n,x)48CR

FE(n,x)51CR

FE(n,x)52FE

CO(n,x)58CO

CO(n,x)57CO

CO(n,x)60CO

CO(n,x)59FE

NI(n,x)51CR

NI(n,x)54MN

NI(n,x)52MNg

NI(n,x)55CO

CU(n,x)51CR

CU(n,x)52MNg

CU(n,x)54MN

CU(n,x)55CO

CU(n,x)56CO

CU(n,x)57CO

CU(n,x)57NI

CU(n,x)58CO

171
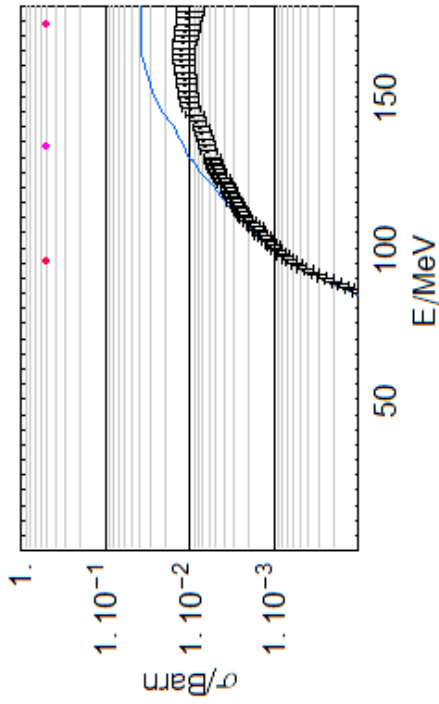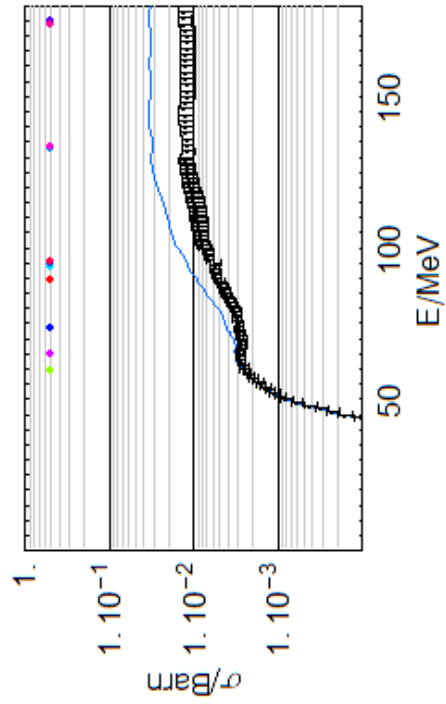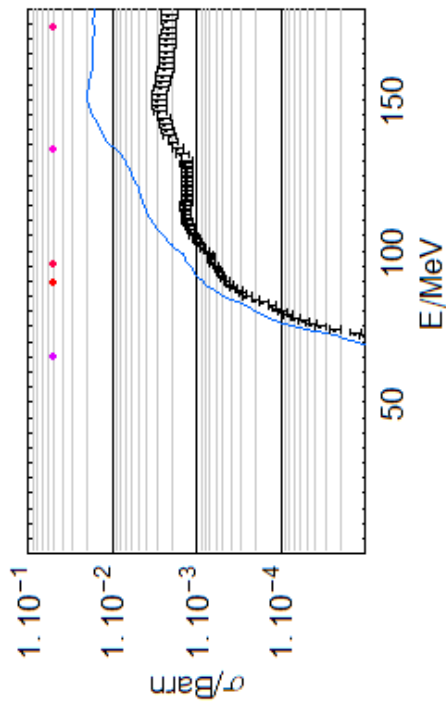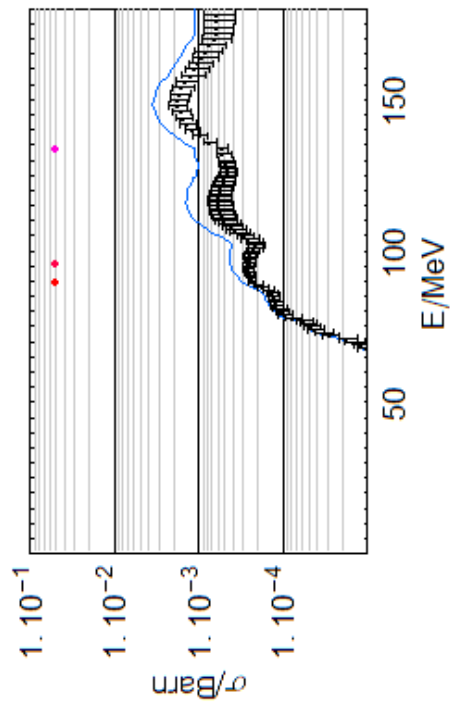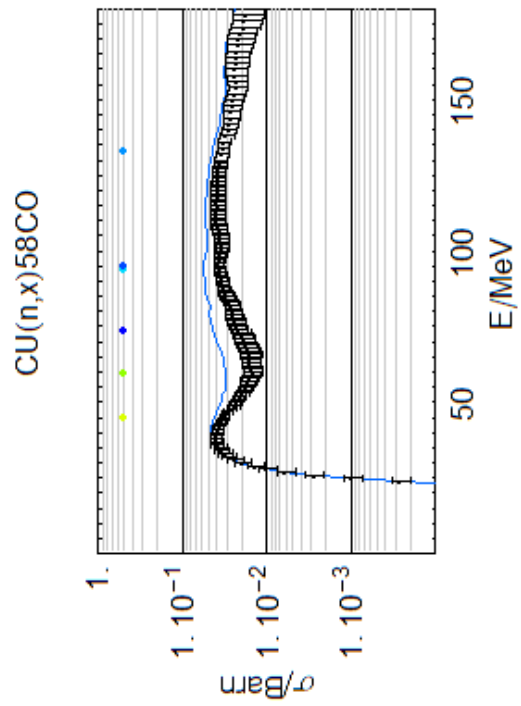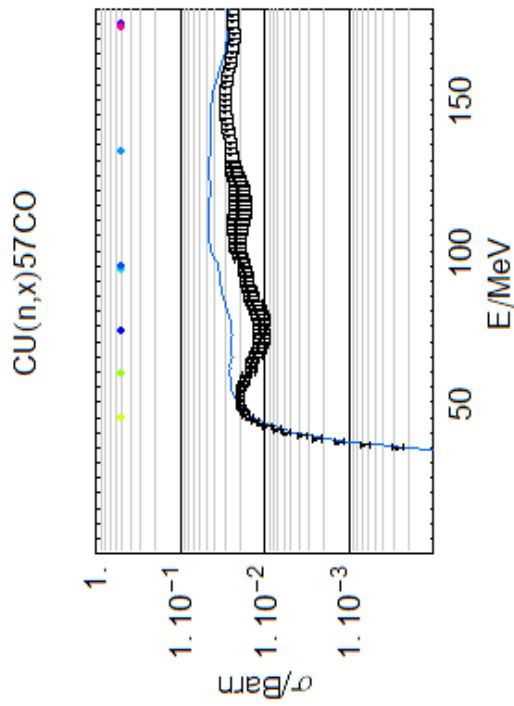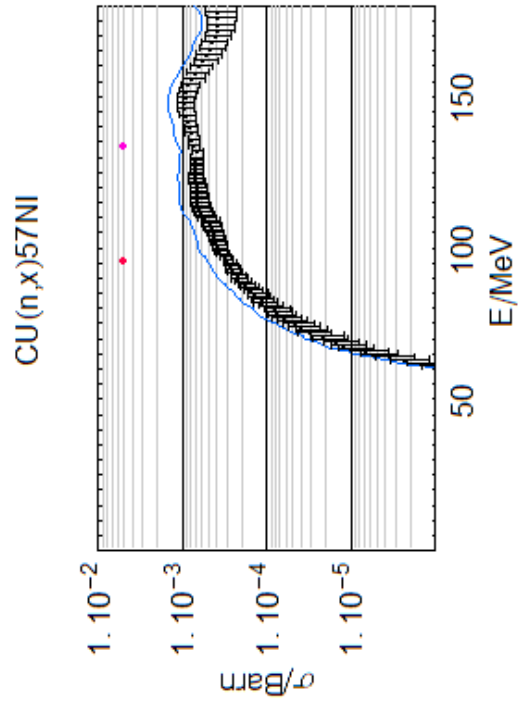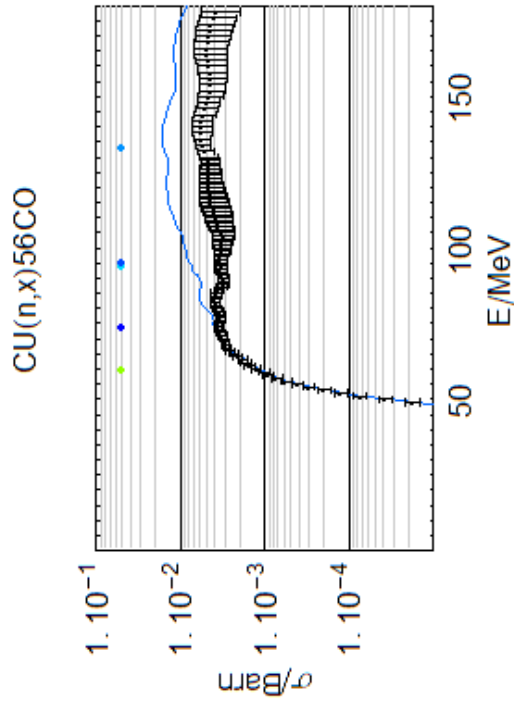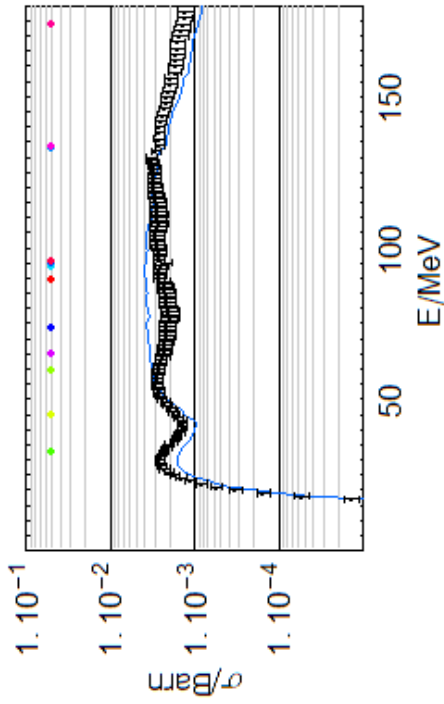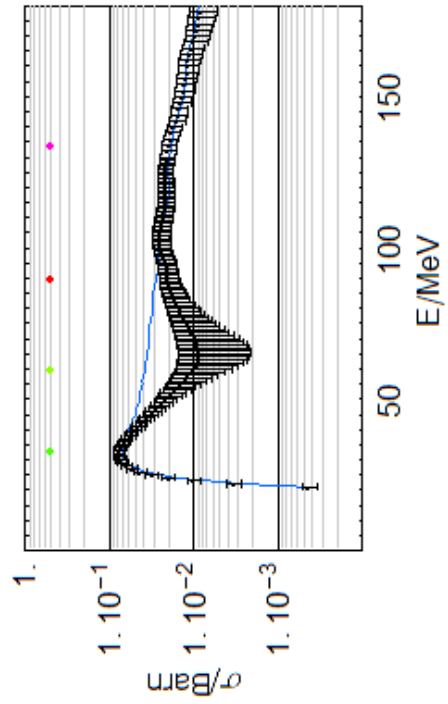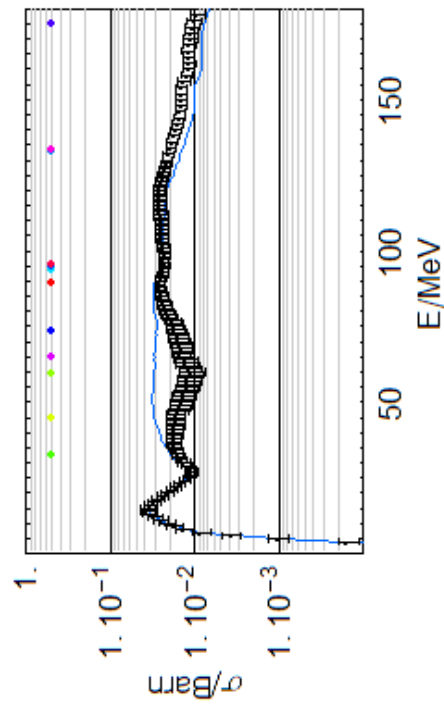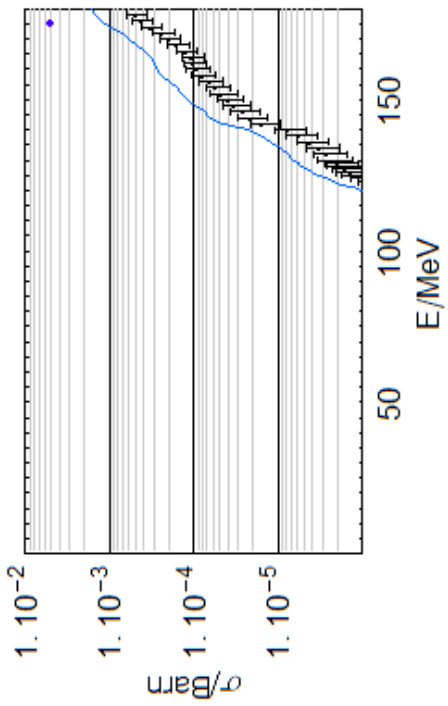
AG(n,x)93MOm
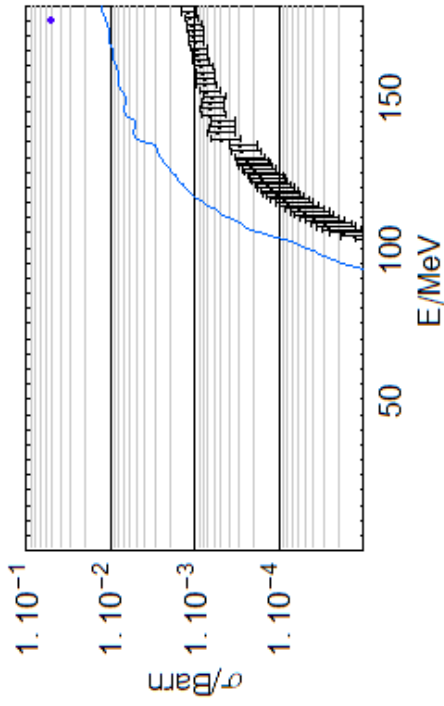
AG(n,x)96TC
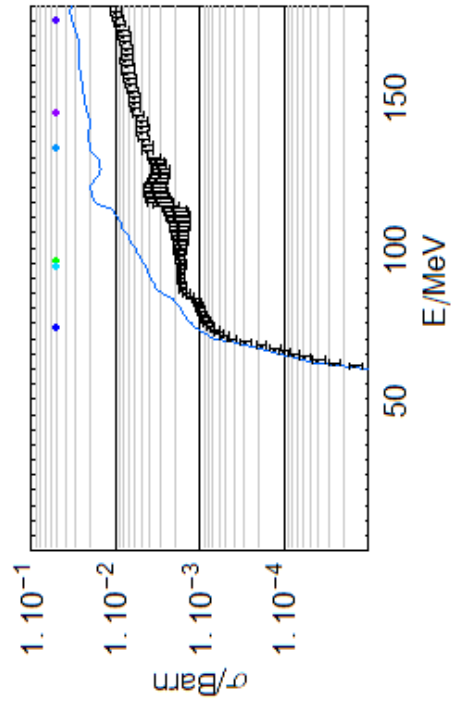
AG(n,x)95TCg
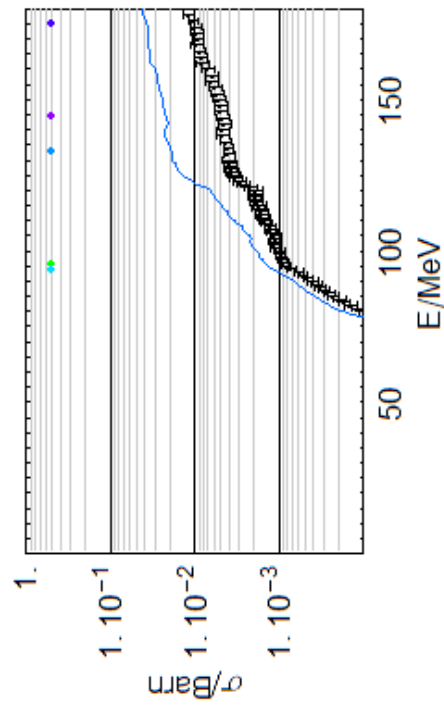
AG(n,x)97RU

AG(n,x)99RHg

AG(n,x)99RHm

AG(n,x)100PD

AG(n,x)101PD

174

AG(n,x)110AGm

E/MeV

σ/Barn

TE(n,x)120SBm (tot)

E/MeV

σ/Barn

TE(n,x)119TEm

E/MeV

σ/Barn

TE(n,x)121TEm

E/MeV

σ/Barn
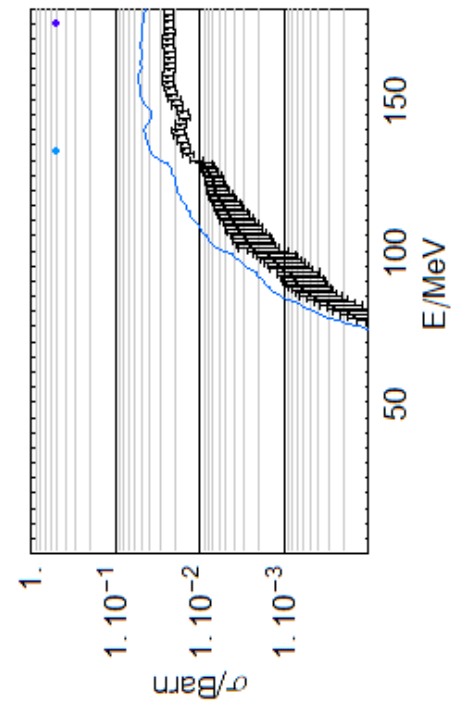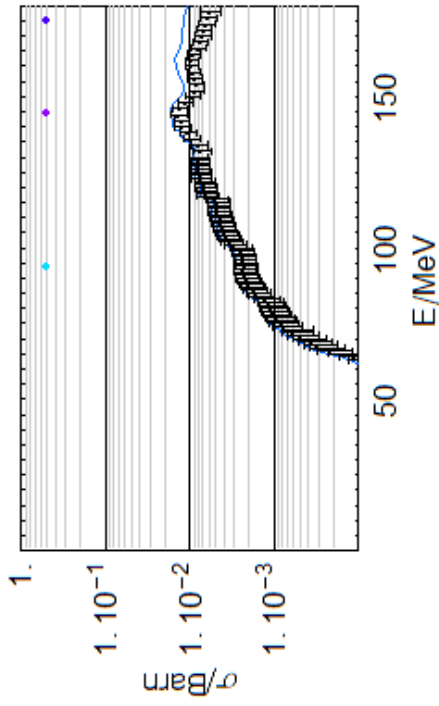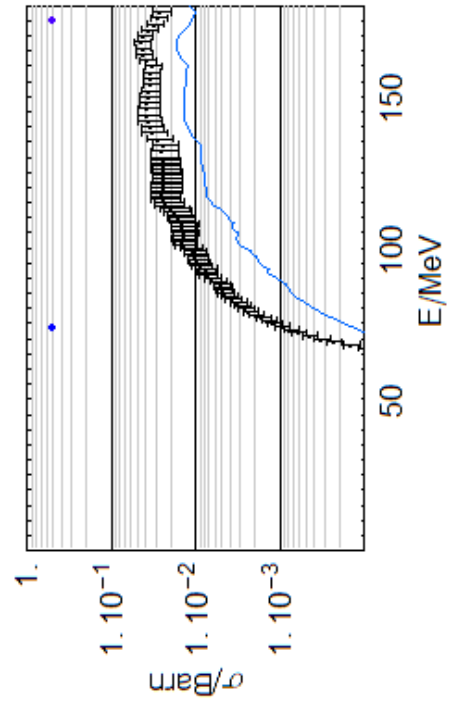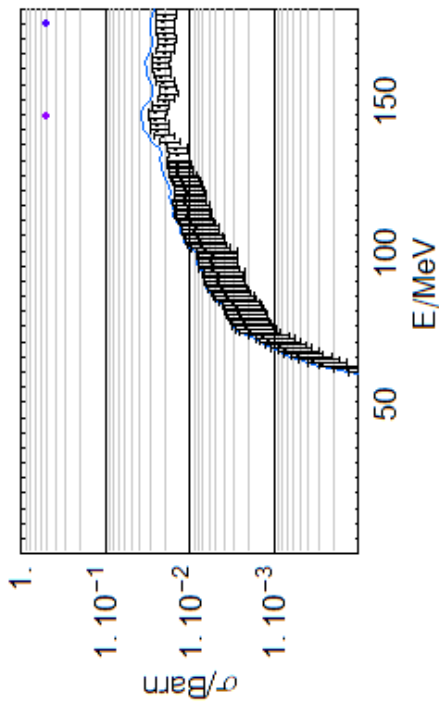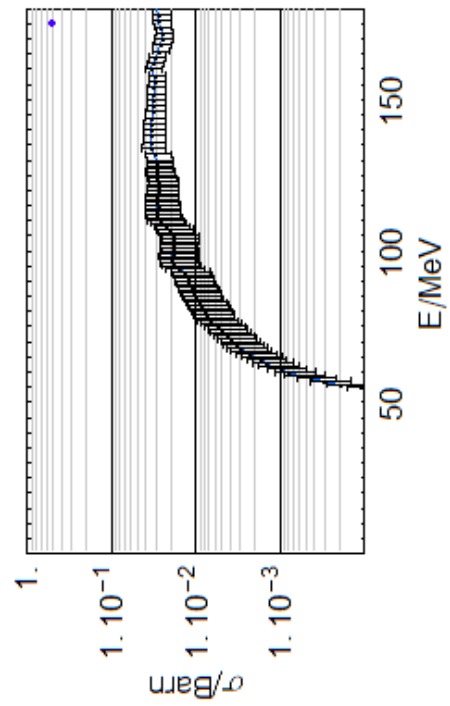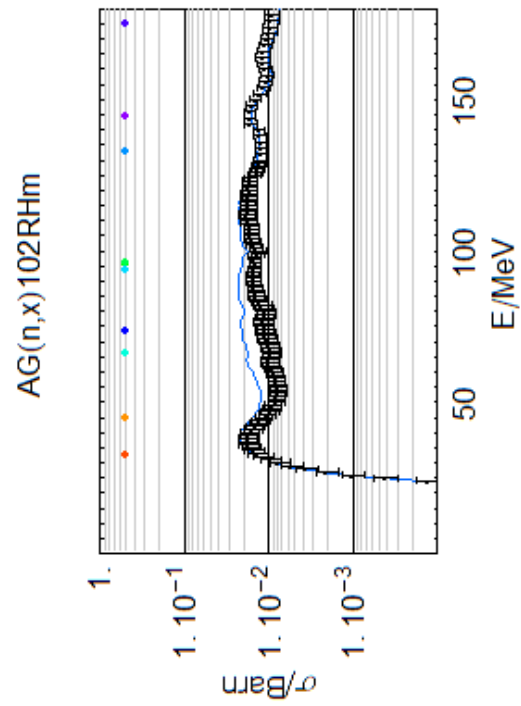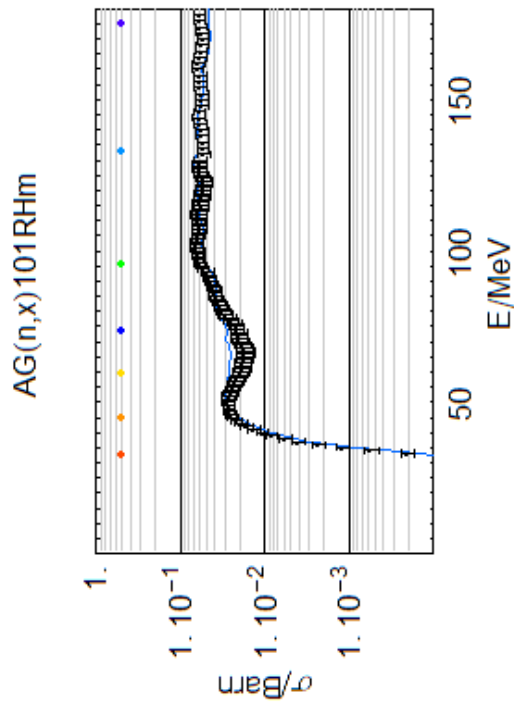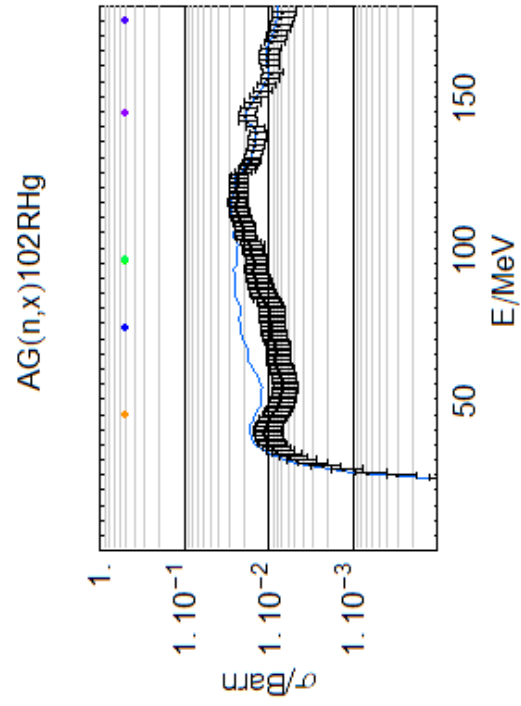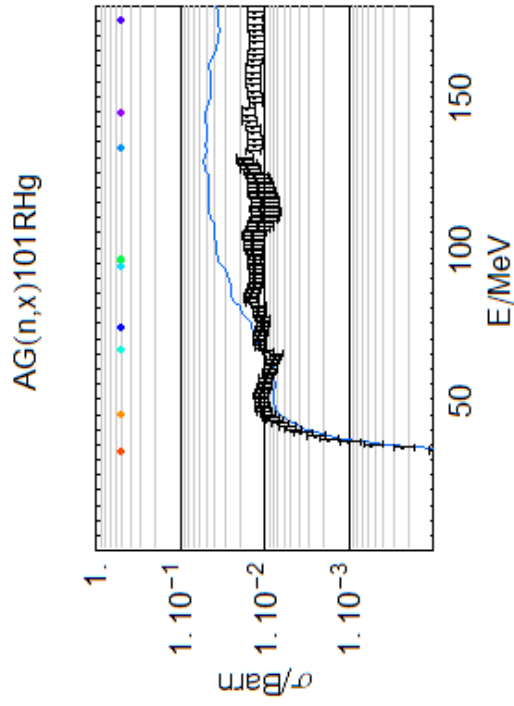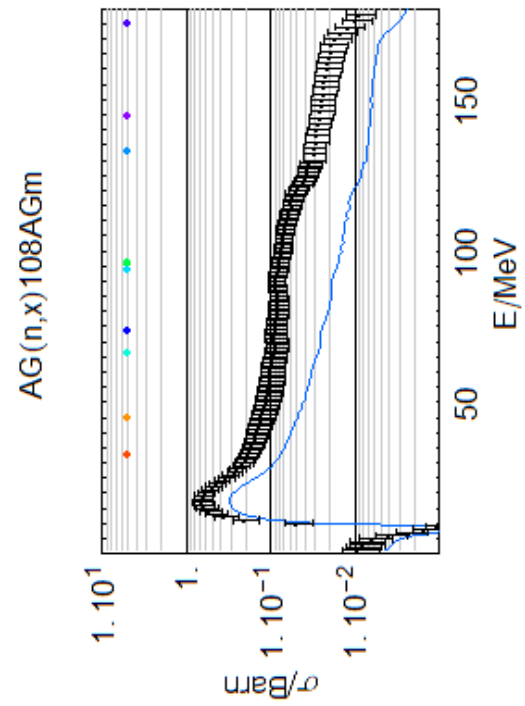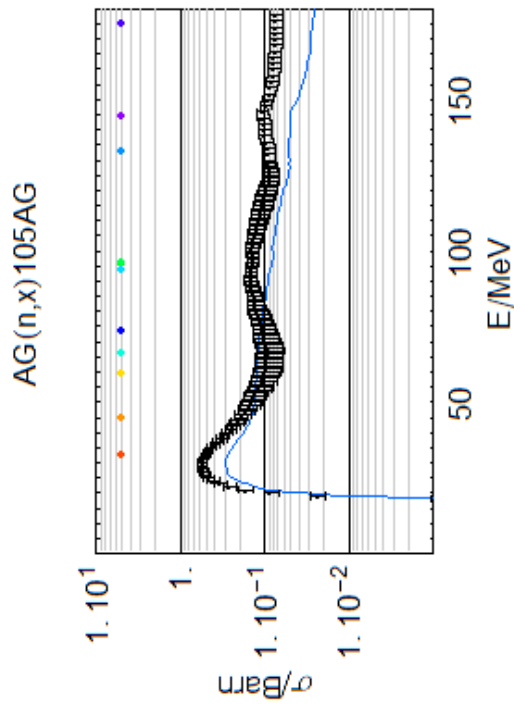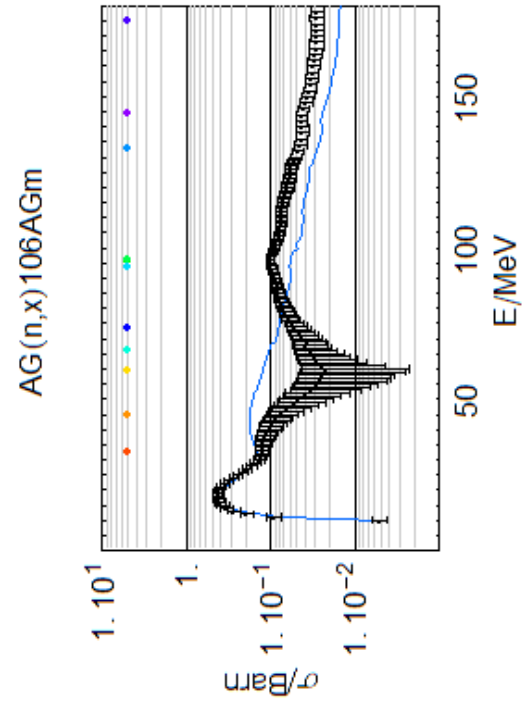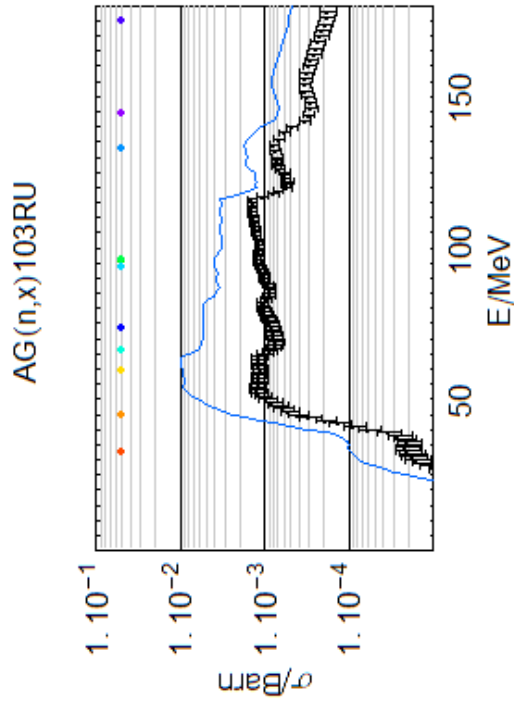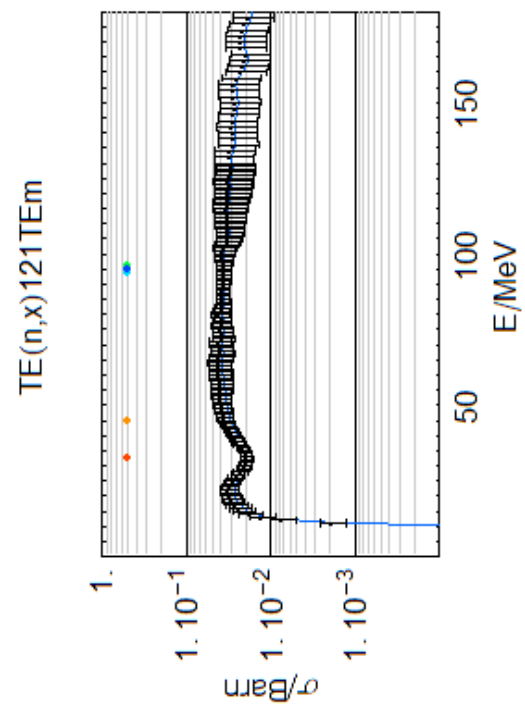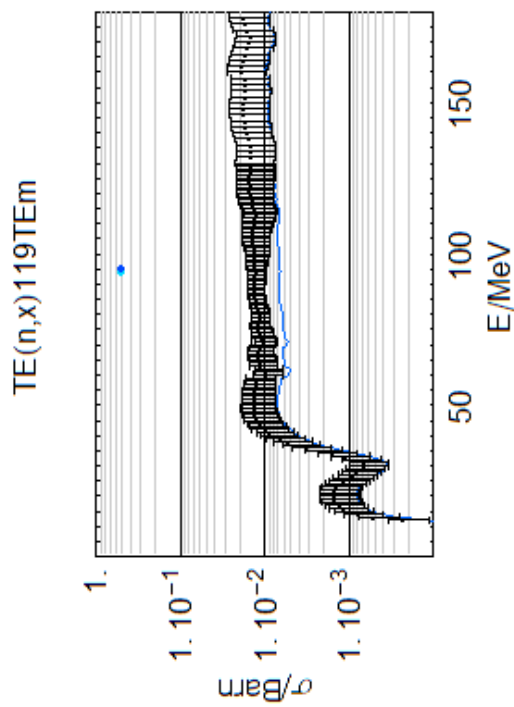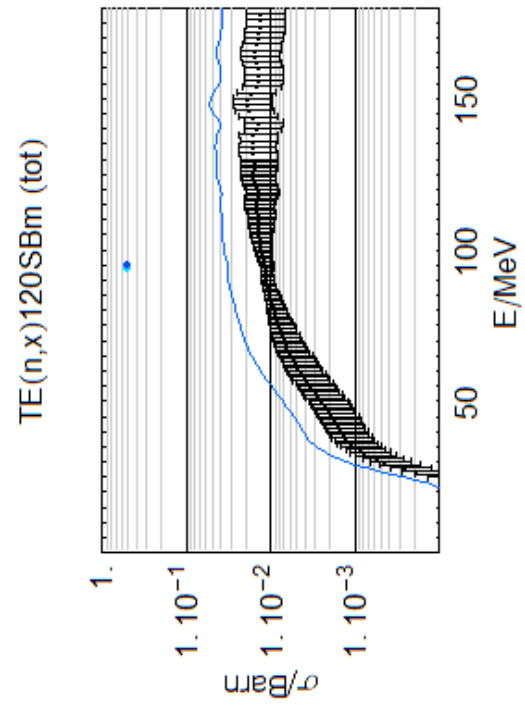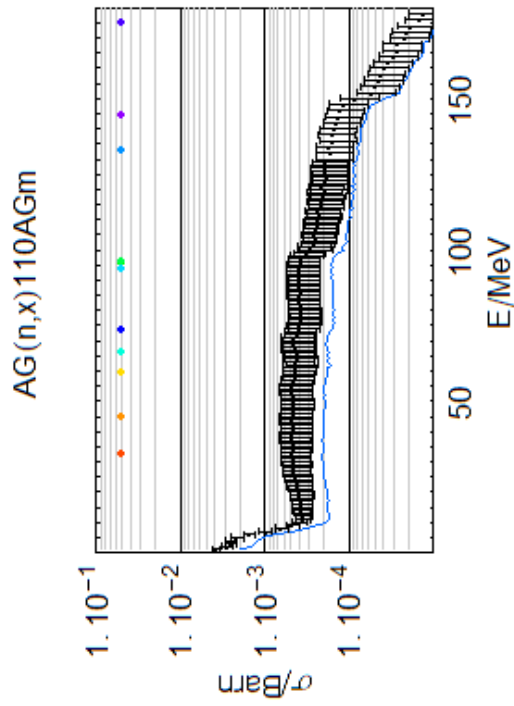
TE(n,x)122SB
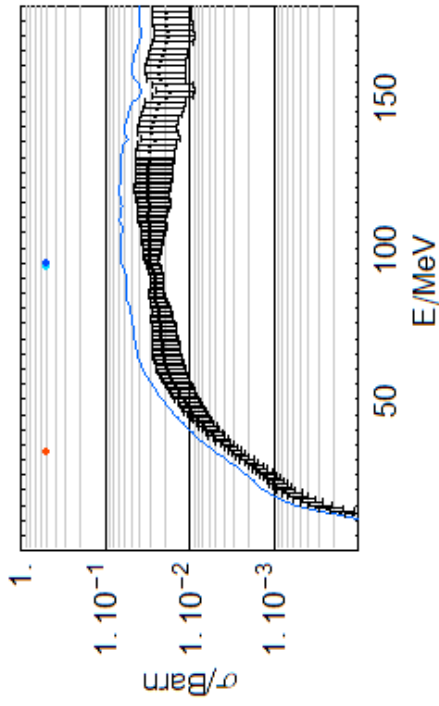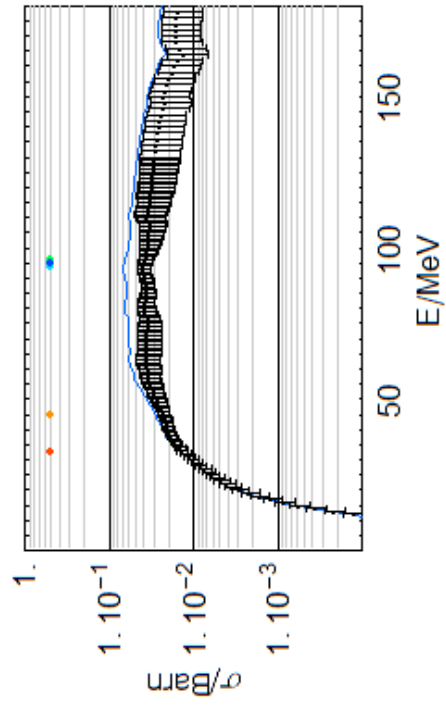
TE(n,x)123TEm

TE(n,x)124SBg

TE(n,x)125SB

TE(n,x)126SBg

TE(n,x)125SNg

PB(n,x)103RU

TE(n,x)127SB

U(n,x)135XE

U(n,x)133I

U(n,x)140BA

U(n,x)136CS

186
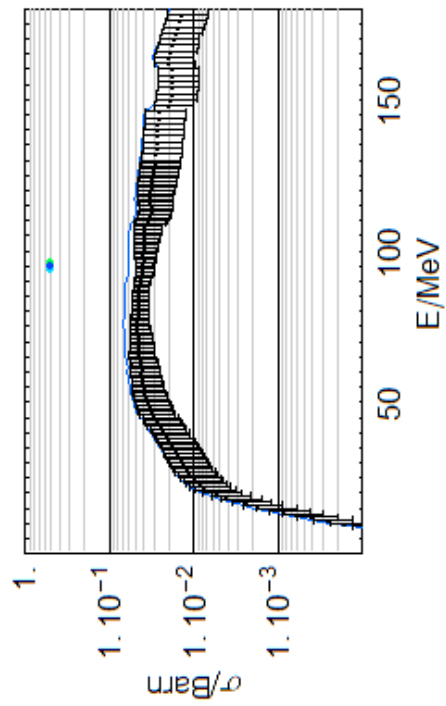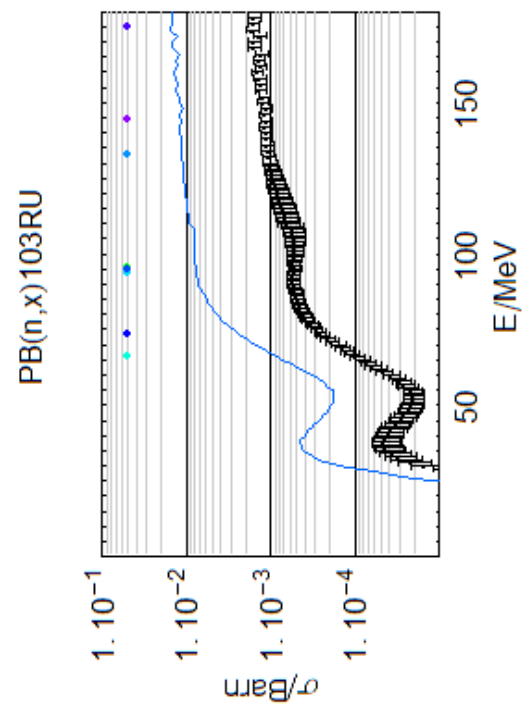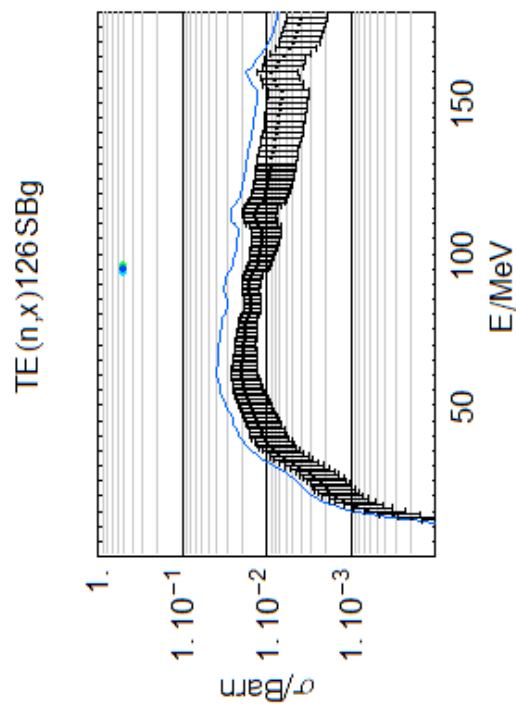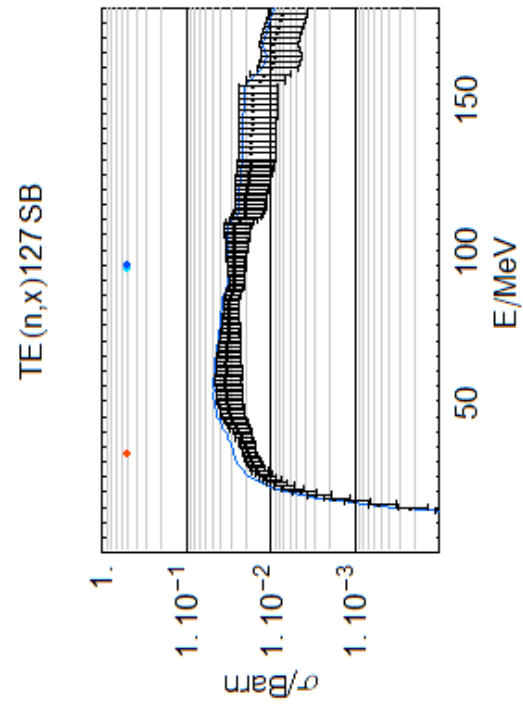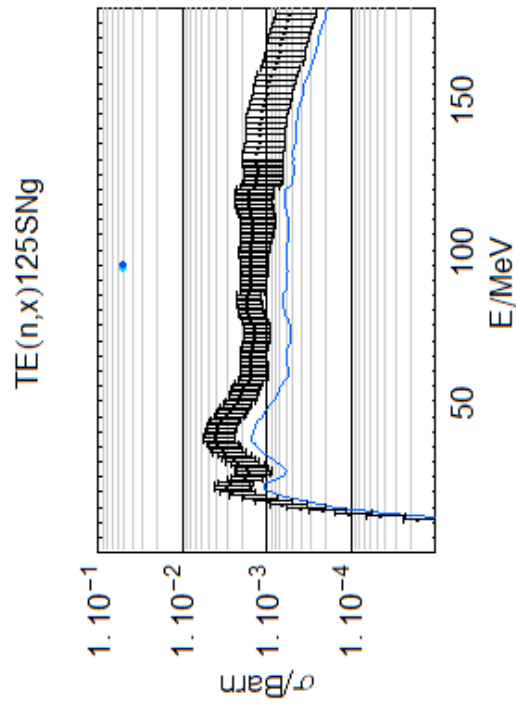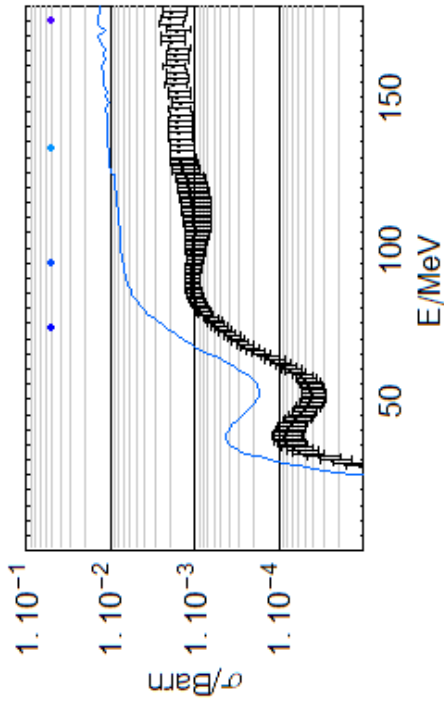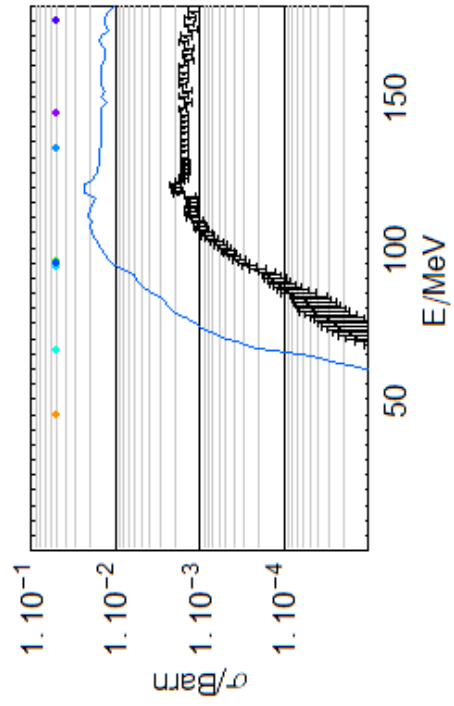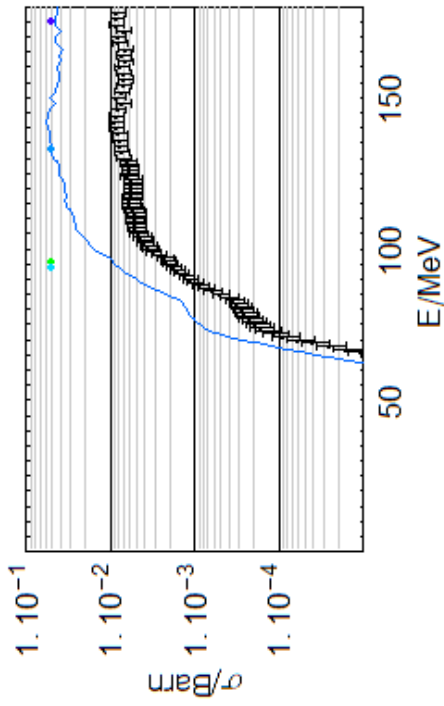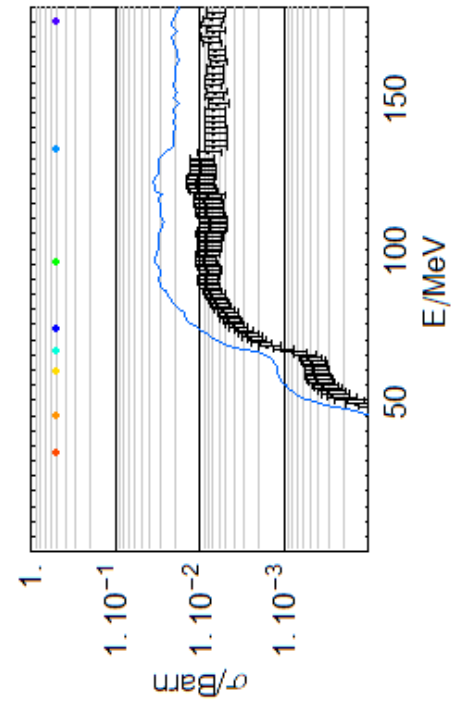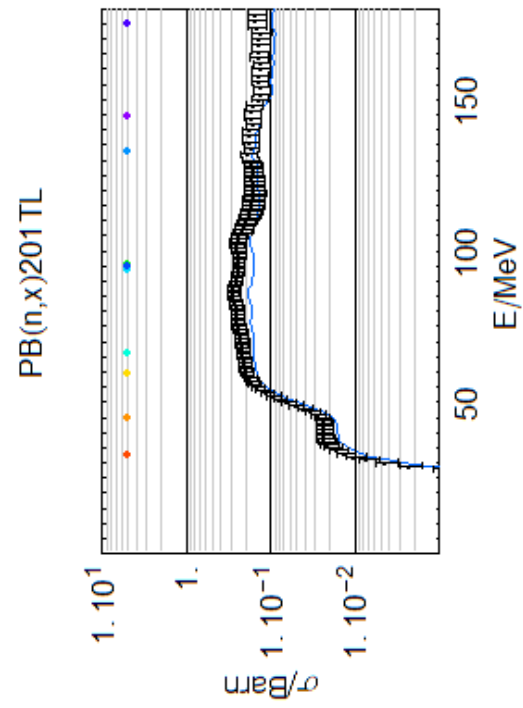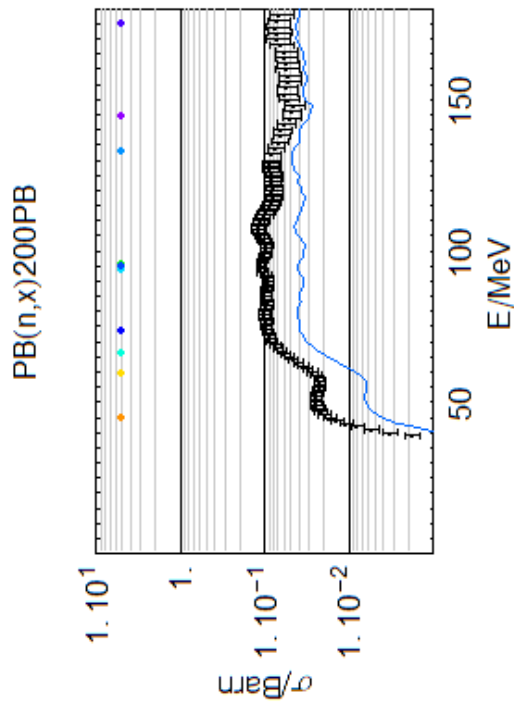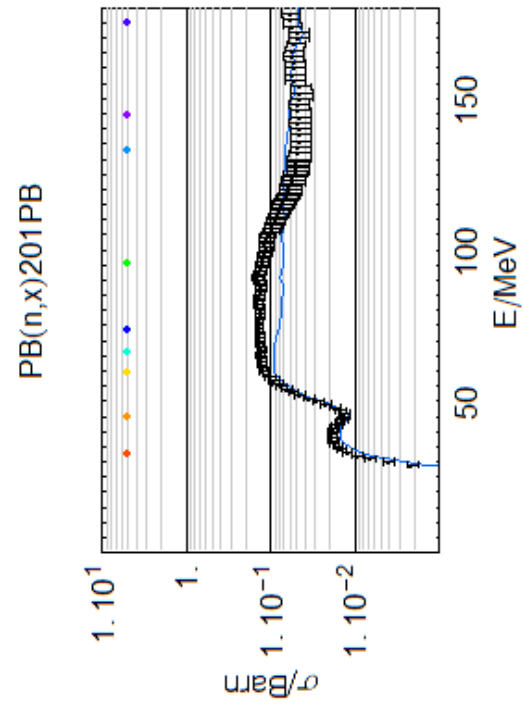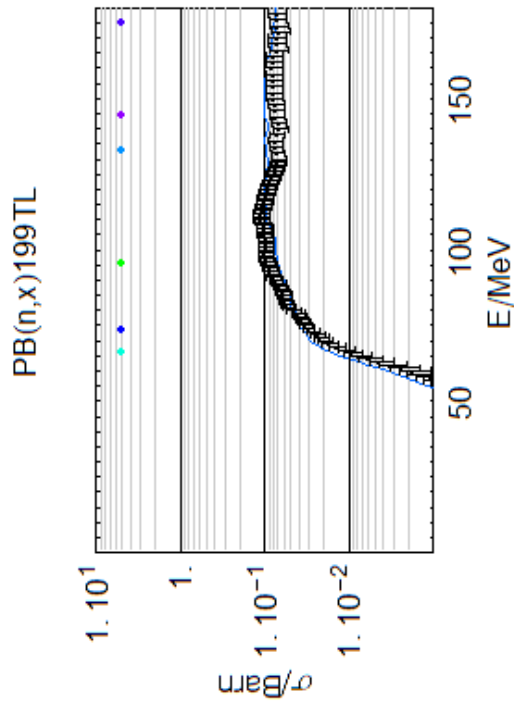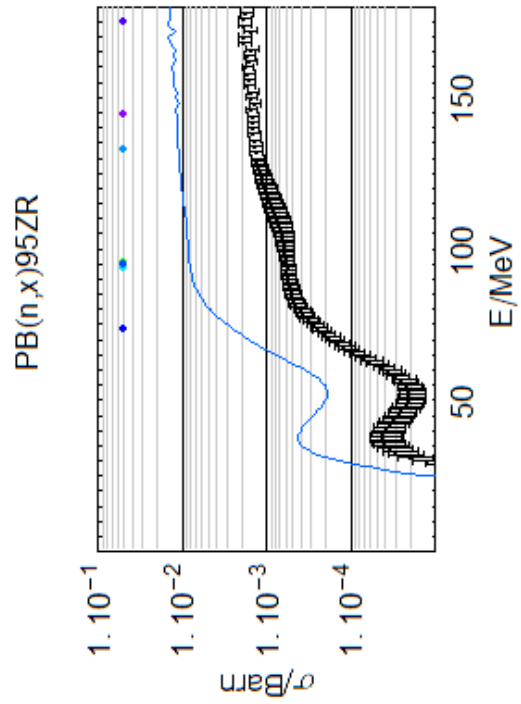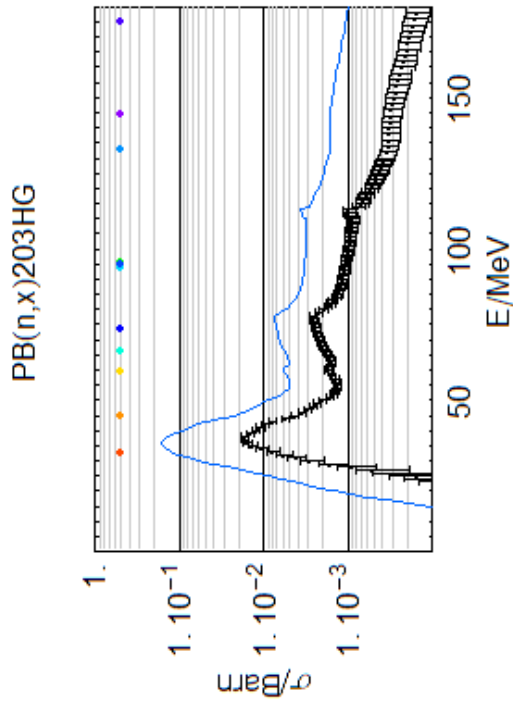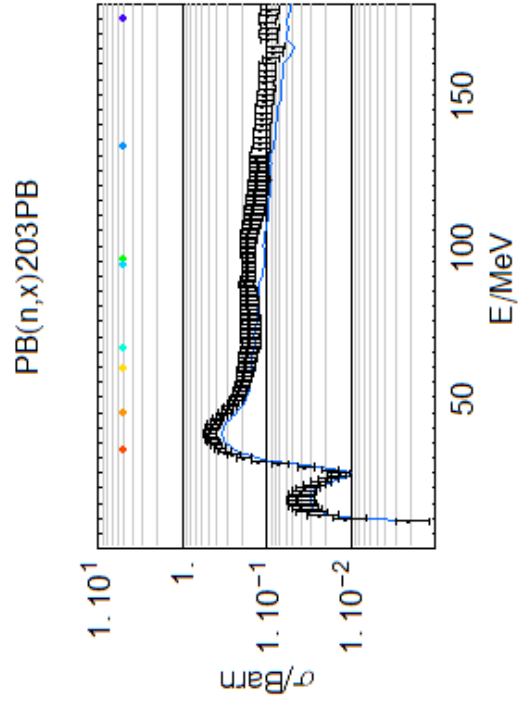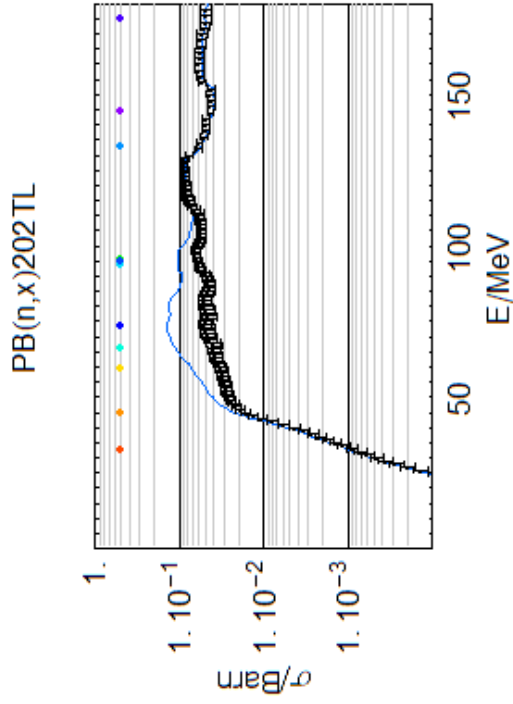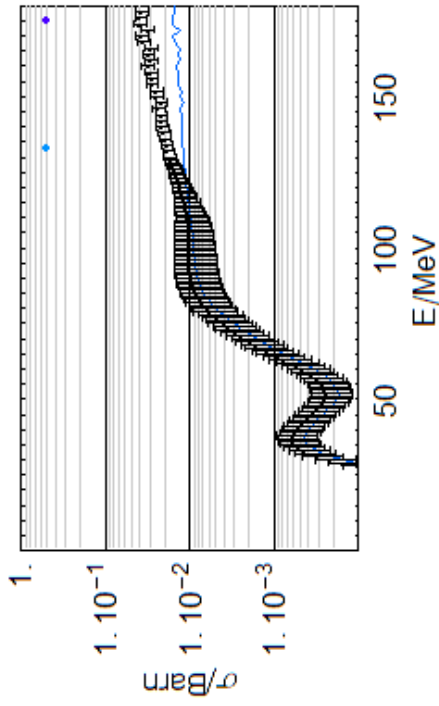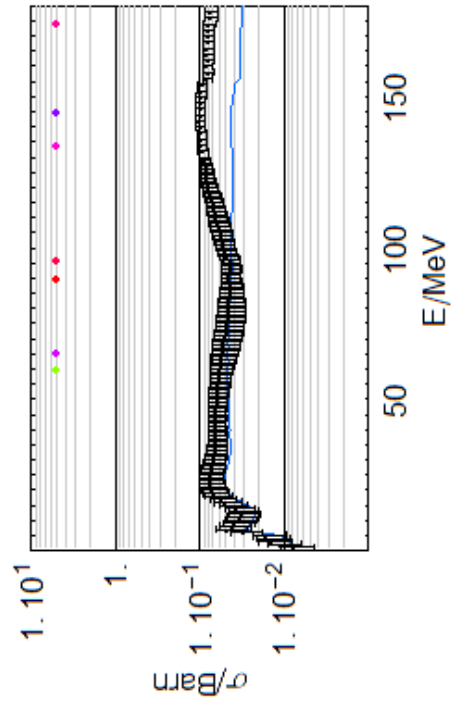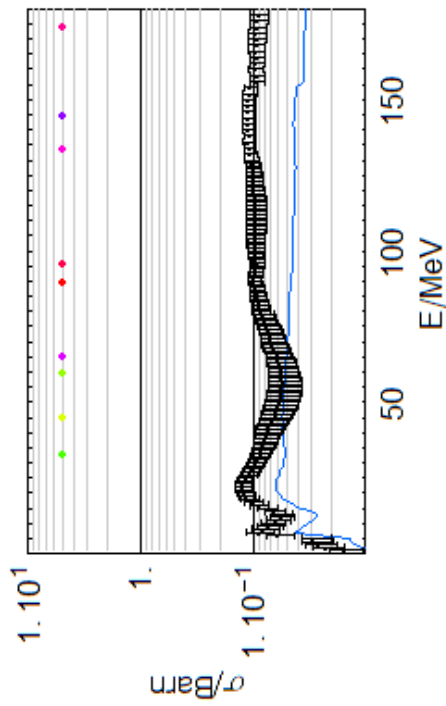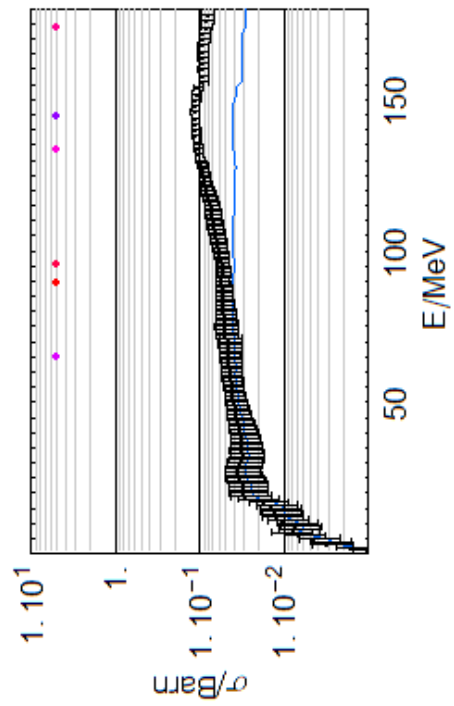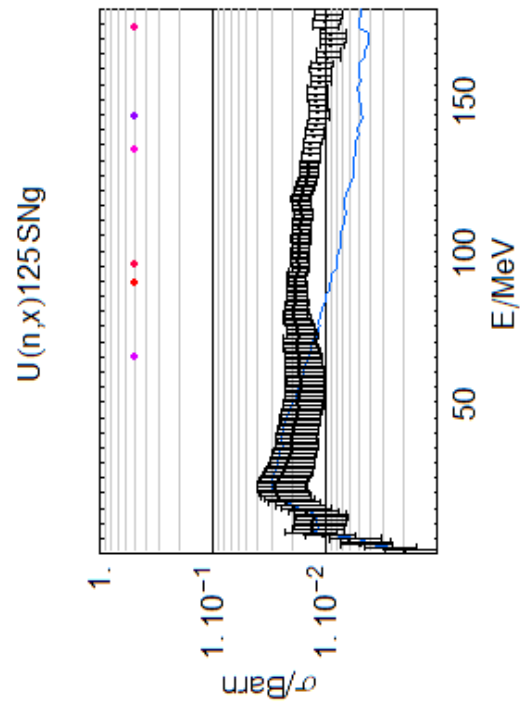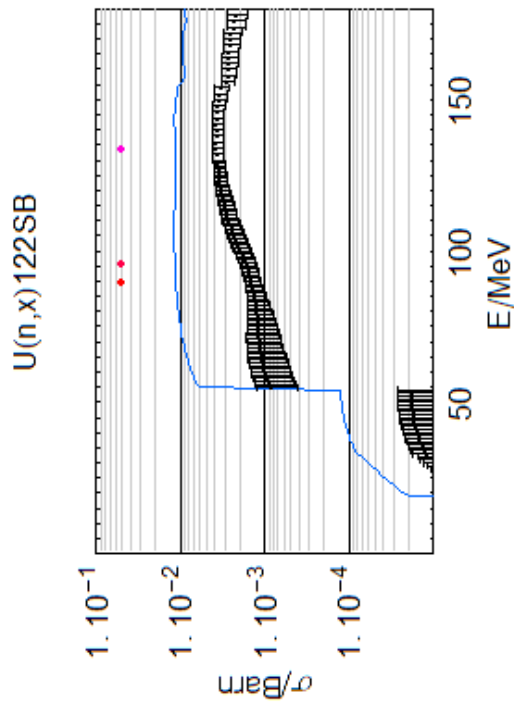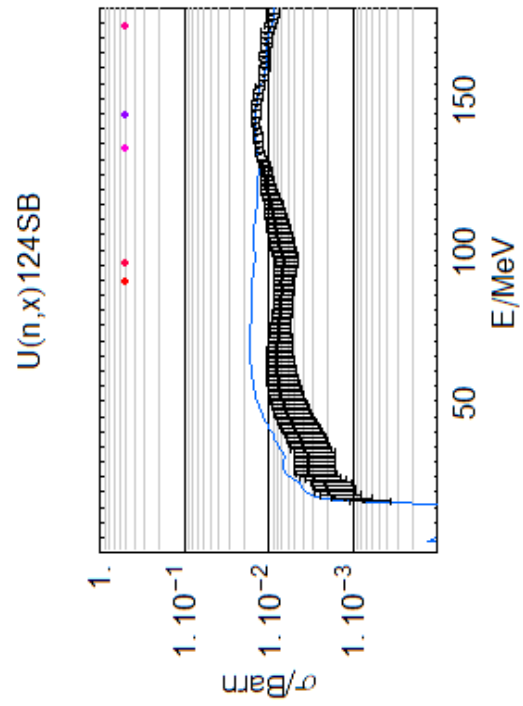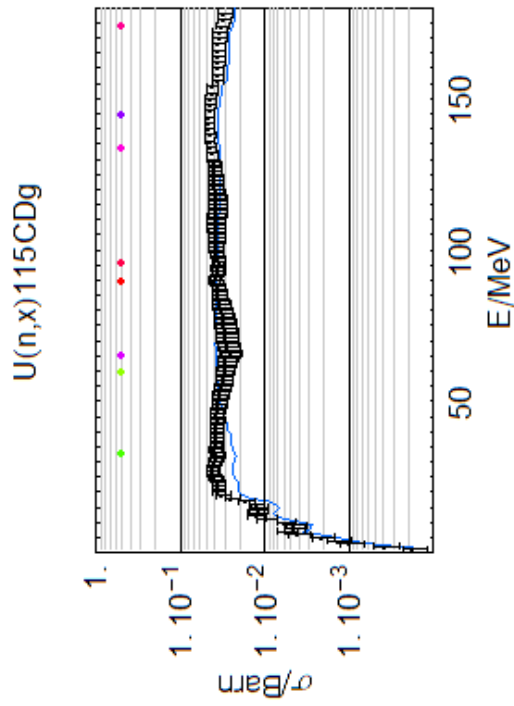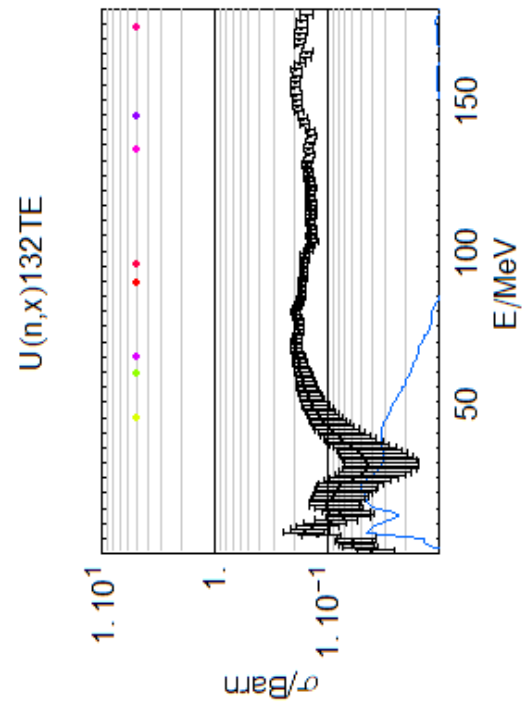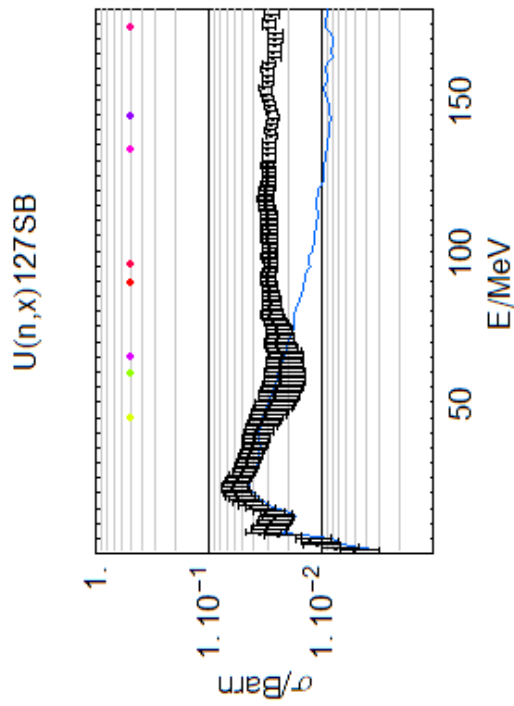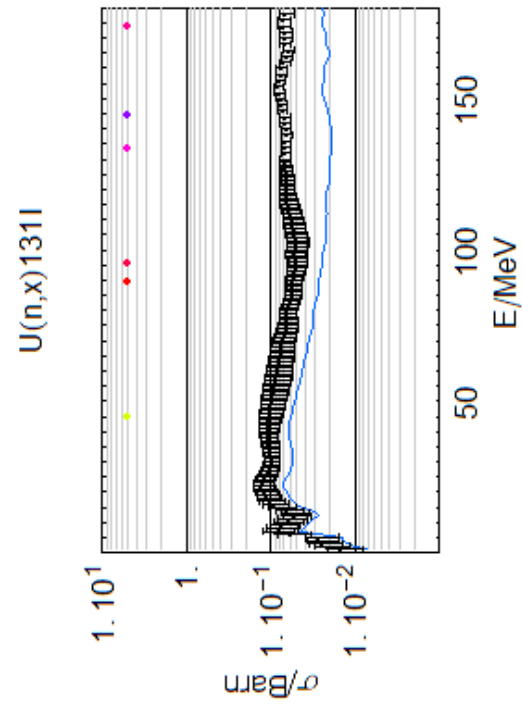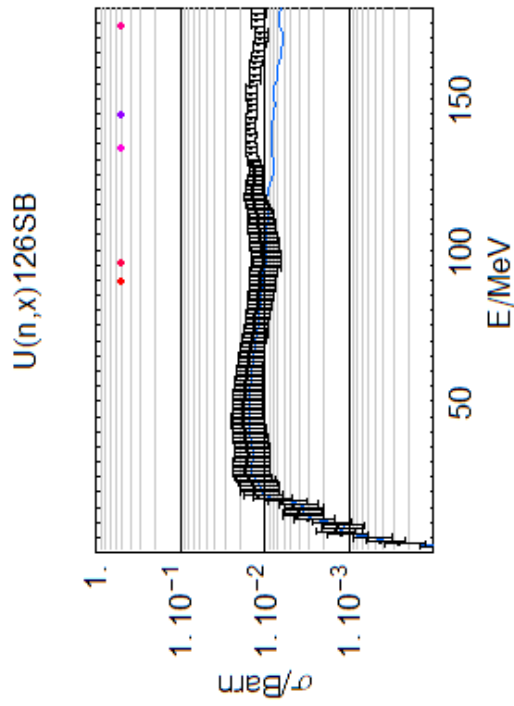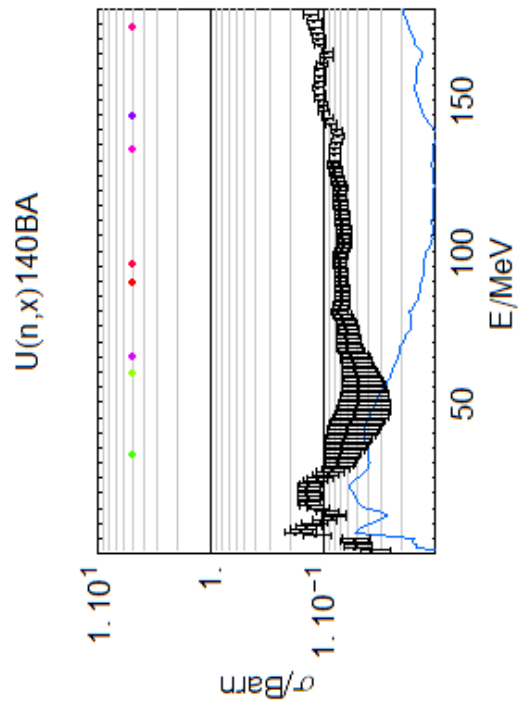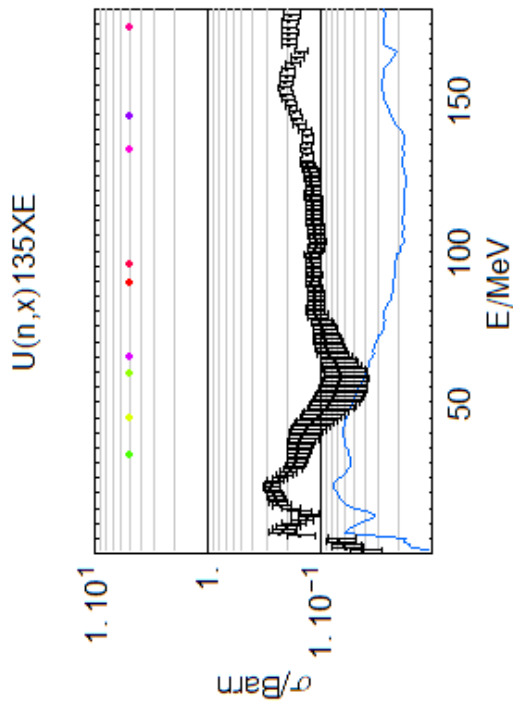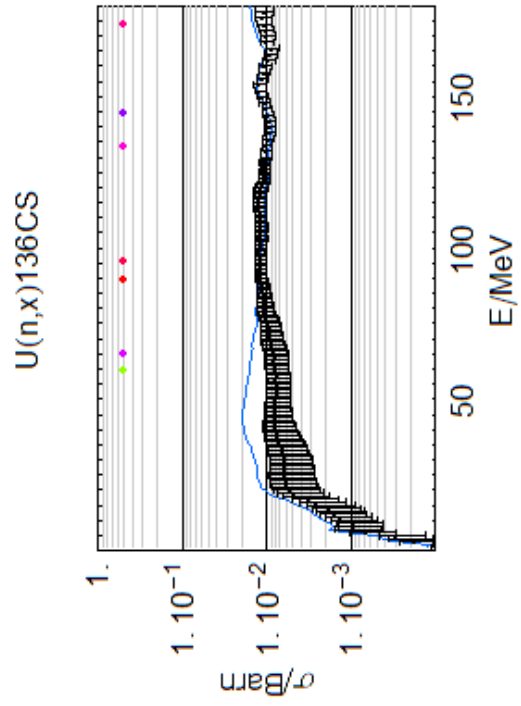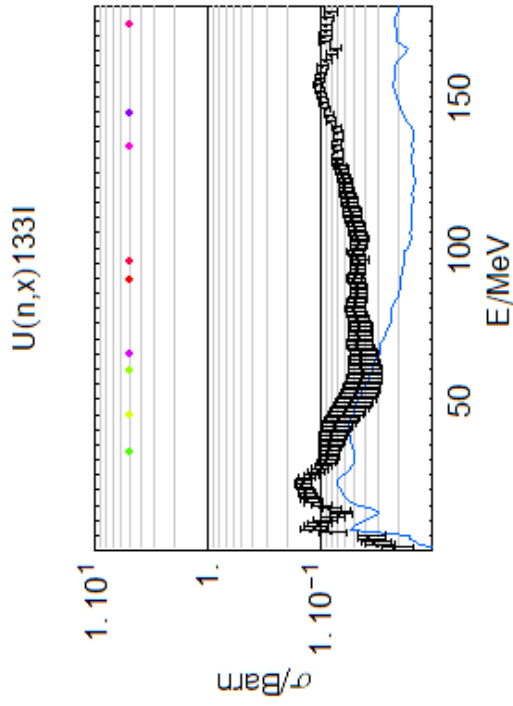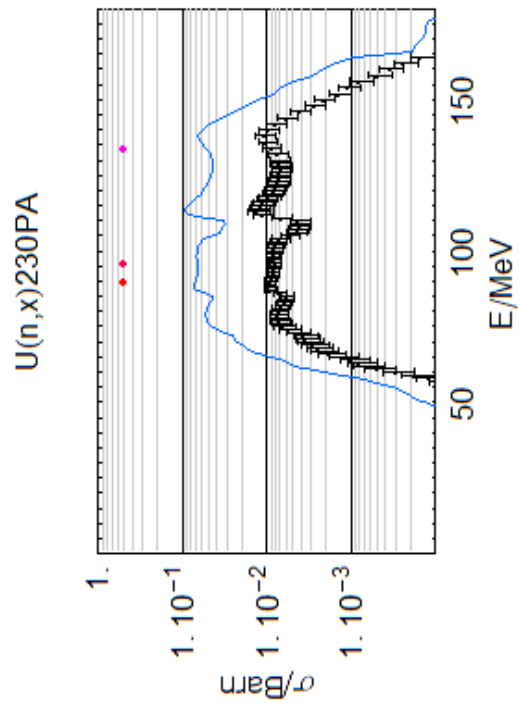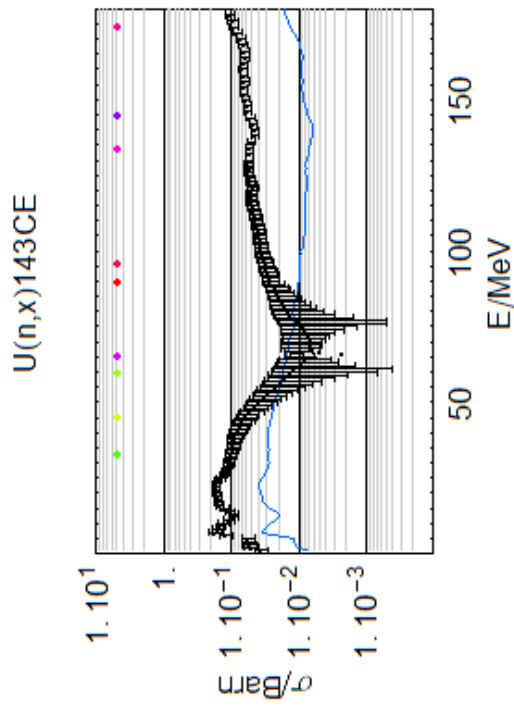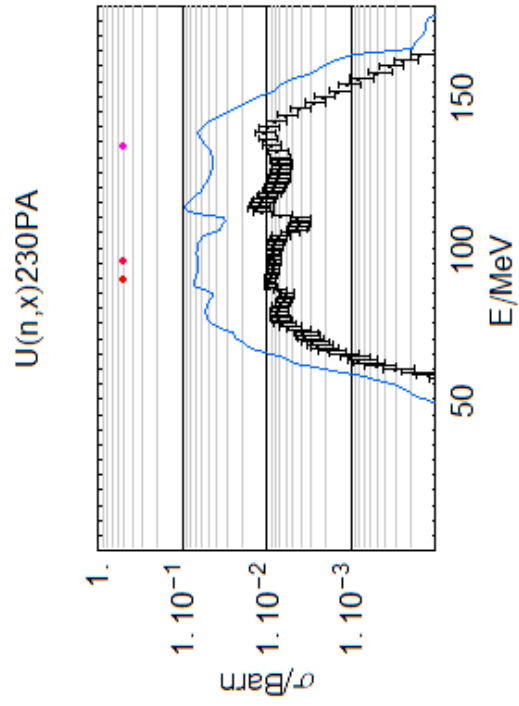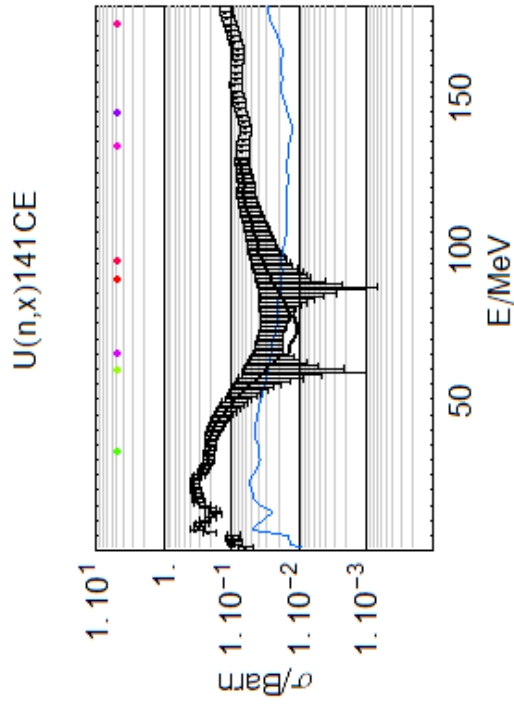
C Production Rates in Meteorites

The following chapter contains figures of all depth dependent production rates, which were calculated in the connection with the present work for artifical meteoroids. The abscissa of the plots is represent the radii of the spherical meteoroids, where 0 determines the center. The ordinate of the plots determine the production rates, where all figures include separately infromation about the production induced by primary protons (red solid), secondary protons (red dashed), secondary neutrons (green dashed) and a sum of this three production modes, the total production rate (black solid). The gray area around total production rate determines the total production uncertainties. The blue markers repesent experimental measured production rates in different depth.

The figures are ordered by meteoroids starting with the iron meteorite of 20 cm diameter which was irradiated with 1600 MeV protons followed by the stony meteoroid of 50 cm diameter which was irradiated with 1600 MeV protons and the stony meteoroids of 10, 30 and 50 cm diameter which were irradiated with 600 MeV protons.

The residual nuclide production in a iron meteorite with a radius of 10 cm irradiated with 1600 MeV protons.
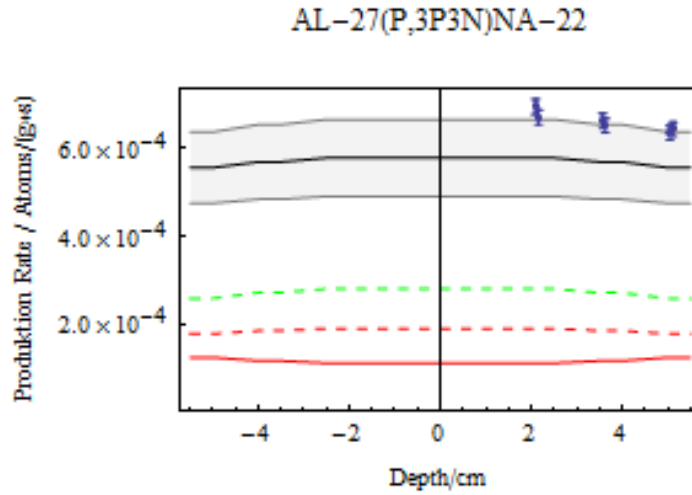
Figure C.1: Production of ^{22}Na from natural aluminum in an artificial iron meteorite with a radius of 10 cm irradiated with 1600 MeV protons.
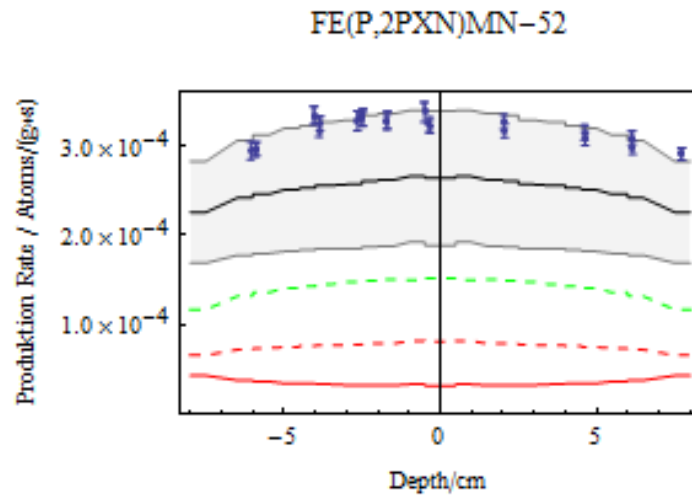
Figure C.2: Production of ^{52}Mn from natural iron in an artificial iron meteorite with a radius of 10 cm irradiated with 1600 MeV protons.

FE(P,2PXN)MN−54
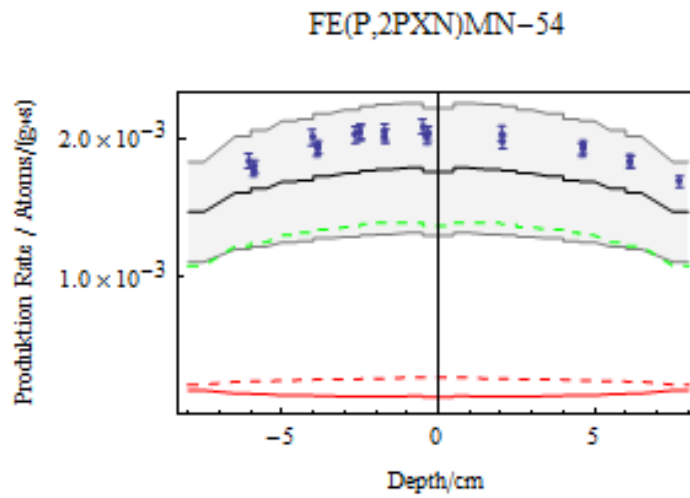
Figure C.3: Production of ^{54}Mn from natural iron in an artificial iron meteorite with a radius of 10 cm irradiated with 1600 MeV protons.
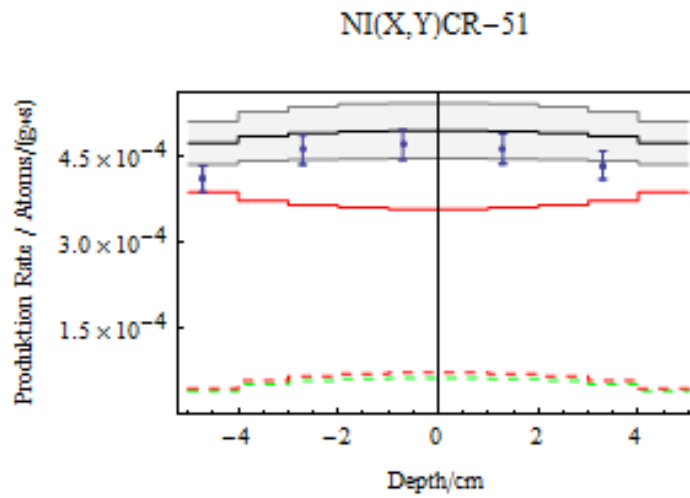
FE(P,3PXN)CR−51
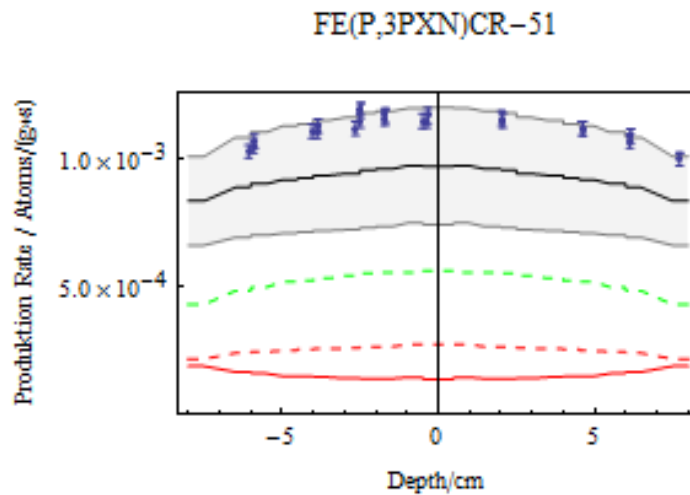
Figure C.4: Production of ^{51}Cr from natural iron in an artificial iron meteorite with a radius of 10 cm irradiated with 1600 MeV protons.
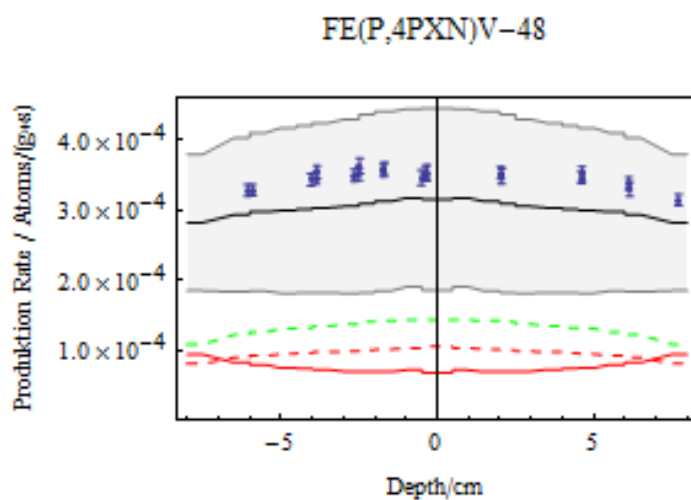
Figure C.5: Production of ^{48}V from natural iron in an artificial iron meteorite with a radius of 10 cm irradiated with 1600 MeV protons.
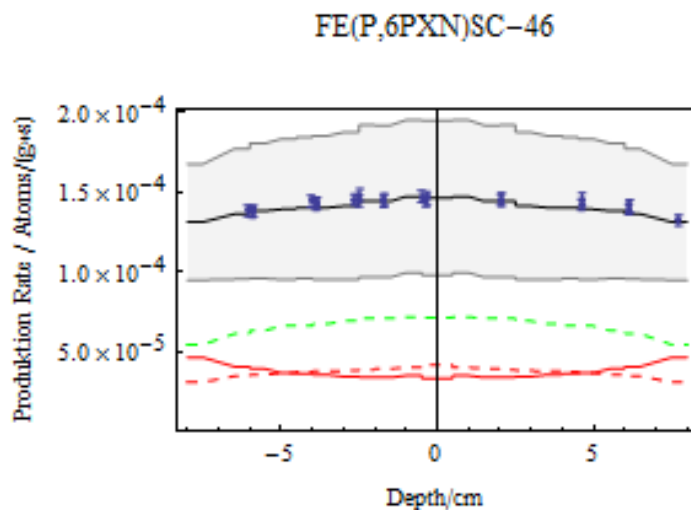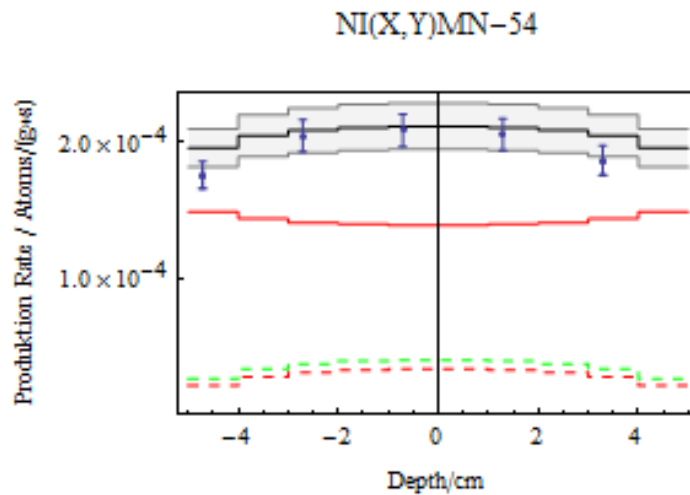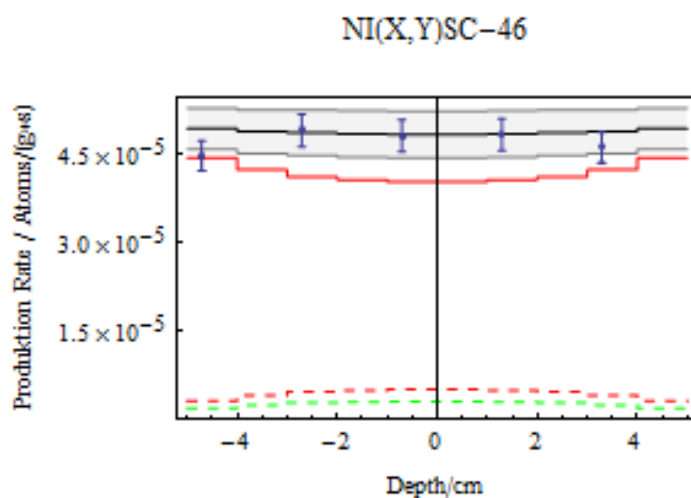

Figure C.6: Production of ^{46}Sc from natural iron in an artificial iron meteorite with a radius of 10 cm irradiated with 1600 MeV protons.
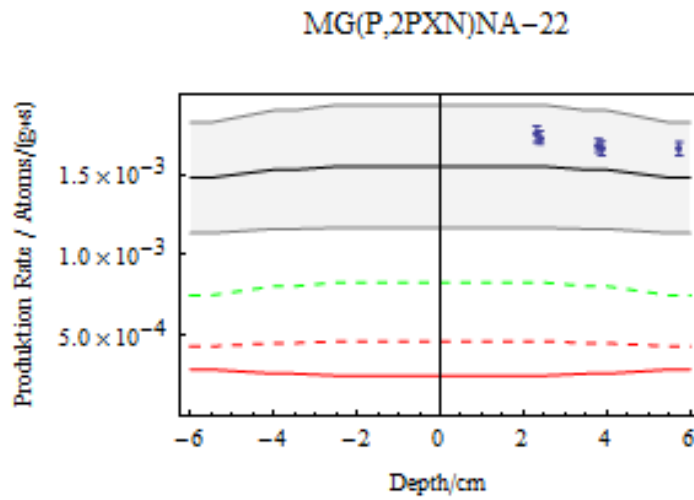
Figure C.7: Production of ^{22}Na from natural magnesium in an artificial iron meteorite with a radius of 10 cm irradiated with 1600 MeV protons.
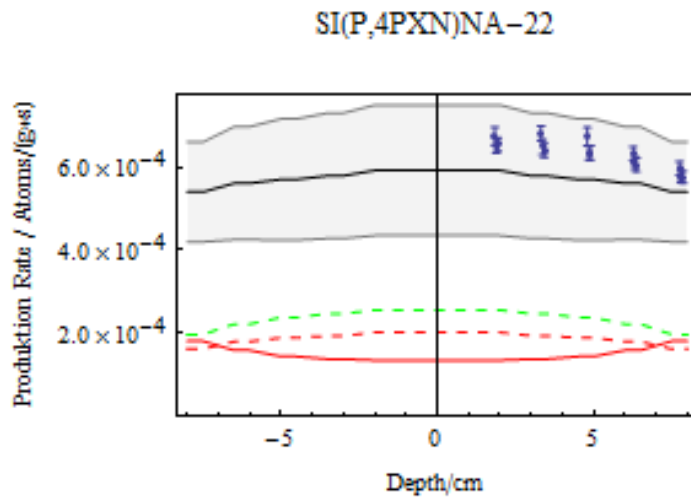
Figure C.8: Production of ^{22}Na from natural silicon in an artificial iron meteorite with a radius of 10 cm irradiated with 1600 MeV protons.

The residual nuclide production in a stony meteorite with a radius of 25 cm irradiated with 1600 MeV protons.
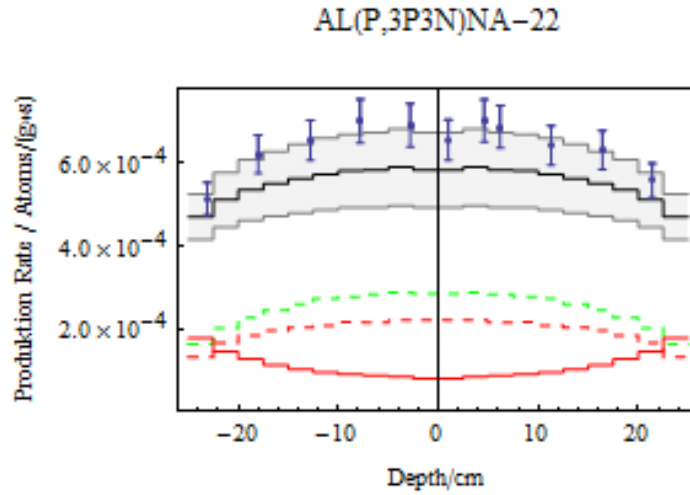
Figure C.9: Production of ^{22}Na from natural aluminum in an artificial gabbro meteorite with a radius of 25 cm irradiated with 1600 MeV protons.
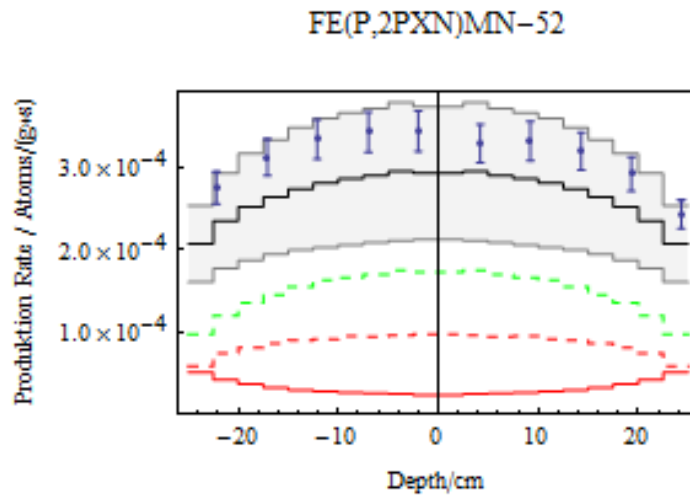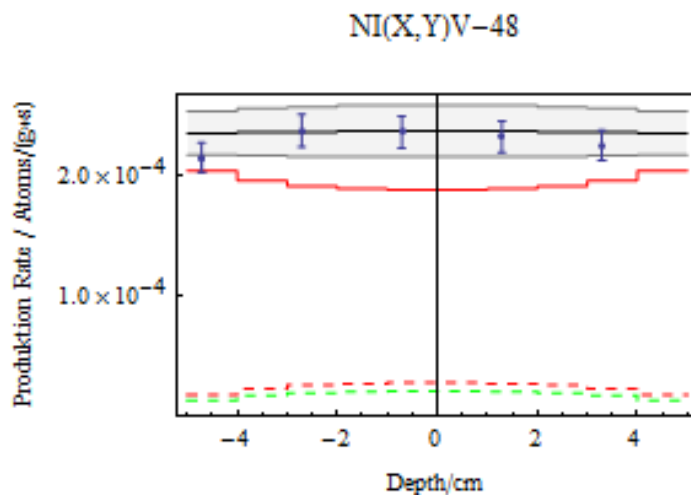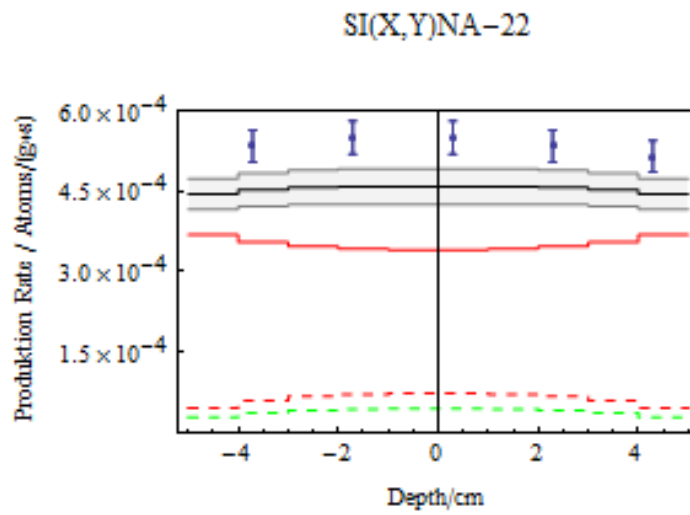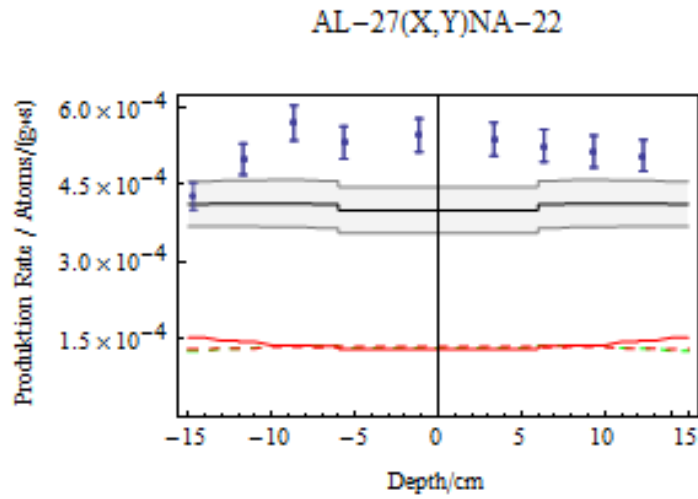

Figure C.10: Production of ^{52}Mn from natural iron in an artificial gabbro meteorite with a radius of 25 cm irradiated with 1600 MeV protons.

FE(P,2PXN)MN–54
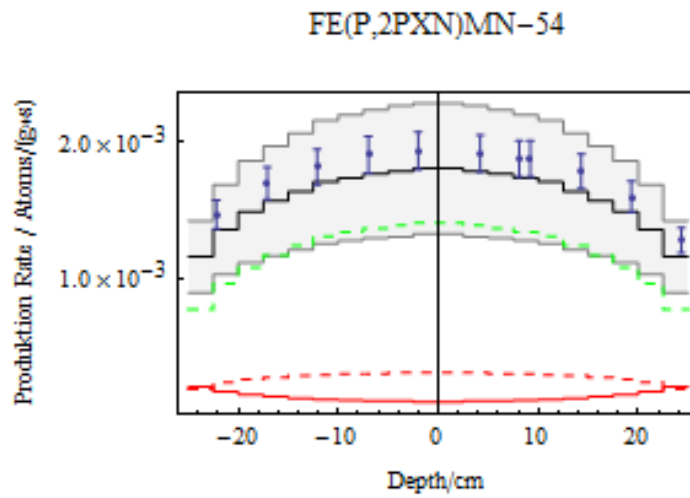
Figure C.11: Production of ^{54}Mn from natural iron in an artificial gabbro meteorite with a radius of 25 cm irradiated with 1600 MeV protons.

FE(P,3PXN)CR–51
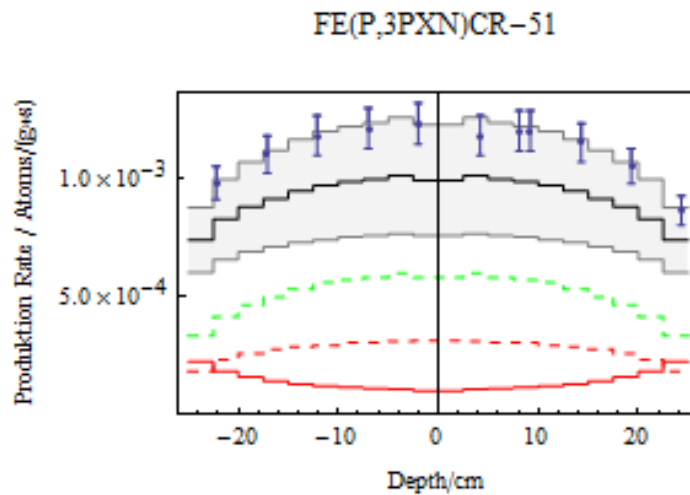
Figure C.12: Production of ^{51}Cr from natural iron in an artificial gabbro meteorite with a radius of 25 cm irradiated with 1600 MeV protons.
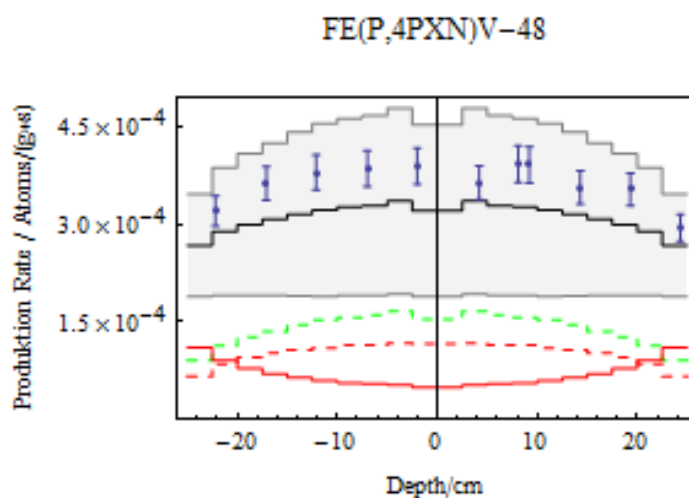
Figure C.13: Production of ^{48}V from natural iron in an artificial gabbro meteorite with a radius of 25 cm irradiated with 1600 MeV protons.
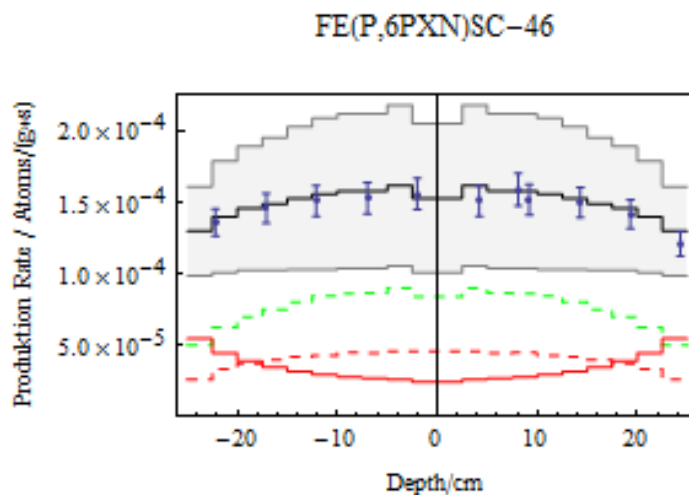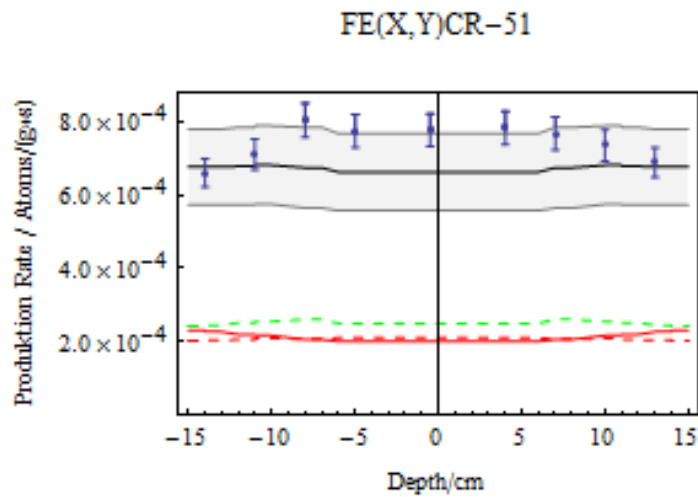

Figure C.14: Production of ^{46}Sc from natural iron in an artificial gabbro meteorite with a radius of 25 cm irradiated with 1600 MeV protons.
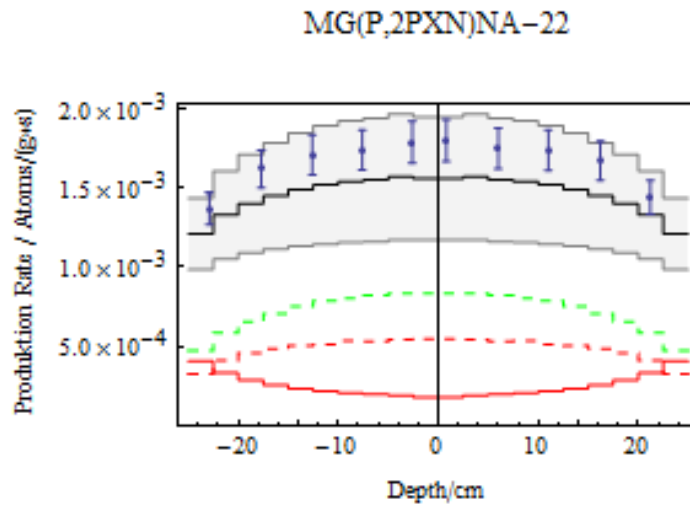
Figure C.15: Production of ^{22}Na from natural magnesium in an artificial gabbro meteorite with a radius of 25 cm irradiated with 1600 MeV protons.
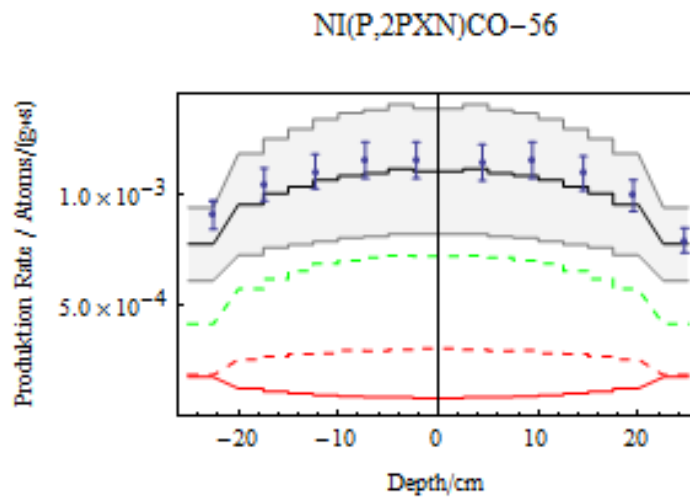
Figure C.16: Production of ^{56}Co from natural nickel in an artificial gabbro meteorite with a radius of 25 cm irradiated with 1600 MeV protons.
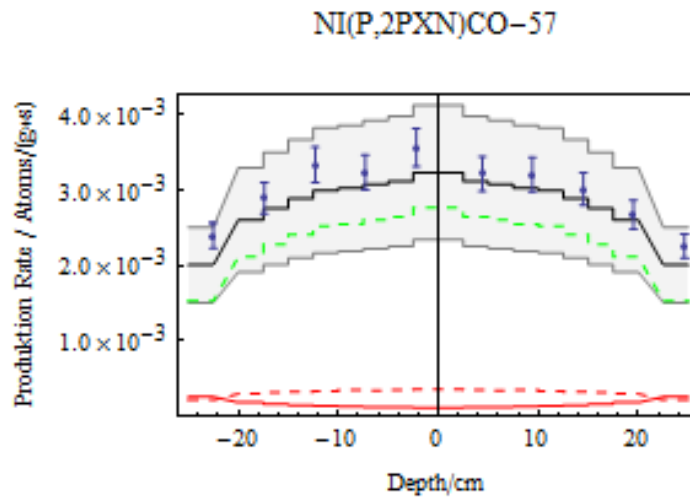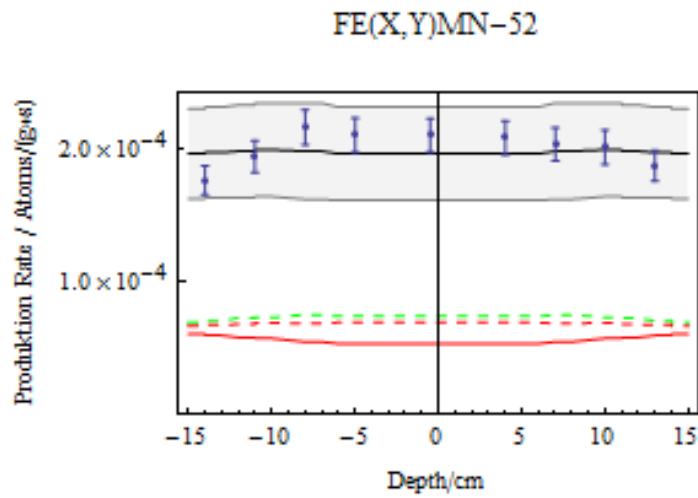
Figure C.17: Production of ^{57}Co from natural nickel in an artificial gabbro meteorite with a radius of 25 cm irradiated with 1600 MeV protons.
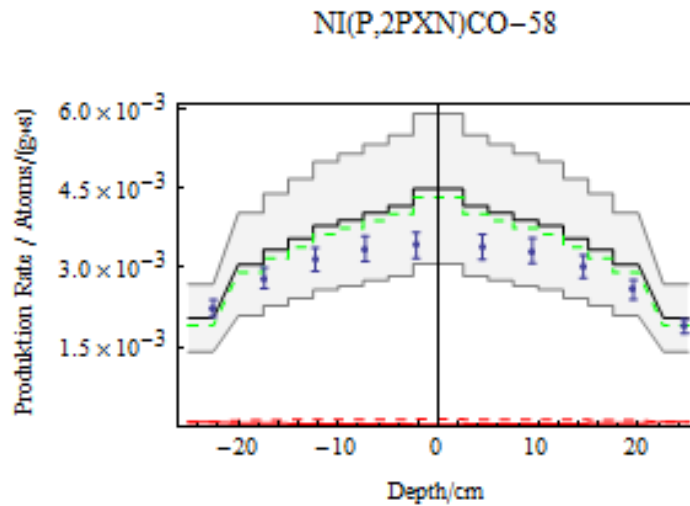
Figure C.18: Production of ^{58}Co from natural nickel in an artificial gabbro meteorite with a radius of 25 cm irradiated with 1600 MeV protons.
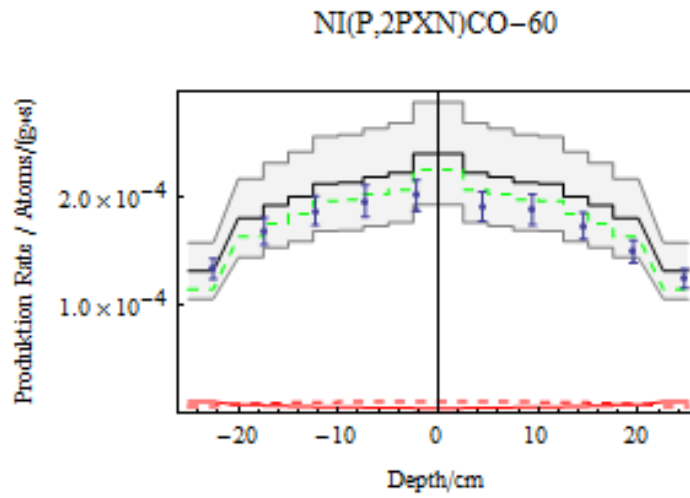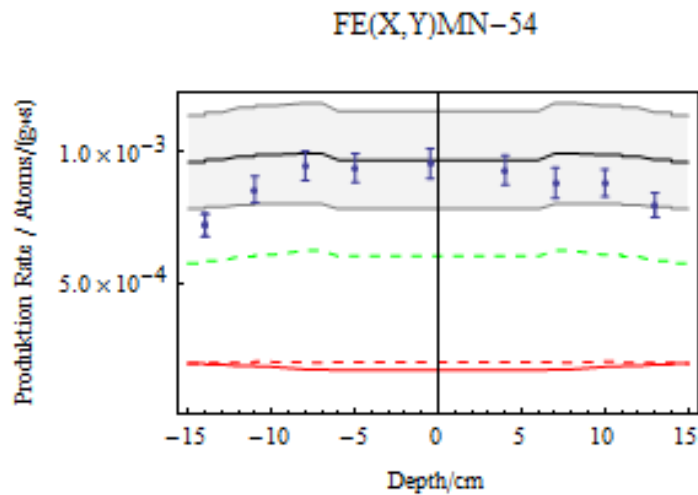
Figure C.19: Production of ^{60}Co from natural nickel in an artificial gabbro meteorite with a radius of 25 cm irradiated with 1600 MeV protons.
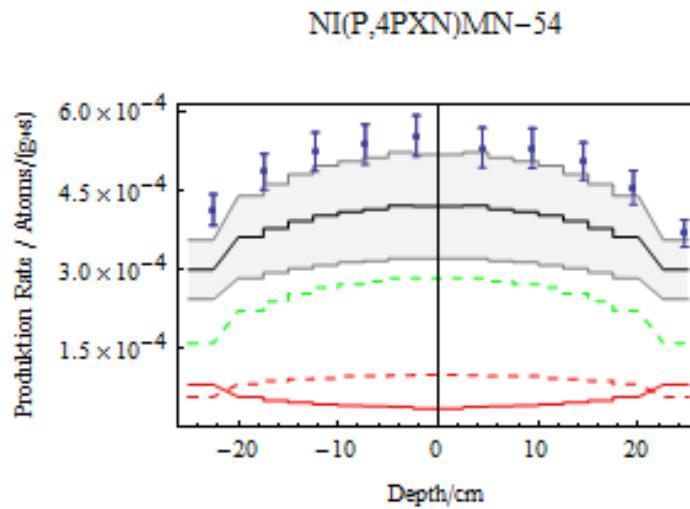
Figure C.20: Production of ^{54}Mn from natural nickel in an artificial gabbro meteorite with a radius of 25 cm irradiated with 1600 MeV protons.
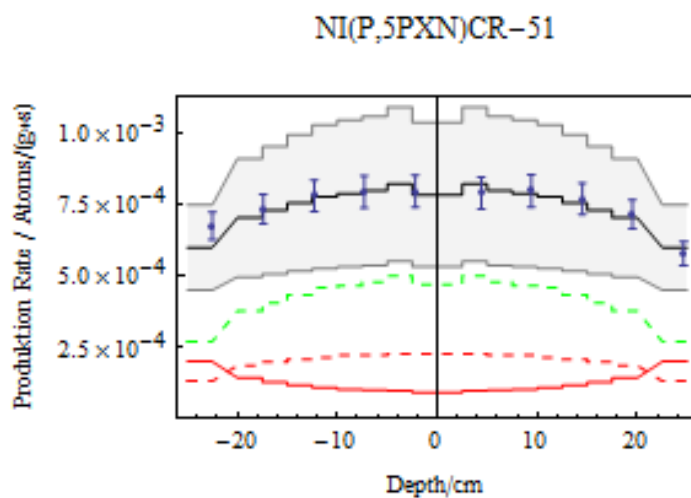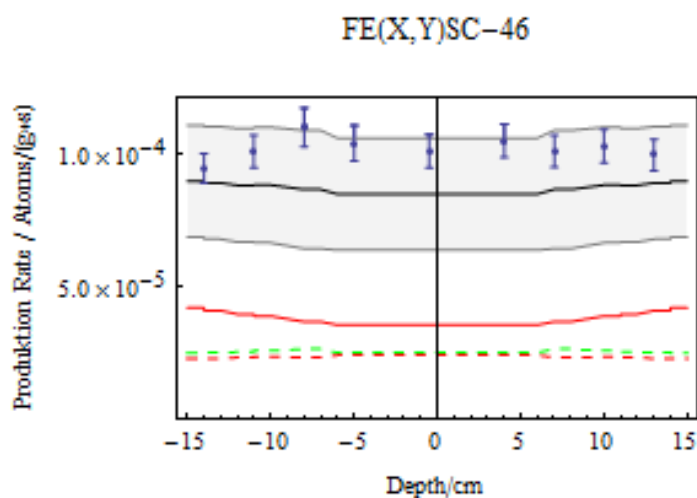
Figure C.21: Production of ^{51}Cr from natural nickel in an artificial gabbro meteorite with a radius of 25 cm irradiated with 1600 MeV protons.
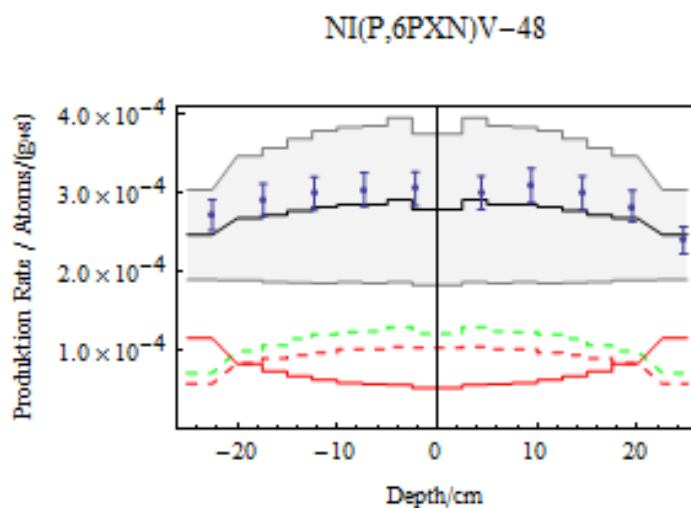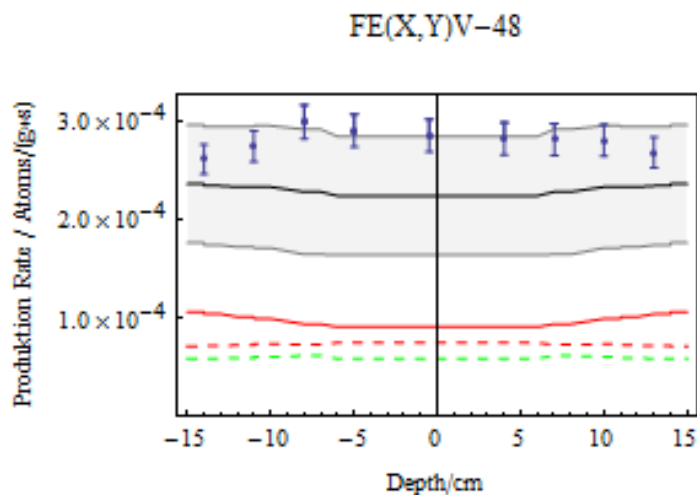

Figure C.22: Production of ^{48}V from natural nickel in an artificial gabbro meteorite with a radius of 25 cm irradiated with 1600 MeV protons.
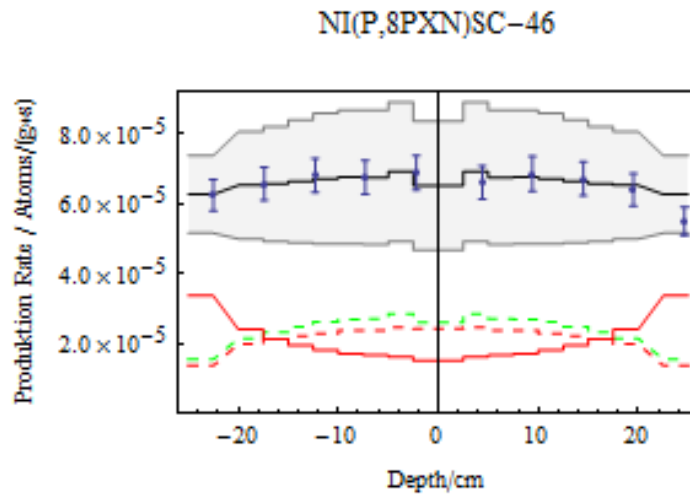
Figure C.23: Production of ^{46}Sc from natural nickel in an artificial gabbro meteorite with a radius of 25 cm irradiated with 1600 MeV protons.
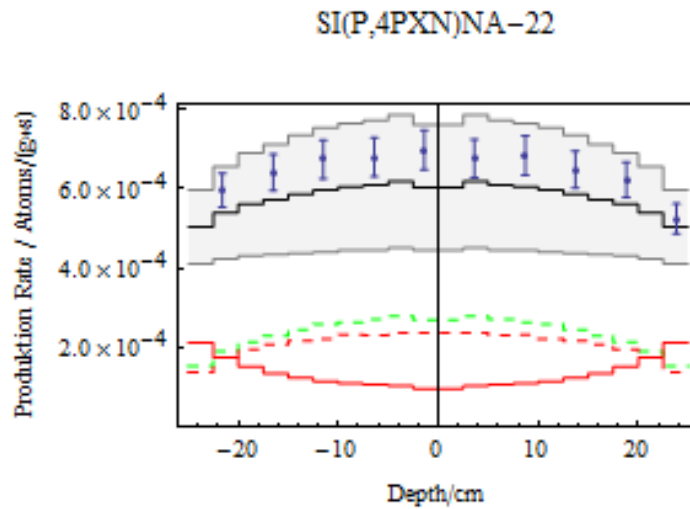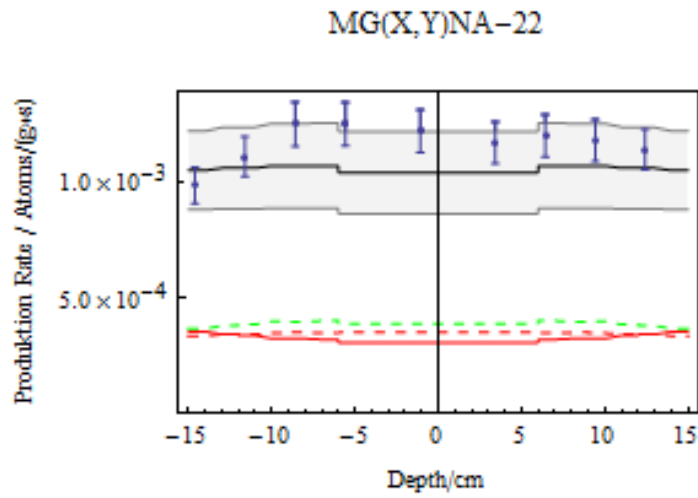

Figure C.24: Production of ^{22}Na from natural silicon in an artificial gabbro meteorite with a radius of 25 cm irradiated with 1600 MeV protons.

The residual nuclide production in a stony meteorite with a radius of 5 cm irradiated with 600 MeV protons.
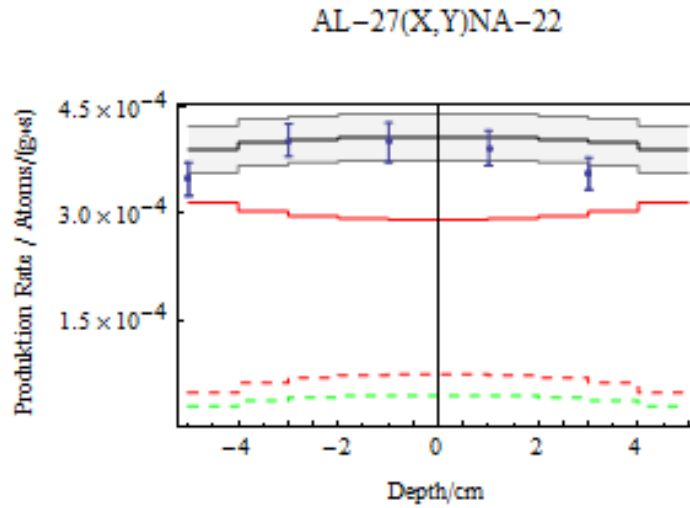
Figure C.25: Production of ^{22}Na from natural aluminum in an artificial gabbro meteorite with a radius of 5 cm irradiated with 600 MeV protons.
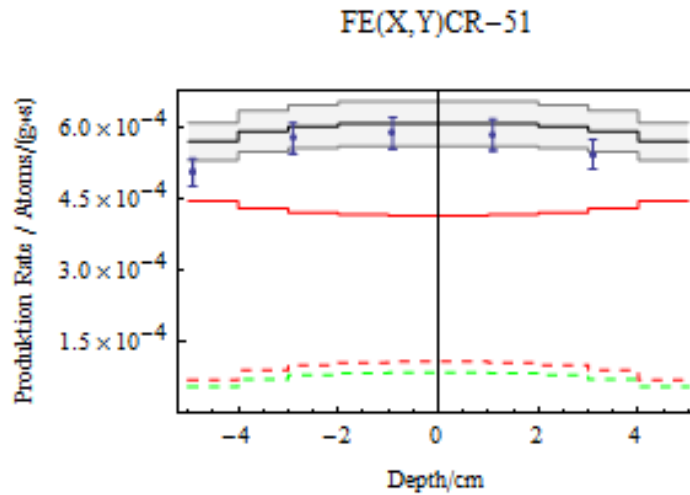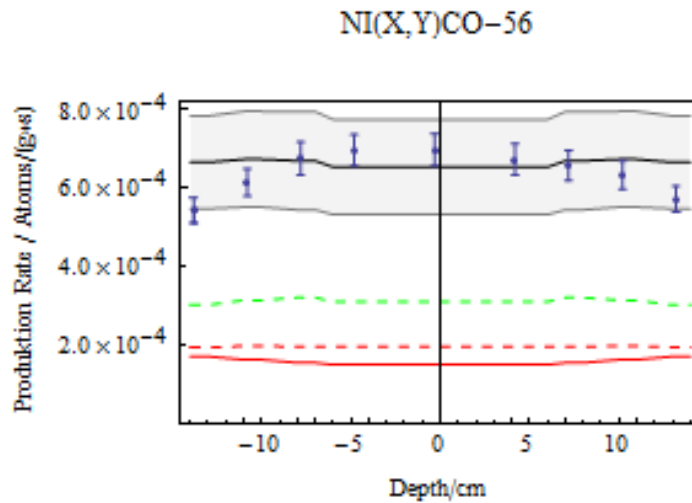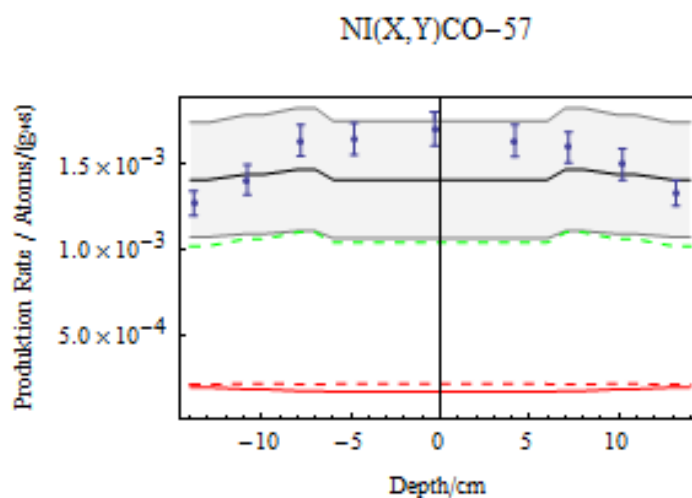

Figure C.26: Production of ^{51}Cr from natural iron in an artificial gabbro meteorite with a radius of 5 cm irradiated with 600 MeV protons.
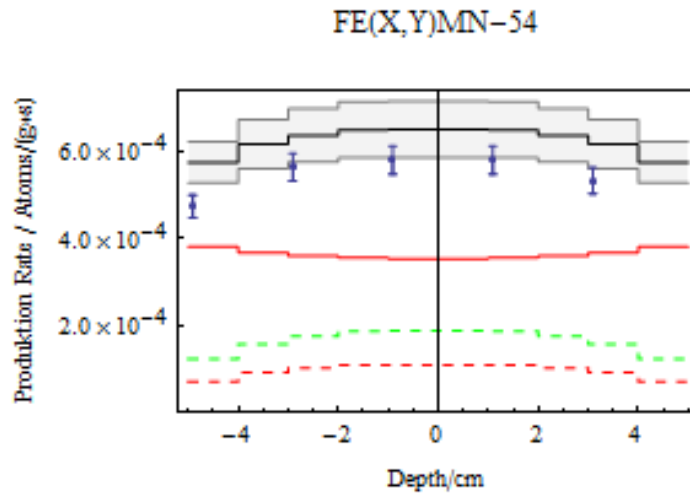
Figure C.27: Production of ^{54}Mn from natural iron in an artificial gabbro meteorite with a radius of 5 cm irradiated with 600 MeV protons.
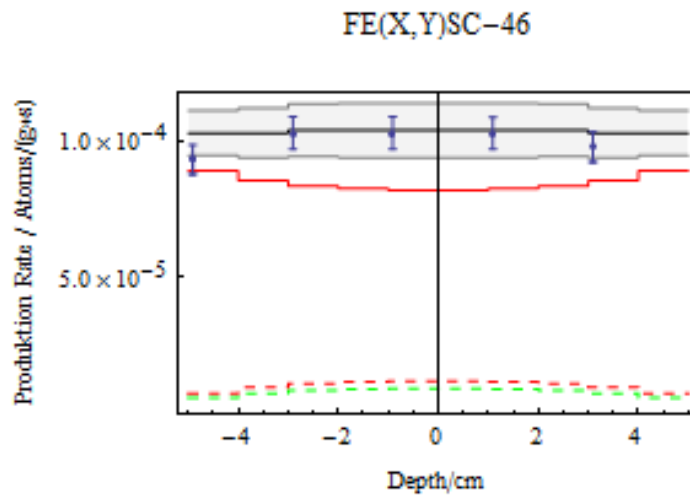
Figure C.28: Production of ^{46}Sc from natural iron in an artificial gabbro meteorite with a radius of 5 cm irradiated with 600 MeV protons.
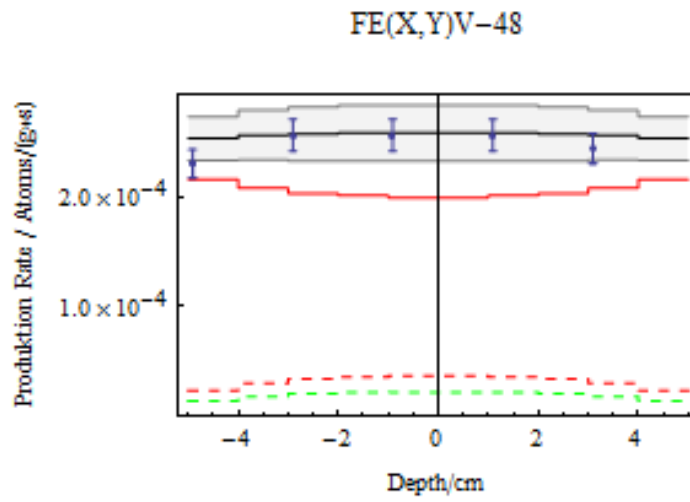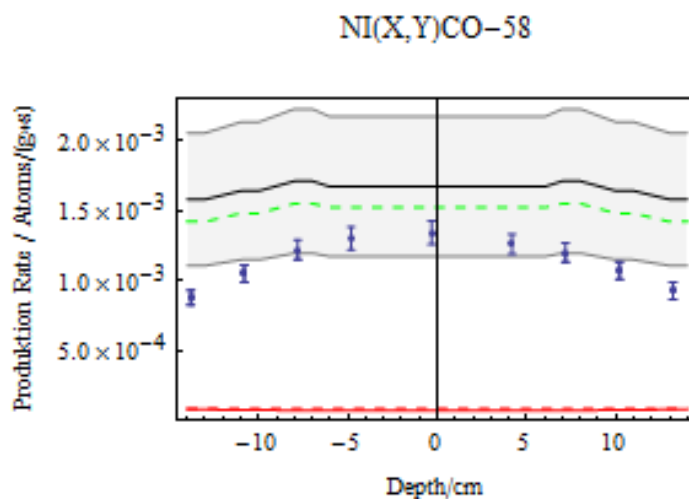
Figure C.29: Production of ^{48}V from natural iron in an artificial gabbro meteorite with a radius of 5 cm irradiated with 600 MeV protons.
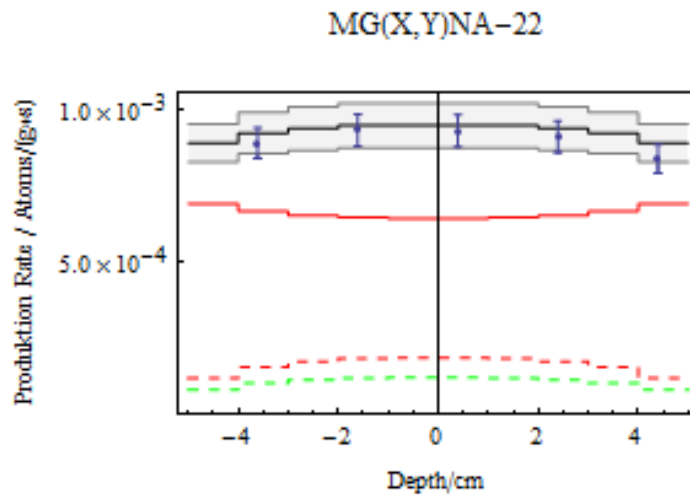
Figure C.30: Production of ^{22}Na from natural magnesium in an artificial gabbro meteorite with a radius of 5 cm irradiated with 600 MeV protons.
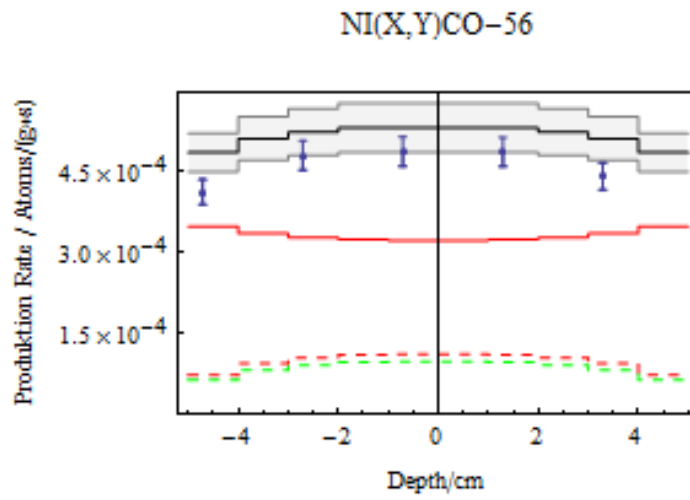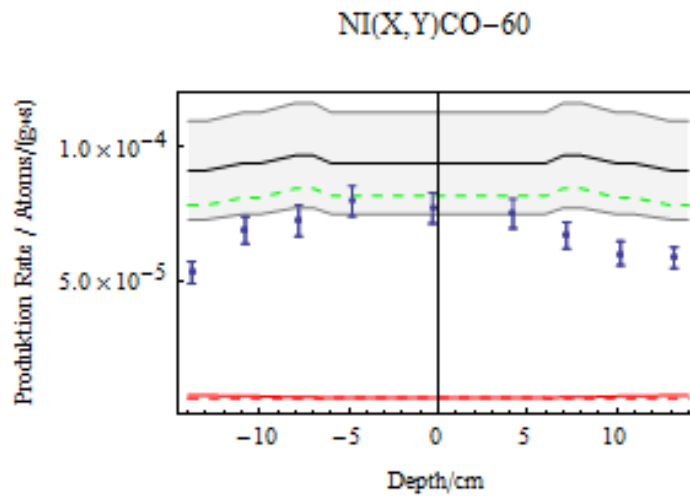
Figure C.31: Production of ^{56}Co from natural nickel in an artificial gabbro meteorite with a radius of 5 cm irradiated with 600 MeV protons.
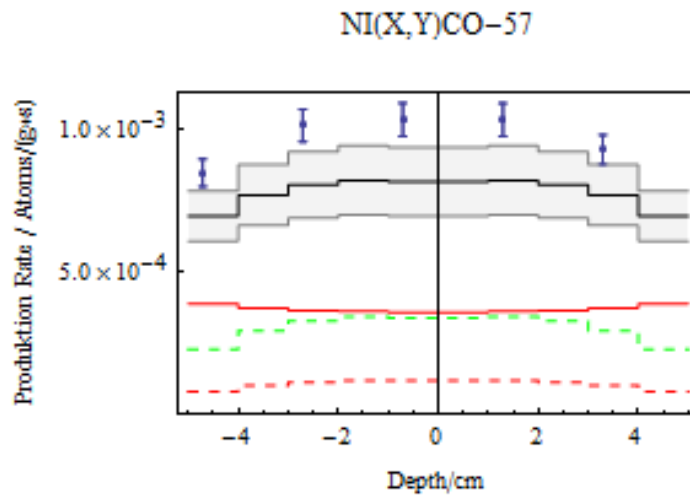
Figure C.32: Production of ^{57}Co from natural nickel in an artificial gabbro meteorite with a radius of 5 cm irradiated with 600 MeV protons.
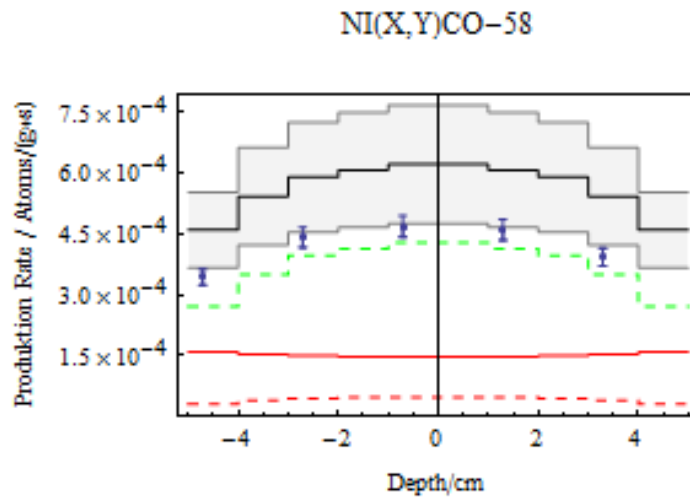
Figure C.33: Production of ^{58}Co from natural nickel in an artificial gabbro meteorite with a radius of 5 cm irradiated with 600 MeV protons.
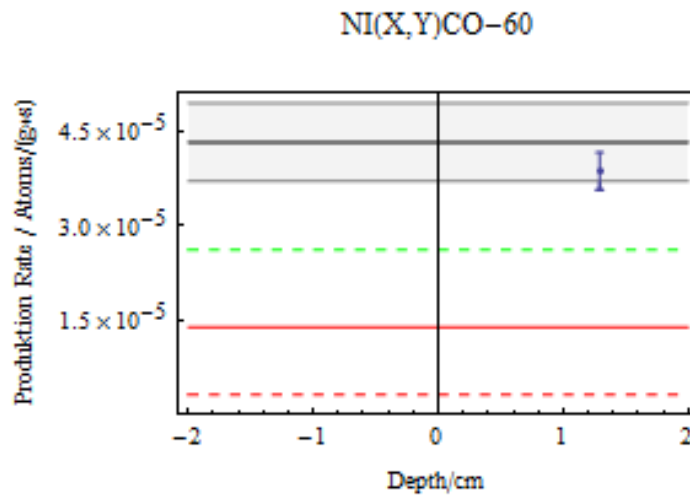
Figure C.34: Production of ^{60}Co from natural nickel in an artificial gabbro meteorite with a radius of 5 cm irradiated with 600 MeV protons.
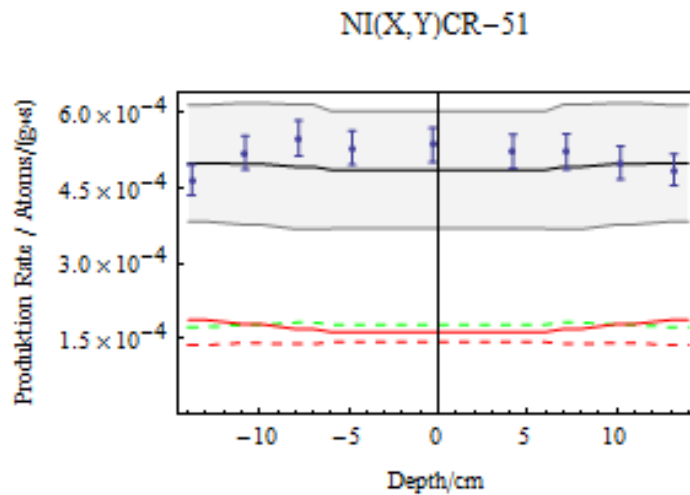
Figure C.35: Production of ^{51}Cr from natural nickel in an artificial gabbro meteorite with a radius of 5 cm irradiated with 600 MeV protons.
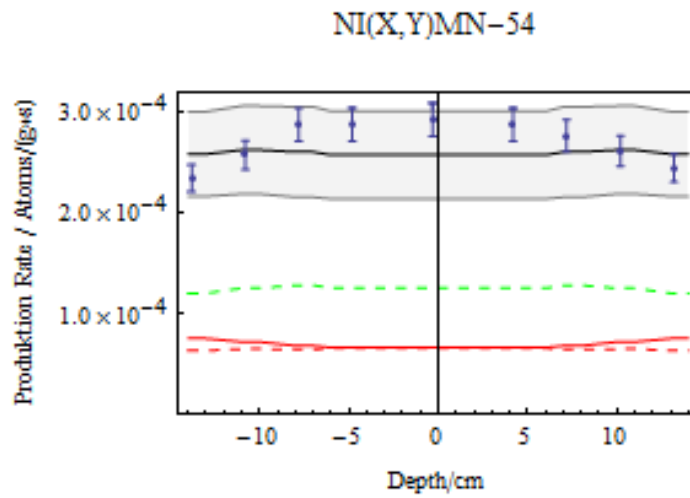

Figure C.36: Production of ^{54}Mn from natural nickel in an artificial gabbro meteorite with a radius of 5 cm irradiated with 600 MeV protons.
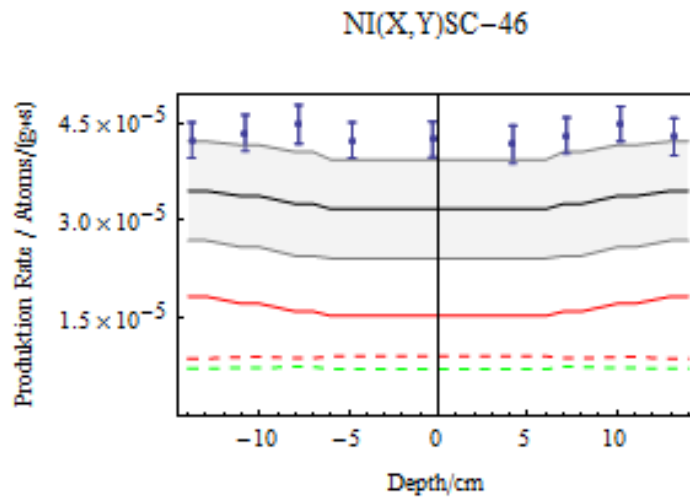
NI(X,Y)SC−46

Figure C.37: Production of ^{46}Sc from natural nickel in an artificial gabbro meteorite with a radius of 5 cm irradiated with 600 MeV protons.
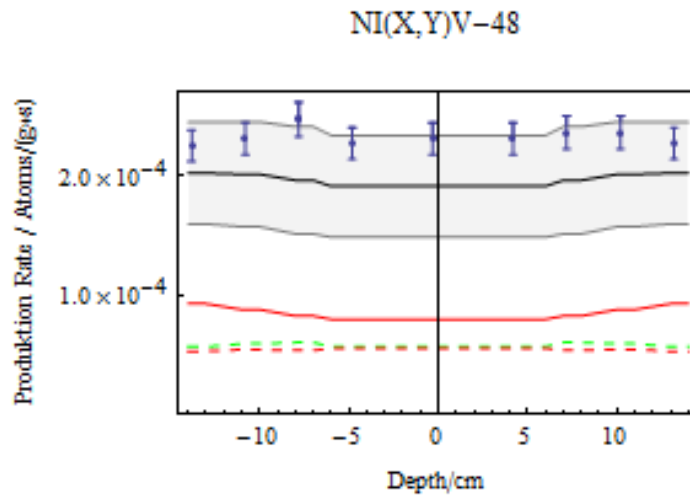
NI(X,Y)V−48

Figure C.38: Production of ^{48}V from natural nickel in an artificial gabbro meteorite with a radius of 5 cm irradiated with 600 MeV protons.

Figure C.39: Production of ^{22}Na from natural silicon in an artificial gabbro meteorite with a radius of 5 cm irradiated with 600 MeV protons.

The residual nuclide production in a stony meteorite with a radius of 15 cm irradiated with 600 MeV protons.
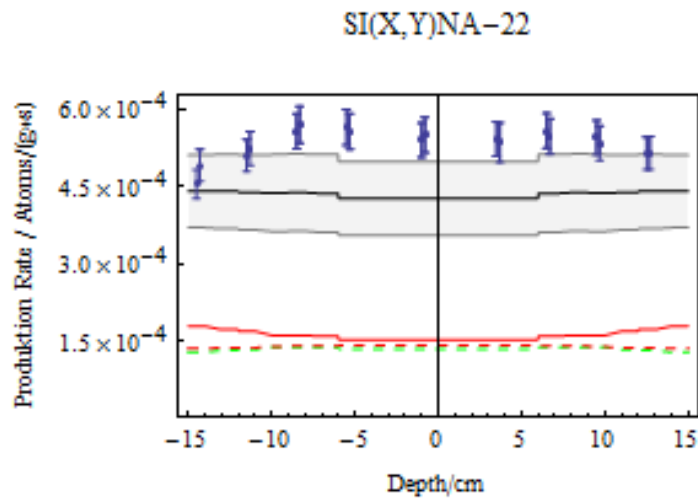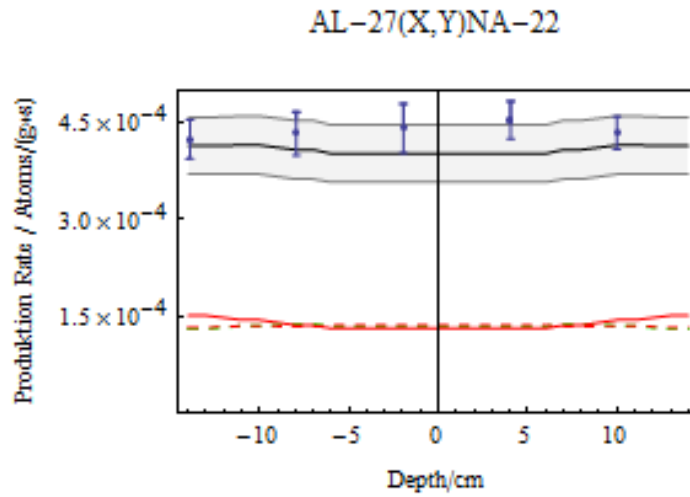

Figure C.40: Production of ^{22}Na from natural aluminum in an artificial gabbro meteorite with a radius of 15 cm irradiated with 600 MeV protons.

Figure C.41: Production of ^{51}Cr from natural iron in an artificial gabbro meteorite with a radius of 15 cm irradiated with 600 MeV protons.

Figure C.42: Production of ^{52}Mn from natural iron in an artificial gabbro meteorite with a radius of 15 cm irradiated with 600 MeV protons.

Figure C.43: Production of ^{54}Mn from natural iron in an artificial gabbro meteorite with a radius of 15 cm irradiated with 600 MeV protons.

Figure C.44: Production of ^{46}Sc from natural iron in an artificial gabbro meteorite with a radius of 15 cm irradiated with 600 MeV protons.
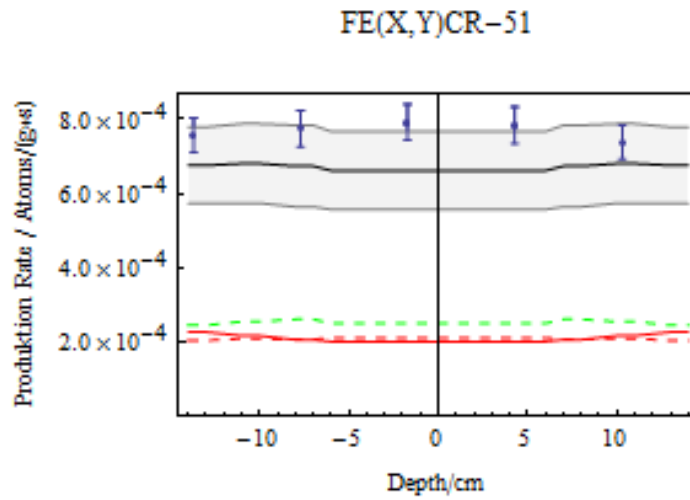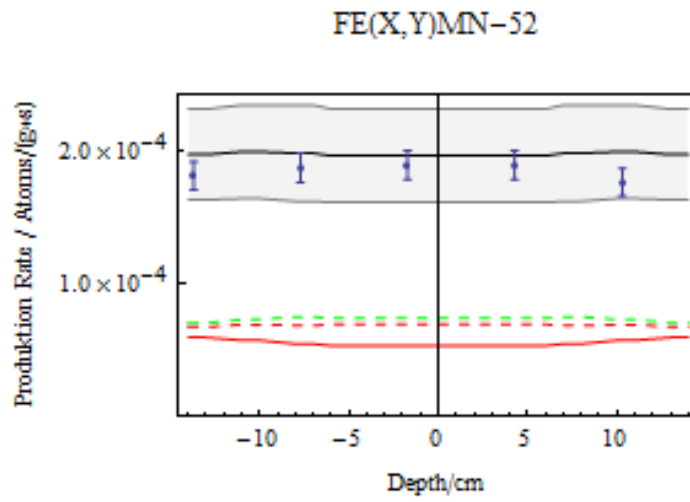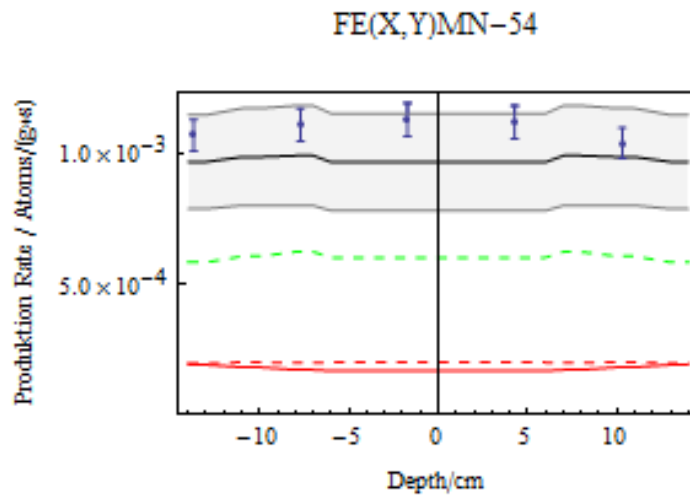

Figure C.45: Production of ^{48}V from natural iron in an artificial gabbro meteorite with a radius of 15 cm irradiated with 600 MeV protons.

Figure C.46: Production of ^{22}Na from natural magnesium in an artificial gabbro meteorite with a radius of 15 cm irradiated with 600 MeV protons.

Figure C.47: Production of ^{56}Co from natural nickel in an artificial gabbro meteorite with a radius of 15 cm irradiated with 600 MeV protons.

213

Figure C.48: Production of ^{57}Co from natural nickel in an artificial gabbro meteorite with a radius of 15 cm irradiated with 600 MeV protons.

Figure C.49: Production of ^{58}Co from natural nickel in an artificial gabbro meteorite with a radius of 15 cm irradiated with 600 MeV protons.
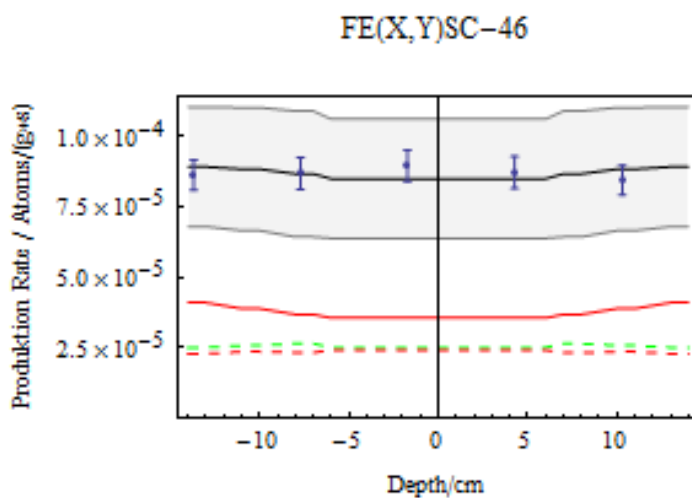
Figure C.50: Production of ^{60}Co from natural nickel in an artificial gabbro meteorite with a radius of 15 cm irradiated with 600 MeV protons.

Figure C.51: Production of ^{51}Cr from natural nickel in an artificial gabbro meteorite with a radius of 15 cm irradiated with 600 MeV protons.

NI(X,Y)MN-54

Figure C.52: Production of ^{54}Mn from natural nickel in an artificial gabbro meteorite with a radius of 15 cm irradiated with 600 MeV protons.

NI(X,Y)SC-46

Figure C.53: Production of ^{46}Sc from natural nickel in an artificial gabbro meteorite with a radius of 15 cm irradiated with 600 MeV protons.
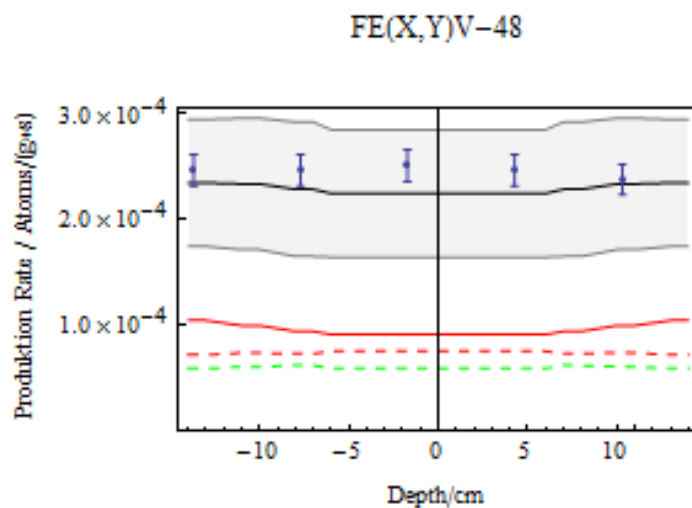
Figure C.54: Production of ^{48}V from natural nickel in an artificial gabbro meteorite with a radius of 15 cm irradiated with 600 MeV protons.
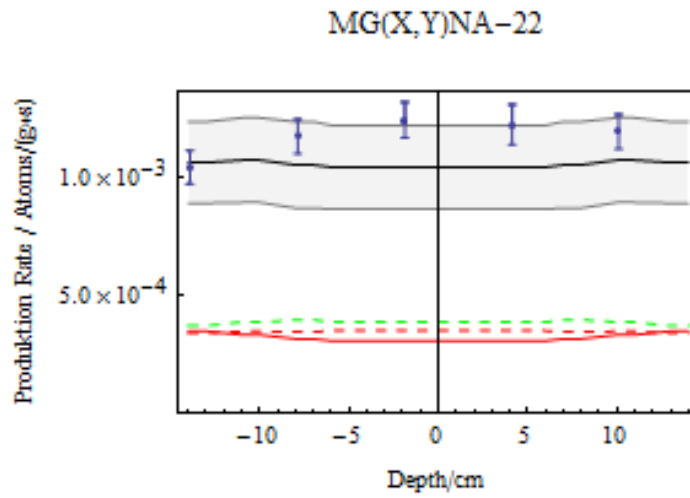

Figure C.55: Production of ^{22}Na from natural silicon in an artificial gabbro meteorite with a radius of 15 cm irradiated with 600 MeV protons.

The residual nuclide production in a stony meteorite with a radius of 25 cm irradiated with 600 MeV protons.

Figure C.56: Production of ^{22}Na from natural aluminum in an artificial gabbro meteorite with a radius of 25 cm irradiated with 600 MeV protons.
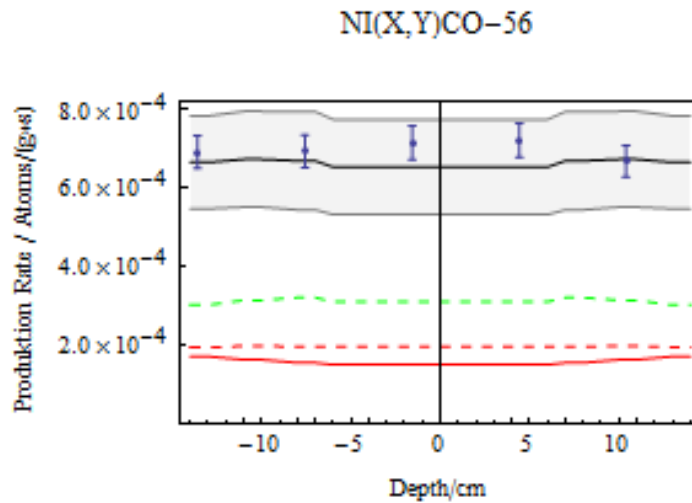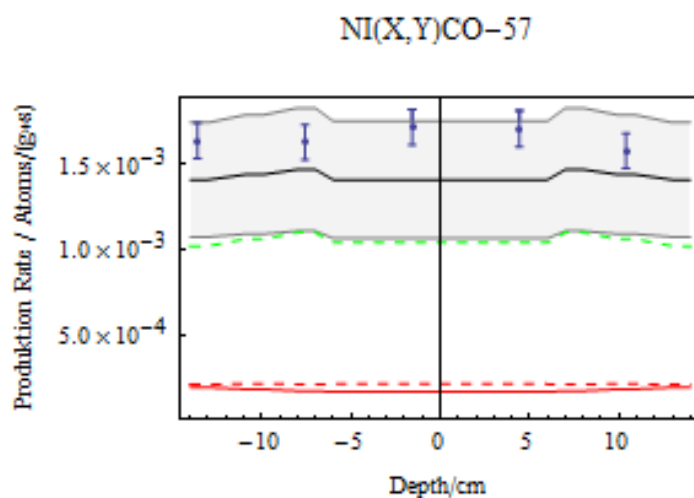

Figure C.57: Production of ^{51}Cr from natural iron in an artificial gabbro meteorite with a radius of 25 cm irradiated with 600 MeV protons.

Figure C.58: Production of ^{52}Mn from natural iron in an artificial gabbro meteorite with a radius of 25 cm irradiated with 600 MeV protons.
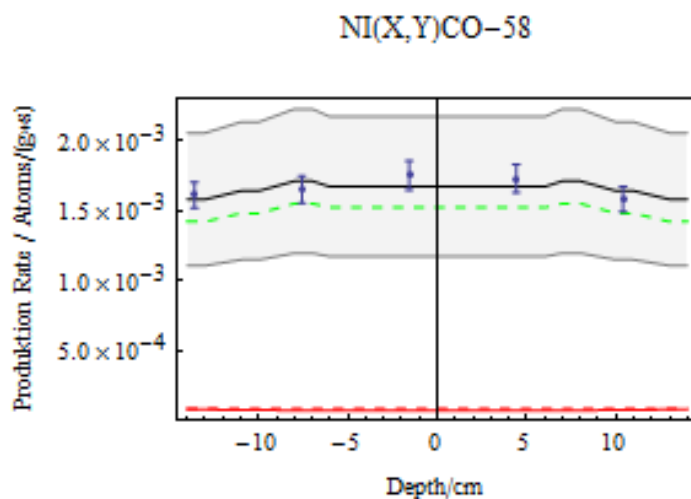

Figure C.59: Production of ^{54}Mn from natural iron in an artificial gabbro meteorite with a radius of 25 cm irradiated with 600 MeV protons.
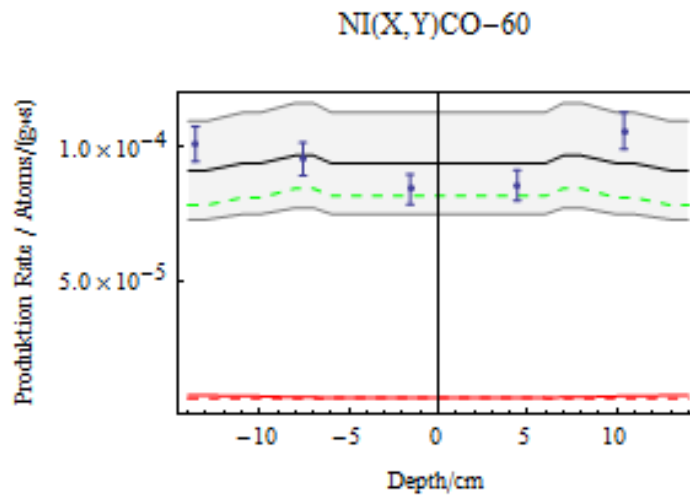
Figure C.60: Production of ^{46}Sc from natural iron in an artificial gabbro meteorite with a radius of 25 cm irradiated with 600 MeV protons.

Figure C.61: Production of ^{48}V from natural iron in an artificial gabbro meteorite with a radius of 25 cm irradiated with 600 MeV protons.

Figure C.62: Production of ^{22}Na from natural magnesium in an artificial gabbro meteorite with a radius of 25 cm irradiated with 600 MeV protons.

Figure C.63: Production of ^{56}Co from natural nickel in an artificial gabbro meteorite with a radius of 25 cm irradiated with 600 MeV protons.
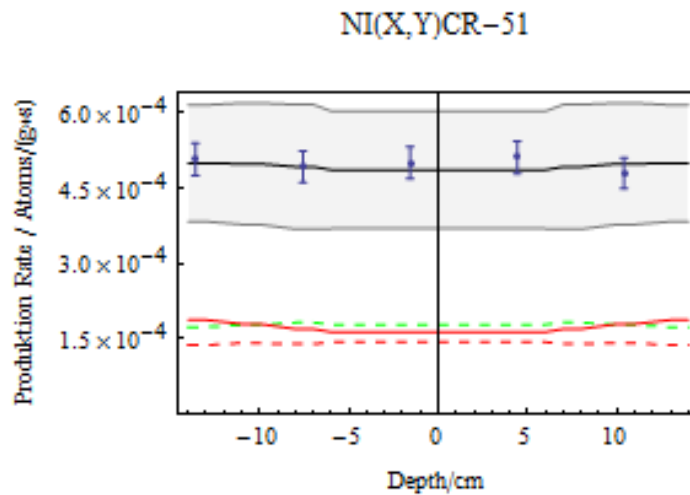
Figure C.64: Production of ^{57}Co from natural nickel in an artificial gabbro meteorite with a radius of 25 cm irradiated with 600 MeV protons.

Figure C.65: Production of ^{58}Co from natural nickel in an artificial gabbro meteorite with a radius of 25 cm irradiated with 600 MeV protons.
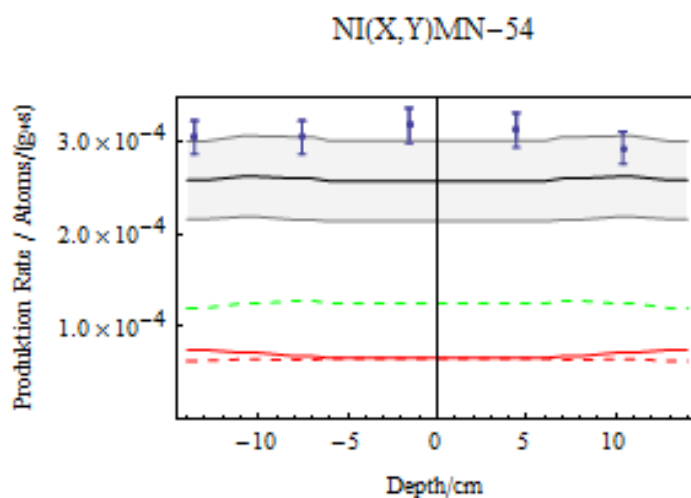
Figure C.66: Production of ^{60}Co from natural nickel in an artificial gabbro meteorite with a radius of 25 cm irradiated with 600 MeV protons.

Figure C.67: Production of ^{51}Cr from natural nickel in an artificial gabbro meteorite with a radius of 25 cm irradiated with 600 MeV protons.

Figure C.68: Production of ^{54}Mn from natural nickel in an artificial gabbro meteorite with a radius of 25 cm irradiated with 600 MeV protons.
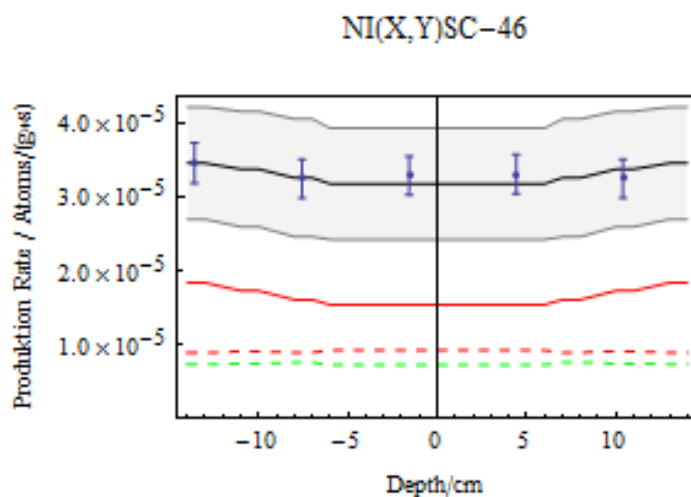

Figure C.69: Production of ^{46}Sc from natural nickel in an artificial gabbro meteorite with a radius of 25 cm irradiated with 600 MeV protons.
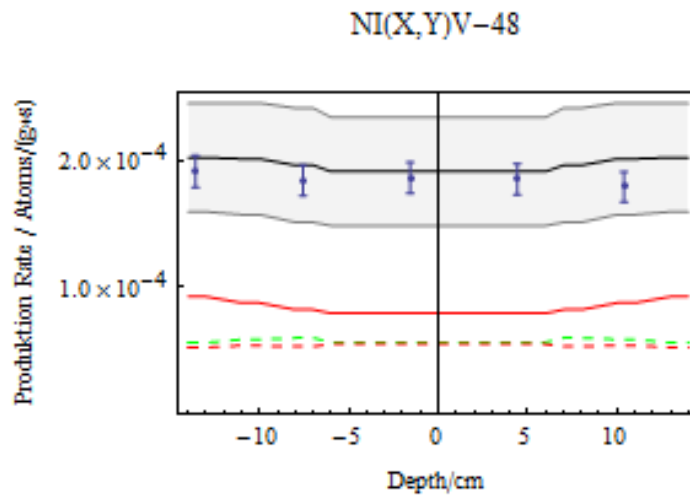
Figure C.70: Production of ^{48}V from natural nickel in an artificial gabbro meteorite with a radius of 25 cm irradiated with 600 MeV protons.
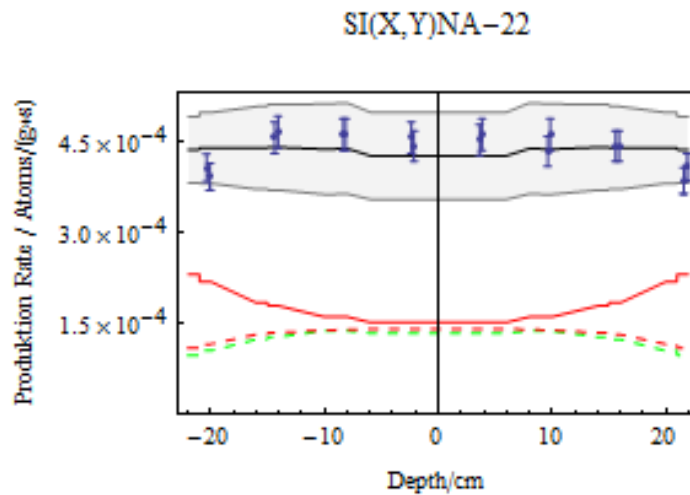

Figure C.71: Production of ^{22}Na from natural silicon in an artificial gabbro meteorite with a radius of 25 cm irradiated with 600 MeV protons.